

# 第五届全国低场核磁共振 技术与应用研讨会

## 论文集



上海理工大学

主办

中国·上海



纽迈电子科技有限公司

协办

**食品与农业领域**..... 1

1 用低场核磁共振法快速测定明胶的凝冻强度-李思东 ..... 2

2 低场核磁共振技术在果胶结构变化方面的研究-张锦胜 ..... 5

3 利用低场和磁共振技术检测哈密瓜品质的研究-周然 ..... 9

4 粮油食品低场核磁共振检测技术研究进展-邵小龙 ..... 12

5 小麦源库关系的核磁共振研究-杜光源..... 15

6 低场核磁共振技术在食品中的应用（油脂或黄酒领域）-王欣..... 18

7 核磁共振波谱法及其在食品脂质分析中的研究进展-刘纯友 ..... 23

8 大豆油煎炸过程理化指标与LF-NMR弛豫特性的相关性研究-史然，王欣，刘宝林，卢海燕，赵婷婷...24

9 低场核磁共振技术检测煎炸油品质-王永巍，王欣，刘宝林，史然，杨培强.....32

10 羟自由基导致肉类肌原纤维蛋白氧化和凝胶性降低-李银，李侠，张春晖，孙红梅，董宪兵.....37

11 A PCR based magnetic assembled sensor for ultrasensitive DNA detection- Wei Ma,z Honghong Yin,z Liguang Xu, Libing Wang, Hua Kuang andChuanlai Xu.....44

12 Discrimination of Edible Vegetable Oil Adulteration with Used Frying Oil by Low Field Nuclear Magnetic Resonance-Qing Zhang & Ahmed S. M. Saleh & Qun Shen.....47

13 Effect of Water Migration between Arabinoxylans and Gluten on Baking Quality of Whole Wheat Bread Detected by Magnetic Resonance Imaging (MRI) -- Juan Li, Ji Kang, Li Wang, Zhen Li, Ren Wang, Zheng Xing Chen and Gary G. Hou ..... 58

14 Rapid detection of Cronobacter sakazakii in dairy food by biofunctionalized magnetic nanoparticle based on nuclear magnetic resonance -- Yu Zhao , Yuting Yao , Ming Xiao , Yan Chen , Charles C.C. Lee , Li Zhang , Kelvin Xi Zhang , Shiping Yang , Ming Gu ..... 66

**生命科学领域**..... 74

1 多功能配位聚合物纳米粒子的合成及应用-杨仕平..... 75

2 间充质干细胞中风治疗中的活体示踪研究-张春富..... 78

3 球状大分子结构 MRI 分子探针及其肿瘤靶向成像应用研究-谭明乾.....81

4 High-Performance Iron-oxide-based MRI Contrast Agents-高锦豪.....83

5 磷酸钙/聚合物复合组装纳米给药系统-段友容.....84

**橡胶、材料、高分子领域**..... 85

1 WATER IN WOOD STUDIED BY TIME - DOMAIN NMR-张明辉 .....86

2 轮胎胶粉干法再生过程中自由基浓度与脱硫活化效果的相关性研究-曾冬.....89

3 低场核磁共振技术在尾砂充填料浆硬化过程中的应用-艾凯明.....92

4 低场核磁共振技术在高分子领域中的最新应用-杨翼.....95

5 核磁共振技术在木材内水分迁移研究中的应用现状与前景-高鑫.....100

6 A Method To Measure Internal Contact Angle in Opaque Systems by Magnetic Resonance Imaging- Weiqin Zhu,Ye Tian,Xuefeng Gao, and Lei Jiang.....104

7 轮胎胶粉干法再生过程中自由基浓度与脱硫活化效果的相关性研究-曾冬.....110

<b>地球物理/多孔介质领域</b> .....	111
1 低场核磁技术应用于水泥水化和水泥基材料孔结构表征的研究-姚武 .....	112
2 低场核磁共振技术在岩石冻融损伤研究中的应用-李杰.....	121
3 多维核磁共振录井技术应用探讨-杜焕福.....	125
4 微流动可视化的新进展-程毅翀.....	133
5 影响水泥基材料中低场核磁共振信号诸因素探讨-李奇.....	139
6 多因素耦合作用下砂岩的核磁共振测试研究-田维刚.....	141
7 钻井液核磁共振录井技术及其应用-王志战.....	144
8 核磁共振确定岩石孔隙结构及应用-刘堂宴.....	145
9 岩石 T2-G 实验采集参数自动匹配方法及应用-吴飞.....	145
10NMR 技术在非常规油气层评价中的应用探讨--王志战, 秦黎明, 陆黄生, 蔡清, 杨培强.....	146
11 冻融循环条件下岩石核磁共振特性的试验研究--周科平, 李杰林, 许玉娟, 张亚民, 杨培强, 陈路平.....	148
12煤中水可动性的核磁共振响应及其影响因素--吕玉民, 胡爱梅, 汤达祯, 宋波, 梁为, 许浩, 林文姬, 胡雄.....	155
<b>其它</b> .....	159
一种微型核磁共振探头的制作工艺-陆荣生 .....	160

## 食品与农业领域

# 用低场核磁共振法快速测定明胶的凝冻强度

李思东 广东海洋大学  
杨培强 上海纽迈电子科技有限公司

## 明胶简介

❖明胶是胶原蛋白的水解产物，是一种无脂肪的高蛋白，且不含胆固醇，明胶按用途可分为以下四类：

- 食用明胶
- 药用明胶
- 工业明胶
- 照相明胶



❖食用明胶作为一种增稠剂，广泛使用于食品工业：果冻、食用色素、高级软糖、冰激凌、干醋、酸奶、冷冻食品等。在化工行业主要用作粘合、乳化和高级化妆品等制作的原料。

Guangdong Ocean University,Zhanjiang,China,524088

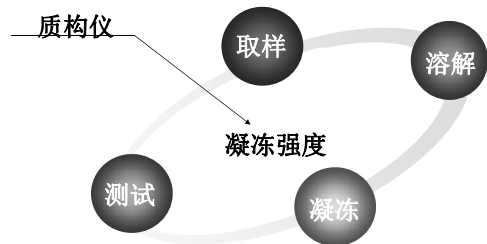
## 明胶的凝冻强度

- 明胶的凝冻强度（俗称冻力）测试：在规定的检测条件下，使用专业的明胶冻力检测仪，将含明胶6.67%的胶液在专用冻力测试瓶中溶解并冷凝一定时间后，冻力检测仪器探头压入胶冻表面4mm时所施加的力，g
- 凝冻强度决定了明胶产品的售价，所以快速测定明胶凝冻强度对研究和生产都具有重要意义。



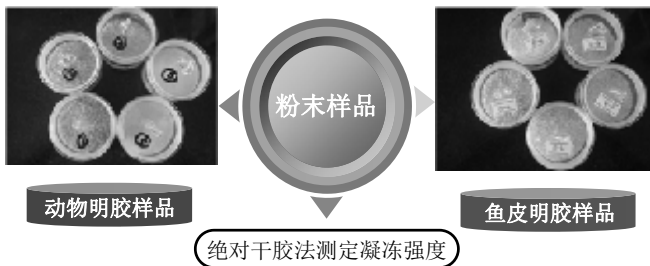
Guangdong Ocean University,Zhanjiang,China,524088

## 质构仪测定明胶凝冻强度



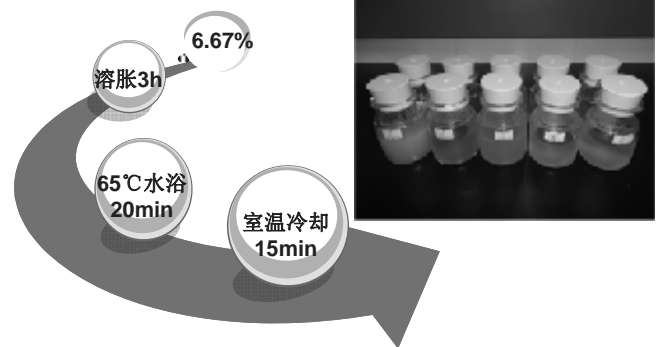
Guangdong Ocean University,Zhanjiang,China,524088

## (1) 明胶样品水分测定



Guangdong Ocean University,Zhanjiang,China,524088

## (2) 溶解明胶样品



Guangdong Ocean University,Zhanjiang,China,524088

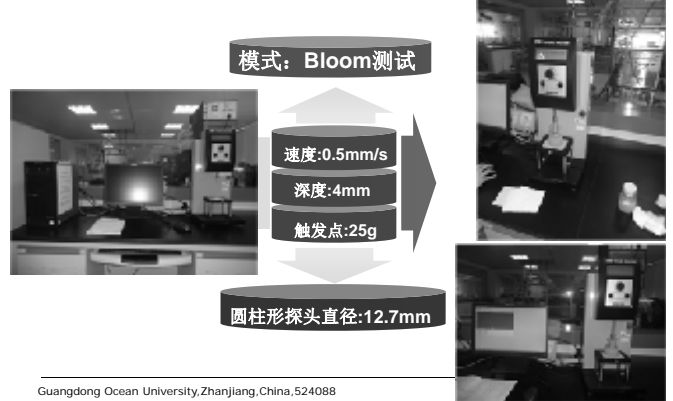
### (3) 明胶溶液的凝冻



(10±0.1)°C条件  
冷冻16~18h  
(温度要求苛刻,  
冷凝时间)

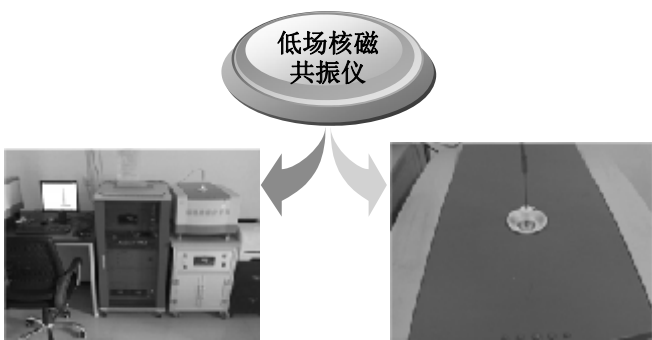
Guangdong Ocean University,Zhanjiang,China,524088

### (4) 质构仪测试



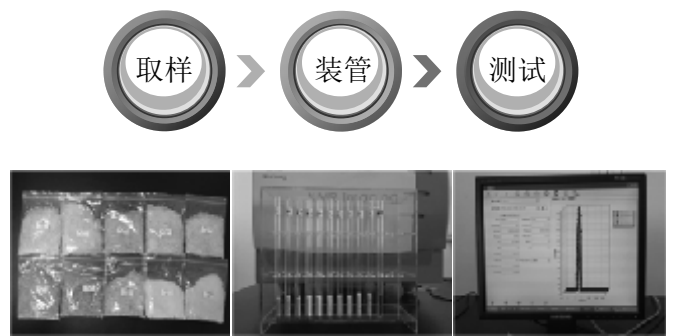
Guangdong Ocean University,Zhanjiang,China,524088

### 用低场核磁共振仪测定明胶的凝冻强度



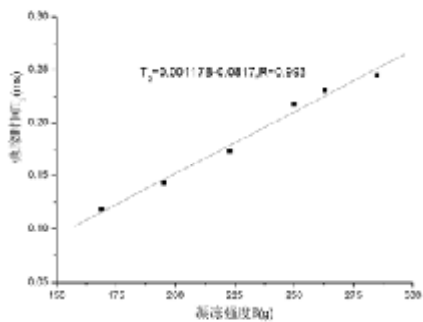
Guangdong Ocean University,Zhanjiang,China,524088

### 低场核磁共振仪测定明胶凝冻强度



Guangdong Ocean University,Zhanjiang,China,524088

### 图1 凝冻强度(B)与弛豫时间(T<sub>2</sub>)的关系



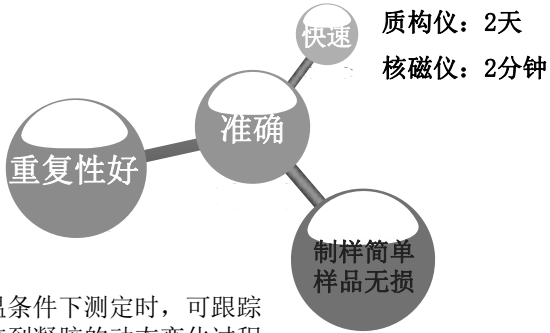
Guangdong Ocean University,Zhanjiang,China,524088

### 明胶分子量(M)、凝冻强度(B)及弛豫时间(T<sub>2</sub>)的关系

从理论上分析, 明胶的凝冻强度高, 则分子量大, 弛豫时间增加, 最终凝冻强度与弛豫时间呈良好的线性关系。

Guangdong Ocean University,Zhanjiang,China,524088

### 低场核磁共振法的优点



变温条件下测定时, 可跟踪  
溶胶到凝胶的动态变化过程

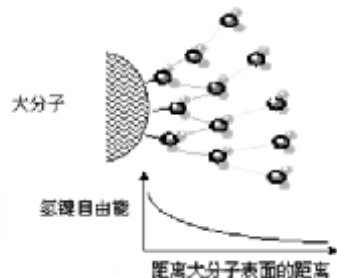
Guangdong Ocean University, Zhanjiang, China, 524088



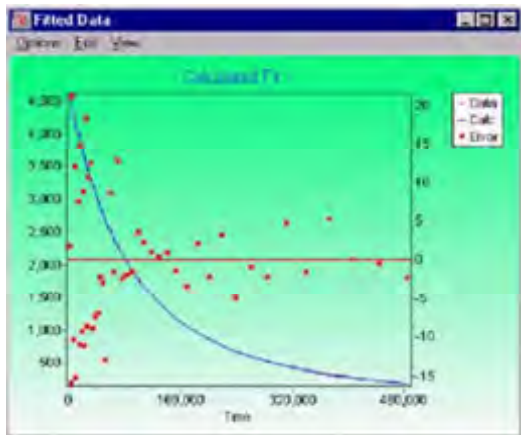
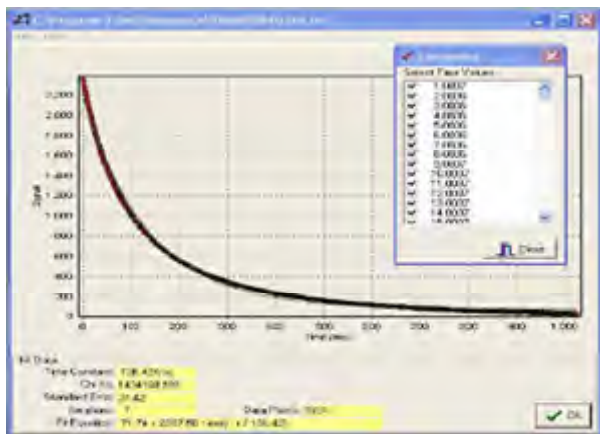
# 南昌大学

张锦胜

## 自由水与束缚水的区分



## 国外软件的计算方法



## 多组分拟合

$$y = Ae^{-\frac{t}{T_1}} + Be^{-\frac{t}{T_2}} + Ce^{-\frac{t}{T_3}}$$

In the above case the single exponential (one component) with time constant  $T_0$  approximates to the double exponential (two components) with time constants  $T_1$  and  $T_2$ . The approximation becomes more valid if  $T_1$  is very similar to  $T_2$ .

Fitting to a double exponential can only be valid if  $T_1$  and  $T_2$  can be resolved given the signal to noise ratio of the data (if  $T_1$  and  $T_2$  are similar the difference between the double and the single exponential may be obscured by the noise present in the data set). This principle may be extended to multiple exponentials (i.e. a triple exponential function may be well approximated by a double exponential function).



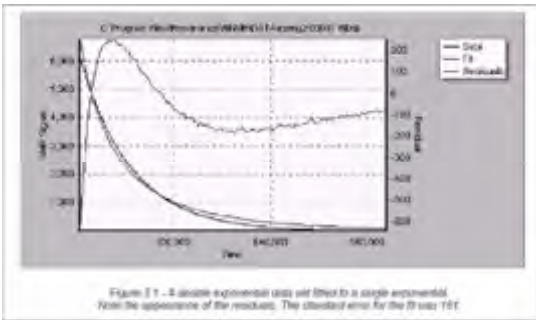


Figure 3.1 - 2 double exponential data set fitted to a single exponential. Note the appearance of the residuals. The standard error for the fit was 161.

- 对于单组分的拟合结果,显示为标准误差为161

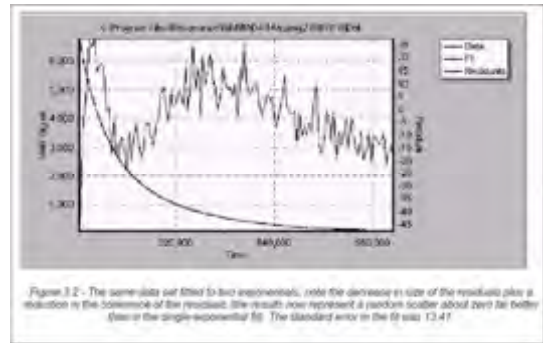


Figure 3.2 - The same data set fitted to two exponentials. Note the decrease in size of the residuals plus a reduction in the coherence of the residuals. The results now represent a random scatter about zero (a) better than in the single-exponential fit. The standard error in the fit was 13.47.

- 采用双组分拟合,标准误差下降为13.4

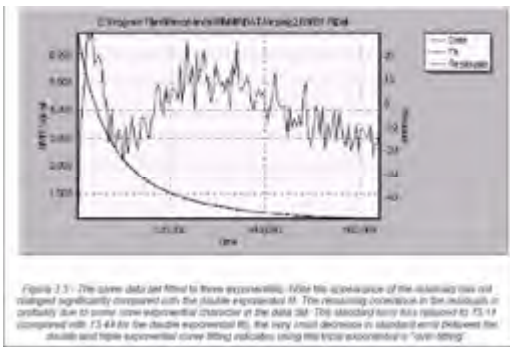


Figure 3.3 - The same data set fitted to three exponentials. Note the appearance of the decreasing size of residuals significantly compared with the double exponential fit. The remaining coherence in the residuals is probably due to some lower exponential character in the data set. The standard error has improved to 13.11 compared with 13.47 for the double exponential fit. The very small decrease in standard error (0.04) over the double and triple exponential curve fitting indicates using the triple exponential is "over-fitting".

- 采用三组分拟合时,标准误差为13.11,并没有明显下降,因此,从统计学上判断,存在过度拟合,也就是从统计学上说,2组分更有说服力。



Chi<sup>2</sup> is defined by the equation:

$$\chi^2 = \sum_{i=1}^n \left( \frac{y_i - \hat{y}_i}{\sigma_i} \right)^2$$

where  $n$  is the number of data points,  $y_i$  are the experimental data values and  $\hat{y}_i$  are the fitted data values.  $\sigma_i$  is assumed to be 1 for all data points.

R<sup>2</sup> (also known as the multiple coefficient of determination) is defined by the following equation:

$$R^2 = 1 - \frac{\sum_{i=1}^n (y_i - \hat{y}_i)^2}{\sum_{i=1}^n (y_i - \bar{y})^2}$$

where  $n$  is the number of data points,  $y_i$  are the experimental data values,  $\hat{y}_i$  are the fitted data values and  $\bar{y}$  is the mean of the experimental data values.

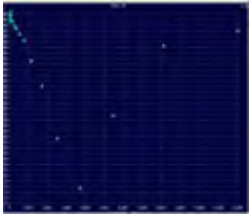
SSE Error, Standard Error  
The standard error is defined by the equation:

$$Std. Error = \sqrt{\frac{\sum_{i=1}^n (y_i - \hat{y}_i)^2}{n - k}}$$

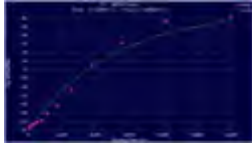
where  $n$  is the number of data points,  $y_i$  are the experimental data values,  $\hat{y}_i$  are the fitted data values and  $k$  is the number of independent variables fitted.

The basic question is: if multiple exponential components are present, are they resolvable given the single to noise ratio of the data set?

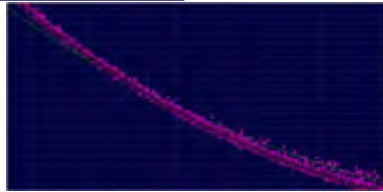
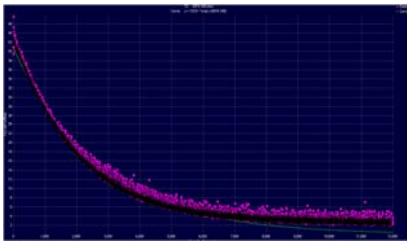
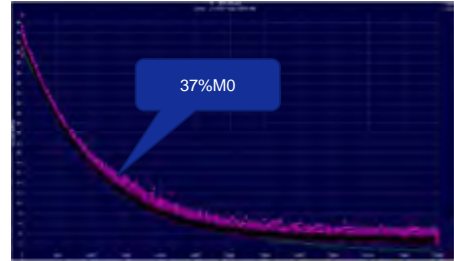
- We need to define criteria that enable us to establish when it is appropriate to fit to a single (or double/triple/greater) exponential. One way is to look for a decrease in the standard error (monitoring coherence in the residuals).
- To establish whether a data set should be fitted to a single or multiple exponential first fit the data using a single exponential.
- Plot the residuals on screen. If the fit is appropriate no coherence should be seen in the residuals (i.e. the residuals should not form a smooth function but should be a random distribution about zero).
- On increasing the number of exponentials the standard error should decrease, the residuals should tend to a random scatter about zero.
- If the standard error does not reduce significantly on increasing the number of exponentials this is normally a good indication that the data has been "over-fitted" - i.e. that number of exponentials either do not exist in the data set or that number of exponentials may not be resolved given the signal to noise ratio of the data set. Note that over-fitting nearly always results in meaningless fitting parameters.
- To summarise, increasing the number of fitting parameters (number of exponentials) will always result in a better fit, but not necessarily result in meaningful results.



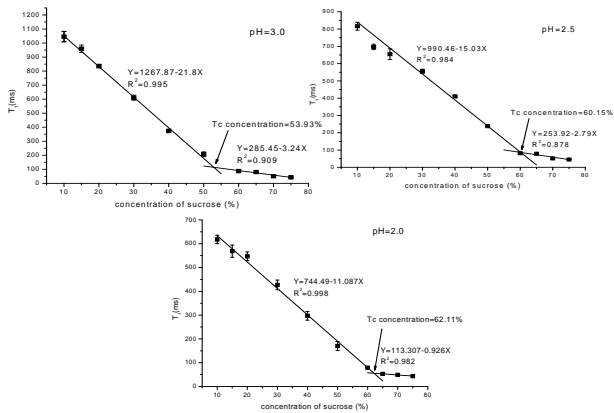
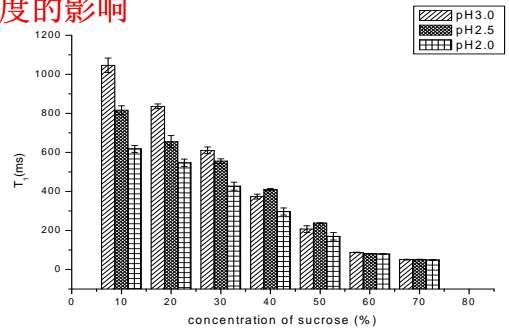
T1测量采用对数布点对于高T1值样品  
反转点前布点太密，均匀布点间隔太大，  
引入误差。



$$T_c = \ln 2 * T1$$



目前做的一些研究  
pH对高甲氧基果胶NMR转折点蔗糖浓度的影响



### 研究发现

- 当蔗糖浓度低于40%时，增加蔗糖浓度或是降低pH都能显著降低果胶体系的弛豫时间 $T_1$ 。当蔗糖浓度处于50%~65%时，这种变化开始变缓，此时果胶开始由流变态向凝胶态转变。
- 果胶体系的弛豫时间 $T_1$ 在蔗糖浓度50%~65%之间会出现NMR转折点，转折点蔗糖浓度即为果胶发生结构变化或由凝胶态向流变态转变的蔗糖浓度，从微观上测得了果胶结构变化的共溶物含量。
- pH降低，果胶体系的NMR转折点蔗糖浓度增大，这说明pH降低，果胶结构发生改变所需的共溶物（蔗糖）含量增多。这可能是因为pH的降低使得果胶分子结合的更加紧密，分子间距离减小，网状结构体积减小，结构所能截留的水分含量下降，多余的水分需要更多的共溶物进行疏水相互作用才能使得体系在结构上发生改变。

## NMR生物传感器

- T1/T2生物传感器
- Gd(III)具有很高的顺磁性
- Gd(III)类微生物传感器的设计与制备

谢 谢

## 利用核磁共振技术 检测哈密瓜品质的研究

报告人：周然 副教授  
单位：上海海洋大学食品学院

www.themegallery.com

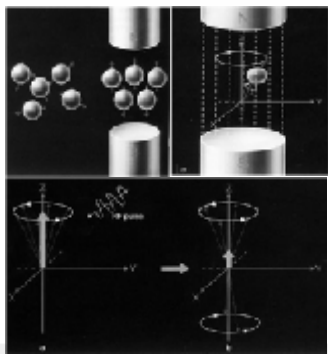
### 主要内容

- 核磁共振技术简介
- 利用NMR技术对哈密瓜的品质进行检测
  - 获得哈密瓜的T1、T2加权像
  - 获得哈密瓜的正常果肉和腐败果肉的T2弛豫时间及含水率
  - 获得哈密瓜的T2-MAP图

### 核磁共振技术简介

#### 基本原理

- 利用H<sup>+</sup>质子在梯度磁场和射频脉冲的作用下产生磁共振现象的原理
- 在层面选定梯度起作用的同时，施加一个有选择性的射频脉冲激励被成像物体
- 然后通过射频线圈接收被激发质子所发出的共振信号，通过空间编码技术和傅立叶转换将其转变成图像信息



### 核磁共振技术简介

- 具有非侵害性，可以对同一果蔬样品重复检测
- 具有非破坏性优点，果蔬材料不需预处理
- 对果蔬材料无放射损伤
- 内部剖面图像和水，糖，油，硬度等信息
- 目前在这方面的研究国内刚刚开始。

### 材料和方法

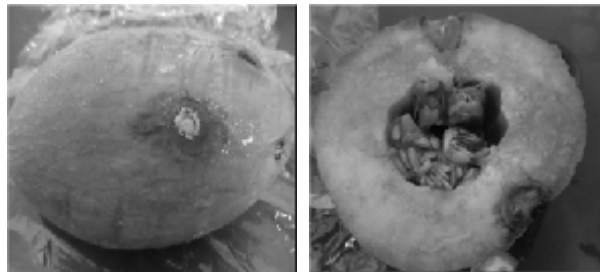
#### 实验材料

- 哈密瓜、天平、含水率测定标样

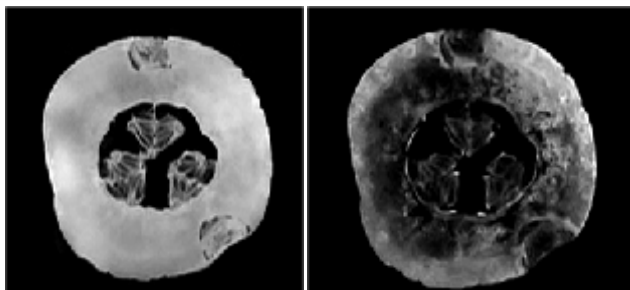
#### 实验仪器

- AniMR-150核磁共振成像分析系统，共振频率1 2.308 MHz，探头线圈直径为150mm
- 实验温度32.00℃

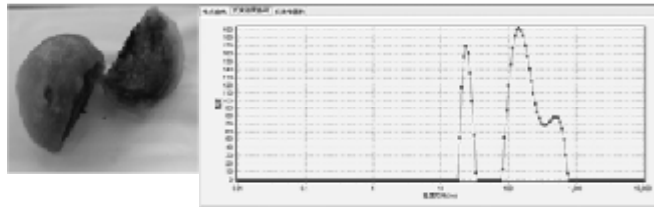
### 1、哈密瓜整体图片和横切照片



### 2、哈密瓜的T1加权像和T2加权像

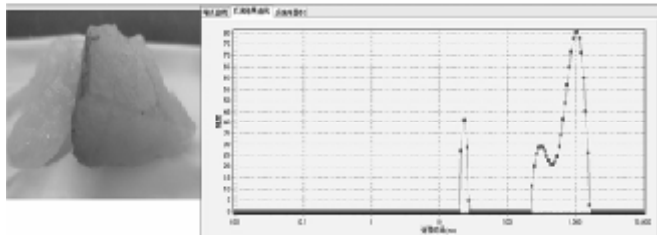


### 3、腐烂果肉部分T2值测试结果



序号	峰位置T2/ms	峰高/任意单位	峰宽/任意单位	峰面积/任意单位	占比
1	110.000	100.000	100.000	100.000	0.228
2	277.000	148.000	200.000	200.000	0.623
3	1000.000	1000.000	1000.000	1000.000	0.149

### 3、正常果肉部分T2值测试结果

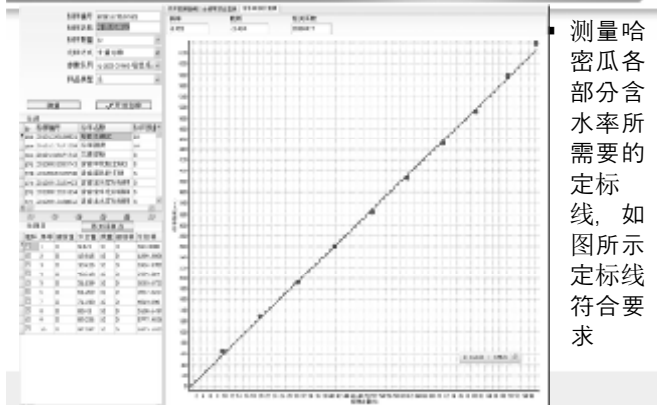


序号	峰位置T2/ms	峰高/任意单位	峰宽/任意单位	峰面积/任意单位	占比
1	175.000	100.000	100.000	100.000	0.100
2	277.000	148.000	200.000	200.000	0.200
3	1000.000	1000.000	1000.000	1000.000	0.700

### 3、结论

- 可以清晰的发现腐烂部分弛豫时间要比正常部分低的多。
- 所以能很好的解释为什么在T2加权像中，腐烂部分是呈现暗色，而正常果肉部分呈现亮色，形成鲜明的对比，可以更直观的看出哈密瓜内部结构和特征区域的变化。

### 4、含水率测定



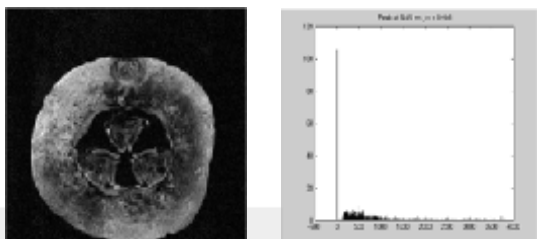
### 4、哈密瓜各部分含水率测试结果

检测名称	水标编号	水标名称	样品名称	测量时间	测含水量	含水量(质量%)
	2012102903521	哈密瓜测试	哈密瓜-果肉	2012-10-29 下午01:14:26	77.317%	4.35
	2012102903521	哈密瓜测试	哈密瓜-籽	2012-10-29 下午01:13:28	73.352%	2.006
	2012102903521	哈密瓜测试	哈密瓜-腐烂	2012-10-29 下午01:12:28	82.774%	3.3948

结论：含水率高的部分不一定弛豫时间就会长。

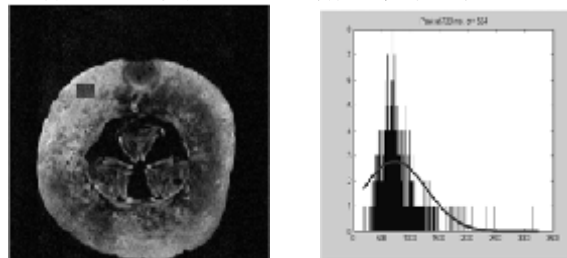
## 5、T2-map图

- 通过改变不同的TE值来做图像的MAPPING处理，可获得哈密瓜的T2-MAP图。
- 腐烂部分
- 从图中可以看出腐烂区域在T2Map像中信号很弱，与旁边正常果肉部分的区别较大



## Related Documents

- 正常果肉部分
- 从图中可以看出T2加权像图中亮色部分T2的平均值为733ms，信号强过腐败部分



## 结论

- 可以通过核磁共振技术对哈密瓜品质进行检测。能直观的看出哈密瓜的果肉内部特征。
- 哈密瓜腐烂部分和正常果肉在弛豫时间和含水率方面都有较大的区别，可以利用这个特点对哈密瓜的品质变化进行监测。

Thank You !



## 粮油食品低场核磁共振检测技术 研究进展

报告人：邵小龙

南京财经大学食品科学与工程学院

南京财经大学  
食品科学与工程学院



源于1956年隶属粮食部的南京粮食学校，目前建有粮食储运国家工程实验室（稻谷平台）、国家粮食局粮油质量检测工程技术研究中心、中加储粮生态研究中心、江苏省粮油品质控制及深加工技术重点实验室、中国粮食流通管理培训中心等科研、教学平台和社会服务机构。

### 低场核磁共振在粮油检测中的应用

#### 1 粮油食品化学成分指标测定

传统测量谷物，油料种子的含水含油量一般采用烘干法和索氏提取法。

哈恩（Hahn）回波序列可以同时测量含水量低于15%的如谷物、油料种子等样品中的水分和油脂含量。

### 低场核磁共振在粮油检测中的应用

#### 1 粮油食品化学成分指标测定

该方法也可以用于测量粮食谷物及其制品，动物饲料，奶粉等低含水量产品的脂肪和水分。

国内国际标准：

《植物油料含油量测定连续波低分辨率核磁共振测定法》（GB/T 15690—2008）、《油籽—油和水含量的平行测定—脉冲核磁共振分光光度法》（ISO10565—1998）和《含油种子残渣—油水含量的同时确定脉冲核磁共振光谱方法》（ISO 10632—2000）。

### 低场核磁共振在粮油检测中的应用

#### 1 粮油食品化学成分指标测定

间接测定化学成分：

反转恢复序列（IR），自由弛豫扩散（FID）和CPMG脉冲序列：建立脂肪、水和蛋白质的预测模型。

混合弛豫信号同时测量带包装的蛋黄酱、人造奶油、调味沙司等产品的脂肪含量。

### 低场核磁共振在粮油检测中的应用

#### 1 粮油食品化学成分指标测定

与其他方法相比优缺点：

如近红外

对于较厚和颜色较深的样品（比如棉花籽中的油脂和蛋白含量），测量结果较差。

**低场核磁共振在粮油检测中的应用**

**2 粮油食品理化指标测定**

FID 序列对样品在同一温度下进行测试计算得到SFC, 该法无需样品称重, 不受温度影响, 方便快捷, 广泛应用于食用油脂、鲜肉、快餐、鱼类产品等等固态脂肪含量测定。

国际标准( AOCs cd16-81, AOCs cd16b-93)

研究应用:

- 测量水包油乳化体系中乳液大小及分布;
- 预测面包硬度;
- 煮熟土豆硬度、黏度、颗粒感、粉质感等9种感官指标。

**粮油食品加工储藏过程研究**

研究粮油食品储藏加工过程的成分和状态变化, 包括:

- 淀粉糊化凝胶、
- 蛋白质变性、
- 油脂融化、
- 玻璃态转变、
- 发芽率、
- ...

**一些应用: 掺假快速检测技术研究**

- 蜂蜜掺假、
- 明胶掺假
- 牛奶掺假、
- 食用油脂掺假问题:

混入动物脂肪; 掺杂毛油、老油等

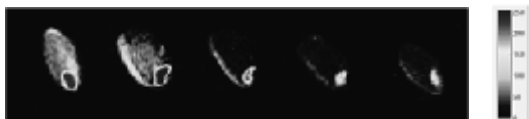
...

**一些应用: 粮油食品成像研究**



油菜籽成像 (伪彩)

**一些应用: 粮油食品成像研究**



高水分稻谷干燥过程中的核磁成像图 (伪彩)

**一些应用: 粮油食品成像研究**

成像应用问题:

低场核磁成像能得到较大尺寸样品(如面团, 淀粉凝胶, 玉米棒等)的内部清晰结构图, 然而对于小麦、稻谷、玉米粒、大豆、芝麻等较小粒径的样品则分辨率不足, 只能显示较简单的结构轮廓。

核磁显微成像技术: 理论上是可以达到纳米尺度显微成像, 场强要求高。



**低场核磁应用于粮油行业中会遇到的问题：**

一方面仪器本身技术有待提高，如优化硬件和算法、提高核磁信号解谱速度和稳定性、提高低场成像速度和清晰度、发展显微成像技术等等。

另一方面低场核磁共振技术目前在粮油食品中的基础应用不够系统，有待全面深入的研究，并建立完善的核磁共振谱数据库；同时，粮油食品的在线检测技术有待开发。

请大家提问。

谢谢大家！

联系方式：sxlion2@gmail.com

西北农林科技大学 杜光源博士

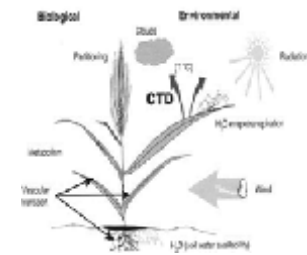
## 小麦源库关系的核磁共振研究

### 小麦源库关系的核磁共振研究

- 一、研究意义
- 二、研究方法
- 三、结果与分析
- 四、结论与致谢

### 一、研究意义

- **源**：制造养料、提供营养物质的器官；
- ↓
- **库**：消耗养料或储藏养料的器官。

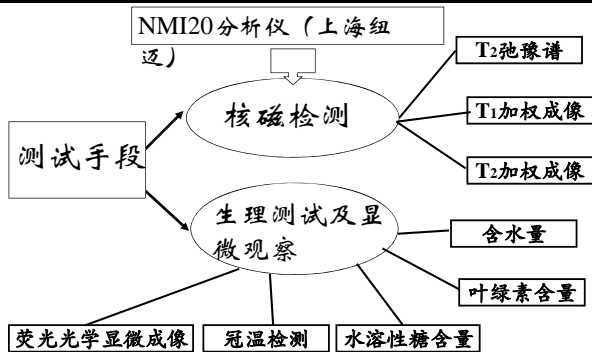


Reynolds, M.P., Nagarajan, S., Razzaque, M.A. & Ageeb, O.A.A. 2001. Heat tolerance. In M.P. Reynolds, I. Ortiz-Monasterio & A. McNab, eds. *Application of physiology in wheat breeding*. Mexico, DF, CIMMYT.

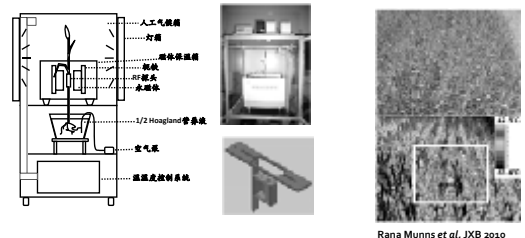
### 一、研究意义

- 对核磁共振设备进行必要的改造，构建小麦的核磁共振活体检测体系
- 探讨利用NMR的 $T_2$ 弛豫谱特征进行小麦叶片和茎含水量及相关生理参数测定的可行性
- 结合核磁共振方法和生理生化检测方法，揭示小麦灌浆的物质(水分和糖分)转运规律

### 二、研究方法



### 二、研究方法



Rana Munns et al, JXB 2010

### 三、结果与分析



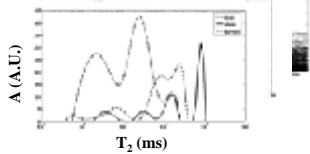
#### 3.1 小麦核磁共振T<sub>2</sub>弛豫谱特征

分离谱

$$S = \sum A_i e^{-T_2/T_{2i}}$$

连续谱

$$S = \int A(T_2) e^{-T_2/T_2} dT_2$$

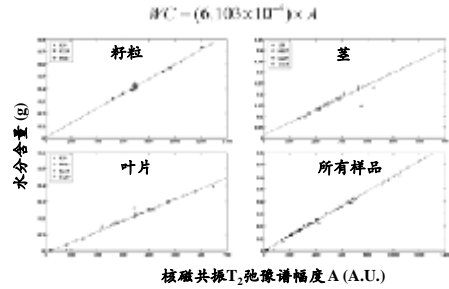


A: 幅度 ↔ 水分含量  
T<sub>2</sub>: T<sub>2</sub>弛豫时间 ↔ 水分子动力学特性

### 三、结果与分析



#### 3.2 核磁共振T<sub>2</sub>弛豫谱幅度与水分含量

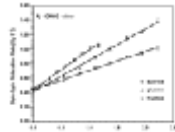


### 三、结果与分析

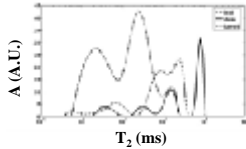


#### 3.3 水溶性糖与核磁共振T<sub>2</sub>弛豫时间

V. Arulmoji, et al.  
Food Chemistry  
132(2012) 1644-1650



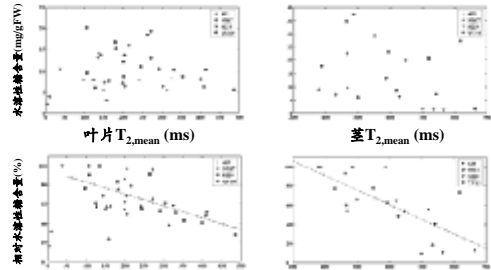
$$T_{2, \text{mean}} = \frac{\int A(T_2) T_2 dT_2}{\int A(T_2) dT_2}$$



### 三、结果与分析



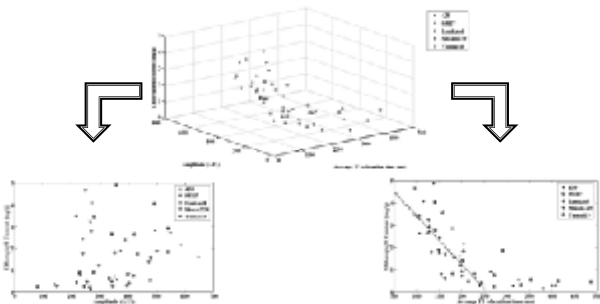
#### 3.4 水溶性糖与核磁共振T<sub>2</sub>弛豫时间



### 三、结果与分析



#### 3.5 小麦叶片生理活性与T<sub>2</sub>弛豫谱

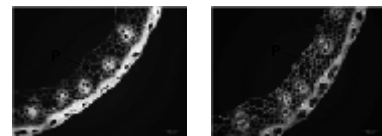


### 三、结果与分析



#### 3.6 小麦T<sub>2</sub>弛豫谱与茎糖分贮存库

Wheat Cultivars	Date	T <sub>2</sub> (ms)		Amplitude (A.U.)	
		T <sub>2s</sub>	T <sub>2l</sub>	A(T <sub>2s</sub> )	A(T <sub>2l</sub> )
439 (Cold)	26-May	85.1 ± 5.3	339.7 ± 8.4	223.3 ± 5.8	171.7 ± 5.2
	2-Jun	124.6 ± 2.2	406.7 ± 2.0	229.6 ± 3.5	183.3 ± 1.9
95H7 (Warm)	26-May	120.7 ± 4.6	369.8 ± 7.7	102.9 ± 1.8	183.0 ± 3.7
	2-Jun	170.4 ± 7.3	803.5 ± 9.2	117.7 ± 4.3	118.3 ± 2.7



小麦439 小麦茎的荧光显微成像 小麦95H7

## 四、结论与致谢



- 小麦的叶片、茎和籽粒的含水量与 $T_2$ 弛豫谱幅度具有极显著线性关系；
- 小麦茎的水溶性糖含量有较大的品种差异，同一小麦品种的相对水溶性糖含量与 $T_{2,mean}$ 成负相关关系；
- 小麦叶片的衰老态势可通过弛豫特性来反映，从衰老初期至降解期， $T_{2,mean}$ 持续增大，进入衰亡期后 $T_{2,mean}$ 锐减；
- 小麦冠层温度较低的小麦蒸腾活性高，叶片持绿功能期较长，茎的水溶性糖贮存容量较大。在这三个因素的影响下，灌浆早中期的冷型小麦叶片光合活性较高，叶片即时光合产物能够及时载出；叶片衰败后，较大的茎水溶性糖库容的活化延续了高灌浆速率水平，有利于产量的提高。

## 四、结论与致谢



- 本文得到国家自然科学基金项目“基于核磁共振技术的‘接力式’灌浆小麦水分和糖分动态分布规律及其机制研究”（31201122）的资助；
- 感谢上海纽迈电子科技有限公司提供的硬件和技术支持；
- 感谢西北农林科技大学中国旱区农业研究院提供的试验平台。特别感谢张嵩午教授对本研究的悉心指导！



## 油脂低场核磁共振 (LF-NMR) 检测方法

—————研究工作进展

王欣 (博士 副教授 18918629281 )  
上海理工大学食品质量与安全研究所



### 课题支撑:

- 低场核磁快速检测地沟油专用仪器的研制 (上海市科委仪器专项重大攻关项目)
- 油脂中降解产物的低场核磁共振快速检测方法研究 (国家自然科学基金项目)

### 协作单位:

- 上海纽迈电子科技有限公司
- 上海市粮食科学研究所



## 报告提纲

- 探索: 检测的可行性
- 尝试: 劣质油品的检测
- 发展: 检测条件的初步优化
- 实战: 卫生部盲样检测
- 反思: 检测条件的再次优化



## 探索: 检测的可行性



## 地沟油?

- 泛指各类劣质油的统称。主要包括来自餐厨废油脂的泔水油、阴沟油、煎炸老油三大类。



## 如何解决“地沟油问题”?

卫生部: 征集“地沟油”的检测方法

简单、快速、有效检测的初筛方法

- ### 一、征集的检测方法归类
- ◆ 仪器检测 (53, 7%)
  - ◆ 指标检测 (440, 58%)
  - ◆ 建立题库 (10, 1%)
  - ◆ 与检测方法无关的电子邮件 (280, 34.0%)

仪器设备昂贵  
耗时长 误差大  
操作繁琐



上海理工大学

### 低场核磁共振检测技术的优势

特点	具体情况
快速	1-2分钟可完成数据采样与分析
无损	主要对物质中的H质子进行表征,不破坏物质原有形态
绿色	对检测物无任何污染,对检测样品无需太复杂的前处理
精确	油水定量分析可精确到0.002%
重复性高	反映H在物质中与周边环境分子间的相互作用,同一样品反复检测差异性较小

第五届全国低场核磁共振技术与应用研讨会 上海 2013-10-12 7

上海理工大学

### 合格食用油的低场核磁共振检测结果与分析

脂肪酸的和比例不同,使得弛豫峰位置和比例不同,因此,每种纯油品都有对应的标准弛豫图谱

第五届全国低场核磁共振技术与应用研讨会 上海 2013-10-12 8

上海理工大学

### 劣质食用油及地沟油的NMR检测特征分析

仅劣质油品的图谱左边均出现了明显的小比例特征峰,记为 $T_{21}$ 可将其定义为劣质油品的特征峰,用于初步鉴别食用油品质。

第五届全国低场核磁共振技术与应用研讨会 上海 2013-10-12 9

上海理工大学

### 油脂煎炸过程中低场NMR特征、与理化性质的相关性

4h开始出现小峰S21  
2.S21小峰随煎炸时间逐渐变大并左移

油脂煎炸过程的低场NMR检测

第五届全国低场核磁共振技术与应用研讨会 上海 2013-10-12 10

上海理工大学

## 尝试：劣质油品的检测

第五届全国低场核磁共振技术与应用研讨会 上海 2013-10-12 11

上海理工大学

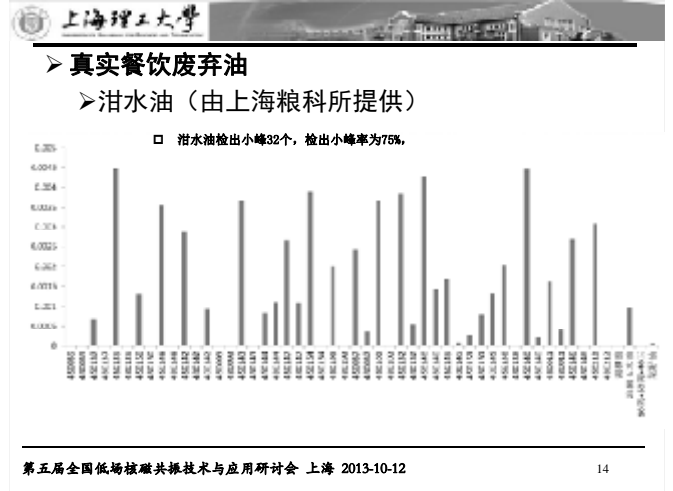
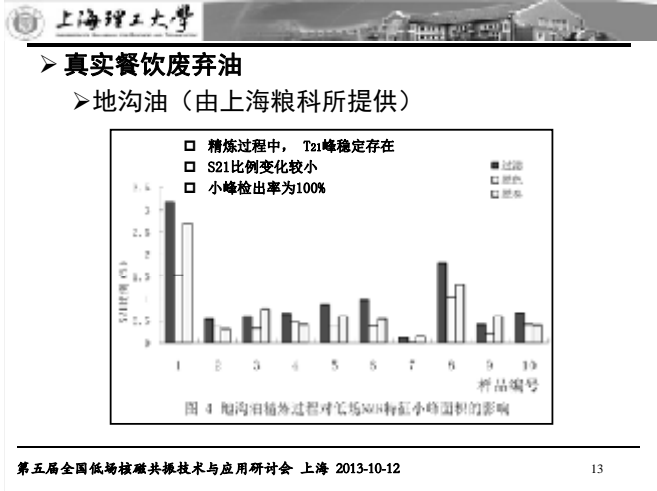
### 市场收集的代表性真实餐饮废弃油

煎炸老油 (由上海粮科所提供)

- 精炼过程中,  $T_{21}$ 峰稳定存在
- $S_{21}$ 比例变化较小
- 小峰检出率为100%,最小为0.11%,最大为6.81%。

图 6 煎炸老油精炼过程中的低场NMR检测

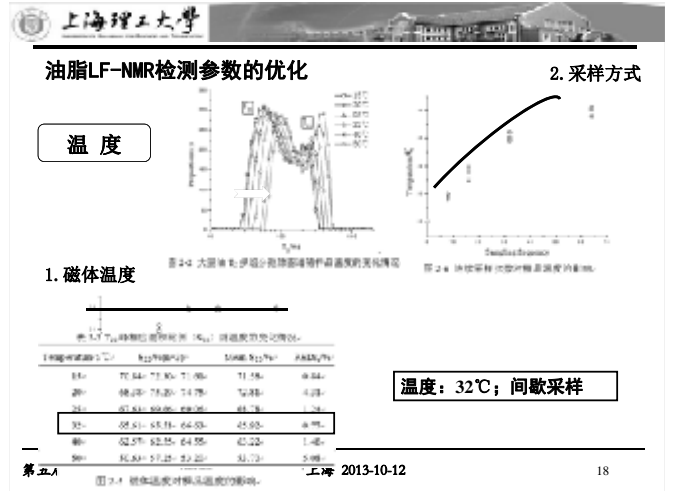
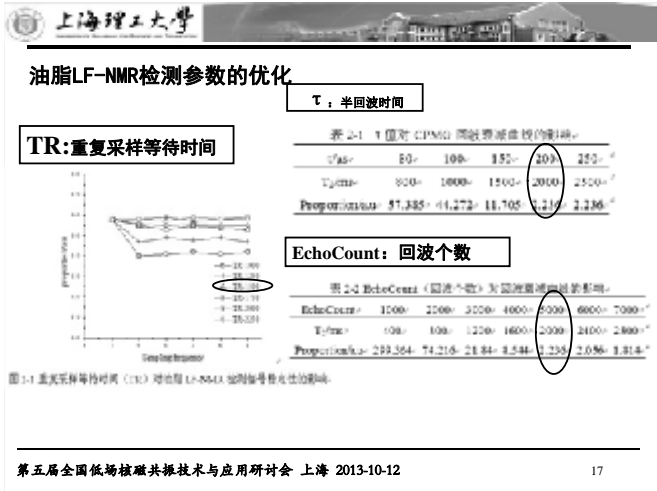
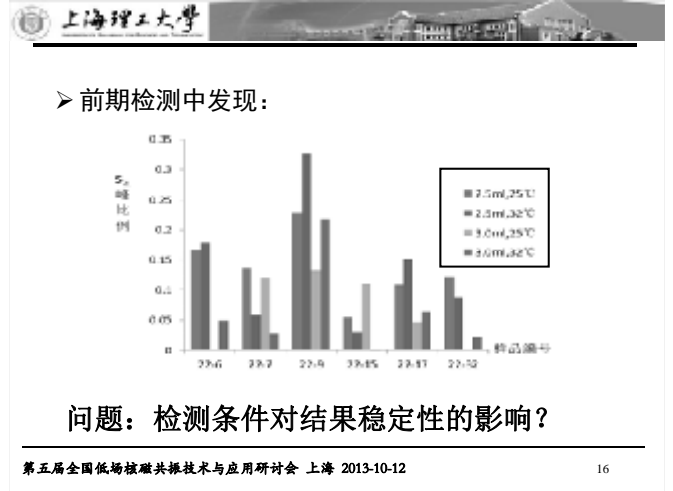
第五届全国低场核磁共振技术与应用研讨会 上海 2013-10-12 12



上海理工大学

# 发展: 检测条件的初步优化

第五届全国低场核磁共振技术与应用研讨会 上海 2013-10-12 15







上海理工大学

### 检测体积

图4 大圆球、椭圆球和球体在子磁干磁体表面磁化层中采样情况

表1 不同采样层厚度对 $T_2$ 测量的影响结果

采样层厚度	2.0	2.5	3.0	3.5	4.0	4.5	5.0
绝对误差	0.004100%	0.004100%	0.004100%	0.004100%	0.004100%	0.004100%	0.004100%
相对误差	0.14100%	0.14100%	0.14100%	0.14100%	0.14100%	0.14100%	0.14100%
绝对误差	0.004100%	0.004100%	0.004100%	0.004100%	0.004100%	0.004100%	0.004100%
相对误差	0.14100%	0.14100%	0.14100%	0.14100%	0.14100%	0.14100%	0.14100%

- 重复采样等待时间 (TR) 2000 ms
- 半回波时间 ( $\tau$ ) 250  $\mu$ s
- 回波个数 (EchoCount) 6000个

第五届全国低场核磁共振技术与应用研讨会 上海 2013-10-12 25

上海理工大学

### 方法的验证

表2 不同 $T_2$ 值及不同采样层厚度对测量结果的影响

采样层厚度	绝对误差	相对误差	绝对误差	相对误差
2.0	0.004100%	0.14100%	0.004100%	0.14100%
2.5	0.004100%	0.14100%	0.004100%	0.14100%
3.0	0.004100%	0.14100%	0.004100%	0.14100%
3.5	0.004100%	0.14100%	0.004100%	0.14100%
4.0	0.004100%	0.14100%	0.004100%	0.14100%
4.5	0.004100%	0.14100%	0.004100%	0.14100%
5.0	0.004100%	0.14100%	0.004100%	0.14100%

表3 不同 $T_2$ 值及不同采样层厚度对测量结果的影响

采样层厚度	绝对误差	相对误差	绝对误差	相对误差
2.0	0.004100%	0.14100%	0.004100%	0.14100%
2.5	0.004100%	0.14100%	0.004100%	0.14100%
3.0	0.004100%	0.14100%	0.004100%	0.14100%
3.5	0.004100%	0.14100%	0.004100%	0.14100%
4.0	0.004100%	0.14100%	0.004100%	0.14100%
4.5	0.004100%	0.14100%	0.004100%	0.14100%
5.0	0.004100%	0.14100%	0.004100%	0.14100%

优化前、后总体准确率: 37.5%、75%      优化前、后总体准确率: 37.5%、100%

第五届全国低场核磁共振技术与应用研讨会 上海 2013-10-12 26

上海理工大学

# 谢谢!

请多提宝贵意见!

## 核磁共振波谱法及其在食品脂质分析中的研究进展

刘纯友 马美湖 靳国峰 蔡朝霞 金永国 黄茜 邱宁

(华中农业大学食品科技学院 湖北 武汉 430070)

**摘要:** 核磁共振波谱法是快速、准确测定有机化合物分子结构的分析方法之一。本文介绍了核磁共振波谱法的基本原理及特点,综述了核磁共振波谱法在测定食品中脂质含量,脂质的脂肪酸组成分析,脂质分子结构的鉴定以及食用油的品质鉴别等方面的研究进展,探讨了核磁共振波谱法在脂质分析中存在的问题,展望了核磁共振波谱法在脂质分析中的应用前景。

**关键词:** 核磁共振; 食品脂质; 分析

## 研究报告

大豆油煎炸过程理化指标与 LF - NMR  
弛豫特性的相关性研究

史 然, 王 欣\*, 刘宝林, 卢海燕, 赵婷婷

(上海理工大学 食品质量与安全研究所, 上海 200093)

**摘要:** 在对大豆油无料/薯条煎炸过程[温度:  $(180 \pm 5)^\circ\text{C}$ , 持续 36 h]中的酸价(AV)、粘度(V)、吸光值(A)及总极性化合物(TPC)含量等及低场核磁共振(LF - NMR)弛豫特性(峰起始时间 $T_{21}$ 、 $T_{22}$ 、 $T_{23}$ 、相应的峰面积比例 $S_{21}$ 、 $S_{22}$ 、 $S_{23}$ 、单组份弛豫时间 $T_{2w}$ )变化规律研究的基础上, 利用多元回归分析建立了理化指标与其 LF - NMR 检测结果的相关性模型, 并进行验证。结果表明: 大豆油的酸价、TPC 含量及 $S_{21}$ 峰面积均随煎炸时间的延长而线性增大,  $T_{21}$ 、 $T_{22}$ 峰起始时间及 $T_{2w}$ 则随煎炸时间的延长而线性减小( $r^2 > 0.90$ ), 粘度、吸光值随煎炸时间的延长逐渐增加并符合二项式关系( $r^2 > 0.90$ ), 而 $T_{23}$ 峰起始时间及 $S_{22}$ 、 $S_{23}$ 与煎炸时间之间无明显规律性变化。煎炸薯条后, 油样的酸价、粘度、TPC 含量、吸光值及 $S_{21}$ 均较无料煎炸显著增大( $P < 0.05$ ), 而 $T_{21}$ 、 $T_{22}$ 峰起始时间及 $T_{2w}$ 显著缩短。多元回归分析表明, 酸价及 TPC 含量与 $T_{2w}$ 、 $T_{21}$ , 粘度与 $T_{2w}$ , 吸光值与 $S_{21}$ 间均可建立良好的相关性模型( $R^2 > 0.93$ )。模型验证合理可靠, 可通过油样的 LF - NMR 检测结果有效预测其理化指标的变化。

**关键词:** 大豆油; 煎炸时间; 理化特性; LF - NMR; 弛豫特性

中图分类号: O657.3; R136.33 文献标识码: A 文章编号: 1004 - 4957(2013)06 - 0653 - 08

doi: 10.3969/j.issn.1004 - 4957.2013.06.001

Relationship between Analytical Indicators of Soybean Oil and LF - NMR  
Characteristics During Frying Process

SHI Ran, WANG Xin\*, LIU Bao-lin, LU Hai-yan, ZHAO Ting-ting

(Institute of Food Safety and Quality, University of Shanghai for Science and Technology, Shanghai 200093, China)

**Abstract:** The development of rapid and simple test is needed in order to capably monitor the frying oil quality and ensure the fried food safety. In this paper, the evolution of several analytical indicators (e. g. acid value, viscosity, absorbance values and TPC content) and the low field Nuclear Magnetic Resonance (LF - NMR)  $T_2$  relaxation characteristics (the relaxation time:  $T_{21}$ ,  $T_{22}$ ,  $T_{23}$ , the corresponding peak area:  $S_{21}$ ,  $S_{22}$ ,  $S_{23}$  and the single component relaxation time:  $T_{2w}$ ) of soybean oil were studied during the frying process of no foodstuff or potato chips ( $180 \pm 5^\circ\text{C}$  for 36 h). The multiple regression analysis method was used to establish the correlation model between LF - NMR results and the analytical indicators. At last, the developed models were experimentally verified. The results indicated that the acid value, TPC content and  $S_{21}$  increased linearly, while  $T_{21}$ ,  $T_{22}$  and  $T_{2w}$  decreased linearly, as the frying process prolonged. And a good binomial relationship was obtained between the viscosity or absorbance values and the frying time ( $r^2 > 0.90$ ). No obvious relationship was found between frying time and  $T_{23}$ ,  $S_{22}$  or  $S_{23}$ . Compared with no foodstuff frying, the acid value, viscosity, TPC content, absorbance values and  $S_{21}$  during potato chip frying process increased significantly, while  $T_{21}$ ,  $T_{22}$  and  $T_{2w}$  obviously shortened ( $P < 0.05$ ). Multiple regression analysis showed that both acid value and TPC content had a good relationship with  $T_{2w}$  and  $T_{21}$ , and

收稿日期: 2013 - 01 - 11; 修回日期: 2013 - 02 - 10

基金项目: 国家自然科学基金项目 (NSFC31201365); 上海市科委重点攻关项目 (11142200403); 上海市教委科研创新项目 (11YZ109)

\* 通讯作者: 王 欣, 博士, 副教授, 研究方向: 食品安全控制与检测, Tel: 18918629281, E-mail: wx0426951@126.com

viscosity had a good linear relationship with  $T_{2w}$ , while absorbance had a good logarithmic relationship with  $S_{21}$  ( $r^2 > 0.93$ ). These models were successfully verified and could be used to predict the variations of physical and chemical indicators by the LF-NMR characteristics of the frying oil.

**Key words:** soybean oil; frying duration; analytical indicator; LF-NMR; relaxation characteristic

煎炸老油是指饮食行业多次煎炸食品残剩的不可再食用的油脂。由于在长时间高温加热过程中,油脂与空气中的氧、煎炸食物所带入水分等成分作用,发生水解、氧化、缩合等一系列复杂的化学反应,产生一系列饱和及不饱和的醛、酮、内酯等物质,甚至变性为三致物质,从而可能对消费者的身体健康产生负面影响<sup>[1]</sup>。由于我国饮食特色,煎炸食品食用量均相对较高。而部分煎炸食品的生产厂家为了降低成本,其所用的煎炸油脂会长时间反复利用;此外,有不法分子被巨额利润所诱惑,大肆收集煎炸老油并经简单加工处理后,以极低价格卖给饮食店、油脂作坊重新使用,或掺入合格食用油中,以假乱真。因此,加强对煎炸油脂品质的监管可有效保障煎炸食品的品质,对避免“地沟油”流入餐饮服务环节,切实保护消费者饮食安全具有重要意义。

常规理化指标如油脂的酸价、粘度、过氧化值、吸光值等被广泛应用于油脂品质的分析。对煎炸油脂而言,油脂的总极性化合物含量也是衡量煎炸油脂品质的重要指标,有研究表明,油脂中的极性成分会严重影响食品的微观结构,也在一定程度上影响食品的质构品质<sup>[2]</sup>。一般以达到 24%~27% 的总极性化合物(TPC)含量作为煎炸油脂使用终点的判断指标<sup>[3]</sup>,对油脂中 TPC 含量的检测一般可用柱层析法进行。而以上理化指标的传统检测方法均需使用大量有机溶剂,操作繁琐且耗时较长。因此,探索一种快速、便捷、灵敏、低成本的新型检测方法成为煎炸油脂品质监测的一个研究重点<sup>[4]</sup>。

低场核磁共振(LF-NMR)被认为是一种非常有潜力的油脂快速检测新技术,并已成功应用于油脂固体脂肪指数及油料种子含油率的测定<sup>[5]</sup>。最近, Franz 等<sup>[6]</sup>对应用低场核磁共振技术监测多种反应过程的研究进展进行了综述,研究表明反应过程中体系组成成分的变化可以通过其低场核磁共振弛豫特性的变化进行监测。而 Martina 等<sup>[7]</sup>的研究则表明煎炸油脂的低场核磁弛豫时间会随其所含的极性化合物含量的增加而缩短,利用这一数学关系,可以对煎炸油的质量进行评判。王永巍等<sup>[8]</sup>应用 LF-NMR 对大豆油的无物料煎炸过程进行研究,发现油脂煎炸过程中  $T_2$  多组分弛豫图谱中出现的特征小峰  $T_{21}$  的面积比例 ( $S_{21}$ ) 及  $T_{2w}$  (单组份弛豫时间) 与煎炸时间、酸价、粘度、吸光值和极性组分含量呈现良好的规律性,认为该方法可以有效反映煎炸油的品质变化。然而该研究对象仅限于无料煎炸大豆油,且未对理化指标与 LF-NMR 弛豫特性之间的相关性进行深入研究。而 Adolfo<sup>[9]</sup>和 Wakako<sup>[10]</sup>等的研究表明,煎炸油的理化性质变化与其油脂品种及煎炸物料相关。因此,开展不同煎炸物料油脂的低场 LF-NMR 弛豫特性与其理化性质的相关性研究将有助于后期将低场核磁共振技术应用于煎炸油脂品质的检测。

在前期建立的油脂 LF-NMR 检测方法的基础上,以大豆油为研究对象,分别对其在无料/薯条煎炸过程 [(180±5) °C, 持续煎炸 36 h] 中多种理化指标(酸价、粘度、吸光值及 TPC 含量等)及 LF-NMR 弛豫特性 ( $T_{21}$ 、 $T_{22}$ 、 $T_{23}$  峰起始时间、 $S_{21}$ 、 $S_{22}$ 、 $S_{23}$ 、 $T_{2w}$ ) 的变化规律进行研究,进而利用多元回归分析建立 LF-NMR 检测结果与其理化指标的相关性模型,并进行了验证。研究可为 LF-NMR 技术应用于煎炸油脂品质监控提供必要的基础数据。

## 1 实验部分

### 1.1 试剂与仪器

乙醚、石油醚、氢氧化钾、正己烷(分析纯,上海国药集团化学试剂有限公司),硅胶(60~100目)为色谱纯,新鲜金龙鱼大豆油(益海嘉里食品工业有限公司);速冻薯条(上海长生食品厂)。

09 款流线型 5.5 L 电炸炉(广州汇利有限公司); PQ-001 型核磁共振分析仪,氢谱,共振频率 23 MHz(上海纽迈电子科技有限公司,配套 T-invfit 反演拟合软件和  $\Phi 15$  mm 核磁共振专用测试管);层析柱(上海市崇明建设玻璃仪器厂); NDJ-1 型旋转粘度计(东莞市精鼎仪器有限公司); 751-G 分光光度计(200~1 000 nm,上海分析仪器厂)。

### 1.2 试验设计

1.2.1 煎炸油的制备 无料煎炸油: 在煎炸锅中加入 6 L 大豆油,每天在油温为 (180±5) °C 下连续

煎炸 12 h, 共持续 36 h; 薯条煎炸油: 在煎炸用油种类、用量及油温与无物料煎炸油制备过程相同的条件下, 每批取 60 g 薯条投入煎炸锅中煎炸 3 min ( $K_{g\_potatoes}/L_{oil} = 1:100$ )<sup>[11]</sup>, 每小时煎炸 4 批, 每天连续煎炸 12 h, 共持续 36 h。在以上煎炸过程中, 取新鲜未煎炸油样作为对照, 随后每 4 h 取 150 mL 油样, 冷却至室温, 滤去沉淀后贮于样品瓶中, 4 °C 冷藏备用进行理化指标分析及 LF-NMR 检测, 并以此数据进行相关性分析。

1.2.2 理化指标检测 ①粘度的测定: 取 100 mL 油样倒入 150 mL 烧杯中, 25 °C 恒温 10 min, 并用玻璃棒搅拌均匀, 立即用旋转粘度计对油样进行测定, 结果取 3 次测量平均值。②吸光值的测定参考 GB/T 22500-2008<sup>[12]</sup>。③酸价的测定参考 GB/T 509.37-2003<sup>[13]</sup>。④极性组分含量测定参考 GB/T 509.202-2003<sup>[14]</sup>。

1.2.3 LF-NMR 横向弛豫时间( $T_2$ ) 测量及数据处理<sup>[15]</sup> 利用 CPMG 脉冲序列测定样品的横向弛豫时间( $T_2$ ) 设备参数设置为: 重复采样等待时间  $TR = 2\ 000\ ms$ , 半回波时间  $\tau = 200\ \mu s$ , 回波个数  $EchoCount = 5\ 000$  个, 重复扫描次数  $NS = 4$  次, 采样点数  $TD = 500\ 050$ , 谱宽  $SW = 250\ kHz$ 。将 2.5 mL 样品移入核磁共振试管, 先在 32 °C 恒温 10 min, 再置于核磁探头中稳定 1 min 后采样, 采样完毕后将样品重新置于 32 °C 恒温 5 min, 以便进行下次采样, 结果取 3 次测量平均值。

利用 T-invfit 软件对 LF-NMR 弛豫测量得到的自由诱导指数衰减曲线进行反演拟合, 可得到油样的多组分弛豫时间( $T_2$ ) 数据图谱并获知样品的  $T_{21}$ 、 $T_{22}$ 、 $T_{23}$  峰起始时间及其相应的峰面积比例  $S_{21}$ 、 $S_{22}$ 、 $S_{23}$ 。当将样品看作一个整体组分分析时, 可反演得到样品的单组份弛豫时间( $T_{2w}$ , 单位: ms)。

1.2.4 相关性分析 利用 SPSS 软件的多元回归分析法, 因变量选取酸价、TPC 含量、粘度、吸光值; 自变量选取 LF-NMR 弛豫结果( $T_{21}$ 、 $T_{22}$ 、 $T_{23}$  峰起始时间、 $S_{21}$ 、 $S_{22}$ 、 $S_{23}$ 、 $T_{2w}$ ), 采用向后剔除变量法, 将不显著的自变量剔除, 最终使模型中只包含显著变量且变量间构成最优组合, 建立 LF-NMR 检测结果与煎炸油理化指标的相关性模型。

1.2.5 模型的验证 参照“1.2.1”的方法制备无料/薯条煎炸油, 从煎炸 2 h 起每 4 h 取 150 mL 油样, 冷却至室温, 滤去沉淀后贮于样品瓶中, 4 °C 冷藏备用进行理化指标分析及 LF-NMR 检测, 并将获得的 LF-NMR 检测数据分别代入“1.2.4”中建立的不同理化指标与 LF-NMR 弛豫特性的相关性模型, 计算获得该理化指标的理论预测值, 并与其实测值建立回归曲线, 分析相关性, 对模型的可靠性进行验证。

### 1.3 数据分析

每组试验均进行 3 次重复, 实验结果以(平均值  $\pm$  相对偏差)表示。应用 Origin8.0、SPSS18.0 软件对数据进行处理及统计分析, 以  $P < 0.05$ (差异显著)作为差异显著性判断标准。

## 2 结果与讨论

### 2.1 理化指标

2.1.1 酸价 酸价反映的是油脂中自由脂肪酸的多少, 是体现油脂酸败程度的重要指标之一。大豆油在无料/薯条 180 °C 煎炸过程中酸价随煎炸时间的变化规律如图 1A 所示。由图可知, 随煎炸时间的延长, 大豆油的酸价逐渐升高, 且与煎炸时间呈良好线性关系( $r^2$  分别为 0.942 和 0.978), 但煎炸 36 h 后, 两组煎炸油的酸价均小于国标规定的油脂煎炸过程中的酸价标准 5 mgKOH/g。与无料煎炸过程相比, 相同的煎炸时间下, 薯条煎炸油的酸价显著升高( $P < 0.05$ )。这是由于在煎炸过程中, 油脂在高温(185 °C 左右)下易发生水解、氧化、分解或聚合等反应, 产生游离脂肪酸, 进而使其酸价升高。而引入煎炸物料(薯条)后, 由于煎炸物料中含有水分较多, 促进了油脂在煎炸条件下的分解, 因而使反应产物相对增加<sup>[16]</sup>, 导致酸价显著升高。

2.1.2 粘度 粘度为油样分子间摩擦力大小的标度, 其大小与其碳链长度有关。大豆油在无料/薯条煎炸过程中粘度(25 °C) 随煎炸时间的变化规律如图 1B 所示。由图可以看出, 随煎炸时间的延长, 两种煎炸条件下大豆油的粘度逐渐增大, 并均呈二项式关系( $r^2$  分别为 0.934 和 0.994), 这是因为油脂在高温下发生热聚合和热氧化聚合反应, 生成了环状聚合物及甘油酯二聚合物等粘稠的成分。同时, 油脂在煎炸过程中还会发生部分水解及缩合反应, 形成分子量较大的醚型化合物, 从而使油脂的粘度增加。此外, 与无料煎炸油相比, 添加薯条进行煎炸后, 由于薯条中的淀粉、水分子也会与油脂分子

在高温下发生反应,使油脂的粘度进一步增大( $P < 0.05$ )<sup>[17]</sup>。

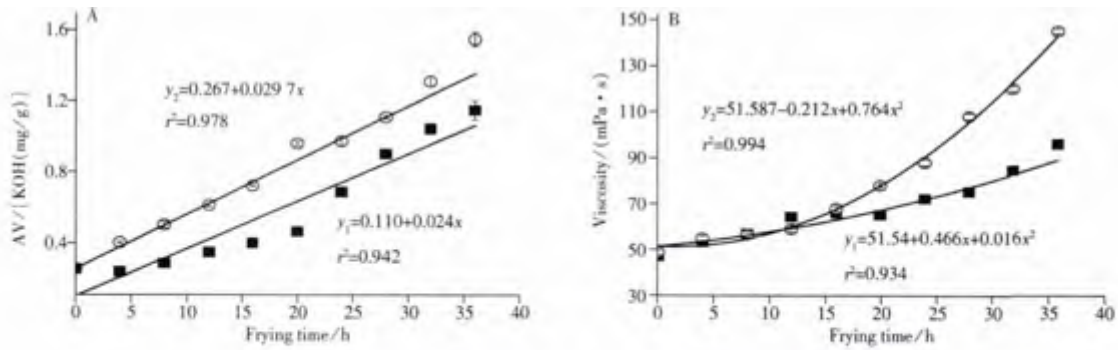


图 1 大豆油不同煎炸过程中酸价(A)及粘度(B)随煎炸时间的变化

Fig. 1 Evolution of the acid value (A) and the viscosity (B) of soybean oil during different frying processes

■ oil samples without foodstuff(无料煎炸大豆油); ○ oil samples with potato chips(薯条煎炸大豆油)

2.1.3 吸光值 油脂色泽是油脂中各种色素的综合体现,随着油脂品质的劣变,其色泽加深,吸光值(A)亦将逐渐增大。大豆油在无料/薯条煎炸过程中吸光值随煎炸时间的变化规律如图 2A 所示。图 2A 表明,随着煎炸时间的延长,两种煎炸条件下大豆油的吸光值均逐渐增加,并趋于平稳。油样吸光值与煎炸时间呈二项式关系( $r^2$  分别为 0.986 和 0.983)。与无料煎炸油相比,当油脂中添加薯条进行煎炸时,大豆油吸光值增加较显著( $P < 0.05$ ),这是由于食物组分与煎炸油相互作用以及煎炸油中所含食品杂质均会加深油脂的颜色所致<sup>[18]</sup>。

2.1.4 TPC 含量 油脂的总极性化合物(TPC)含量是衡量煎炸油脂品质的重要指标。大豆油在无料/薯条煎炸过程中 TPC 含量随煎炸时间的变化规律如图 2B 所示。由图可见,在煎炸过程中,两种煎炸条件下大豆油的 TPC 含量均逐渐升高,且与煎炸时间呈良好线性关系( $r^2$  分别为 0.989 和 0.978)。与无料煎炸油相比,添加薯条进行煎炸 36 h 后,油脂的 TPC 含量显著升高( $P < 0.05$ ),这是由于食物物料中的成分尤其是其中包含的水分会加速油脂的水解、分解和聚合反应而生成各种极性较大的化合物,从而促进煎炸油极性化合物含量的增加<sup>[19]</sup>。

## 2.2 LF-NMR 弛豫特性

### 2.2.1 多组分弛豫图谱( $T_2$ ) 大豆油在无料/薯

条煎炸过程中 LF-NMR 检测得到的多组分弛豫图谱( $T_2$ ) 如图 3 所示。参照文献 [8] 对  $T_2$  图谱的命名方法,将各峰按出现顺序分别命名为  $T_{21}$  峰、 $T_{22}$  峰及  $T_{23}$  峰,对应的峰面积比例表示为  $S_{21}$ 、 $S_{22}$  及  $S_{23}$ 。

由图 3A、B 可以看出,经无料/薯条煎炸后,大豆油的多组分弛豫图谱( $T_2$ ) 变化规律相似,煎炸初期的大豆油  $T_2$  图谱均由  $T_{22}$ 、 $T_{23}$  两个主峰构成,随着煎炸时间的延长,在其图谱 18 ms 左右有  $T_{21}$  小峰出现,且图谱有逐渐左移趋势,峰面积比例  $S_{21}$  逐渐增大, $S_{22}$ 、 $S_{23}$  比例也略有变化。大豆油在无料煎炸 4 h 后开始出现  $T_{21}$  小峰,而加入薯条煎炸 2 h 后便出现  $T_{21}$  小峰,为了进一步分析煎炸过程中 LF-NMR 信号的变化规律,将  $T_{21}$ 、 $T_{22}$ 、 $T_{23}$  峰起始时间随煎炸时间的变化情况列于图 4。

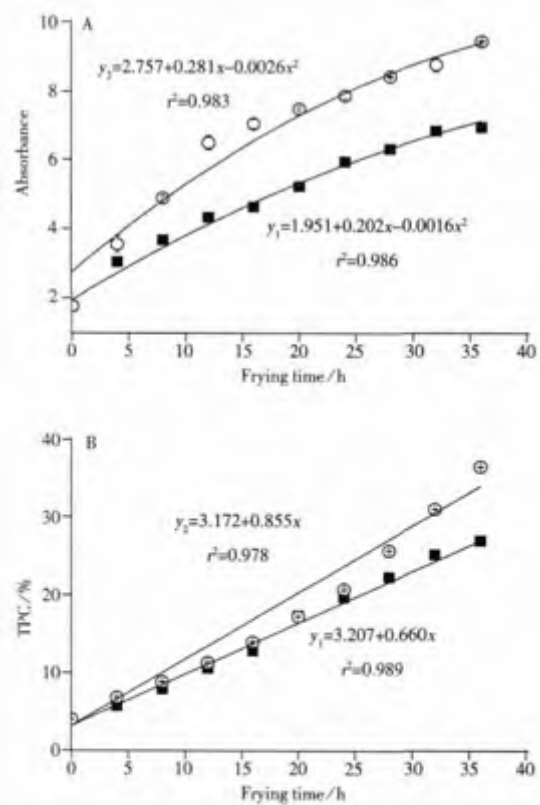


图 2 大豆油不同煎炸过程中吸光值 (A) 及 TPC 含量(B) 随时间的变化

Fig. 2 Evolution of the absorbance values (A) and the TPC levels (B) of soybean oil during different frying processes

■ oil samples without foodstuff;  
○ oil samples with potato chips

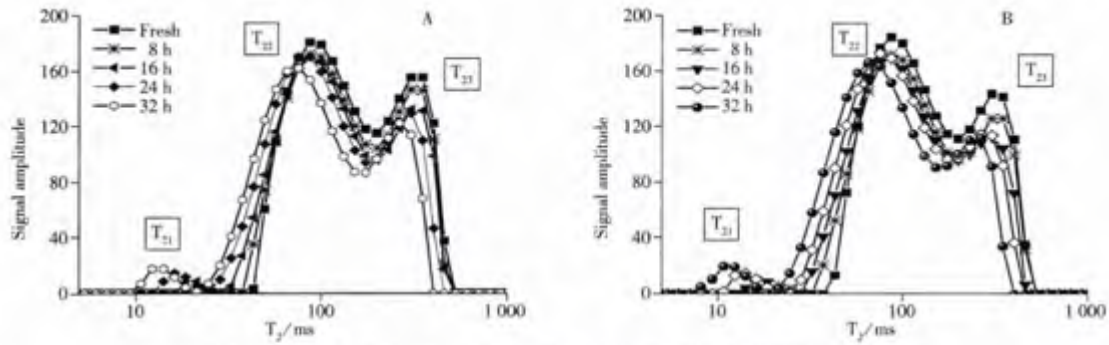


图 3 大豆油无料(A)/薯条(B)煎炸过程中  $T_2$  弛豫图谱随时间的变化

Fig. 3 Distribution of the  $T_2$  relaxation times in soybean oil during the frying process of no foodstuff (A) or potato chips (B)

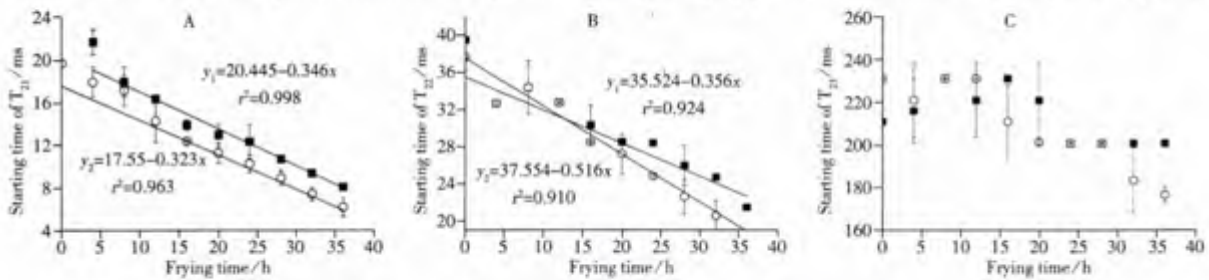


图 4  $T_{21}$  (A)、 $T_{22}$  (B)、 $T_{23}$  (C) 峰起始时间随煎炸时间的变化

Fig. 4 Evolution of the starting time of peak  $T_{21}$  (A),  $T_{22}$  (B) and  $T_{23}$  (C) during different frying processes

■ oil samples without foodstuff; ○ oil samples with potato chips

由图 4A、B 可以看出, 在无料/薯条煎炸条件, 大豆油  $T_{21}$ 、 $T_{22}$  峰起始时间均随煎炸时间的延长而缩短, 且呈良好线性关系 ( $r^2 > 0.90$ ), 与无料煎炸过程相比, 引入薯条煎炸使得  $T_{21}$ 、 $T_{22}$  峰起始时间的缩短速度加快。而图 4C 中  $T_{23}$  峰起始时间则随煎炸时间无明显规律性变化。这一变化可能与油脂在高温煎炸过程中发生水解、热聚合及热氧化聚合等复杂化学反应而生成脂质氧化物和过氧化物等产物相关, 与油脂中的甘油三酯成分相比, 煎炸过程中形成的氧化产物聚合度相对增大, 而 LF - NMR 检测得到的  $T_2$  弛豫时间能够反映自旋核子种类及其物理化学环境的变化。当氧化产物形成并积累到一定程度后, 在  $T_2$  谱图上出现了  $T_{21}$  特征峰, 且随反应产物聚合度的增加, 其分子中氢质子所受束缚力增大, 导致弛豫过程缩短, 从而表现为  $T_2$  值缩小<sup>[20]</sup>。且随着煎炸时间的延长, 油脂中所形成氧化物质聚合度亦逐渐增大, 从而导致油样  $T_2$  弛豫分布逐渐左移, 而以  $T_{21}$ 、 $T_{22}$  峰起始时间的减小最为显著。进一步研究了油脂在煎炸过程中各峰面积比例 ( $S_{21}$ 、 $S_{22}$ 、 $S_{23}$ ) 随煎炸时间的变化 (如图 5 所示)。结果表明, 随煎炸时间的延长, 无料/薯条煎炸条件油样的  $S_{21}$  逐渐增大,  $S_{22}$  呈增大趋势, 而  $S_{23}$  呈减小趋势。其中,  $S_{21}$  与煎炸时间呈良好线性关系 ( $r^2 > 0.90$ ), 与无料煎炸过程相比, 引入薯条煎炸使得  $S_{21}$  的增加速度加快, 说明煎炸物料的引入加剧了煎炸油脂的化学反应程度。这是由于,  $T_{21}$  特征峰反映的是在煎炸过程中区别于甘油三酯成分的一类氧化产物的形成及积累过程, 随着煎炸时间的延长, 具有类似  $T_{21}$  值的化合物含量增加, 从而使其 LF - NMR 的信号响应增加, 导致  $T_2$  图谱中相应峰面积 ( $S_{21}$ ) 增加。

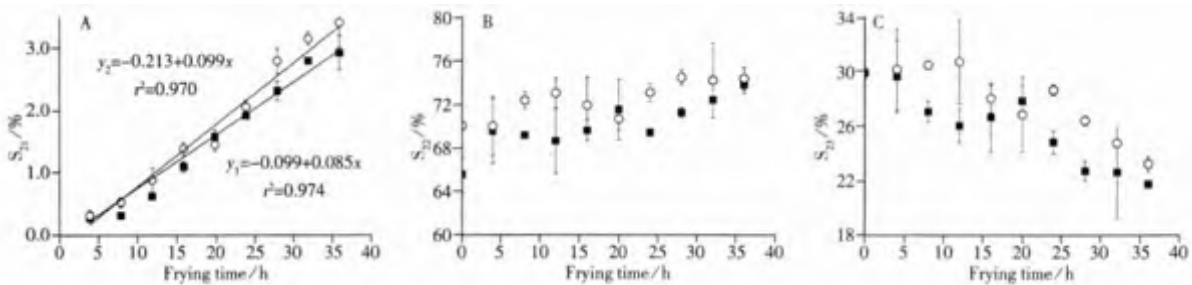


图 5  $S_{21}$  (A)、 $S_{22}$  (B)、 $S_{23}$  (C) 随煎炸时间的变化

Fig. 5 Evolution of the peak area  $S_{21}$  (A),  $S_{22}$  (B) and  $S_{23}$  (C) during different frying processes

■ oil samples without foodstuff; ○ oil samples with potato chips

2.2.2 单组份弛豫时间( $T_{2w}$ ) 将不同煎炸时间的油样看作一个整体组分进行反演,可得到大豆油煎炸过程中的单组份弛豫图谱。结果表明,随煎炸时间延长,薯条煎炸油的单组份弛豫时间( $T_{2w}$ )逐渐减小。图 6 为无料/薯条煎炸条件下大豆油的  $T_{2w}$  值随煎炸时间的变化关系。由图可见,在无料/薯条煎炸条件,大豆油  $T_{2w}$  值均随煎炸时间的延长而显著缩短,且二者之间呈良好线性关系( $r^2 > 0.90$ );此外,与无料煎炸过程相比,引入薯条煎炸使得  $T_{2w}$  值缩短速度加快。这是由于,油样的组成成分在高温煎炸过程中发生的水解、热聚合及热氧化聚合等复杂化学反应作用下发生了改变,从而使得 LF-NMR 检测得到的反映样品整体特征的  $T_{2w}$  弛豫特性也发生了改变<sup>[9]</sup>。

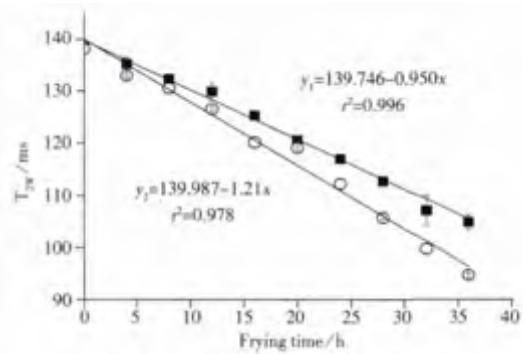


图 6  $T_{2w}$  随煎炸时间的变化情况

Fig. 6 Evolution of the single-component relaxation time ( $T_{2w}$ ) during different frying processes

■ oil samples without foodstuff; ○ oil samples with potato chips

### 2.3 油脂煎炸过程中理化指标与 LF-NMR 弛豫特性的相关性模型的建立及验证

从以上分析可看出,油脂的理化指标及其 LF-NMR 的多个检测指标均随煎炸时间呈规律性变化,为进一步研究油脂煎炸过程中理化指标与 LF-NMR 弛豫特性是否存在一定的相关性,利用多元回归分析法建立了 LF-NMR 检测结果与煎炸油理化指标的相关模型。通过采用向后剔除变量法,将不显著的自变量剔除,最终使模型中只包含显著变量且变量间构成最优组合。所建立的酸价、粘度、吸光值及 TPC 含量与 LF-NMR 检测结果( $T_{21}$ 、 $T_{22}$ 、 $T_{23}$ 峰起始时间、 $S_{21}$ 、 $S_{22}$ 、 $S_{23}$ 、 $T_{2w}$ )间的相关性模型如表 1 所示。

表 1 LF-NMR 检测结果与各项理化指标的回归模型

Table 1 Correlation models between LF-NMR results and the analytical indicators

Dependent variable (因变量)	Independent variable (自变量)	Regression equation* (回归方程)	$r^2$	Level of significance (显著水平)
Acid value(酸价, AV)	$T_{2w}$ , $T_{21}$	$AV_1 = 5.536 + 0.038T_{21} - 0.045T_{2w}$	0.965	0.000
		$AV_2 = 3.477 - 0.028T_{21} - 0.019T_{2w}$	0.962	0.000
Viscosity(粘度, V)	$T_{2w}$	$V_1 = 391.84 - 4.134T_{2w} + 0.0121(T_{2w})^2$	0.939	0.000
		$V_2 = 826.79 - 10.71T_{2w} + 0.0368(T_{2w})^2$	0.992	0.000
Absorbance(吸光值, A)	$S_{21}$	$A_1 = 2.97 - 3.60S_{21} - 0.544(S_{21})^2$	0.952	0.000
		$A_2 = 2.93 - 1.82S_{21} - 0.149(S_{21})^2$	0.978	0.000
Total polar compounds (总极性物质含量, TPC)	$T_{2w}$ 、 $T_{21}$	$TPC_1 = 92.392 - 0.250T_{21} - 0.601T_{2w}$	0.993	0.000
		$TPC_2 = 116.955 + 0.490T_{21} - 0.895T_{2w}$	0.987	0.000

\* 1. oil samples without foodstuff; 2. oil samples with potato chips

由表 1 可知, TPC 含量、酸价与  $T_{2w}$ 、 $T_{21}$  间均存在良好的相关性,  $r^2$  可达 0.96 以上; 油脂粘度与  $T_{2w}$ 、吸光值与  $S_{21}$  呈二项式关系( $r^2 = 0.939 \sim 0.992$ )。此外,对模型进行验证试验,将验证油样的 LF-NMR 检测数据分别代入表 1 所建立的相关性模型中,计算获得该理化指标的理论预测值,其与实测值的相符性分析结果见图 7。由图 7 可见,各理化指标的理论预测值与实测值之间有较高的相符性,  $r^2$  可达 0.938 ~ 0.996,说明在试验范围内,表 1 中建立的回归方程具有较好的预测效果,通过油样的 LF-NMR 弛豫特性(如  $T_{2w}$ 、 $T_{21}$ 、 $S_{21}$  等)可有效反映油样理化指标的变化规律。

## 3 结论

本文以常用的大豆油为研究对象,对其无料/薯条煎炸过程中多种常规理化指标(酸价、粘度、吸光值及 TPC 含量等)及其 LF-NMR 弛豫特性的变化规律进行了研究。研究结果表明:随煎炸时间延长,大豆油的酸价、TPC 含量及  $S_{21}$  峰面积均线性增大,  $T_{21}$ 、 $T_{22}$  峰起始时间及  $T_{2w}$  线性减小( $r^2 > 0.90$ ),粘度、吸光值的升高规律则符合二项式关系( $r^2 > 0.90$ ),  $T_{23}$  峰起始时间及  $S_{22}$ 、 $S_{23}$  与煎炸时间之间无明显规律性变化。煎炸薯条可使油样的酸价、粘度、TPC 含量、吸光值及  $S_{21}$  均较无料煎炸时显著增大( $P < 0.05$ ),而  $T_{21}$ 、 $T_{22}$  峰起始时间及  $T_{2w}$  显著缩短。多元回归分析表明,酸价及 TPC 含量与



$T_{2w}$ 、 $T_{21}$ , 粘度与  $T_{2w}$ , 吸光值与  $S_{21}$  间均可建立良好的相关性模型( $r^2 > 0.93$ )。模型验证合理可靠, 说明可通过油样的 LF - NMR 弛豫特性检测结果有效预测其理化指标的变化。本研究可为将 LF - NMR 技术有效应用于煎炸油脂品质快速有效监控提供必要的基础数据。

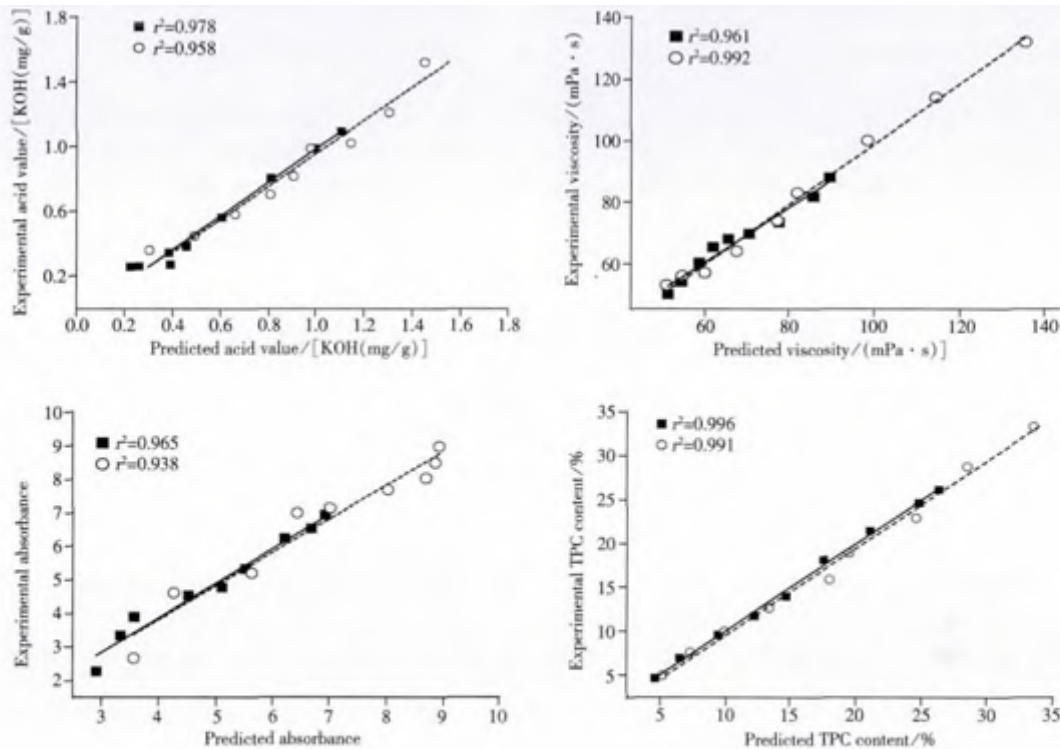


图 7 酸价、粘度、吸光值及 TPC 含量实测值与预测值关系曲线

Fig. 7 Correlation plot of the experimental value versus LF - NMR analysis predicted value of acid value, viscosity, absorbance values and TPC content

■ oil samples without foodstuff; ○ oil samples with potato chips

#### 参考文献:

- [1] Hui Y H. *Bailey's Industrial Oil & Fat Products*. 2nd ed. Xu S G, Qiu A Y, transl. Beijing: China Light Industry Press( Hui Y H. 贝雷: 油脂化学与工艺学. 2 版. 徐生庚, 裘爱泳, 译. 北京: 中国轻工业出版社), 2001: 520 - 526.
- [2] Deng Y, Wu Y, Yang M D, Yu S M, Li Y F. *Trans. Chin. Soc. Agric. Eng.* ( 邓云, 吴颖, 杨铭铎, 余善鸣, 李云飞. 农业工程学报), 2004, 20(6): 160 - 164.
- [3] María D G, Patricia S U. *Food Control*, 2012, (24): 50 - 56.
- [4] Xiao X S, Bi Y L, Peng Y H, Li X Y. *China Oils and Fats*. ( 肖新生, 毕艳兰, 彭元怀, 李潇颖. 中国油脂), 2006, 31(5): 35 - 38.
- [5] Henrik T P, Lars M, Siren B E. *JAOCs*, 2000, 77(10): 1069 - 1077.
- [6] Franz D, Markus C, Michael M, Gisela G. *Prog. Nucl. Magn. Reson. Spectrosc.*, 2012, (60): 52 - 70.
- [7] Martina H, Harriette H, Heinz - Dieter I. *Talanta*, 1998, (47): 447 - 454.
- [8] Wang Y W, Wang X, Liu B L, Shi R. *Food Sci.* ( 王永巍, 王欣, 刘宝林, 史然. 食品科学), 2012, 6: 171 - 175.
- [9] Adolfo F V, Ana B G. *Food Chem.*, 2006, (98): 214 - 219.
- [10] Wakako T, Akiko M, Kaori U. *Food Chem.*, 2010, (123): 976 - 982.
- [11] Farhoosh R, Tavassoli - Kafrani M H. *Food Chem.*, 2010, (122): 381 - 385.
- [12] GB/T 22500 - 2008. Animal and Vegetable Fats and Oils - Determination of Ultraviolet Absorbance Expressed as Specific UV Extinction. National Standards of the People's Republic of China ( 动植物油脂紫外吸光度的测定. 中华人民共和国国家标准).
- [13] GB/T 509.37 - 2003. Method for Analysis of Hygienic Standard of Edible Oils. National Standards of the People's Republic of China ( 国标食用植物油卫生分析标准. 中华人民共和国国家标准).
- [14] GB/T 509.202 - 2003. Determination of Polar Compounds in Edible Vegetable Oils Used in Frying Food. National Standards of the People's Republic of China ( 食用植物油煎炸过程中的极性化合物含量(PC)测定. 中华人民共和国国家标准).

- 标准)。
- [15] Shi R, Wang X, Liu B L, Zhao T T, Lu H Y. *J. Instrum. Anal.* (史然, 王欣, 刘宝林, 赵婷婷, 卢海燕. 分析测试学报), **2012**, 31(11): 1365–1372.
- [16] Hara E, Ogawa Y, Totani Y. *J. Oleo Sci.*, **2006**, (55): 167–172.
- [17] Kalogianni E P, Karapantsios T D, Miller R. *J. Food Eng.*, **2011**, 105: 169–179.
- [18] Krokida M K, Oreopoulou V, Maroulis Z B, Marinos K D. *J. Food Eng.*, **2001**, 48: 219–225.
- [19] Baik O–D, Mittal G S. *Food Res. Int.*, **2005**, 38(2): 183–191.
- [20] Ruan R S, Lin X Y, Zhang J S, Liu Y H, Li J, Chen L. *The Application of Nuclear Magnetic Resonance (NMR) Technology in the Food and Biological Systems*. Beijing: China Light Industry Press(阮榕生, 林向阳, 张锦胜, 刘玉环, 李筠, 陈灵. 核磁共振技术在食品和生物体系中的应用. 北京: 中国轻工业出版社), **2009**: 1–36.

欢迎订阅 欢迎投稿 欢迎刊登广告

## 《分析测试学报》

国内刊号: CN 44–1318/TH

国际标准刊号: ISSN 1004–4957

国际刊名化代码 CODEN: FCEXES

邮发代号: 46–104

国外代号: BM 6013

广告经营许可证: 440000100186

《分析测试学报》是由中国广州分析测试中心、中国分析测试协会共同主办的全国性学术刊物, 中文核心期刊。刊登质谱学、光谱学、色谱学、波谱学、电化学、电子显微学等方面的分析测试新理论、新方法、新技术的研究成果, 介绍新仪器装置及在生物、医药、化学化工、商检、食品检验等方面实用性强的实验技术。适合科研院所、高等院校、检测机构、医药、卫生以及厂矿企业分析测试工作和管理人员阅读。

经过多年的发展, 本刊已成为国内知名的化学类核心期刊。2011年, 影响因子在全国化学类刊物排名中位列第5名, 被引频次每年递增约30%, 稿源丰富, 基金论文比超过70%。近几年, 本刊发表的论文被CA(美国化学文摘)收录率达94%, 2006年引文频次在CA千种表中国部分中列第38名, 并被国际上其它知名的数据库如日本科技文献速报、俄罗斯文摘、英国分析文摘(AA)、《质谱公报》等收录。在《中文核心期刊要目总览》2011年版的化学类期刊列第9位; 入选2012年度“中国国际影响力优秀学术期刊”; 进入由全国8000种期刊遴选出的500种科技期刊组成的“中国科技期刊精品数据库”; 中国学术期刊综合评价数据库(CAJCED)统计刊源; 中国科技论文统计源期刊(中国科技核心期刊); 《中国科学引文数据库》来源期刊; 中国期刊全文数据库(CJFD)收录期刊 《中国核心期刊(遴选)数据库》收录 《中国学术期刊(光盘版)》全文收录期刊 《中国期刊网》全文收录期刊 《中国学术期刊文摘(中、英文版)》收录为源期刊等。

本刊为月刊, 国内外公开发行人。大16开, 单价: 12.00元/册, 全年144元。请在全国各地邮局订阅。未在邮局订到者可直接向本编辑部补订。补订办法: 请从邮局汇款至广州市先烈中路100号《分析测试学报》编辑部, 邮编: 510070, 写明订户单位、详细地址、收刊人姓名、邮编及补订份数(全年或某期), 电话: (020) 87684776 或 37656606, <http://www.fxcsxb.com>(可在线投稿), E-mail: [fxcsxb@china.com](mailto:fxcsxb@china.com)。

# 低场核磁共振技术检测煎炸油品质

王永巍<sup>1</sup>, 王欣<sup>1,\*</sup>, 刘宝林<sup>1</sup>, 史然<sup>1</sup>, 杨培强<sup>2</sup>

(1.上海理工大学食品质量与安全研究所, 上海 200093; 2.上海纽迈电子科技有限公司, 上海 200333)

**摘要:**应用低场核磁共振技术对无对象煎炸大豆油油样进行检测, 通过对多组分  $T_2$  弛豫图谱以及峰面积比例  $S_{21}$  和单组份弛豫时间  $T_{2w}$  分析, 煎炸 4h 后图谱中 10ms 左右出现明显特征小峰, 且  $S_{21}$  和  $T_{2w}$  与煎炸时间、酸价、黏度、吸光度和极性组分含量呈现良好的规律性, 相关系数在 0.941 ~ 0.997 之间, 说明可以利用低场核磁共振检测的  $S_{21}$  和  $T_{2w}$  有效反映煎炸油的品质变化。但与过氧化值之间无明显规律性。结果可为后期煎炸油的低场核磁共振技术快速检测提供基础。

**关键词:** 低场核磁共振; 煎炸油; 快速检测;  $T_2$  弛豫图谱

## Application of Low-Field Nuclear Magnetic Resonance (LF-NMR) to Analyze Frying Oil Quality

WANG Yong-wei<sup>1</sup>, WANG Xin<sup>1,\*</sup>, LIU Bao-lin<sup>1</sup>, SHI Ran<sup>1</sup>, YANG Pei-qiang<sup>2</sup>

(1. Institute of Food Quality and Safty, University of Shanghai for Science and Technology, Shanghai 200093, China ;  
2. Shanghai Niumag Corporation, Shanghai 200333, China)

**Abstract:** Low-field nuclear magnetic resonance (LF-NMR) was used to analyze soybean oil without objects in it during frying. Multi-component  $T_2$  relaxation spectra, peak area ratio  $S_{21}$  and single component relaxation time  $T_{2w}$  were determined. An obvious characteristic peak appeared at 10 ms in the multi-component  $T_2$  relaxation spectrum after 4 h of frying.  $S_{21}$  and  $T_{2w}$  were correlated with frying time, acid value, viscosity, absorbance and polar component content with a correlation coefficient between 0.941 and 0.997. Thus,  $S_{21}$  and  $T_{2w}$  could effectively reflect the quality of frying oil. However, they had no obvious correlation with peroxide value. These results will be very helpful for the application of LF-NMR to rapidly detect frying oil quality.

**Key words:** low-field nuclear magnetic resonance (LF-NMR); frying oil; rapid detection;  $T_2$  relaxation spectrum

中图分类号: TS227

文献标识码: A

文章编号: 1002-6630(2012)06-0171-05

深度油炸能快速熟制食品并赋予其香脆的风味, 煎炸食品一直深受大众喜欢, 在世界各地的消费量每年都呈现显著的递增趋势。煎炸食品的质量与煎炸油的质量紧密相关<sup>[1]</sup>。油脂在煎炸过程, 发生聚合、氧化、分解和水解反应, 色泽逐渐变深, 黏度增大而且气味劣化, 产生大量对人体有害的物质<sup>[2]</sup>。对于食品生产厂家, 油脂的长时间多次利用会大大降低成本, 因此近年来煎炸废油非法回收利用现象频频见诸于全国各地媒体, 对油脂质量的监督管理成为监管部门的重中之重。

传统的油脂检测方法有感官评价、物理化学指标的评价(如吸光度、黏度、酸价、过氧化值等)、极性组分总含量的测定等。但是这些指标的检测需要大量的时间和化学试剂, 很难在线快速对油脂品质变化程度做出

评价<sup>[3]</sup>。新型检测方法如化学感官系统电子鼻和近红外傅里叶变换仪可以快速检测油样, 但其与常规指标的相关系数并不高, 且价格昂贵<sup>[4]</sup>。因此, 寻找一种快速、便捷、灵敏、低成本的新型检测方法成为油脂行业的一个新的研究方向<sup>[4]</sup>。低场核磁共振分析仪器设备体积小, 检测样品快速、无损、实时、无需任何化学试剂, 且价格低廉(市场价约为上述仪器的 1/3)。目前, 低场核磁共振技术主要对检测对象的纵向弛豫时间( $T_1$ )、横向弛豫时间( $T_2$ )、扩散系数以及 CPMG(carr-purcell-meiboom-gill)回波数据进行分析, 在油脂检测中应用广泛, Rudi 等<sup>[5]</sup>利用时域 NMR 技术对样品进行复合弛豫分析, 在同一时间测定纵向和横向弛豫时间  $T_1$  和  $T_2$ , 使得生产过程中的油水含量可同时被测定; Miquel 等<sup>[6]</sup>利

收稿日期: 2011-07-21

基金项目: 上海市教委科研创新项目(11YZ109)

作者简介: 王永巍(1985—), 男, 硕士研究生, 研究方向为食品安全快速检测。E-mail: wangyongwei16@163.com

\* 通信作者: 王欣(1975—), 女, 副教授, 博士, 研究方向为食品冷冻冷藏、食品安全。E-mail: wx0426951@126.com

用 NMR 研究榛子油在巧克力中的移动情况, 并获得其扩散常数; Martina 等<sup>[7]</sup>建立了 NMR 弛豫时间与深度煎炸油的极性组分总量建立关系, 发现 NMR 弛豫时间能较好的反应极性组分含量; 王乐等<sup>[8]</sup>利用脉冲式 NMR 方法测定油脂中 SFC 含量, 以鉴别食用植物油掺伪餐饮业废油脂; 周凝等<sup>[9]</sup>应用 LF-NMR 的  $T_2$  弛豫反演图谱研究米糠毛油掺伪食用油, 发现米糠毛油在  $T_2$  弛豫图谱 10ms 左右出现特征峰, 且该峰面积比( $S_{21}$ )随着毛油掺伪量增加而线性递增。文献调研表明, 目前国内外关于低场 NMR 技术在深度煎炸油品质快速检测方面的研究报道很少, 因此利用核磁共振技术对深度煎炸油进行快速检测研究具有重要意义。

本研究拟利用低场核磁共振技术(low-field nuclear magnetic resonance, LF-NMR)对无煎炸对象的大豆油油样进行检测, 对其横向弛豫时间多组分与单组分反演数据进行分析, 在对煎炸过程中低场 NMR 检测结果变化规律探讨的基础上, 进一步分析低场核磁共振检测结果与油样的酸价、黏度、吸光度、极性组分含量以及过氧化值等指标的关联性, 为低场核磁共振技术应用于煎炸废油检测提供基础数据。

## 1 材料与方法

### 1.1 材料与试剂

金龙鱼大豆油 益海嘉里食品工业有限公司。

乙醚、石油醚、三溴甲烷、冰乙酸、硫代硫酸钠、氢氧化钾、正己烷等(均为分析纯) 上海国药集团化学试剂有限公司。

### 1.2 仪器与设备

09 款流线型 5.5L 电炸炉 广州汇利有限公司; NMI-20 型核磁共振分析仪(氢谱、共振频率 21.959MHz、磁体强度 0.52T, 配套 T-invit 反演拟合软件和 15mm 核磁共振专用测试管) 上海纽迈电子科技有限公司; 层析柱(定制) 上海市崇明建设玻璃仪器厂; NDJ-1 型旋转黏度计 东莞市精鼎仪器有限公司; 751-G(200~1000nm) 分光光度计 上海分析仪器厂。

### 1.3 方法

#### 1.3.1 大豆油煎炸实验

将 5L 大豆油倒入电炸炉, 控温在  $(180 \pm 2)$  进行无料空炸, 每隔 2h 取样 150mL 置于样品瓶中, 密封存放于  $-20$  的冰箱冷冻室中待测。

#### 1.3.2 NMR 横向弛豫时间( $T_2$ )测量

利用 CPMG 脉冲序列测定样品的横向弛豫时间( $T_2$ )。将 4mL 样品移入直径 15mm 的核磁共振专用试管, 置于样品槽进行测定, 测量温度为  $(32 \pm 0.1)$ 。设备参数设置如下: 采样点数(TD) 500170, 谱宽(SW)

250kHz, 采样重复时间(TR)1500ms, 重复扫描次数(NS) 4, 回波时间( $\tau$ )200 $\mu$ s, 回波个数(EchoCount)5000。

#### 1.3.3 煎炸油常规指标检测

黏度: 取 150mL 油样倒入 250mL 烧杯中, 将其置于 25 恒温水浴锅中, 用 NDJ-1 型旋转黏度计对油样进行测定; 吸光度: 参考 GB/T 22500—2008《动植物油脂》紫外吸光度的测定<sup>[10]</sup>; 酸价的测定: 参考 GB/T 509.37—2003《国标食用植物油卫生分析标准》, 指示剂法<sup>[11]</sup>; 极性组分含量测定: 参考 GB/T 509.202—2003《食用植物油煎炸过程中的极性组分(PC)测定》<sup>[12]</sup>; 过氧化值的测定: 参考 GB/T 509.37—2003《国标食用植物油卫生分析标准》, 指示剂法<sup>[11]</sup>。

### 1.4 数据的处理

NMR 弛豫测量得到的图为自由诱导指数衰减曲线, 其数学模型为:  $A(t) = A_{0i} \exp(-\frac{t}{T_{2i}})$ , 式中:  $A(t)$  为衰减到时间  $t$  时的幅值大小;  $A_{0i}$  为第  $i$  个组分平衡时的幅值大小;  $T_{2i}$  为第  $i$  个组分的横向弛豫时间<sup>[13]</sup>。利用 T-invit 软件对  $i$  个组分进行反演拟合, 可得到油样的多组分弛豫时间  $T_2$  及数据图谱。本软件使用综合迭代算法, 结果为离散型与连续型相结合的  $T_2$  谱。反演结果为生成弛豫图、各个弛豫过程的弛豫幅值、其对应的时间常数及其面积分数。当将  $i$  个组分当作一个整体组分时, 可反演出油样的单组份弛豫时间  $T_{2w}$ 。

实验所得数据应用 Origin 8.0 软件进行图形绘制并进行线性、指数、二项式等进行曲线拟合。

## 2 结果与分析

### 2.1 NMR 检测数据分析

#### 2.1.1 多组分 $T_2$ 弛豫图谱及数据分析

在相同参数条件下, 对 30 个掺伪油样品进行低场 NMR 检测获得大豆油空炸 60h 的多组分  $T_2$  对比弛豫图谱, 为了便于观察, 以每隔 8h 取一个油样的图谱为例说明, 如图 1 所示。

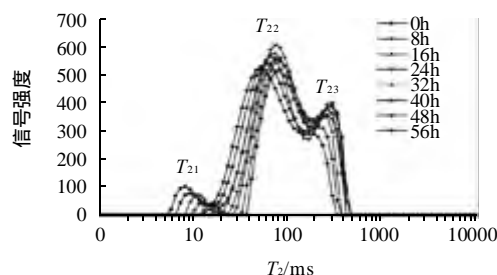


图 1 大豆煎炸油多组分弛豫图谱

Fig.1 Multi-component  $T_2$  relaxation spectra of soybean oil

由图1可见,第1个峰为 $T_{21}$ 峰,第2个峰为 $T_{22}$ 峰,第3个峰为 $T_{23}$ 峰。空炸大豆油的弛豫图谱图形大致相同,其中0h和2h时油样的弛豫图谱主要有 $T_{22}$ 和 $T_{23}$ 两个主峰,未见 $T_{21}$ 峰,从4h开始油样图谱在10ms左右有 $T_{21}$ 小峰出现,且波谱有明显的左移趋势;随着煎炸时间的延长,其峰面积比例 $S_{21}$ 逐渐增大。对峰面积比例 $S_{21}$ 随煎炸时间的变化进行了数据拟合,结果如图2所示。 $S_{21}$ 与煎炸时间呈现良好的线性关系, $y = -0.911 + 0.117x$  ( $R^2 = 0.971$ ,  $P < 0.0001$ )。说明可以利用 $S_{21}$ 有效反映煎炸油随煎炸时间的品质变化。

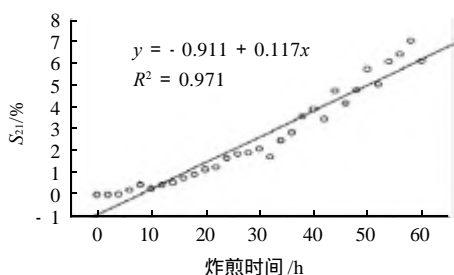


图2 大豆煎炸油峰面积比例 $S_{21}$ 与煎炸时间的相关性  
Fig.2 Correlation between  $S_{21}$  and frying time

### 2.1.2 单组份弛豫时间 $T_{2w}$ 数据分析

将油样看作仅由一类物质组成的整体,进行单组分反演,得到大豆油煎炸过程中的总弛豫时间 $T_{2w}$ ,为了便于观察,每隔8h取一个油样的单组份弛豫数据,图谱如图3所示。

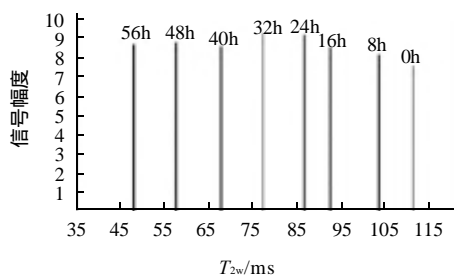


图3 大豆煎炸油的单组份弛豫图谱  
Fig.3 Single component relaxation spectra of soybean oil

由图3可知,大豆油经煎炸后,其单组份弛豫时间 $T_{2w}$ 随煎炸时间延长呈现线性减小趋势,由油样的 $T_{2w}$ 的变化能简单推断出大豆油是否使用过以及其使用时间的长短。对单组份弛豫时间 $T_{2w}$ 随煎炸时间的变化进行了数据拟合,结果如图4所示。 $T_{2w}$ 与煎炸时间呈现良好的线性关系, $y = 113.392 - 1.192x$  ( $R^2 = 0.997$ ,  $P < 0.0001$ )。说明也可以利用 $T_{2w}$ 有效反映煎炸油随煎炸时间的品质变化。

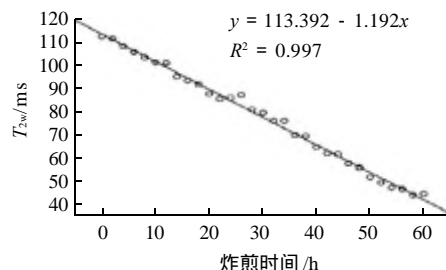


图4 大豆煎炸油单组份弛豫时间与煎炸时间的相关性  
Fig.4 Correlation between single component relaxation time and frying oil

## 2.2 大豆油各检测指标与LF-NMR数据之间的相关性分析

### 2.2.1 酸价与LF-NMR数据间的相关性

酸价是油脂评价的重要指标之一,用来衡量油脂中游离脂肪酸的含量。大豆油煎炸过程中酸价的变化与 $S_{21}$ 和 $T_{2w}$ 的关系如图5所示。

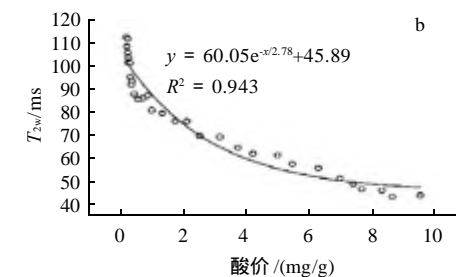
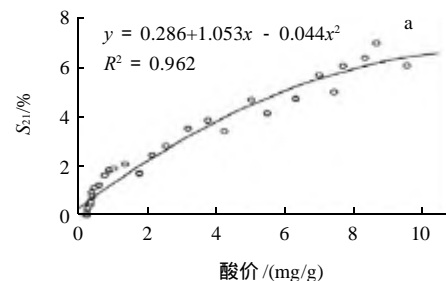


图5 酸价与大豆煎炸油 $S_{21}$ (a)和 $T_{2w}$ (b)的相关性  
Fig.5 Correlation between acid value and  $S_{21}$  (a) or  $T_{2w}$  (b)

由图5a可知, $S_{21}$ 随着酸价的增大而逐渐增大,且酸价与 $S_{21}$ 之间的变化符合公式 $y = 0.286 + 1.053x - 0.044x^2$  ( $R^2 = 0.962$ ,  $P < 0.0001$ ),而由图5b可知, $T_{2w}$ 随着酸价的增大呈现指数减小,拟合公式为 $y = 60.05e^{-x^{2.78}} + 45.89$  ( $R^2 = 0.943$ ,  $P < 0.0001$ )。说明可以利用 $S_{21}$ 或 $T_{2w}$ 有效反映大豆煎炸油随煎炸时间的酸价变化规律。这可能是因为随煎炸时间延长而逐渐增大,游离脂肪酸增多,油样组织结构的不均匀性增加而造成油样内部磁场不均匀,以致使弛豫时间减小<sup>[14]</sup>。

## 2.2.2 黏度与 LF-NMR 数据间的相关性

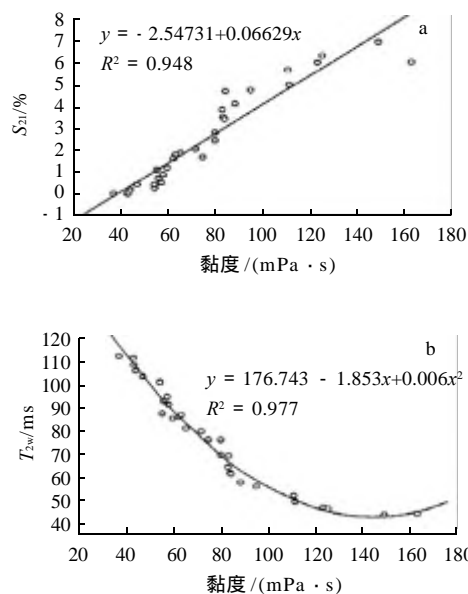


图6 黏度与大豆煎炸油  $S_{21}$ (a)和  $T_{2w}$ (b)的相关性  
Fig.6 Correlation between viscosity and  $S_{21}$  (a) or  $T_{2w}$  (b)

黏度是评价油脂煎炸过程中品质变化的重要指标,随着煎炸时间的延长,油脂发生热聚合和氧化聚合反应,使聚合物含量增加。而聚合物为大分子物质,其黏度大于油脂,煎炸油黏度自然也随之增大,如图6所示,煎炸过程中油脂的黏度与  $S_{21}$  有良好的线性关系即:  $y = -2.54731 + 0.06629x$  ( $R^2 = 0.948$ ,  $P < 0.0001$ ),而与  $T_{2w}$  呈现良好的二项式关系,拟合公式为  $y = 176.743 - 1.853x + 0.006x^2$  ( $R^2 = 0.977$ ,  $P < 0.0001$ ),说明可以利用  $S_{21}$  或  $T_{2w}$  有效反映大豆煎炸油随煎炸时间的黏度变化规律。油脂在高温下黏度增大,分子发生聚合,分子团变大,氢质子受到束缚的机会增大,自由度减小,以致多组分  $T_2$  弛豫图谱左移,单组分弛豫时间  $T_{2w}$  缩短。

## 2.2.3 吸光度与 LF-NMR 数据间的相关性

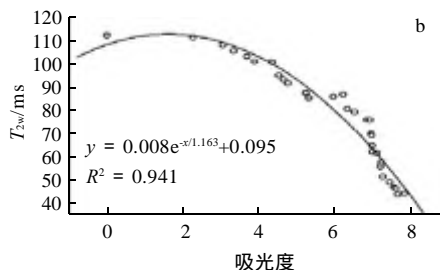
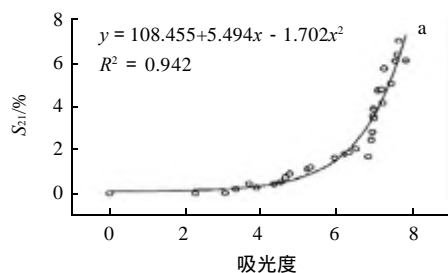


图7 吸光度与大豆煎炸油  $S_{21}$ (a)和  $T_{2w}$ (b)的相关性  
Fig.7 Correlation between absorbance and  $S_{21}$  (a) or  $T_{2w}$  (b)

利用油脂在特征波长下的吸光度,可以表示油脂的色泽情况<sup>[15]</sup>。图7a为油脂煎炸过程中色泽变化与 LF-NMR 测得的  $S_{21}$  之间的变化规律。随着煎炸时间的延长吸光度逐渐增大,油样色泽逐渐加深。二者之间符合公式:  $y = 108.455 + 5.494x - 1.702x^2$  ( $R^2 = 0.942$ ,  $P < 0.0001$ )。图7b则表明,随着吸光度增大,  $T_{2w}$  呈现指数减小趋势,符合公式  $y = 0.008e^{x/1.163} + 0.095$  ( $R^2 = 0.941$ ,  $P < 0.0001$ )。说明可以利用  $S_{21}$  或  $T_{2w}$  有效反映大豆煎炸油随煎炸时间的吸光度变化规律。有报道称<sup>[3]</sup>,油脂在煎炸过程中,产生的色素类物质和杂质是影响吸光度变化的主要原因。

## 2.2.4 极性组分(PC)含量与 LF-NMR 数据间的相关性

PC 含量可作为衡量油脂品质的一个优良指标<sup>[16-18]</sup>。随着煎炸时间延长,PC 含量增大,PC 含量与 NMR 检测数据间的关系如图8所示。

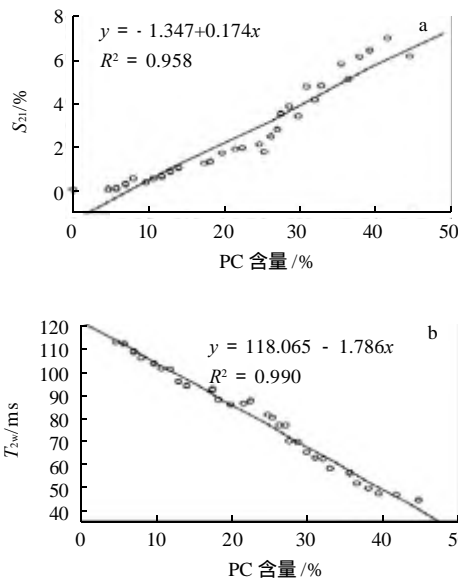


图8 PC含量与大豆煎炸油  $S_{21}$ (a)和  $T_{2w}$ (b)的相关性  
Fig.8 Correlation between polar component content and  $S_{21}$  (a) or  $T_{2w}$  (b)

结果表明,随着极性化合物含量的增加, $S_{21}$ 峰面积比例线性增大( $y = -1.347 + 0.174x$ ,  $R^2 = 0.958$ ),而单组份弛豫时间 $T_{2w}$ 呈良好的线性减小关系( $y = 118.065 - 1.786x$ ,  $R^2 = 0.990$ )。说明也可以利用 $S_{21}$ 或 $T_{2w}$ 有效反映大豆煎炸油随煎炸时间的PC含量变化规律。正常大豆油中极性组分含量很少,在煎炸过程中,油脂氧化、聚合、分解、水解等反应产生了大量极性化合物,这也可能是导致 $S_{21}$ 变化的原因之一。PC的增加使油样不均匀性增大,从而使内部分子间的磁场不均匀, $T_{2w}$ 变小。PC含量的增加也是使 $T_{2w}$ 弛豫时间变小原因之一。

### 2.2.5 过氧化值与LF-NMR数据间的相关性

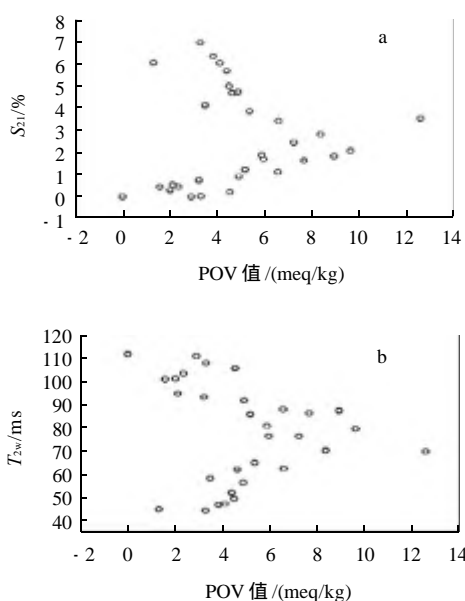


图9 过氧化值与大豆煎炸油 $S_{21}$ (a)和 $T_{2w}$ (b)的相关性  
Fig.9 Correlation between peroxide value and  $S_{21}$  (a) or  $T_{2w}$  (b)

过氧化值是非常重要的指标,人体摄入过量的过氧化脂质,会引起细胞的衰老、动脉粥样硬化以及癌变。有报道称,过氧化值在油脂煎炸中变化但无规律<sup>[19]</sup>,本实验中过氧化值在煎炸过程中同样呈现无规律性。将LF-NMR测得的 $S_{21}$ 与 $T_{2w}$ 和过氧化值进行关联分析,由图9可知, $S_{21}$ 和 $T_{2w}$ 与过氧化值相关性极低,说明LF-NMR测得数据 $S_{21}$ 和 $T_{2w}$ 不能推测出过氧化值的变化情况。

### 3 结论

低场核磁共振技术是一种非常有潜力的油脂快速检测新技术。对大豆煎炸油的低场核磁共振检测结果表明,煎炸4h后 $T_2$ 弛豫图谱中10ms左右出现明显特征小峰,且 $S_{21}$ 和 $T_{2w}$ 与煎炸时间、酸价、黏度、吸光度和极性组分含量呈现良好的规律性,相关系数在0.941~0.997之间,说明可以利用低场核磁共振检测的 $S_{21}$ 和 $T_{2w}$ 有效反映煎炸油的品质变化。但与过氧化值之间无明显规律性。本结果可为后期煎炸油的快速检测技术提供基本的研究基础。

### 参考文献:

- [1] BLUMENTHAL M M. A new look at the chemistry and physics of deep fat frying[J]. Food Technology, 1991, 45(2): 68-72.
- [2] 李东锐, 毕艳兰, 肖新生, 等. 食用油煎炸过程中的品质变化研究[J]. 中国油脂, 2006, 31(6): 34-36.
- [3] 黄兴, 姚庭香, 王吉良, 等. 煎炸油质变检验方法探讨[J]. 食品科学, 1995, 16(8): 50-53.
- [4] 肖新生, 毕艳兰, 彭元怀, 等. 煎炸油检测方法的比较[J]. 中国油脂, 2006, 31(5): 35-38.
- [5] RUDI T, GUTHAUSEN G, BURK W. Simultaneous determination of fat and water content in caramel using time domain NMR[J]. Food Chemistry, 2008, 106(4): 1375-1378.
- [6] MIQUEL M E, CALI S, COUZENS P J, et al. Kinetics of the migration of lipids in composite chocolate measured by magnetic resonance imaging [J]. Food Research International, 2001, 34(9): 773-781.
- [7] MARTINA H, HARIETTE H, HEINZ-DIETER I, et al. Determination of total polar parts with new methods for the quality survey of frying fats and oils[J]. Talanta, 1998, 47(2): 447-454.
- [8] 王乐, 黎勇, 胡建华. 核磁共振法鉴别食用植物油掺伪餐饮业废油脂[J]. 中国油脂, 2008, 38(10): 75-77.
- [9] 周凝, 刘宝林, 王欣, 等. 米糠毛油掺伪食用植物油的低场核磁共振检测[J]. 食品发酵与工业, 2011, 37(3): 177-181.
- [10] GB/T 22500—2008 动植物油脂 紫外吸光度的测定[S].
- [11] GB/T 509.37—2003 国标食用植物油卫生分析标准[S].
- [12] GB/T 509.202—2003 食用植物油煎炸过程中的极性组分(PC)测定[S].
- [13] ABRAHAM R J, FISHER J, LOFTUS P. Introduction to NMR spectroscopy[M]. Chichester, UK: Wiley, 1991: 86.
- [14] 汪红志, 张学龙, 武杰. 核磁共振成像技术实验教程[M]. 北京: 科学出版社, 2008.
- [15] 朱展才. 分光光度法测定植物油脂色泽[J]. 分析化学, 1994, 22(12): 1228.
- [16] RAYNER C, ROWNEY M, ZEGLINSKI P. Composition and quality of deep fat frying oil from fast food outlets in Victoria[J]. Food Australia, 1998, 50(2): 88-91.
- [17] SEBEDIO T L, KAITARANTA T, GRANDGIRARD A. Quality assessment of industrial prefried french fries[J]. Journal of the American Oil Chemists' Society, 1991, 68(5): 299-302.
- [18] 邓云, 杨铭铎, 李健, 等. 煎炸油脂中极性成分的色谱分析[J]. 食品发酵与工业, 2006, 32(5): 127-130.
- [19] 姚晓敏, 孙向军, 徐建强. 煎炸油质变检验探讨[J]. 食品科技, 2000 (4): 56-57.

# 羟自由基导致肉类肌原纤维蛋白氧化和凝胶性降低

李 银, 李 侠, 张春晖\*, 孙红梅, 董宪兵

(中国农业科学院农产品加工研究所/农业部农产品加工综合性重点实验室, 北京 100193)

**摘 要:** 为研究羟自由基 ( $\cdot\text{OH}$ ) 氧化体系中肌原纤维蛋白 (myofibrillar protein, MP) 氧化及其凝胶特性的变化, 试验分析了羟自由基氧化体系中不同  $\text{H}_2\text{O}_2$  浓度对蛋白氧化程度及 MP 凝胶白度、持水力、质构特性 (texture profiles analysis, TPA) 与弹性模量等特征指标的影响。结果表明: 随  $\text{H}_2\text{O}_2$  浓度的增加, MP 中羰基值上升, 蛋白氧化程度加剧, 凝胶白度、保水性、硬度、咀嚼性及弹性模量则与  $\text{H}_2\text{O}_2$  浓度呈显著负相关。与对照组相比, 当  $\text{H}_2\text{O}_2$  浓度增加至 20 mmol/L 时, 羰基含量增加至 2.82 nmol/mg 蛋白 ( $p < 0.05$ ), 凝胶白度、持水性及硬度则分别下降了 2.83%、14.65% 及 52.77% ( $p < 0.05$ )。扫描电镜 (scanning electron micrograph, SEM) 观察表明, MP 氧化导致凝胶微观结构破坏, 形成空隙较大且分布不均的网络; 低场核磁共振分析 (nuclear magnetic resonance, NMR) 结果显示, 随  $\text{H}_2\text{O}_2$  浓度的增加, MP 凝胶中的一部分不易流动水“态变”为自由水, 凝胶持水力降低。综上所述,  $\cdot\text{OH}$  氧化体系中肌原纤维蛋白氧化会影响其凝胶形成, 破坏蛋白凝胶结构, 降低凝胶功能, 这为肉类生产加工过程中蛋白氧化控制提供理论参考。

**关键词:** 蛋白质, 核磁共振, 肉, 羟自由基氧化体系, 肌原纤维蛋白, 微观结构

doi: 10.3969/j.issn.1002-6819.2013.12.036

中图分类号: TS251.5<sup>+</sup>1

文献标志码: A

文章编号: 1002-6819(2013)-12-0286-07

李 银, 李 侠, 张春晖, 等. 羟自由基导致肉类肌原纤维蛋白氧化和凝胶性降低[J]. 农业工程学报, 2013, 29(12): 286—292.

Li Yin, Li Xia, Zhang Chunhui, et al. Oxidation and decrease of gelling properties for meat myofibrillar protein induced by hydroxyl radical[J]. Transactions of the Chinese Society of Agricultural Engineering (Transactions of the CSAE), 2013, 29(12): 286—292. (in Chinese with English abstract)

## 0 引 言

畜禽宰后加工与贮藏过程中脂肪氧化、金属离子及内源氧化剂等引起的氧化反应会对肉与肉制品中的蛋白质造成氧化损伤<sup>[1]</sup>。蛋白氧化会导致其结构与功能的显著变化, 如发生交联聚合、降解及氨基酸侧链的改变等<sup>[2-3]</sup>。这些氧化效应会造成肉品色泽、口感劣变, 保水、保油性降低, 影响了肉品的可接受性, 缩短了产品的货架期<sup>[4]</sup>。肌原纤维蛋白 (myofibrillar protein, MP) 是肌肉中最重要的一类功能性蛋白, 主要包括肌球蛋白、肌动蛋白、肌动球蛋白、原肌球蛋白和肌钙蛋白等, 在热诱导作用下这类蛋白可以形成三维网络结构, 能赋予肉制品尤其是凝胶类产品良好的感官、质构及保水、保油性<sup>[5]</sup>。

肌肉蛋白的凝胶特性作为肉与肉制品加工中最重要的功能特性之一, 近年来关于肌原纤维蛋白凝胶特性影响因素研究多集中在 pH 值、离子强度及不同的添加剂等方面<sup>[6-9]</sup>, 关于肌原纤维蛋白氧化对其凝胶特性的影响研究虽在国外有一些相关报道, 但影响机制尚不完全清楚, 而国内关于此方面的研究并不多, 结合低场核磁共振技术 (low-field, nuclear magnetic resonance, NMR) 分析氧化对蛋白水合力影响及对凝胶中水分从不易流动水向自由水的“态变”研究也较少。本文通过测定凝胶保水性、白度、硬度、贮藏模量 ( $G'$ ) 等凝胶特征指标, 并借助扫描电镜及低场核磁共振技术分析氧化对凝胶微观结构及其水分组成与分布的影响, 多角度分析羟自由基 ( $\cdot\text{OH}$ ) 氧化体系中  $\cdot\text{OH}$  介导的肌原纤维蛋白氧化及其对凝胶特性的影响效应, 探讨  $\cdot\text{OH}$  介导的蛋白氧化及对蛋白凝胶特性的影响机制。

本研究借助铁-抗坏血酸-过氧化氢 ( $\text{Fe}^{3+}\text{-Vc-H}_2\text{O}_2$ ) 之间的化学反应, 构建羟基自由基氧化模型体系。通过分析模型体系条件下  $\text{H}_2\text{O}_2$  浓度对肌原纤维蛋白凝胶特性的影响, 探讨肉与肉制品贮藏加工过程中蛋白氧化效应, 以期肉类生产加工过程中蛋白氧化控制提供理论参考。

收稿日期: 2013-02-03 修订日期: 2013-05-15

基金项目: 国家自然科学基金 (31271902); 农业 (行业) 科技资助项目 (200903012, 201303083, 201303082)

作者简介: 李 银 (1988—), 女, 湖北咸宁人, 北京 中国农业科学院农产品加工研究所/农业部农产品加工综合性重点实验室, 100193。

Email: yin198802@163.com

\*通信作者: 张春晖 (1971—), 男, 河南固始人, 研究员, 研究方向为肉品科学。北京 中国农业科学院农产品加工研究所/农业部农产品加工综合性重点实验室, 100193。Email: dr\_zch@yahoo.com.cn



## 1 试验材料与方法

### 1.1 试验材料与试剂

试验用肉为北京五肉联有限公司提供的, 宰后 0~4℃ 成熟 24 h 的猪肉冷却肉的背最长肌 (*Longissimus*), 去除可见脂肪组织及结缔组织后用于提取肌原纤维蛋白。

试验所用试剂: 乙二醇-双-(2-氨基乙醚) 四乙酸 (ethylene glycol bis(2-aminoethyl) tetraacetic acid, EGTA) 购于美国 sigma 公司; 牛血清清蛋白 (albumin from bovine serum, BSA) 购于北京拜尔迪生物技术有限公司; 其他试剂均购于国药集团化学试剂有限公司, 均为分析纯。

### 1.2 主要仪器

CR22GII 高速冷冻离心机(日本 Hitachi 公司); T6 紫外分光光度计(北京普析通用有限公司); 电子天平(赛多利斯科学仪器(北京)有限公司); TXF200-S12 可编程恒温循环水浴锅(英国 Grant 公司); TA-XT2i 质构分析仪(英国 Stable Micro System 公司); Physica MCR 301 流变仪(奥地利 Anton Paar 有限公司); CR-400 色差仪(柯尼卡美能达(日本)公司); Eiko IB-5 型离子溅射喷金仪(日本 Hitachi 公司); H-7500 型扫描电镜(日本 Hitachi 公司); NM-2011 低场核磁共振仪(上海纽迈电子科技有限公司)。

### 1.3 试验方法

#### 1.3.1 肌原纤维蛋白的提取

参考 Xiong 等<sup>[10]</sup>的方法从猪背最长肌中分离提取肌原纤维蛋白, 将切碎的肉块与 4 倍体积的分离缓冲液 (0.1 mol/L NaCl, 10 mmol/L Na<sub>3</sub>PO<sub>4</sub>, 2 mmol/L MgCl<sub>2</sub>, 1 mmol/L EGTA, pH 值 7.0) 混合匀浆后离心 (4℃, 2 000×g, 15 min), 所得沉淀再重复洗涤, 离心 2 次。随后再按上述操作作用 4 倍体积 0.1 mol/L NaCl 溶液洗涤, 离心 2 次, 并在最后 1 次离心前用 2 层纱布过滤, 再用 0.1 mol/L HCl 溶液将其 pH 值调至 6.0, 最后得到的蛋白膏用于构建羟基自由基氧化模型体系。蛋白质浓度用双缩脲法测定, 采用牛血清清蛋白作为标准蛋白。

#### 1.3.2 FeCl<sub>3</sub>/Vc/H<sub>2</sub>O<sub>2</sub> (铁/抗坏血酸/过氧化氢) 氧化体系构建

参考 Xiong<sup>[11]</sup>的方法构建以下氧化体系: 反应历程为 Vc+Fe<sup>3+</sup>→Fe<sup>2+</sup>, Fe<sup>2+</sup>+H<sub>2</sub>O<sub>2</sub>→·OH, FeCl<sub>3</sub> 浓度为 0.01 mmol/L, Vc 浓度为 0.1 mmol/L, H<sub>2</sub>O<sub>2</sub> 浓度分别为 0.5、1、5、10、20 mmol/L。肌原纤维蛋白分散于上述氧化体系中 (最终质量浓度为 40 mg/mL), 在 4℃ 条件下氧化 24 h 后用 1 mmol/L 乙二胺四乙酸 (ethylene diamine tetraacetic acid,

EDTA) EDTA) 终止。以上的氧化反应均在 15 mmol/L 哌嗪 -N,N'- 双 (2-乙磺酸) (piperazine-1,4-bisethanesulfonic acid, PIPES) 为缓冲溶液 (pH 值 6.0, 离子强度 0.6 mol/L) 中进行。空白对照为新鲜猪背最长肌中提取出来后, 未加氧化剂直接于 4℃ 放置 24 h 的肌原纤维蛋白 (在本试验中将 H<sub>2</sub>O<sub>2</sub> 浓度定义为 0)。

#### 1.3.3 羰基值测定

参考 Levine<sup>[12]</sup>等测定羰基的方法, 在 1.5 mL 的离心管中, 加入 0.1 mL 的蛋白溶液与 0.5 mL 2,4-二硝基苯肼的 2 mol/L HCl 溶液, 在 25℃ 下反应 40 min, 空白样品中不含 2,4-二硝基苯肼的 2 mol/L HCl。然后加入 0.5 mL 质量分数为 20% 的三氯乙酸 (trichloroacetic acid, TCA), 震荡后离心 (11 000×g, 5 min) 弃上清, 蛋白沉淀用 1 mL 的乙醇-乙酸乙酯溶液 (体积比为 1:1) 洗涤 3 次, 挥发完溶剂后将蛋白质悬浮于 1 mL 6 mol/L 盐酸胍溶液中, 在 37℃ 条件下水浴保温 30 min。以空白为对照 370 nm 下测吸光值, 蛋白质羰基衍生物的含量 (nmol/mg·蛋白) 使用摩尔吸光系数为 22 000 L/(mol·cm) 计算。

#### 1.3.4 蛋白热诱导凝胶制备

将氧化后的肌原纤维蛋白用含有 0.6 mol/L NaCl, 15 mmol/L 哌嗪 -1,4- 二乙磺酸 (piperazine-1,4-bisethanesulfonic acid, PIPES) 的缓冲液 (pH 值 6.0) 将其质量浓度调至 30 mg/mL 后, 分别称取 5.0 g 的蛋白反应液于直径约 25 mm, 高度约 55 mm 的带盖玻璃瓶中, 在程序升温水浴锅中以 1℃/min 线性升温速率从 20℃ 加热至 75℃, 并于 75℃ 保温 20 min 后, 立即取出冷水浴后, 于 4℃ 冰箱中放置 24 h 后, 制得高度大约为 12 mm 左右凝胶体, 用于测定其白度、保水性、质构、微观结构及低场核磁水分“态变”分析。

#### 1.3.5 凝胶保水性测定

参考 Kocher 等<sup>[13]</sup>的离心法测定凝胶保水性 (water holding capacity, WHC), 将制备好的蛋白凝胶准确称其质量后, 于 4℃ 下 6 000×g 离心 15 min, 记录离心前后离心管的质量以及空管质量。WHC (%) 计算如下

$$WHC(\%) = \frac{m_1 - m}{m_2 - m} \times 100\%$$

式中,  $m_1$  为离心出液体后离心管与凝胶的质量, g;  $m_2$  为离心前离心管与凝胶的质量, g;  $m$  为空管质量, g。

#### 1.3.6 凝胶白度测定

参考陆剑锋等<sup>[14]</sup>的方法测定蛋白凝胶的白度值 (whiteness,  $W$ )。用色差仪测定蛋白凝胶的色差值, 其中亮度值  $L^*$ ; 红度值  $a^*$  (正值表示偏红,

负值表示偏绿)；黄度值  $b^*$  (正值表示偏黄, 负值表示偏蓝)。测前用标准白板 ( $L^*=25.60$ ,  $a^*=-0.30$ ,  $b^*=0.27$ ) 校正色差计。凝胶白度值计算如下

$$W = 100 - \sqrt{(100 - L^*)^2 + a^{*2} + b^{*2}}$$

### 1.3.7 凝胶质构测定

测量前将凝胶从 4℃ 冰箱取出, 室温下放置 30 min 后, 参考高建华等<sup>[15]</sup>的方法并做稍加修改进行质构剖面分析 (texture profile analysis, TPA), 测量参数设定: 探头 P/0.5R, 侧前下降速率为 1.0 mm/s, 测试速度 0.5 mm/s, 测后速度 1.0 mm/s, 压缩比 50%, 最小感应力 0.05 N, 数据的采集频率为每秒采集 50 个数据点用质构仪自带软件的 TPAFRAC.MAC 过程进行分析。

### 1.3.8 凝胶流变学特性测定

参考 Li 等<sup>[16]</sup>的方法并略微修改, 氧化后的肌原纤维蛋白用 PIPES 缓冲液 (pH 值 6.0) 将其质量浓度调至 30 mg/mL 后进行测量。测量参数为: 使用直径 25 mm 的平板夹具, 以 1℃/min 的升温速率从 20℃ 加热至 75℃, 振荡频率为 1 Hz, 狭缝为 1 mm。在平板夹具上好保护盖后, 滴加硅油, 防止样品水分蒸发影响测定结果。

### 1.3.9 扫描电镜观察凝胶微观结构测定 (scanning electron micrograph, SEM)

凝胶微观结构测定参考 Palka 等<sup>[17]</sup>的方法并稍加修改。取空白对照组、5 及 20 mmol/L  $H_2O_2$  组的凝胶样品, 用手术刀切成约 3 mm×3 mm×5 mm 的小条, 用体积分数为 3% 的戊二醛浸泡过夜固定, 再用 0.1 mol/L pH 值 7.2 的磷酸缓冲液洗涤 3 次; 然后质量分数 1% 锇酸固定 2 h, 再用体积分数 30%、50%、70%、90%、95% 及 100% 乙醇进行脱水, 每次 10 min 直至除去样品中的水分为止, 再用 100% 乙醇重复脱水 3 次, 保证样品绝对无水; 再经乙酸异戊酯置换后经  $CO_2$  临界点干燥, 真空离子溅射喷金仪喷金后进行微观结构观察。

### 1.3.10 凝胶水分分布与组成测定 (low-field NMR)

参考吴焯等<sup>[18]</sup>的方法采用低场 NMR 弛豫测定空白对照组、5 mmol/L  $H_2O_2$  及 20 mmol/L  $H_2O_2$  组凝胶样品水分分布及组成, 测定条件: 质子共振频率为 22.6 MHz, 测量温度为 32℃。将大约 1.0 g 样品放入 15 mm 核磁管中, 随后立即放入 NM-2011 核磁共振成像仪中进行分析。采用 Carr-Purcell-Meiboom-Gill (CPMG) 序列测定样品弛豫时间  $T_2$  值。测量参数为:  $\tau$ -值 (90° 脉冲与 180° 脉冲之间的时间) 为 100  $\mu$ s,

重复扫描 16 次, 重复间隔时间为 3 000 ms 得到 15000 个回波, 所得 CPMG 指数衰减曲线采用仪器自带的 MultiExp Inv Analysis 软件进行反演, 得到  $T_2$  值。

### 1.3.11 数据分析

本试验中除电镜试验外, 所有样品均至少设置 3 个重复。用 SAS 9.2 (statistic analysis system, SAS) 对结果进行方差分析, 使用最小显著差异法 (LSD) 进行显著性分析 ( $P < 0.05$ )。并用 SAS 9.2 进行各指标之间的相关性分析。

## 2 结果与分析

### 2.1 $H_2O_2$ 浓度对肌原纤维蛋白中羰基含量的影响

蛋白质中羰基的产生可作为蛋白氧化的重要指标之一, 羰基主要由氨基酸侧链 (通常为易受自由基攻击的带有 NH 或者  $NH_2$  的氨基酸残基) 及肽键的氧化断裂产生<sup>[19]</sup>。羰基含量越高表明蛋白质氧化程度越高<sup>[5,20]</sup>。图 1 为羟自由基 ( $\cdot OH$ ) 氧化体系中  $H_2O_2$  浓度对肌原纤维蛋白羰基含量的影响, 由图可知, 随着  $H_2O_2$  浓度的增加, 蛋白质羰基含量也呈现上升趋势, 空白对照组肌原纤维蛋白羰基含量为 1.17 nmol/mg 蛋白, 当  $H_2O_2$  浓度达到 20 mmol/L 时, 羰基含量增加至 2.82 nmol/mg ( $P < 0.05$ )。羰基含量的增加可能是由于羟自由基 ( $\cdot OH$ ) 对氨基酸侧链或肽链的氧化攻击造成<sup>[21]</sup>。在此氧化体系中,  $H_2O_2$  浓度越高,  $\cdot OH$  浓度越高, 导致羰基含量不断增加, 从而较为直观地反映出蛋白的氧化程度。

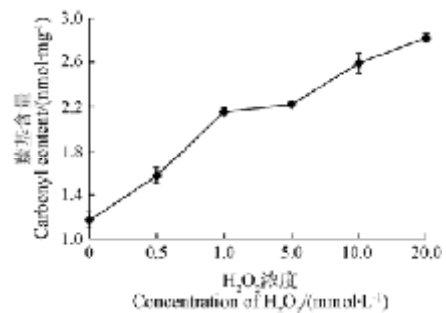


图 1  $H_2O_2$  浓度对羰基含量的影响

Fig.1 Concentration effect of  $H_2O_2$  on carbonyl content

### 2.2 蛋白氧化对凝胶白度、质构及保水性的影响

蛋白凝胶的白度反应了蛋白质的变性程度, 白度值越低, 表明蛋白氧化变性程度越严重<sup>[22]</sup>。Xia 等<sup>[23]</sup>研究报道蛋白凝胶白度值的下降可能是由于氧化产物与蛋白质的氨基酸侧链发生的非酶褐变引起的。表 1 结果显示, 随着  $H_2O_2$  浓度的增加, 蛋白凝胶的白度值显著下降, 氧化程度加剧, 与对照组的肌原纤维蛋白相比,  $H_2O_2$  浓

度为 20 mmol/L 时, 蛋白凝胶白度值降低了 2.83% ( $P<0.05$ ), 这表明  $H_2O_2$  浓度越高, 蛋

白质氧化变性越严重。

表 1  $H_2O_2$  浓度对肌原纤维蛋白凝胶白度、保水性及质构特性的影响  
Table 1 Effect of  $H_2O_2$  concentration on whiteness, water holding capacity and texture of gel

$H_2O_2$ 浓度 Concentration of $H_2O_2$ /(mmol $L^{-1}$ )	白度 Whiteness	硬度 Hardness/g	黏聚性 Gumminess	弹性 Springiness	咀嚼性 Chewiness/g	保水性 Water holding capacity/%
0	89.89±0.16 <sup>a</sup>	226.16±9.22 <sup>a</sup>	0.59±0.02 <sup>a</sup>	0.73±0.02 <sup>a</sup>	96.92±4.55 <sup>a</sup>	64.17±0.93 <sup>a</sup>
0.5	89.03±0.07 <sup>ab</sup>	191.00±14.9 <sup>b</sup>	0.55±0.01 <sup>a</sup>	0.67±0.04 <sup>b</sup>	65.32±4.19 <sup>b</sup>	62.78±0.85 <sup>ab</sup>
1.0	88.41±0.84 <sup>bc</sup>	152.35±12.58 <sup>c</sup>	0.54±0.03 <sup>a</sup>	0.68±0.02 <sup>ab</sup>	55.78±2.24 <sup>b</sup>	62.49±1.19 <sup>b</sup>
5.0	87.84±1.37 <sup>bc</sup>	137.43±7.88 <sup>cd</sup>	0.42±0.03 <sup>b</sup>	0.66±0.03 <sup>bc</sup>	40.79±5.31 <sup>c</sup>	58.17±0.59 <sup>c</sup>
10.0	87.81±1.13 <sup>bc</sup>	116.03±6.3 <sup>de</sup>	0.41±0.05 <sup>b</sup>	0.58±0.05 <sup>d</sup>	27.89±6.36 <sup>cd</sup>	54.72±0.38 <sup>d</sup>
20.0	87.35±0.22 <sup>c</sup>	106.89±23.29 <sup>e</sup>	0.39±0.10 <sup>b</sup>	0.60±0.03 <sup>cd</sup>	25.07±9.87 <sup>d</sup>	54.77±1.18 <sup>d</sup>

注: 同一列的不同字母表示差异显著 ( $P<0.05$ ), 下同

Note: Different letters in the same column indicate significant differences ( $P<0.05$ ). The same as below.

硬度是蛋白凝胶最重要的功能特性之一, 凝胶的弹性、黏聚性及咀嚼性也影响着凝胶的功能特性<sup>[24]</sup>。由表 1 的结果可知, 凝胶的质构特性指标(硬度、黏聚性、弹性及咀嚼性)都随  $H_2O_2$  浓度的增加而下降。其中, 凝胶的硬度从 226.16 g (空白对照) 降低至 106.89 g ( $H_2O_2$  浓度 20 mmol/L), 降低了 52.7% ( $P<0.05$ ), 崔旭海等的研究也得出了类似的结论<sup>[25]</sup>。氧化可能会导致蛋白质溶解度下降, 减少参与成胶的蛋白量, 从而降低凝胶强度<sup>[26]</sup>, 同时氧化程度越高凝胶保水性越低, 也会导致凝胶强度下降。

与凝胶质构特性结果相似, 蛋白凝胶的保水性也随  $H_2O_2$  浓度的增加而显著下降(表 1)。与空白对照相比, 当  $H_2O_2$  浓度增加到 20 mmol/L 时, 蛋白凝胶保水性从 64.17% 下降至 54.77%, 下降了 14.65% ( $P<0.05$ )。蛋白凝胶中的水分主要是通过蛋白水合作用和毛细管作用束缚在凝胶网络中的, 氧化会使蛋白质结构遭到破坏, 使凝胶中形成很多空隙, 导致蛋白质的水合作用和毛细管作用下降, 随着凝胶网络中空隙的增多, 凝胶的保水力也显著降低<sup>[27]</sup>。

### 2.3 蛋白氧化对凝胶流变学特性的影响

为研究蛋白氧化对其凝胶形成能力的影响, 本试验测定了氧化后肌原纤维蛋白的流变学特性(图 2)。 $G'$  称为弹性模量, 它是描述固体材料抵抗形变能力的物理量, 能够反映蛋白质的弹性品质, 以及蛋白凝胶的转变温度<sup>[23,25]</sup>。 $G'$  越大说明凝胶弹性越强, 肌原纤维蛋白的  $G'$  大体上在起初的升温阶段有一段平稳期(温度低于 45 $^{\circ}C$ ); 随着温度的升高,  $G'$  上升至最大值, 随后急剧下降(50 $^{\circ}C$  附近有最大峰, 该温度为肌球蛋白的变性温度<sup>[28]</sup>); 最后  $G'$  随着温度升高稳步上升, 直至加热终点(75 $^{\circ}C$ ), 这与 Liu 等<sup>[5]</sup>研究肌原纤维蛋白流变学特性曲线相一致。45~55 $^{\circ}C$  转变峰的出现主要是由于在该温度

范围内, 蛋白结构打开, 蛋白质相互作用增强, 蛋白开始加速聚集形成凝胶<sup>[29]</sup>。随着  $H_2O_2$  浓度的增加, 肌原纤维蛋白  $G'$  (45~55 $^{\circ}C$ ) 的峰值明显下降(图 2), 这表明氧化显著影响了肌原纤维蛋白凝胶弹性, 随着蛋白氧化程度的加剧, 凝胶弹性模量显著下降, 这与本试验对质构的相关结果相吻合。

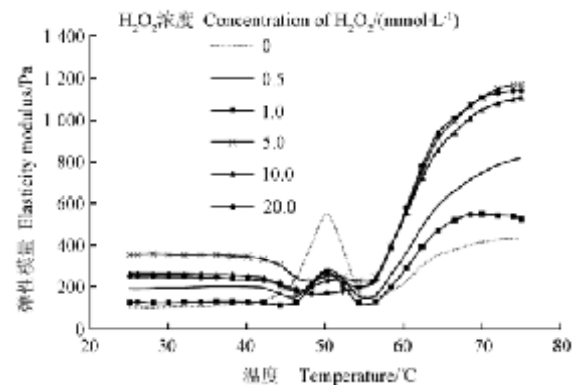


图 2  $H_2O_2$  浓度对肌原纤维蛋白凝胶弹性模量的影响  
Fig.2 Effect of  $H_2O_2$  concentration on  $G'$  of gel

### 2.4 蛋白氧化对凝胶微观结构的影响

由图 3 扫描电镜图可知, 不同氧化程度的肌原纤维蛋白凝胶微观结构存在明显差异。空白对照组蛋白形成的凝胶网状结构致密、形状规则、空隙较小、且分布均匀(图 3a); 而氧化组肌原纤维蛋白则形成结构粗糙, 空隙较大, 且分布不均匀的凝胶网络(图 3b、3c); 氧化剂浓度对最终凝胶的微观结构有很大的影响, 不同氧化程度 MP 凝胶微观结构存在明显的差异, 与 5 mmol/L 的较低  $H_2O_2$  浓度组相比(图 3b), 20 mmol/L 高  $H_2O_2$  浓度组凝胶微观结构的网孔更多且孔径更大, 大面积的孔壁发生断裂, 网络结构破坏严重, 蛋白胶束的聚集增加, 且更不均匀(图 3c)。这可能是由于随着  $H_2O_2$  浓度的增大, 肌原纤维蛋白溶解度下降, 从而导致热诱

导凝胶形成过程中蛋白过度交联, 阻止活性功能基团的有序结合, 最终阻碍有序凝胶网络的形成<sup>[26]</sup>,

进而也会降低凝胶的弹性(图2), 空隙的加大也会显著影响凝胶的保水性及质构特性(表1)。

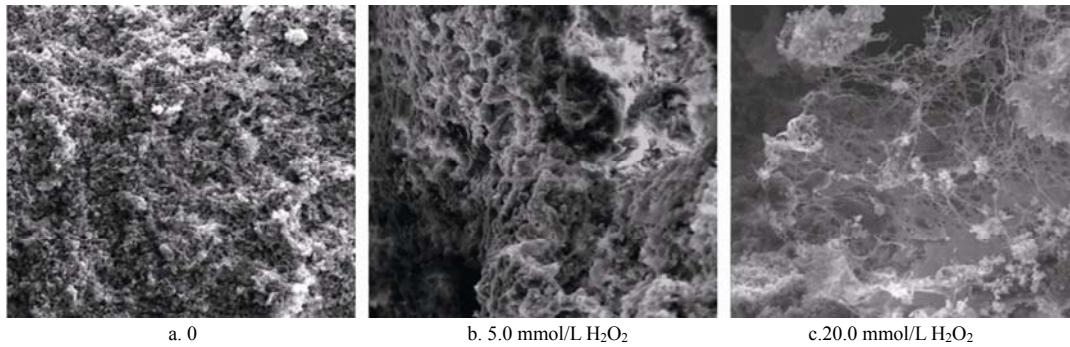
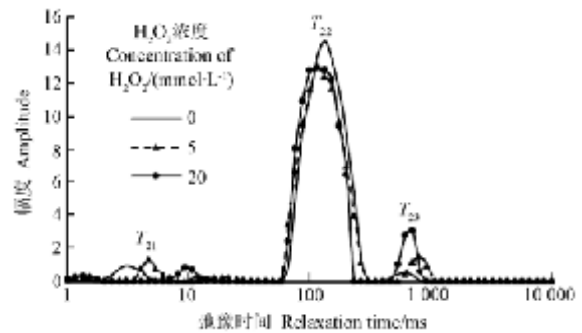


图3 肌原纤维蛋白凝胶结构扫描电镜图(放大倍数500×)  
Fig.3 Scanning electron microscope of myofibrillar protein gel (magnification 500×)

## 2.5 蛋白氧化对凝胶水分分布及组成的影响

从低场核磁 NMR  $T_2$  图谱可以看出(图4), 肌原纤维蛋白凝胶  $T_2$  在 1~10 000 ms 的弛豫时间内分布有 3 个峰, 这与 Goetz<sup>[30]</sup>用 NMR 研究乳清蛋白与卵蛋白及吴焯<sup>[18]</sup>研究兔肌球蛋白热凝胶的结果一致。 $T_2$  值对应的 3 个峰分别对应凝胶中 3 种状态的水: 结合水  $T_{21}$ , 不易流动水  $T_{22}$  及自由水  $T_{23}$ , 各峰与横坐标面积百分比即为各组分水所占百分含量, 分别记为  $P_{21}$ ,  $P_{22}$ ,  $P_{23}$ 。从各峰面积积分的结果可知,  $H_2O_2$  浓度对结合水含量  $P_{21}$  影响不大 ( $P>0.05$ ); 不易流动水含量  $P_{22}$  随  $H_2O_2$  浓度增加而下降, 与空白对照组  $P_{22}$  (94.03%) 相比,  $H_2O_2$  浓度为 5 mmol/L 及 20 mmol/L 时,  $P_{22}$  分别下降了 2.87% ( $p<0.05$ )、5.89% ( $p<0.05$ ); 自由水含量  $P_{23}$  随  $H_2O_2$  浓度增加而增加, 从空白对照组的 1.37% 增加至 5 mmol/L 时的 4.25% ( $p<0.05$ ) 和 20 mmol/L 时的 7.56% ( $p<0.05$ )。这表明, 随着  $H_2O_2$  浓度的增大, 凝胶中的一部分不易流动水“态变”为自由水, 而自由水是凝胶中结合最不紧密的水, 也是离心最易损失的水, 因此,  $H_2O_2$  浓度越大, 自由水含量越高, 凝胶保水性越低, 这与本试验关于凝胶保水性的研究结果相一致。



注:  $T_{21}$ 、 $T_{22}$ 、 $T_{23}$  分别指凝胶中结合水, 不易流动水及自由水的弛豫时间。  
Note:  $T_{21}$ ,  $T_{22}$ ,  $T_{23}$  represent relaxation time of bound water, immobile water and free water of gel.

图4  $H_2O_2$  浓度对肌原纤维蛋白凝胶  $T_2$  弛豫时间的影响  
Fig.4 Effect of  $H_2O_2$  concentration on  $T_2$  of myofibrillar protein gel

## 2.6 相关性分析

相关性分析结果显示,  $H_2O_2$  浓度与肌原纤维蛋白中羰基含量显著正相关 ( $r=0.832$ ,  $p<0.05$ ), 与凝胶的保水性 ( $r=0.884$ ,  $p<0.05$ ) 及硬度 ( $r=0.819$ ,  $p<0.05$ ) 显著负相关; 羰基含量与保水性显著负相关 ( $r=0.906$ ,  $p<0.05$ ), 与白度 ( $r=0.969$ ,  $p<0.01$ ), 硬度 ( $r=0.996$ ,  $p<0.01$ ), 及咀嚼性 ( $r=0.970$ ,  $p<0.01$ ) 极显著负相关。这表明  $H_2O_2$  浓度越高, 蛋白氧化程度越严重, 凝胶的白度、保水性、硬度及咀嚼性越差(表2)。

表2 各指标相关性分析

Table 2 Correlation analysis between indexes of gel

	$H_2O_2$ 浓度 Concentration of $H_2O_2$	羰基含量 Carbonyl content	白度 Whiteness	保水性 Water holding capacity	硬度 Hardness	咀嚼性 Chewiness
$H_2O_2$ 浓度 Concentration of $H_2O_2$	1.000	0.832*	-0.781	-0.884*	-0.819*	-0.783
羰基含量 Carbonyl content		1.000	-0.969**	-0.906*	-0.996**	-0.970**
白度 Whiteness			1.000	0.889*	0.956**	-0.979**
保水性 Water holding capacity				1.000	0.906*	0.920**
硬度 Hardness					1.000	0.975**
咀嚼性 Chewiness						1.000

注: \*表示  $p<0.05$  水平差异显著; \*\*表示  $p<0.01$  水平差异显著。

Note: \*represents significantly different at  $p<0.05$ ; \*\* represents significantly different at  $p<0.01$ .

### 3 结 论

在羟自由基模型体系中,  $\text{H}_2\text{O}_2$  浓度 (0~20.0 mmol/L) 越大, 肌原纤维蛋白氧化越严重, 所形成凝胶的白度、硬度、弹性、黏聚性、咀嚼性及保水性越低; 氧化会影响凝胶的形成能力及凝胶的微观结构, 导致疏松多孔且不规则凝胶网络的形成; 同时羟自由基介导的蛋白氧化也会造成凝胶中一部分结合紧密的不易流动水“态变”为自由流动水, 从而降低凝胶的保水力。

综上所述, 在羟自由基氧化体系中,  $\text{H}_2\text{O}_2$  对蛋白质的氧化存在着明显的浓度效应, 进而显著影响凝胶特性。在肉与肉制品的加工与贮藏过程中, 应尽量控制肌肉蛋白氧化, 避免其对肉品质造成的影响。

#### [参 考 文 献]

- [1] Xiong Y L, Decker E A. Alterations in muscle protein functionality by oxidative and antioxidative processes[J]. *Journal of Muscle Foods*, 1995, 6(2): 139—160.
- [2] Srinivasan S, Hultin H O. Chemical, physical, and functional properties of cod proteins modified by a nonenzymic free-radical-generating system[J]. *Journal of Agriculture and Food Chemistry*, 1997, 45(2): 310—320.
- [3] Li S J, King A J. Lipid oxidation and myosin denaturation in dark chicken meat[J]. *Journal of Agriculture and Food Chemistry*, 1996, 44(10): 3080—3084.
- [4] Kanner J, Hazan B, Doll L. Catalytic “free” iron ions in muscle foods[J]. *Journal of Agricultural and Food Chemistry*, 1988, 36(3): 412—415.
- [5] Liu G, Xiong Y L, Butterfield D A. Chemical, physical and gel-forming properties of oxidized myofibrils and whey- and soy-protein isolates[J]. *Food Chemistry and Toxicology*, 2000, 65(5): 811—818.
- [6] 杨速攀, 彭增起. 肌原纤维蛋白凝胶研究进展[J]. *河北农业大学学报*, 2003, 26(增 1): 160—166.  
Yang Supan, Peng Zengqi. Study advances on gelation of myofibrils[J]. *Journal of Agricultural University of Hebei*, 2003, 26(supp.1): 160—166. (in Chinese with English abstract)
- [7] Gang Liu, Xiong Y L. Gelation of Chicken muscle myofibrillar proteins treated with protease inhibitors and phosphates[J]. *Journal of Agriculture and Food Chemistry*, 1997, 45(9): 3437—3442.
- [8] 王淑杰, 周亚军, 苏丹, 等. 鹿肉盐溶蛋白热诱导凝胶特性影响因素试验[J]. *农业机械学报*, 2010, 9(41): 122—127.  
Wang Shujie, Zhou Yajun, Su Dan, et al. Properties of venison protein gelatin and mathematical model[J]. *Transactions of Chinese Society for Agricultural Machinery*, 2010, 9(41): 122—127. (in Chinese with English abstract)
- [9] 费英, 韩敏义, 杨凌寒, 等. pH 对肌原纤维蛋白二级结构及其热诱导凝胶特性的影响[J]. *中国农业科学*, 2010, 43(1): 164—170.  
Fei Ying, Han Minyi, Yang Linghan, et al. Studies on the secondary structure and heat-induced gelation of pork myofibrillar proteins as affected by pH[J]. *Scientia Agricultura Sinica*, 2010, 43(1): 164—170. (in Chinese with English abstract)
- [10] Wu M G, Xiong Y L, Chen J. Rheology and microstructure of myofibrillar protein-plant lipid composite gels: Effect of emulsion droplet size and membrane type[J]. *Journal of Food Engineering*, 2011, 106(4): 318—324.
- [11] Park D, Xiong Y L, Alderton A L. Concentration effects of hydroxyl radical oxidizing systems on biochemical properties of muscle myofibrillar protein[J]. *Food Chemistry*, 2007, 101(3): 1239—1246.
- [12] Levine R L, Williams J A, Stadtman E R, Shacter E. Carbonyl assays for determination of oxidatively modified proteins[J]. *Method in Enzymology*, 1994, 233: 346—357.
- [13] Kocher P N, Foegeding E A. Microcentrifuge-based method for measuring water-holding of protein gels[J]. *Journal of Food Science*, 1993, 58(5): 1040—1046.
- [14] 陆剑锋, 邵明栓, 林琳, 等. 卡拉胶和超高压对鱼糜凝胶性质的影响[J]. *农业机械学报*, 2011, 12(42): 164—170.  
Lu Jianfeng, Shao Mingshuan, Lin Lin, et al. Effects of Ultra-high Pressure and carrageenan on gelling properties of surimi from silver carp, *Hypophthalmichthys molitrix*[J]. *Transactions of Chinese Society for Agricultural Machinery*, 2011, 12(42): 164—170. (in Chinese with n English abstract)
- [15] 高建华, 戴思齐, 刘家明, 等. 六种果皮原料果胶的理化及凝胶特性比较[J]. *农业工程学报*, 2012, 28(16): 288—292.  
Gao Jianhua, Dai Siqi, Liu Jiaming, Li Jiajia, et al. Comparison of physicochemical and gelation properties of pectins extracted from six pericarps[J]. *Transactions of the Chinese Society of Agricultural Engineering (Transactions of the CSAE)*, 2012, 28(16): 288—292. (in Chinese with English abstract)
- [16] Li J, Ould Eleya M M, Gunasekaren S. Gelation of whey protein and xanthan mixture: Effect of heating rate on rheological properties[J]. *Food Hydrocolloids* 2006, 20(5): 678—686.
- [17] Palka K, Daun H. Changes in texture, cooking losses, and myofibrillar structure of bovine M. semitendinosus during heating[J]. *Meat Science*, 1999, 51(3), 237—243.
- [18] 吴焯, 许柯, 徐幸莲, 等. 低场核磁共振研究 pH 值对兔肌球蛋白热凝胶特性的影响[J]. *食品科学*, 2010, 31(9): 6—11.  
Wu Ye, Xu Ke, Xu Xinglian, et al. Effect of pH on gelation properties of rabbit myosin[J]. *Food Science*, 2010, 31(9): 6—11. (in Chinese with English abstract)
- [19] Stadtman E R. Protein oxidation and aging[J]. *Science*, 1992, 257(5074): 1220—1224.
- [20] Dean R T, Fu S L, Stocker R, et al. Biochemistry and pathology of radical-mediated protein oxidation[J]. *Biochemical Journal*, 1997, 324: 1—18.
- [21] Butterfield D A, Stadtman E R. Protein oxidation processes in aging brain. Timiras P S, edit. *Advances in Cell Aging and Gerontology* [M], Elsevier Science Press, Netherlands:1997, 2: 161—191.
- [22] Hwang J S, Lai K M, Hsu K C. Changes in textural and rheological properties of gels from tilapia muscle proteins induced by high pressure and setting[J]. *Food Chemistry*, 2007, 104(2): 746—753.
- [23] Xia Xiufang, Kong Baohua, Xiong Youling, et al. Decreased gelling and emulsifying properties of myofibrillar protein from repeatedly frozen-thawed porcine longissimus muscle are due to protein denaturation and susceptibility to aggregation[J]. *Meat Science*, 2010, 85(3): 481—486.
- [24] 潘君慧. 冻藏方式、猪肉蛋白氧化及猪肉品质关系的研究[D]. 南京: 江南大学, 2011.  
Pan Junhui. The Relationships of Frozen Storage Porcine Myofibrillar Protein Oxidation and Quality of Pork Products[D]. NanJing: Jiangnan University, 2011. (in Chinese with English abstract)

- [25] 崔旭海, 孔保华. 自由基引起的氧化对牛乳清蛋白凝胶特性的影响[J]. 农业工程学报, 2009, 25(增1): 222—228. Cui Xuhai, Kong Baohua. Effects of protein oxidation by a free radical-generating system on gel characteristics of bovine whey protein[J]. Transactions of the Chinese Society of Agricultural Engineering (Transactions of the CSAE), 2009, 25(supp.1): 222—228. (in Chinese with English abstract)
- [26] Smyth A B, Smith D M, O'Neill E. Disulfide bonds influences the heat-induced gel properties of chicken breast muscle myosin[J]. Journal of Food Science, 1998, 63(4): 584—588.
- [27] Martinaud A, Mercier Y, Marinova P, et al. Comparison of oxidative processes on myofibrillar proteins from beef during maturation and by different model oxidation systems[J]. Journal of Agricultural and Food Chemistry, 1997, 45(7): 2481—2487.
- [28] Deng Y, Rosenvold K, Karlsson A H, et al. Relationship between thermal denaturation of porcine muscle proteins and water-holding capacity[J]. Journal of Food Science, 2002, 67(5): 1642—1648.
- [29] Xiong Y L, Blanchard S P. Myofibrillar protein gelation: Viscoelastic changes related to heating procedures[J]. Journal of Food Science, 1994, 59(4): 734—738.
- [30] Goetz J, Koehler P. Study of the thermal denaturation of selected proteins of whey and egg by low resolution NMR[J]. Journal of Food Science and Technology, 2005, 38(5): 501—512.

## Oxidation and decrease of gelling properties for meat myofibrillar protein induced by hydroxyl radical

Li Yin, Li Xia, Zhang Chunhui<sup>\*</sup>, Sun Hongmei, Dong Xianbing

(Comprehensive Key Laboratory of Agro-Products Processing, Ministry of Agriculture, Institute of Agro-Products Processing Science and Technology, Chinese Academy of Agricultural Sciences, Beijing 100193, China)

**Abstract:** Oxidation and changes of gelling properties of myofibrillar protein (MP) induced by the hydroxyl radical ( $\cdot\text{OH}$ ) were studied in this paper. Pork myofibrillar protein was suspended in 15 mmol/L piperazine-N, N-bis(2-ethane sulfonic acid) (PIPES) buffer (pH 6.0), and 0.6 mol/L NaCl, and incubated at 4°C for 24 h with ferric ion ( $\text{Fe}^{3+}$ ) and ascorbic acid (Vc) at six concentrations of hydrogen peroxide (0, 0.5, 1.0, 5.0, 10.0, 20.0 mmol/L  $\text{H}_2\text{O}_2$ ). The indexes including protein carbonyl content and whiteness, water-holding capacity (WHC), and texture profile analysis (TPA) of MP gel were measured. The ability of MP to form a fine gel network was described in terms of shear storage modulus ( $G'$ ), and it was analyzed by small strain oscillatory rheological testing. The microstructure of MP gel was observed by scanning electric microscopy (SEM). The transverse relaxation time ( $T_2$ ) and water distribution of MP gel were analyzed by low-field nuclear magnetic resonance (low-field NMR). Correlation analysis between indexes of MP gel was also performed to establish possible linkages between concentration of  $\text{H}_2\text{O}_2$  and different parameters of MP gel in this study. The results showed that carbonyl content steadily increased with  $\text{H}_2\text{O}_2$  concentration, increased from 1.17 nmol/mg protein (non-oxidized MP) to 2.82 nmol/mg protein (20.0 mmol/L  $\text{H}_2\text{O}_2$ ). With increasing  $\text{H}_2\text{O}_2$  concentration, the whiteness and WHC of MP gel decreased significantly ( $p < 0.05$ ) (89.89, 64.17% respectively for non-oxidized MP gel, 87.35, 54.77% respectively for 20.0 mmol/L  $\text{H}_2\text{O}_2$ ). The texture (hardness, springiness, cohesiveness and chewiness) and shear storage modulus ( $G'$ ) also attenuated with increasing  $\text{H}_2\text{O}_2$  concentration. The SEM results demonstrated that oxidation of protein could significantly affect the microstructure of MP gel. The non-oxidized MP gel exhibited a compact and homogeneous fine network microstructure, whereas the oxidation process produced empty spaces and changed the compact and fine gel structure to a coarser network, and the effect increased with higher  $\text{H}_2\text{O}_2$  concentration. The low-field NMR relaxation measurement results indicated that the oxidation degree of protein had no effect on the bound water ( $T_{21}$ ) of MP gel but had significant effects on immobile water ( $T_{22}$ ) and free water ( $T_{23}$ ) of MP gel.  $T_{22}$  water content ( $P_{22}$ ) decreased with increasing  $\text{H}_2\text{O}_2$  concentration (94.03% for non-oxidized MP gel, 91.16% for 5 mmol/L  $\text{H}_2\text{O}_2$ , 88.14% for 20 mmol/L  $\text{H}_2\text{O}_2$ ).  $T_{23}$  water content ( $P_{23}$ ) increased with  $\text{H}_2\text{O}_2$  concentration (1.37% for non-oxidized MP gel, 4.25% for 5 mmol/L  $\text{H}_2\text{O}_2$ , 7.56% for 20 mmol/L  $\text{H}_2\text{O}_2$ ). Taken together, these results demonstrate that with increasing  $\text{H}_2\text{O}_2$  concentration, some part of the immobile water of MP gel shifts to free water, and the free water would become the potential centrifuge drip loss. Correlation analysis results showed that concentration of  $\text{H}_2\text{O}_2$  was highly negatively correlated with whiteness, WHC, hardness and chewiness ( $p < 0.05$ ). Based on the synthetic evaluation on the testing results of the MP gel, it can be concluded that the  $\cdot\text{OH}$  will result in oxidation of MP, and have detrimental effects on the gelling property of porcine MP. Therefore, it is imperative to inhibit the oxidation of MP during storage and processing of meat to avoid losing the functional properties of porcine MP.

**Key words:** proteins, nuclear magnetic resonance (NMR), meats, hydroxyl radical ( $\cdot\text{OH}$ ) oxidizing system, myofibrillar protein (MP), microstructure

## A PCR based magnetic assembled sensor for ultrasensitive DNA detection†

Cite this: DOI: 10.1039/c3cc41674g

Received 5th March 2013,  
Accepted 23rd April 2013

DOI: 10.1039/c3cc41674g

www.rsc.org/chemcomm

Wei Ma,<sup>‡</sup> Honghong Yin,<sup>‡</sup> Liguang Xu, Libing Wang, Hua Kuang\* and Chuanlai Xu

**An ultrasensitive method for DNA detection based on magnetic assembly induced by polymerase chain reaction (PCR) was developed. The sensor showed a low limit of detection (LOD) of 4.26 aM with a wide range of target DNA from 0.01 fM to 10 000 fM.**

Highly sensitive and selective sequence-specific DNA detection has become increasingly important in a wide range of applications, and is mainly used for clinical diagnostics,<sup>1</sup> detection of pathogenic diseases and the detection of genetically modified organisms (GMOs).<sup>2–5</sup> Furthermore, there is also enormous potential for this technique to be used in new drug research and development, gene therapy, food safety testing and detecting environmental contamination.<sup>6–10</sup> Therefore, a simple and ultrasensitive detection method for extremely low concentrations of nucleic acids seems to be essential to meet the above increasing demands.

Numerous methods for the analysis and quantification of specific DNA sequences in a large number of organisms have been developed. Quantitative PCR is a powerful conventional tool for the detection of trace amounts of DNA due to its excellent amplification and quantitative properties, while the post-analysis of PCR products using gel electrophoresis is time-consuming.<sup>11–16</sup> Meanwhile, nonspecific PCR products are very easily generated in SYBR Green real-time PCR due to the non-selective combination of dyes and double-stranded DNA, which has an influence on the accurate quantification. In recent years, various DNA biosensors based on oligonucleotide functionalized nanoparticles have continued to attract considerable research attention, because of the specific properties of nanomaterials, including optical, electrochemical, thermometric, piezoelectric, magnetic, fluorescent or micromechanical, all of which can be magnified and used as detection signals for qualitative and quantitative analysis.<sup>17–26</sup> PCR, as a useful tool with the excellent exponential amplification power, could be combined with nanoparticles. The assembled nanoparticle superstructures induced by PCR could re-generate special

properties.<sup>27–29</sup> PCR-based gold nanoparticle assembly also provides a novel technique for signal magnification, which could be used in the field of sensitive DNA detection with 0.1 fM sensitivity.<sup>30,31</sup>

As an important nanomaterial, well-established MNPs have been widely studied in nanotechnology. MNPs have the properties of high magnetization, super paramagnetism, a wide range of magnetic anisotropy and can easily be functionalized and modified with other molecules due to the presence of various groups on their surface.<sup>32,33</sup> Thus, the multifunctional MNPs have many applications in biology and biomedicine, including bioseparation, detection, drug delivery and in magnetic resonance imaging (MRI).<sup>34–39</sup> MRI is a powerful technique for the analysis of the location and type of nucleus in some substances, and the internal images of objects can be drawn. Nowadays, this technique is being widely used in clinical diagnosis and biodetection. In particular, super paramagnetic nanoparticles have been utilized for the detection of harmful elements and other substances as contrast agents in MRI and fabricated NMR sensors, which have made significant contributions to food safety, environmental protection and many other fields.<sup>40–44</sup>

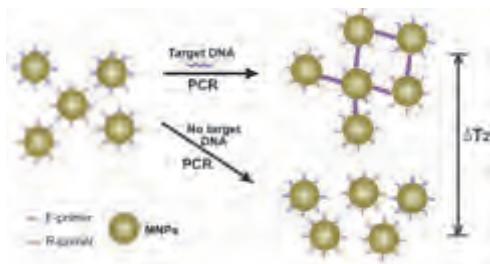
In this communication, we report a new strategy for the ultrasensitive detection of target DNA based on the magnetic relaxation switch produced by the aggregation of MNPs. Following the hybridization of DNA-labeled monodisperse nanoparticles, it is difficult to achieve an ultrasensitive detection level without further signal amplification. In order to improve the sensitivity of the method, PCR was introduced to assist in the assembly of MNPs and amplify the degree of assembly due to the exponential amplification of target DNA (Scheme 1). The primer-modified nanoparticles were hybridized with a DNA template in the same system imitating the reaction procedures of a conventional PCR. Under different concentrations of target DNA, MNPs displayed different aggregation states. When target DNA was increased exponentially, the aggregation of MNPs increased. Therefore, the transverse relaxation time (T<sub>2</sub>) of the surrounding water protons in the solution was different. The greater the degree of aggregation of the MNPs, the longer the T<sub>2</sub> relaxation time. Furthermore, the signal intensity of MRI varied accordingly.

The magnetic nanoparticles used in our assay were Fe<sub>3</sub>O<sub>4</sub> nanoparticles bearing carboxyl groups with a mean diameter of 8–10 nm, which were purchased from Gao's group.<sup>45</sup>

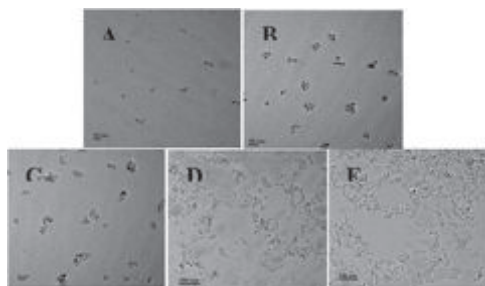
School of Food Science and Technology, State Key Lab of Food Science and Technology, Jiangnan University, Wuxi, JiangSu 214122, P. R. China.  
E-mail: khecho@163.com

† Electronic supplementary information (ESI) available. See DOI: 10.1039/c3cc41674g

‡ These authors contributed equally to this communication.



**Scheme 1** The scheme of the method for DNA detection based on MNP assembly induced by PCR.



**Fig. 1** Representative TEM images of MNP assembly for different cycle numbers under 10 000 fM of target DNA: (a) 0 cycle, (a) 5 cycles, (a) 10 cycles, (a) 20 cycles, (a) 30 cycles.

Their dispersibility in solution was excellent, as shown in Fig. 1(A). The original concentration of MNPs was  $1.3 \text{ mg mL}^{-1}$ , while the actual amount was diluted 20 times in PBS solution containing 0.01 M sodium phosphate and 137 mM NaCl. In order to activate the carboxyl group-modified MNPs and enhance the combination of carboxyl groups of MNPs and amino groups of DNA, 0.2 mg EDC and 0.2 mg NHS were added to 1 mL of the above MNP solution diluted with PBS. After reacting for approximately 15 min, the amino-modified upstream and downstream primers at a final concentration of 4  $\mu\text{M}$ , respectively, were introduced and incubated with MNPs at room temperature with a slow shake. After six hours, excess primers were removed by ultrafiltration (3000 MW cutoff membrane; Millipore) for 3 min at  $10\,000 \text{ r min}^{-1}$ . Ultrafiltration was performed five times with ultrapure water to ensure that the unbound primers were entirely removed. The residual MNPs were re-suspended in ultrapure water and then stored at 4 °C until use.

After ultrafiltration, the zeta potential of primer-modified MNPs was measured to ensure the successful combination of MNPs and DNA fragments. The original MNPs carried negative charge owing to the presence of carboxyl groups. When DNA possessing negative charge was anchored on the MNPs, the total negative charge of the complex increased on the surface of MNPs with the surrounding DNA. By comparing the variation in zeta potential of MNPs before and after conjugation with DNA, a 2 mV enhancement from  $-2.68 \text{ mV}$  to  $-4.96 \text{ mV}$  was observed. Meanwhile, the size of MNPs after DNA conjugation showed an obvious shift as observed from measuring the size change (ESI,† Fig. S1). This confirmed that DNA was successfully conjugated with MNPs through carboxyl groups and amino groups.

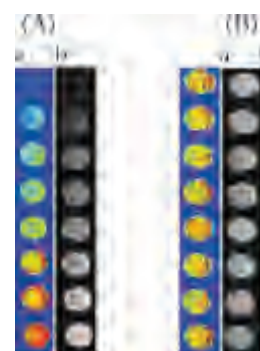
The whole process of MNP assembly was carried out in PCR tubes according to the procedures of a conventional PCR. The PCR mixture was reacted in a final volume of 50  $\mu\text{L}$ . The selected target DNA was from a specific DNA fragment of genetically modified corn MON 810.

To ensure close assembly of MNPs, oligonucleotides with 41 nucleotides in length were selected as target DNA. The specificity was confirmed by standard nucleotide BLAST on NCBI. Before PCR on the surface of MNPs was carried out, conventional PCR was conducted to identify the optimal PCR cycling parameters. Under the following conditions: an initial denaturation of 2 min at 94 °C, followed by 30 cycles at 94 °C for 30 s, 60 °C for 30 s, 72 °C for 1 min, and a final extension of 7 min at 72 °C, the PCR products showed a single target band on agarose gel electrophoresis in the third lane (ESI,† Fig. S2). Due to the use of amino-modified primers, the band was located at a position above the 50 bp marker. As a result, the above PCR cycling parameters were employed in the assembly of MNPs.

Under optimized conditions and different concentrations of target DNA, the aggregation states of MNPs varied. At the same time, the degree of MNP assembly displayed an increasing trend under a certain DNA concentration during the process of MNP PCR. With an increase in PCR cycles, the aggregation of MNPs was greater. In Fig. 1, typical transmission electron microscopy (TEM) images of MNP assembly for 0, 5, 10, 20, 30 cycle numbers show the change in each assembled structure under 10 000 fM of target DNA. Primer-modified monodisperse MNPs gradually aggregated due to amplification of the DNA template.

To estimate the alteration in diameter of the assembled MNPs, the sizes of the formed MNPs under different concentrations of target DNA were measured using dynamic light scattering (DLS). The typical size distributions of the MNP aggregates are shown in Fig. S3 (ESI†). Following the addition of different concentrations of target DNA to the PCR system, the size of MNPs gradually increased with increasing target DNA 30 cycles later. The change in MNP size distributions shown by DLS strongly indicated that the assembly of MNPs took place through PCR and the degree of MNP aggregation was diverse corresponding to the concentrations of target DNA.

Fig. 2(A) shows the MR images of the final PCR products at different concentrations of target DNA. It is clear that the brightness of the MR image gradually increased from top to bottom. This color change can be explained by the assembly of MNPs with the aid of PCR amplification which induced a change in T2 relaxation time. Higher concentrations of DNA led to the formation of more MNP aggregates, which resulted in an increase in T2 relaxation time. Therefore, the negative control without target DNA was dark blue and the sample



**Fig. 2** The T2 value image (a) and MR image (b). (A) The detection of target DNA: from top to bottom, the concentrations of target DNA were 0 fM, 0.01 fM, 0.1 fM, 1 fM, 10 fM, 100 fM, 1000 fM, 10 000 fM. (B) The detection of nonspecific DNA: from top to bottom, the concentrations of nonspecific DNA were 0 fM, 0.01 fM, 0.1 fM, 1 fM, 10 fM, 100 fM, 1000 fM, 10 000 fM.



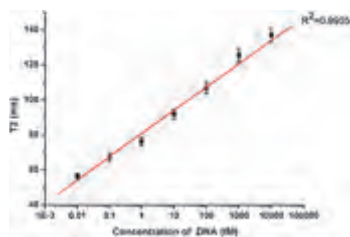


Fig. 3 The standard curve of the determination of target DNA.

with the highest concentration of target DNA was bright red in color. The DNA concentration range varied from 0 to 10 000 fM.

For the quantification of original DNA concentrations, these were calculated according to the T2 values of different concentrations of target DNA. The standard curve of these determinations was obtained by the T2 values of target DNA which ranged from 0.01 fM to 10 000 fM. As a result, a low limit of detection of 4.26 aM was obtained in this target DNA range of 0.01 fM to 10 000 fM with an excellent correlation  $R^2 = 0.9905$  (Fig. 3).

A specificity test was performed using another type of nonspecific DNA fragment as a template. The detected T2 values were not obviously different from those of the negative control without the DNA template, and the color of the MR image is shown in Fig. 2(B). This was due to the fact that the primers did not recognize and hybridize with the nonspecific DNA, therefore the DNA template was not amplified and the primer-modified MNPs were not assembled under any of the DNA concentrations. Thus, this method indicated that the test had perfect specificity for detecting specific DNA fragments.

The reproducibility and reliability of this sensor were evaluated by determining the recovery ratio of target DNA in the detection system with  $\lambda$ DNA.  $\lambda$ DNA has a large and complex DNA sequence, and the specificity of the used target DNA in this assay was compared with  $\lambda$ DNA from standard nucleotide BLAST on NCBI, which showed a perfect result without repeated fragments. Therefore,  $\lambda$ DNA could be used to imitate a complicated environment to assess the accuracy of this method. The target DNA was added to 10 pM of  $\lambda$ DNA at concentrations ranging from 0.01 fM to 10 000 fM. The results, which are shown in Table S1 (ESI<sup>†</sup>), indicated that the recovery was satisfactory in the range of 96.8–106%. Thus, matrix interference was negligible for the detection of target DNA, which demonstrated the capacity of this sensor in the analysis of real samples.

Using MRI as a detection signal, an ultrasensitive magnetic relaxation switch sensor was developed to detect and quantify target DNA. With the aid of PCR on the surface of MNPs, MNPs were assembled and aggregation was different when DNA concentrations were changed. Due to exponential amplification of the DNA template, the sensitivity of this method was significantly improved. This sensor is simple, highly sensitive, specific and has an extremely low LOD of 4.26 aM. In addition, a high-throughput detection level can also be realized using a nuclear magnetic resonance spectrometer.

This work is financially supported by the National Natural Science Foundation of China (21071066, 20835006, 91027038, 21101079, 21175034).

## Notes and references

1 M. H. Pournaghi-Azar, M. S. Hejazi and E. Alipour, *Anal. Chim. Acta*, 2006, **570**, 144.

- 2 X. Mao, L. Yang, X.-L. Su and Y. Li, *Biosens. Bioelectron.*, 2006, **21**, 1178.
- 3 B. Padmavathy, R. V. Kumar and B. M. Jaffar Ali, *J. Nanobiotechnol.*, 2012, **10**, 8.
- 4 I. Mannelli, M. Minunni, S. Tombelli and M. Mascini, *Biosens. Bioelectron.*, 2003, **18**, 129.
- 5 E. Michelini, P. Simoni, L. Cevenini, L. Mezzanotte and A. Roda, *Anal. Bioanal. Chem.*, 2008, **392**, 355.
- 6 M. Centola, M. B. Frank, A. I. Bolstad, P. Alex, A. Szanto, M. Zeher, T. O. Hjelmervik, R. Jonsson, B. Nakken, G. Szegedi and P. Szodoray, *Scand. J. Immunol.*, 2006, **64**, 236.
- 7 L. B. Hendry, V. B. Mahesh, E. D. Bransome and D. E. Ewing, *Mutat. Res., Genet. Toxicol. Environ. Mutagen.*, 2007, **623**, 53.
- 8 R. D. Snyder and L. B. Hendry, *Environ. Mol. Mutagen.*, 2005, **45**, 100.
- 9 G. Marrazza, I. Chianella and M. Mascini, *Anal. Chim. Acta*, 1999, **387**, 297.
- 10 G. S. Sayler, M. S. Shields, E. T. Tedford, A. Breen, S. W. Hooper, K. M. Sirotkin and J. W. Davis, *Appl. Environ. Microbiol.*, 1985, **49**, 1295.
- 11 C. A. Heid, J. Stevens, K. J. Livak and P. M. Williams, *Genome Res.*, 1996, **6**, 986.
- 12 C. Orlando, P. Pinzani and M. Pazzagli, *Clin. Chem. Lab. Med.*, 1998, **36**, 255.
- 13 L. Ke, Z. Chen and W. Yung, *Mol. Cell. Probes*, 2000, **14**, 127.
- 14 A. Giulietti, F. Overbergh, D. Valckx, B. Decallonne, R. Bouillon and C. Mathieu, *Methods*, 2001, **25**, 386.
- 15 W. M. Freeman, S. J. Walker and K. E. Vrana, *BioTechniques*, 1999, **26**, 112.
- 16 A. Heim, C. Ebnet, G. Harste and P. P. Åkerblom, *J. Med. Virol.*, 2003, **70**, 228.
- 17 K. Sato, K. Hosokawa and M. Maeda, *J. Am. Chem. Soc.*, 2003, **125**, 8102.
- 18 J. Song, Z. Li, Y. Cheng and C. Liu, *Chem. Commun.*, 2010, **46**, 5548.
- 19 S. J. Park, T. A. Taton and C. A. Mirkin, *Science*, 2002, **295**, 1503.
- 20 C. H. Liu, Z. P. Li, B. A. Du, X. R. Duan and Y. C. Wang, *Anal. Chem.*, 2006, **78**, 3738.
- 21 W. Russ Algar, M. Massey and U. J. Krull, *Trends Anal. Chem.*, 2009, **28**, 292.
- 22 B. Dubertret, *Nat. Mater.*, 2005, **4**, 797.
- 23 Z. Li, E. Cheng, W. Huang, T. Zhang, Z. Yang, D. Liu and Z. Tang, *J. Am. Chem. Soc.*, 2011, **133**, 15284.
- 24 Z. Zhu, W. Liu, Z. Li, B. Han, Y. Zhou, Y. Gao and Z. Tang, *ACS Nano*, 2012, **6**, 2326.
- 25 Z. Li, Z. Zhu, W. Liu, Y. Zhou, B. Han, Y. Gao and Z. Tang, *J. Am. Chem. Soc.*, 2012, **134**, 3322.
- 26 J. Gong, G. Li and Z. Tang, *Nano Today*, 2012, **7**, 564.
- 27 W. Chen, A. Bian, A. Agarwal, L. Liu, H. Shen, L. Wang, C. Xu and N. A. Kotov, *Nano Lett.*, 2009, **9**, 2153.
- 28 Y. Zhao, L. Xu, L. M. Liz-Marzán, H. Kuang, W. Ma, A. Asenjo-García, F. J. García de Abajo, N. A. Kotov, L. Wang and C. Xu, *J. Phys. Chem. Lett.*, 2013, **4**, 641.
- 29 Y. Zhao, L. Xu, H. Kuang, L. Wang and C. Xu, *J. Mater. Chem.*, 2012, **22**, 5574.
- 30 H. Kuang, S. Zhao, W. Chen, W. Ma, Q. Yong, L. Xu, L. Wang and C. Xu, *Biosens. Bioelectron.*, 2011, **26**, 2495.
- 31 M. Cai, F. Li, Y. Zhang and Q. Wang, *Nano Res.*, 2010, **3**, 557.
- 32 S. P. Gubin, Y. A. Koksharov, G. Khomutov and G. Y. Yurkov, *Russ. Chem. Rev.*, 2007, **74**, 489.
- 33 T. Osaka, T. Matsunaga, T. Nakanishi, A. Arakaki, D. Niwa and H. Iida, *Anal. Bioanal. Chem.*, 2006, **384**, 593.
- 34 Q. A. Pankhurst, J. Connolly, S. Jones and J. Dobson, *J. Appl. Phys.*, 2003, **36**, R167.
- 35 C. C. Berry and A. S. Curtis, *J. Appl. Phys.*, 2003, **36**, R198.
- 36 M. Arruebo, R. Fernández-Pacheco, M. R. Ibarra and J. Santamaría, *Nano Today*, 2007, **2**, 22.
- 37 V. I. Shubayev, T. R. Pisanic and S. Jin, *Adv. Drug Delivery Rev.*, 2009, **61**, 467.
- 38 I. J. Bruce and T. Sen, *Langmuir*, 2005, **21**, 7029.
- 39 C. Rümenapp, B. Gleich and A. Haase, *Pharm. Res.*, 2012, **29**, 1165.
- 40 Z. Xu, H. Kuang, W. Yan, C. Hao, C. Xing, X. Wu, L. Wang and C. Xu, *Biosens. Bioelectron.*, 2012, **32**, 183.
- 41 W. Ma, C. Hao, W. Ma, C. Xing, W. Yan, H. Kuang, L. Wang and C. Xu, *Chem. Commun.*, 2011, **47**, 12503.
- 42 I. Koh, R. Hong, R. Weissleder and L. Josephson, *Angew. Chem.*, 2008, **120**, 4187.
- 43 S. Taktak, R. Weissleder and L. Josephson, *Langmuir*, 2008, **24**, 7596.
- 44 T. Atanasijevic and A. Jasanoff, *Nat. Protoc.*, 2007, **2**, 2582.
- 45 C. Liu, Q. Jia, C. Yang, R. Qiao, L. Jing, L. Wang, C. Xu and M. Gao, *Anal. Chem.*, 2011, **83**, 6778.

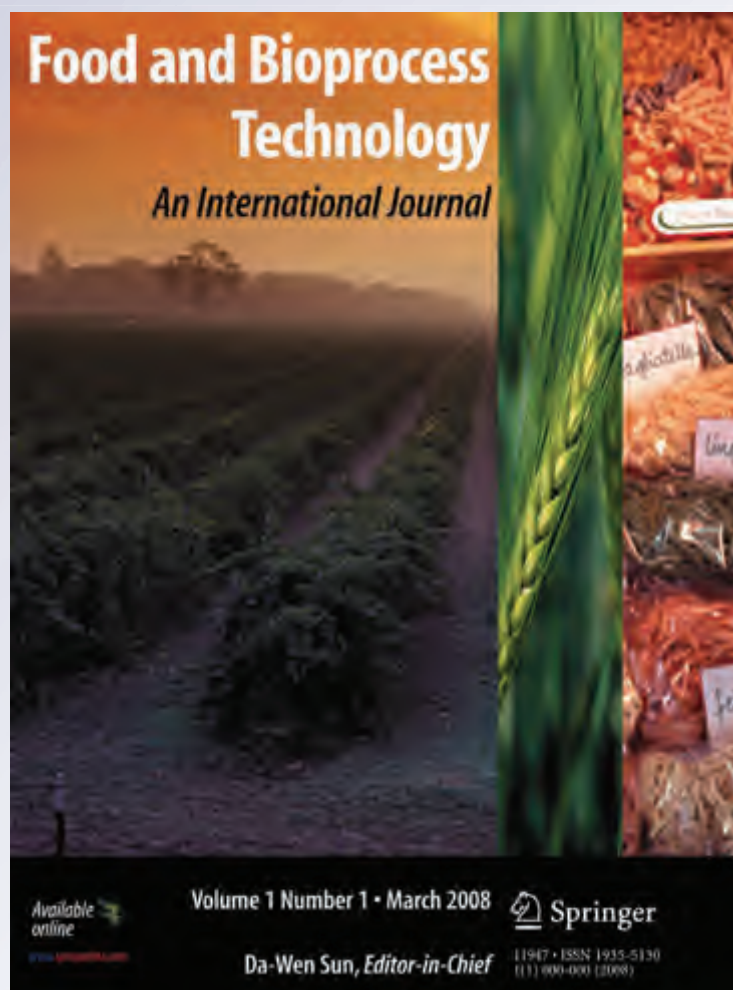
# *Discrimination of Edible Vegetable Oil Adulteration with Used Frying Oil by Low Field Nuclear Magnetic Resonance*

**Qing Zhang, Ahmed S. M. Saleh & Qun Shen**

**Food and Bioprocess Technology**  
An International Journal

ISSN 1935-5130

Food Bioprocess Technol  
DOI 10.1007/s11947-012-0826-5



 Springer

**Your article is protected by copyright and all rights are held exclusively by Springer Science+Business Media, LLC. This e-offprint is for personal use only and shall not be self-archived in electronic repositories. If you wish to self-archive your work, please use the accepted author's version for posting to your own website or your institution's repository. You may further deposit the accepted author's version on a funder's repository at a funder's request, provided it is not made publicly available until 12 months after publication.**

# Discrimination of Edible Vegetable Oil Adulteration with Used Frying Oil by Low Field Nuclear Magnetic Resonance

Qing Zhang · Ahmed S. M. Saleh · Qun Shen

Received: 26 September 2011 / Accepted: 7 March 2012  
© Springer Science+Business Media, LLC 2012

**Abstract** Pleasant flavor and nutritional benefits of vegetable oils lead to an increase in their consumption amount. In addition, due to being apparently similar to commercially qualified vegetable oils (QVOs), used frying oil (UFO) is added into it to seek high profit by the unscrupulous traders. Thus, the authenticity assurance of commercial oil and fat products remains a challenge to scientists both in terms of its health and commercial perspectives. This work focused on using low field nuclear magnetic resonance (LF-NMR) to discriminate the adulteration of commercial corn, peanut, rapeseed, and soybean oils with two kinds of UFOs. The differences between the transverse relaxation distributions ( $T_2$  distributions) of qualified oil and UFO were in the appearance of the third peak (A), which could be assigned to polymer products that were produced during the deep-fat frying process and the shift of  $T_2$  value of the peaks. In addition, the A peak area accounted for the whole area of peaks linearly increasing along with the increase in adulteration proportion. Based on the changes of peak area, a simple linear equation was built and the determination coefficients ( $R^2$ ) were all higher than 0.93. Therefore, as a rapid, convenient, and nondestructive method, LF-NMR application could be used to detect adulteration of vegetable oils with UFO.

**Keywords** Edible vegetable oil · Used frying oil · Adulteration · Low field nuclear magnetic resonance · Relaxation time ·  $T_2$  distribution

## Introduction

Adulteration of edible oil is a common phenomenon in market trade resulting from unscrupulous traders seeking to make exorbitant profits and difficulty in detection of mixed oils and fats (Tay et al. 2002). Due to its pleasant flavor and nutritional benefits, the amount of vegetable oil consumption has expanded rapidly in the last years. Consequently, there has been a significant increase in quantity of UFO yearly. As a potential adulterant to edible vegetable oil, its determination has been an interesting study for considerations of health hazards and market order. Many complex physical and chemical reactions have been taking place in the UFO during the longtime high-temperature treatment, so the physical and chemical properties are significantly different compared to fresh oils and fats. However, once the UFO undergoes some refining processes such as absorption and membrane filtration, the differences between the UFO and fresh oils and fats are not easy to discriminate (Bhattacharya et al. 2008; Miyagi et al. 2003).

Many instrumental detection methods based on the chemical components or physical properties of oils and fats have been developed and applied to assess the adulteration of oils and fats. These methods are gas chromatography (GC) (Hajimahmoodi et al. 2005), headspace mass spectrometry (Lorenzo et al. 2002), high-performance liquid chromatography (HPLC) (Cunha and Oliveira 2006), differential scanning calorimetry (DSC) (Chiavaro et al. 2008), Fourier transform infrared spectroscopy (FTIR) (Lerma-García et al. 2010; Zhang et al. 2012), synchronous fluorescence (Poulli et al. 2006), nuclear magnet resonance (NMR) (Smejkalová and Piccolo 2010), dielectric spectroscopy (Cataldo et al. 2010), and electronic nose (Gan et al. 2005). In addition, the combination of instrumental analysis

Q. Zhang · A. S. M. Saleh · Q. Shen (✉)  
College of Food Science and Nutritional Engineering,  
National Engineering and Technology Research Center for Fruits  
and Vegetables, China Agricultural University,  
Beijing 100083, China  
e-mail: shenqun@cau.edu.cn

with chemometrics (Zhang et al. 2006) enriched the data processing ways and got more convincing consequences. All of these methodologies obtained satisfactory results and could be used to a practical situation. However, laborious, time-consuming, sample devastation and expensive instrument exist in these methods. Along with quick advancement in the development of instrument about edible oil quality, the detection of adulteration technologies have been progressing towards the characteristics of fastness, convenience, simplicity, and objectiveness which are low field nuclear magnetic resonance's (LF-NMR) advantages.

From general NMR theory (Slichter 1990; Price 1997; Blümich et al. 2008), when a hydrogen-containing material is placed in a uniform magnetic field and then an RF pulse is offered, the H proton resonates and absorbs the RF pulse energy. When the RF pulse is terminated, the H proton will release the absorbed energy to get back to the thermal equilibrium, and this energy liberation course is the so-called NMR signal which can be detected by a dedicated coil. There are two relaxation times named as longitudinal relaxation ( $T_1$ ) and transverse relaxation ( $T_2$ ) to characterize the time of the recovery process of energy equilibrium.  $T_1$  relaxation is also called spin–lattice relaxation which corresponds to the energetic exchange between excited nuclear spins and lattice and refers to the total energy reduction.  $T_2$  relaxation is also called spin–spin relaxation which is the interaction among the nuclear magnetic moments (spins) and refers to the total energy of the nuclear system that remains unchanged (Bakmutov 2004). Commonly, the  $T_2$  value is lower than the  $T_1$  value of the same material. For samples with different chemical properties, such as hydrogen content and chemical structure of hydrogen-containing compound, the relaxation times are different.

As a rapid, convenient, and nondestructive method, LF-NMR has been abundantly used in food material property measurements and quality control (Todt et al. 2001; Micklander et al. 2002; Todt et al. 2006a) based upon detection of the mobility and distribution of water and fat hydrogen protons (Blümich et al. 2009) which extensively exist in food matrix. Different kinds of protons, e.g., those bound in free water or in more structured water or even protons attached to lipids, proteins, and carbohydrates, can be distinguished by LF-NMR (Pedersen et al. 2000). The proton mobility and distribution in different compounds in the food matrix decide the relaxation time. Therefore, measurements of water content and its existing forms in food tissue and oil content of food materials by LF-NMR were the most interesting research items and have obtained certain consistency compared to the traditionally proposed content test methods (Thybo et al. 2003; Sørland et al. 2004; Todt et al. 2006b).

Chemometric methods such as principal component analysis (PCA) and partial least squares (PLS) have been also

successfully used to process data obtained to optimize large and highly colinear datasets of multiecho pulse sequences from LF-NMR (Viereck et al. 2008). PLS combined with linear discriminate analysis (LDA) to exploit invisible changes of the internal characteristics of blanched sweet corn yielded a satisfactory classification rate of 94.3 % and performed well in firmness prediction of processed sweet corn (Shao and Li 2010). Therefore, the application of chemometric methods is a common and effective way to classify food materials.

The main objective of this study was to detect the adulteration of edible vegetable oil with UFO by LF-NMR application. In addition, conventional chemical indices of oils and fats were measured to estimate the authenticity of the studied oils and to find the differences between the fresh edible vegetable oils and the UFO.

## Materials and Methods

### Samples

Due to being commonly consumed by people, commercial corn oil (CO), peanut oil (PO), rapeseed oil (RO), and soybean oil (SO) were purchased from a local supermarket; they were all pure and qualified products. Used frying oil<sub>1</sub> (UFO<sub>1</sub>) was collected from a sales stand of twisted cruller at the local street. Used frying oil<sub>2</sub> (UFO<sub>2</sub>) was obtained from local KFC stores.

Due to the deeply dark color, the raw UFO samples were discolored by activated clay. The discoloration procedure was conducted as follows: during the heating of raw UFO held at 100 °C, 5–10 % activated clay was added and stirred slowly for 30 min. Then, the mix was filtered by gauze, and the filtrate was centrifuged at 9,000 r/min for 5 min, and the supernatant was collected. All the oil samples were preserved in a refrigerator at 4 °C until analysis.

### Chemicals

Activated clay, diethyl ether, ethanol, glacial acetic acid, isooctane, cyclohexane, potassium hydroxide, phenolphthalein, potassium iodide, sodium thiosulfate, starch, iodine monochloride, and all the other chemicals used in the study were purchased from Beijing Chemical Works Company. All the reagents and chemicals were of analytical grade.

### Instruments

An electronic analytical balance (Acculab, Sartorius, ALC-110.4, Goettingen, Germany) was used to accurately weigh the oil samples. A high-speed refrigerated centrifuge (GL-20 G-II, Shanghai Anke Centrifuge, Shanghai, China) was used to help the discoloration procedure. Transverse relaxation

measurement was performed by an NMI20-Analyst (Niumag Electric Corporation, Shanghai, China) equipped with a permanent magnet with field strength of 0.53 T and a probe head with RF coil of 18 mm diameter, combined with a windows analysis platform and integrated with an inversion of a multiexponential fitting analysis (T-invfit) program (Wang et al. 2004).

#### Analysis of Chemical Indices

The three most conventional chemical indices to evaluate the quality alteration of the studied oil samples were determined. Acid values (AV) of the oil samples were conducted according to the AOCS Official Method Cd 3 d-63: Acid Value (AOCS 2009a). Peroxide value (POV) of the oil samples was conducted according to the AOCS Official Method Cd 8b-90: Peroxide Value, Acetic Acid–Isooctane Method (AOCS 2003). Iodine value (IV) of the oil samples was conducted according to the AOCS Official Method Cd 1 d-92: Iodine Value of Fats and Oils Cyclohexane–Acetic Acid Method (AOCS 2009b).

#### Measurement of Transverse Relaxation

UFO<sub>1</sub> and UFO<sub>2</sub> were proportionally added into the four commercially QVOs, respectively. Four QVOs were set as control, and the additional ratio between UFO and qualified oil was set as follows: 0.5, 1, 2, 5, 10, 20, 50, and 100 %. Each oil sample was loaded into a 1.8-ml screw-capped plastic vial and then stored in a refrigerator set up at 4 °C before relaxation measurement.

The plastic vial contained oil sample that was put into an 18-mm diameter glass test tube and then the tube that contained oil sample was placed in the center of the RF coil. The LF-NMR relaxation times were measured using the Carr–Purcell–Meiboom–Gill (CPMG) (Carr and Purcell 1954; Meiboom and Gill 1958) pulse sequence on the NMI20-Analyst operating at a resonance frequency for protons of 22 MHz. The frequency offset of RF pulse was 623.29 kHz. The relaxation measurements were carried with an  $\tau$  value (time between 90° and 180° pulses) of 200  $\mu$ s. The pulse width of 90° and 180° pulses were 24.50 and 49.00  $\mu$ s,

respectively. Data from 5,000 echoes was acquired as four scan repetitions at 31.99–32.00 °C. The repetition time between subsequent scans was 1.5 s. The dead time between the end of the RF pulse and the beginning of sampling was 50  $\mu$ s. The received signal frequency range of the receiver was 250 kHz. The first and second signal gain adjustments were 20 and 3, respectively. After acquiring the CPMG sequence of the oil sample, the T-invfit software was used to inverse the obtained CPMG sequence into a spin–spin relaxation time ( $T_2$ ) distribution.

#### Data Processing

All experiments were carried out in triplicate. A two-factor (adulteration proportion and QVO oil variety) analysis of variance (ANOVA) which was achieved by SPSS 17.0 (SPSS Corporation, Chicago, USA) was used to analyze the data, and linear regression analysis (LRA) and graph drawings were conducted by origin 7.5 (OriginLab Corporation, Northampton, England).

## Results and Discussion

### Chemical Index Analysis and $T_2$ Distribution of the Oil Samples

#### Chemical Indices of the Studied Oil Samples

Edible oil quality is closely related to the consumer's health and can be showed by the conventional chemical indices. The AVs, POVs, and IVs of the oil samples are shown in Table 1. By means of ANOVA, there were significant differences among the AVs, POVs, and IVs of six oil samples, respectively, except AVs between CO and SO, POVs between CO and RO, and POVs between CO and SO. According to Codex Stan (1999), the AVs of all four QVOs were less than 0.6 mg KOH/g oil, indicating that they were all in the required quality limit except for PO, and the AVs of two UFOs were higher than 0.6 mg KOH/g oil,

**Table 1** Chemical indices of the studied oil samples

Indices	CO	PO	RO	SO	UFO <sub>1</sub>	UFO <sub>2</sub>
AV (mg/g)	0.124±0.007e	0.731±0.005c	0.261±0.006 d	0.116±0.004e	1.568±0.021b	4.300±0.064a
POV (mmol/kg)	3.704±0.141 d,e	5.914±0.113c	3.579±0.154e	4.029±0.156 d	7.507±0.188b	8.306±0.234a
IV (g/100 g)	120.3±1.729b	101.3±1.307 d	112.7±1.307c	125.7±1.729a	92.67±0.653e	44.33±0.653 f

Each data was expressed as the mean of three measurements  $\pm$  standard deviation. Different letters in the same row of different oil samples do significantly differ ( $p < 0.05$ )

CO corn oil, PO peanut oil, RO rapeseed oil, SO soybean oil, UFO<sub>1</sub> used frying oil 1, UFO<sub>2</sub> used frying oil 2, AV acid value, POV peroxide value, IV iodine value

explaining that their quality had deteriorated. POVs of all studied oil samples were less than 10 mEq of active oxygen per kilogram of oil, indicating that all four QVOs were qualified because they were kept in good reservation conditions before the experimental analysis, and the two UFOs were in bad quality because they had undergone longtime deep-frying before the experiment. It is well known that the POV increased at the beginning and decreased after deep oxidation (Gray 1978). IVs of all four QVOs were in the range required by the codex standard which could state that the unsaturated compounds have not severely degraded, and IVs of two UFOs were much lower because the carbon-carbon double bond broke during the deep-frying course.

All of these parameters could demonstrate that the quality of UFOs overstepped the continued utilization range, and all of them were the expression of the complex chemical reaction products produced during the thermal treatment. As reported by Choe and Min (2007), hydrolysis, oxidation, and polymerization reactions were the main alterations that occurred during the deep-frying process and result in a lot of complex products which contribute to the bad quality of frying oil.

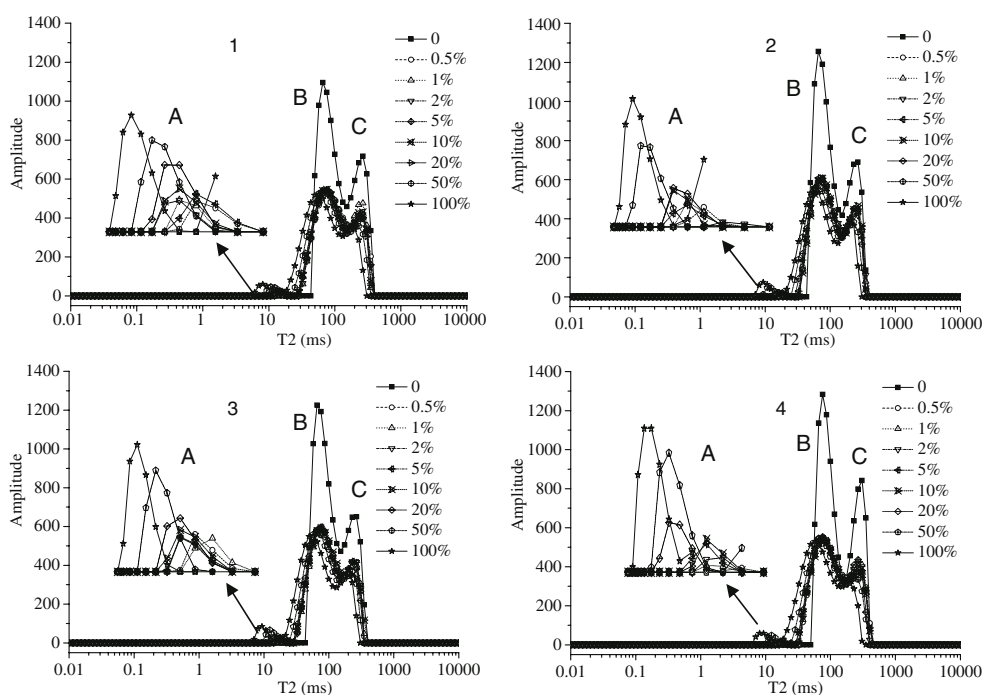
#### *T<sub>2</sub> Distributions of the Studied Oil Samples and Theory Analysis*

*T<sub>2</sub>* distributions of six unitary oil samples were measured before the adulteration experiment, and the spectra are displayed in Figs. 1 and 2. According to the spectra, four QVOs showed the same peak distribution (two peaks), indicating that the amplitude and *T<sub>2</sub>* values of the peaks

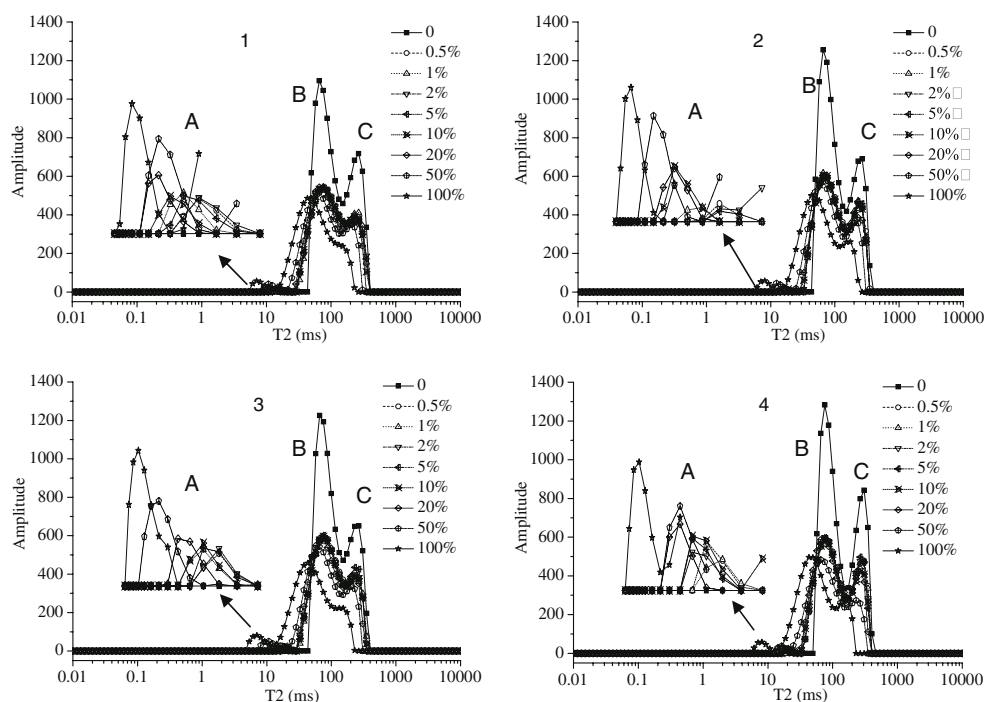
are similar. This might attribute to the resemblance of the main triacylglycerol (TAG) component existing in oils and fats. Nevertheless, the *T<sub>2</sub>* distribution of UFO was significantly different with that of the qualified oils which embodied that the amplitude value decreased and *T<sub>2</sub>* value of the peaks shifted towards the left. Most important of all, a third peak marked as A in the little value area of *T<sub>2</sub>* clearly appeared compared with the *T<sub>2</sub>* distribution of QVO. It is worth mentioning that the overlap among the three peaks which indicated that the complex constituents of the oils and fats could be attributed to the low sensitivity of LF-NMR. However, this did not influence the detection efficiency of LF-NMR on QVOs adulterated with UFO from the adulteration detection point of view.

*T<sub>2</sub>* distribution mainly depends on the homogeneity of the magnetic field where the hydrogen proton locates, and the homogeneity of the magnet field is mainly determined by the main magnetic field (magnet) and the local magnetic field (precessional motion of hydrogen proton) of the internal composition of the measured material (Blümich et al. 2008; Fukui 2008). Therefore, when the main magnetic field's intensity is stabilized, the factor influencing *T<sub>2</sub>* distribution is the research object's constituents or the interior chemical structure of the components in detail. For a mixture, if the molecular sizes of the constituents are uniform, the internal magnetic fields where the hydrogen proton locates made by these molecules are relatively uniform. As a result, when the RF is withdrawn, the losing speed in coherence of the precessional motion frequency (in phase) is slow, *T<sub>2</sub>* value is relatively long, and vice versa.

**Fig. 1** *T<sub>2</sub>* distributions of CO (a), PO (b), RO (c), and SO (d) adulterated with proportioned UFO<sub>1</sub>. (The abbreviations are the same as shown in Table 1. The three peaks that appeared were marked as A, B, and C, respectively)



**Fig. 2**  $T_2$  distributions of CO (a), PO (b), RO (c), and SO (d) adulterated with proportioned UFO<sub>2</sub>. (The abbreviations are the same as shown in Table 1. The three peaks that appeared were marked as A, B, and C, respectively)



$T_2$  distribution of oils and fats shows the spin–spin relaxation profile of hydrogen protons, which lie in the different chemical structural environments of oil and fat components. This profile reflects the speed of energy equilibrium recovery process.  $T_2$  and amplitude values represent the speed and strength of spin–spin relaxation, respectively. Generally, hydrogen protons of different structural positions in the same molecule have different  $T_2$  and amplitude values. However, due to the assembly of hydrogen protons in a similar chemical environment and the low magnetic field strength of LF-NMR, the obtained  $T_2$  distribution of oil sample just showed several peaks. Therefore,  $T_2$  distribution of qualified oil had two peaks which could be assumed that there were two types of hydrogen protons existing in different chemical environments in the qualified oil composition. Three peaks appeared in the  $T_2$  distribution of UFO accounting for three types of hydrogen protons. Thus, the appearance of the A peak indicated that there was a third type of hydrogen protons existing in UFO.

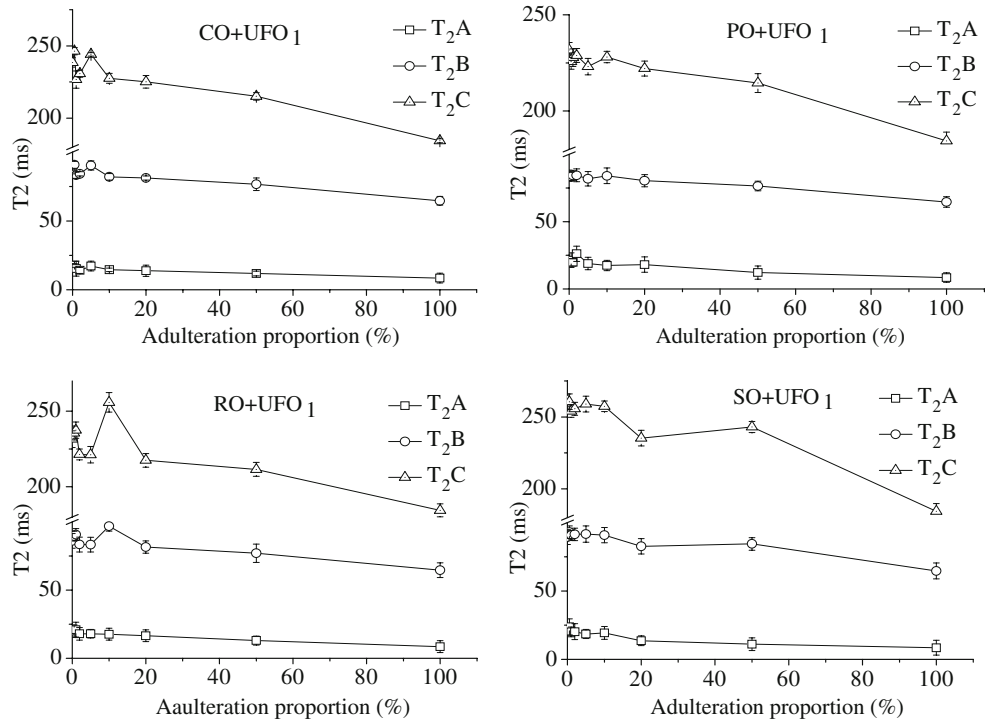
The qualified edible oil (refined) has approximately 99 % of TAGs, and these TAGs are mainly composed of glycerol combined with C16 or C18 of fatty acids. That's to say, the components have good homogeneity of molecular size. Thus, hydrogen protons have relatively similar chemical environments. UFO had undergone many complicated chemical reactions and a lot of products were produced. These products could be separated into three kinds: (i) decomposition products with molecular weight were less than 600 Das such as free fatty acids, diglycerides, monoglycerides, little molecule

of alcohols, aldehydes, ketones, hydrocarbons, lactones, cyclic monomers, etc.; (ii) oxidized TAGs which had hydroxyl, keto, and epoxy groups in the fatty acyl chains with molecular weight between 900 and 1,000 Da and similar to the molecular weight of original TAGs; and (iii) polymers with molecular weight higher than 1,800 Da such as highly polymerized compounds, oligomers, trimers, dimers, etc. (Paul and Mittal 1997; Sahin and Sumnu 2009). Based on the discrepancies of the constituents and their molecular weight and the  $T_2$  distribution between qualified edible oil and UFO, the A peak could be supposed to the decomposition products or the polymers.

On one hand, a lot of hydrogen-containing products increased the frequency of the hydrogen protons' chemical exchanges between the products as a result of the increase of transverse relaxation and a lower  $T_2$  value. However, many of these decomposition products were volatile and were lost during the deep-fat frying course. Therefore, the appearance of the A peak resulting in these decomposition products was not observed. On the other hand, the most possible products for A peak were polymer compounds like TAG dimers, oligomers, and cyclic polymers. Due to the large molecular structure, the free motion of hydrogen proton linked to the polymers' molecular backbone was restricted by the effect of steric hindrance, which made the motion degree or the motion free path decrease. As a result, the time which was taken by the hydrogen protons to recover the energy equilibrium after the impact of RF was reduced, i.e., the  $T_2$  value of the A peak was lower.



**Fig. 3** The change profiles of the QVOs adulterated with UFO<sub>1</sub> along with the increase in adulteration proportion. ( $T_2A$ ,  $T_2B$ , and  $T_2C$  represented the weighted  $T_2$  distribution values of  $A$  peak,  $B$  peak, and  $C$  peak, respectively. The abbreviations are the same as shown in Table 1)

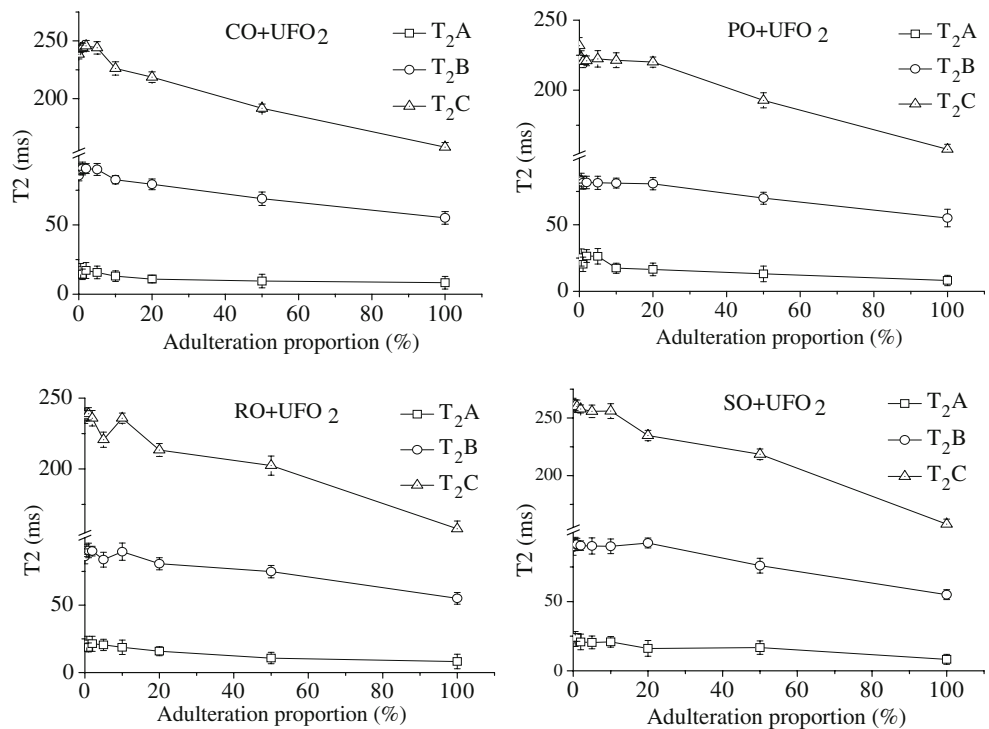


Discrimination of Adulteration

On the grounds of the above-mentioned  $T_2$  distribution differences among the oil samples, the UFOs were proportionally added into the qualified oils to conduct an adulteration determination test. As shown in Figs. 1 and 2,  $T_2$  distributions of the two adulteration methods had the same variation tendency. After amplifying the  $T_2$  distribution,

along with the increase of adulteration proportion, the amplitude values of the B peak and C peak decreased, while the amplitude values of the A peak increased.  $T_2$  values of the A peak, B peak, and C peak shifted left when the adulteration proportion increased. By observation of a peaks' area, the ratio of the A peak's area accounted for the whole area of peaks increased along with the increase of adulteration proportion. Along with the increase of adulteration proportion,  $T_2$  values

**Fig. 4** The change profiles of the QVOs adulterated with UFO<sub>2</sub> along with the increase in adulteration proportion. ( $T_2A$ ,  $T_2B$ , and  $T_2C$  represented the weighted  $T_2$  distribution values of  $A$  peak,  $B$  peak, and  $C$  peak, respectively. The abbreviations are the same as shown in Table 1)



**Table 2** Tests of between-subjects effects. Dependent variable: area ratio

Source	QVO + UFO <sub>1</sub>					QVO + UFO <sub>2</sub>				
	Type III sum of squares	df	Mean square	F	Significance	Type III sum of squares	df	Mean square	F	Significance
Corrected model	143.443 <sup>a</sup>	35	4.098	20,300.131	0.000	130.709 <sup>a</sup>	35	3.735	10,210.925	0.000
Intercept	119.297	1	119.297	59,0903.782	0.000	120.397	1	120.397	32,9185.846	0.000
QVO variety	4.064	3	17.124	84,820.831	0.000	2.476	3	0.825	2,256.381	0.000
Adulteration proportion	136.995	8	1.355	6,709.912	0.000	124.663	8	15.583	42,606.177	0.000
QVO variety * adulteration proportion <sup>b</sup>	2.384	24	0.099	492.008	0.000	3.571	24	0.149	406.826	0.000
Error	0.015	72	0.000			0.026	72	0.000		
Total	262.754	108				251.132	108			
Corrected total	143.458	107				130.736	107			

QVO qualified vegetable oils

<sup>a</sup> R square=1.000 (adjusted R square=1.000)

<sup>b</sup> QVO variety \* adulteration proportion means the interaction effect between QVO variety and adulteration proportion

of the peaks gradually decreased until they reached the minimum value of the whole UFO. Therefore, if the UFO was blended into QVO, the peaks' amplitude value and  $T_2$  values of the adulteration samples were lower than that of QVOs.

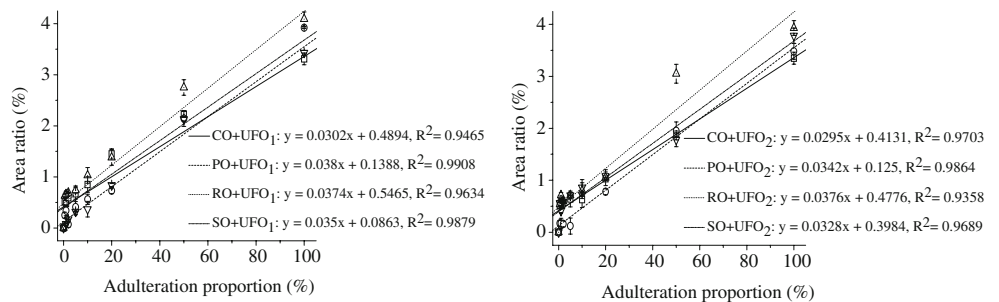
The decrease in amplitude values of the B peak and C peak stated that the contents of hydrogen proton which contributed to the peaks were decreased after adding UFO into QVOs. This was consistent with decrease in TAGs content of UFO undergoing many chemical reactions. It was interesting that the significant decrease in the amplitude of the B peak and C peak appeared when the UFO was added into QVOs by a very small proportion. This might relate to the constituent term fluctuation between QVO and QVO adulterated with UFO, and there might be a gradient descent of amplitude values of the B peak and C peak when UFO was added into QVOs by a very small quantity. The experiment of UFO quantity lower than 0.5 % had not been referred to for the consideration of unapplicable adulteration practice. However, as the adulteration proportion increased, this variation tendency in the amplitude of the B peak and C peak became slow. This might be attributed to the linear detection range of LF-NMR which could affect the decreasing span of amplitude values of the B peak and C peak.

Based on the above-mentioned discussions and amplitude values of peak of the  $i$ th relaxation time and the  $i$ th relaxation times of the peak by means of a spectrum analysis software,  $T_2$  values of the A peak, B peak, and C peak were calculated. For the objectivity of the  $T_2$  value, weighted means of each peak's  $T_2$  value were calculated according to the following equation:

$$\bar{T}_2 = \frac{\sum_{i=1}^n A_i T_{2i}}{\sum_{i=1}^n A_i}$$

where  $\bar{T}_2$  = geometric weighted average transverse relaxation time,  $A_i$  = the amplitude value of peak of the  $i$ th relaxation time, and  $T_{2i}$  = the  $i$ th relaxation time of the peak. The adulteration proportion was set as abscissa, and the weighted  $T_2$  value was set as ordinate (Figs. 3 and 4). As shown in the graphs,  $T_2$  values of the three peaks fluctuated under the lower adulteration proportion. However, there was a same decrease phenomenon of the  $T_2$  values when the adulteration proportion was higher than 10 %.  $T_2$  value of peaks was decreased in the wake of adulteration proportion increase. The extent of the decrease of  $T_2C$  was highest;  $T_2B$  takes second place and  $T_2A$  was the lowest, which estimated

**Fig. 5** The relationship between area ratio of A peak accounted for the whole peaks and adulteration proportion of the QVOs adulterated UFO. (The abbreviations are the same as shown in Table 1)



the relaxation time to be significantly shift left to the  $T_2$  distribution of the adulterated oil samples.

The results of the ANOVA analysis were shown in Table 2. QVO + UFO<sub>1</sub> was taken as an example, and the significant probabilities of QVO variety, adulteration proportion, and QVO variety \* adulteration proportion were all 0.000 which was less than 0.05, indicating that all the QVO varieties, adulteration proportions, and interaction effects between them had significant influence on the area ratios. In addition, the annotation of the corrected model showed that the multiple correlation coefficient was 1.000, indicating that there was a significant correlation relationship between the area ratios and the factors. Similar ANOVA results were also seen for QVO + UFO<sub>2</sub>. Therefore, a simple linear equation between the area ratios and adulteration proportions was built to illustrate the relationship (Fig. 5). As shown in the linearity curves, when the adulteration proportions were lower than 10 %, the area ratios had a certain fluctuation. However, in terms of the total situation, the linearity of each curve was very clear, and the determination coefficients ( $R^2$ ) of the linear equations were all above 0.93.

The limit of detection (LOD) was calculated from the data of Fig. 5 using the following formula:  $LOD = \frac{3.3\sigma}{S}$ , where  $\sigma$  was the standard deviation of the response, i.e., the standard error of the regression statistics;  $S$  was the slope of the calibration curve (ICH Q2B 1996). After the calculations, the LOD values were 28 % for CO + UFO<sub>1</sub>, 11 % for PO + UFO<sub>1</sub>, 23 % for RO + UFO<sub>1</sub>, and 13 % for SO + UFO<sub>1</sub> and were 21 % for CO + UFO<sub>2</sub>, 14 % for PO + UFO<sub>2</sub>, 31 % for RO + UFO<sub>2</sub>, and 21 % for SO + UFO<sub>2</sub>. From these values, it can be seen that LODs of the applied adulterations of QVOs were all greater than 10 %, and even the LOD of RO + UFO<sub>2</sub> was 31 %. This might be attributed to the complex component of the studied sample and the lower sensitivity of the LF-NMR. However, the appearance of the A peak and the extent of the increase of the area of the A peak could be used to conduct qualitative and quantitative analyses for the authentication of QVOs adulterated with UFO.

## Conclusions

Chemical parameters of the studied oil samples indicated that the UFOs were deeply deteriorated which could reflect many complex chemical reactions taking place during the deep-fat frying process according to previous studies. By adopting the LF-NMR to measure the transverse relaxation profiles of QVOs adulterated with UFOs and analyzing the measured  $T_2$  distributions, the third peak, named as the A peak, which could be ascribed to the polymers produced during the longtime deep-fat frying procedure, appeared in UFO's  $T_2$  distribution, and its area increased along with adulteration proportion increase. Meanwhile, the weighted

$T_2$  values of the spectrum peaks were also calculated and had a certain relationship with the adulteration proportion. A simple linear equation was built to explain the positive correlation between the area ratio and the adulteration proportion, and  $R^2$  values were all higher than 0.93. The results stated that the A peak and its area variation in the wake of adulteration proportion could supply the basis for the qualitative and quantitative analyses of QVOs mixed with UFO.

**Acknowledgments** Project of oil quality and safety control technology research and industrialization demonstration (2009BADB9B08) of the "Eleventh Five-Year" Technology Support Program is acknowledged. The authors would like to thank the engineers who are working in Shanghai Niumag Corporation Ltd. for their kind help during the experiment and the equation derivation.

## References

- AOCS. (2009a). *Official method Cd 3 d-63. Sampling and analysis of commercial fats and oils: acid value*. Champaign-Urbana, Illinois, USA: American Oil Chemists' Society.
- AOCS. (2009b). *Official method Cd 1 d-92. Sampling and analysis of commercial fats and oils: iodine value, cyclohexane-acetic acid method*. Champaign-Urbana, Illinois, USA: American Oil Chemists' Society.
- AOCS. (2003). *Official method Cd 8b-90. Sampling and analysis of commercial fats and oils: peroxide value, acetic acid-isooctane method*. Champaign-Urbana, Illinois, USA: American Oil Chemists' Society.
- Bakhtmutov, V. I. (2004). *Practical NMR relaxation for chemists*. Chichester, UK: Wiley.
- Bhattacharya, A. B., Sajilata, M. J., Tiwari, S. R., & Singhal, R. S. (2008). Regeneration of thermally polymerized frying oils with adsorbents. *Food Chemistry*, 110(3), 562–570.
- Blümich, B., Casanova, F., & Appelt, S. (2009). NMR at low magnetic fields. *Chemical Physics Letters*, 477(4–6), 231–240.
- Blümich, B., Perlo, J., & Casanova, F. (2008). Mobile single-sided NMR. *Progress in Nuclear Magnetic Resonance Spectroscopy*, 52(4), 197–269.
- Carr, H. Y., & Purcell, E. M. (1954). Effects of diffusion on free precession in nuclear magnetic resonance experiments. *Physical Review*, 94, 630–638.
- Cataldo, A., Piuzzi, E., Cannazza, G., Benedetto, E. D., & Tarricone, L. (2010). Quality and anti-adulteration control of vegetable oils through microwave dielectric spectroscopy. *Measurement*, 43(8), 1031–1039.
- Chiavaro, E., Rodriguez-Estrada, M. T., Barnaba, C., Vittadini, E., Cerretani, L., & Bendini, A. (2008). Differential scanning calorimetry: a potential tool for discrimination of olive oil commercial categories. *Analytica Chimica Acta*, 625(2), 215–226.
- Choe, E., & Min, D. B. (2007). Chemistry of deep-fat frying oils. *Journal of Food Science*, 72(5), 77–86.
- Codex Alimentarius: codex standard for named vegetable oils. Codex STAN 210-1999, 2001.
- Cunha, S. C., & Oliveira, M. B. P. P. (2006). Discrimination of vegetable oils by triacylglycerols evaluation of profile using HPLC/ELSD. *Food Chemistry*, 95(3), 518–524.
- Fukui, H. (2008). The Theory of nuclear spin-spin couplings. In G. A. Webb (Ed.), *Modern magnetic resonance* (pp. 79–83). Dordrecht, Netherlands: Springer.

- Gan, H. L., Che Man, Y. B., Tan, C. P., NorAini, I., & Nazimah, S. A. H. (2005). Characterisation of vegetable oils by surface acoustic wave sensing electronic nose. *Food Chemistry*, *89*(4), 507–518.
- Gray, J. I. (1978). Measurement of lipid oxidation: a review. *Journal of the American Oil Chemists' Society*, *55*(6), 539–546.
- Hajimahmoodi, M., Heyden, V. Y., Sadeghi, N., Jannat, B., Oveisi, M. R., & Shahbazian, S. (2005). Gas-chromatographic fatty-acid fingerprints and partial least squares modeling as a basis for the simultaneous determination of edible oil mixtures. *Talanta*, *66*(5), 1108–1116.
- ICH Q2B, 1996 ICH Q2B., 1996. Validation of analytical procedures: methodology. Geneva.
- Lerma-García, M. J., Ramis-Ramos, G., Herrero-Martínez, J. M., & Simó-Alfonso, E. F. (2010). Authentication of extra virgin olive oils by Fourier-transform infrared spectroscopy. *Food Chemistry*, *118*(1), 78–83.
- Lorenzo, I. M., Pavón, J. L. P., Laespada, M. E. F., Pinto, C. G., & Cordero, B. M. (2002). Detection of adulterants in olive oil by headspace-mass spectrometry. *Journal of Chromatography. A*, *945*(1–2), 221–230.
- Meiboom, S., & Gill, D. (1958). Modified spin-echo method for measuring nuclear relaxation times. *Review Science Instrument.*, *29*, 688–691.
- Micklander, E., Peshlov, B., Purslow, P. P., & Engelsens, S. B. (2002). NMR-cooking: monitoring the changes in meat during cooking by low-field 1H-NMR. *Trends in Food Science & Technology*, *13* (9–10), 341–346.
- Miyagi, A., Subramanian, R., & Nakajima, M. (2003). Membrane and additional adsorption processes for quality improvement of used frying oils. *Journal of the American Oil Chemists' Society*, *80*(9), 927–932.
- Paul, S., & Mittal, G. S. (1997). Regulating the use of degraded oil/fat in deep-fat/oil food frying. *Critical Reviews in Food Science and Nutrition*, *37*(7), 635–662.
- Pedersen, H. T., Munck, L., & Engelsens, S. B. (2000). Low-field <sup>1</sup>H nuclear magnetic resonance and chemometrics combined for simultaneous determination of water, oil, and protein contents in oilseeds. *Journal of America Oil Chemists' Society*, *77*(10), 1069–1076.
- Poulli, K. I., Mousdis, G. A., & Georgiou, C. A. (2006). Synchronous fluorescence spectroscopy for quantitative determination of virgin olive oil adulteration with sunflower oil. *Analytical and Bioanalytical Chemistry*, *386*(5), 1571–1575.
- Price, W. S. (1997). Pulsed-field gradient nuclear magnetic resonance as a tool for studying translational diffusion: part 1. Basic theory. *Concepts in Magnetic Resonance*, *9*(5), 299–336.
- Sahin, S., & Sumnu, S. G. (2009). *Advances in deep-fat frying of foods*. London, UK: Taylor & Francis.
- Shao, X. L., & Li, Y. F. (2010). Classification and prediction by LF NMR. *Food and Bioprocess Technology*. doi:10.1007/s11947-010-0455-9.
- Slichter, C. P. (1990). *Principles of magnetic resonance*. Springer Series in Solid-State Sciences (3 rdth ed.). Berlin Heidelberg, Germany: Springer.
- Smejkalová, D., & Piccolo, A. (2010). High-power gradient diffusion NMR spectroscopy for the rapid assessment of extra-virgin olive oil adulteration. *Food Chemistry*, *118*(1), 153–158.
- Sørland, G. H., Larsen, P. M., Lundby, F., Rudi, A. P., & Guiheneuf, T. (2004). Determination of total fat and moisture content in meat using low field NMR. *Meat Science*, *66*(3), 543–550.
- Tay, A., Singh, R. K., Krishnan, S. S., & Gore, J. P. (2002). Authentication of olive oil adulterated with vegetable oils using Fourier transform infrared spectroscopy. *LWT- Food Science and Technology*, *35*(1), 99–103.
- Thybo, A. K., Andersen, H. J., Karlsson, A. H., Dønstrup, S., & Stødkilde-Jørgensen, H. (2003). Low-field NMR relaxation and NMR-imaging as tools in differentiation between potato sample and determination of dry matter content in potatoes. *Lebensmittel-Wissenschaft und Technologie*, *36*(3), 315–322.
- Todt, H., Burk, W., Guthausen, G., Guthausen, A., Kamlowski, A., & Schmalbein, D. (2001). Quality control with time-domain NMR. *European Journal of Lipid Science and Technology*, *103*(12), 835–840.
- Todt, H., Guthausen, G., Burk, W., Schmalbein, D., & Kamlowski, A. (2006a). Time-domain NMR in quality control: standard applications in food. In G. A. Webb (Ed.), *Modern magnetic resonance* (pp. 1739–1743). Dordrecht, Netherlands: Springer.
- Todt, H., Guthausen, G., Burk, W., Schmalbein, D., & Kamlowski, A. (2006b). Water/moisture and fat analysis by time-domain NMR. *Food Chemistry*, *96*(3), 436–440.
- Viereck, N., Nørgaard, L., Bro, R., & Engelsens, S. B. (2008). Chemometric analysis of NMR data. In G. A. Webb (Ed.), *Modern magnetic resonance* (pp. 1833–1843). Dordrecht, Netherlands: Springer.
- Wang, Z. D., Xiao, L. Z., & Liu, T. Y. (2004). A new method for multi-exponential inversion of NMR relaxation measurements. *Science in China Series G: Physics Mechanics and Astronomy*, *47*(3), 265–276.
- Zhang, G. W., Ni, Y. N., Churchill, J., & Kokot, S. (2006). Authentication of vegetable oils on the basis of their physico-chemical properties with the aid of chemometrics. *Talanta*, *70*(2), 293–300.
- Zhang, Q., Liu, C., Sun, Z. J., Hu, X. S., Shen, Q., & Wu, J. H. (2012). Authentication of edible vegetable oils adulterated with used frying oil by Fourier transform infrared spectroscopy. *Food Chemistry*, *132*(3), 1607–1613.

## Effect of Water Migration between Arabinoxylans and Gluten on Baking Quality of Whole Wheat Bread Detected by Magnetic Resonance Imaging (MRI)

Juan Li,<sup>†</sup> Ji Kang,<sup>†</sup> Li Wang,<sup>†</sup> Zhen Li,<sup>†</sup> Ren Wang,<sup>†</sup> Zheng Xing Chen,<sup>\*,†</sup> and Gary G. Hou<sup>\*,§</sup>

<sup>†</sup>School of Food Science and Technology, State Key Laboratory of Food Science and Technology, Jiangnan University, Wuxi, Jiangsu 214122, People's Republic of China

<sup>§</sup>Wheat Marketing Center, 1200 N.W. Naito Parkway, Suite 230, Portland, Oregon 97209, United States

**ABSTRACT:** A new method, a magnetic resonance imaging (MRI) technique characterized by  $T_2$  relaxation time, was developed to study the water migration mechanism between arabinoxylan (AX) gels and gluten matrix in a whole wheat dough (WWD) system prepared from whole wheat flour (WWF) of different particle sizes. The water sequestration of AX gels in wheat bran was verified by the bran fortification test. The evaluations of baking quality of whole wheat bread (WWB) made from WWF with different particle sizes were performed by using SEM, FT-IR, and RP-HPLC techniques. Results showed that the WWB made from WWF of average particle size of 96.99  $\mu\text{m}$  had better baking quality than those of the breads made from WWF of two other particle sizes, 50.21 and 235.40  $\mu\text{m}$ .  $T_2$  relaxation time testing indicated that the decreased particle size of WWF increased the water absorption of AX gels, which led to water migration from the gluten network to the AX gels and resulted in inferior baking quality of WWB.

**KEYWORDS:** magnetic resonance imaging (MRI), arabinoxylan (AX), gluten, water migration, whole wheat bread

### ■ INTRODUCTION

Whole wheat bread (WWB) is one of the fastest-growing staple foods in Western countries.<sup>1</sup> Many scientific studies have confirmed its antioxidative activity and other nutritional functions in epidemiology.<sup>2–5</sup> However, due to the less cohesive (also water partitioning during mixing and baking) property of whole wheat dough (WWD) compared with that of white dough, the baking qualities of WWB, including loaf volume, specific volume, and interior structure (the porosity of bread), are inferior to those of white bread,<sup>6</sup> which has restricted a wider acceptance of WWB by consumers.<sup>7</sup> In Asian countries, there are many fewer whole wheat products and a lower market shares, leading to increased incidence rates of chronic diseases and reduced value of grains (more grain components go to feed).<sup>8</sup>

The relationship between the particle size of wheat bran and the volume of bread has been investigated, but the results were inconclusive and controversial. Some studies have shown that the wheat bran has a negative effect on bread volume,<sup>9,10</sup> especially small bran particles.<sup>11,12</sup> Wheat bran particles can deleteriously affect the gluten network, decrease dough resilience, and impair the framework of gas cells and, thus, gas retention. These effects can lead to low bread specific volume and inferior baking quality.<sup>13</sup> However, other research has shown that bread made from smaller bran particle size flour had a larger volume than bread made with coarser bran flour.<sup>14</sup> Meanwhile, there were some results suggesting that bread with the medium particle size (415  $\mu\text{m}$ ) of wheat bran had larger volume than either the refined (278  $\mu\text{m}$ ) or the coarse group (609  $\mu\text{m}$ ).<sup>9</sup> More studies are still needed to investigate the effect of whole wheat flour (WWF) particle size on its baking quality.

Arabinoxylans (AX) are important nonstarch polysaccharides that form the cell walls of cereal endosperm and bran.<sup>15</sup> Ferulic acid (FA) is a major phenolic acid in wheat, where it is mainly esterified to the arabinose backbone of AX.<sup>16,17</sup> In wheat bran, it is concentrated in cell walls. Incorporation of ferulic acid into arabinose residues enhances the formation of intermolecular cross-links of AX, leading to gel formation.<sup>18</sup> Previous research reported that the AX gels can inhibit the formation of gluten network by changing water distribution among gluten and other macromolecules and result in a less extensible gluten.<sup>19</sup> This is especially true when AX gels compete with the gluten network for water during mixing, restraining the gluten network from water uptake.<sup>20</sup> Gill<sup>21</sup> proposed the redistribution of water from nonstarch polysaccharides to gluten during fermentation. Jacobs<sup>7</sup> theorized that AX tightly binds water in the dough system, reducing the availability of water for developing the gluten network. Roman-Gutierrez et al.<sup>22</sup> compared the water vapor adsorption properties of wheat flour and flour components (pentosans, gluten, and starch) using a controlled atmosphere microbalance, and the theoretical distribution of water between the flour components was determined under a water vapor environment. Roman-Gutierrez et al. demonstrated that the water vapor adsorption properties of wheat flour depended only on the ability of the flour components to interact directly with the water molecules, which may not apply to the bread dough system that traps a large amount of water

Received: March 19, 2012

Revised: June 13, 2012

Accepted: June 15, 2012

Published: June 15, 2012

inside macromolecular complexes formed by the swollen components.

The magnetic resonance imaging (MRI) technique is a tool for the noninvasive determination of moisture distribution in high-moisture samples, including grain kernels.<sup>23</sup> Traditionally, MRI was applied to examine macro-water distribution and migration in grain, such as water migration in single rice kernels during the tempering process,<sup>24</sup> water penetration into rice grains during soaking,<sup>25</sup> and water redistribution in grain kernels during drying.<sup>26</sup> Moreover, MRI techniques have been developed to show the internal structure of bread, which can simplify the complicated and time-consuming process of sensory and visual instrumental evaluation and reduce costs.<sup>27,28</sup> MRI has been considered to be an accurate and nondestructive method for visualizing the internal network structure of bread<sup>29</sup> and calculating the porosity of air cells.<sup>30–32</sup>

The present work was undertaken to evaluate the effect of WWF particle size on bread-baking performances that were characterized by loaf volume and crumb porosity. To gain more insight into relationships between particle size and bread quality, a MRI technique was applied to examine the water migration between macromolecules (AX gels and gluten). To the best of our knowledge, despite the plenitude of hypotheses that have been proposed concerning water migration and competitive water absorption between AX gels and the gluten network, no definitive evidence has been presented to support these mechanisms. The present study's goal was to verify the water migration pattern and competitive water absorption mechanism between AX gels and gluten through the MRI technique and to confirm that it was the mechanism of inferior loaf volume of WWB caused by refined particle size flour.

## MATERIALS AND METHODS

**Wheat Grain.** Wheat grain (Zheng 9023 cultivar, harvested in 2008) was obtained from Jin Lenong Agriculture Development Co., Ltd. (Henan Province, China).

**WWF Analysis.** Ash content (12% moisture basis) was 1.60% and protein content (12% moisture basis,  $N \times 5.7$ ) was 13.0%, as reported by the supplier. Farinograph curves were obtained according to AACC International Approved Method 54-21.

**Chemicals.** Bakery sugar, salt, shortening, and instant dry yeast were purchased from a local supermarket. The chemicals used for preparing scanning electron microscopy (SEM) samples and testing the content of FA were of analytical grade and purchased from Sinopharm Chemical Reagent Co. (Shanghai, China).

**WWF Milling.** The WWF was milled from intact wheat kernel samples using a Waring blender (DFY-400, Wenling Dade Traditional Chinese Medicine Machinery Co., Ltd., Zhejiang Province, China) by grinding for 5 min. The coarse flour was superfine ground by the ultramicro pulverizer (MZP-4, Hengtai Dongqi Powder and Equipment Co., Ltd., China) for 15, 25, and 35 min, respectively to achieve the desired particle sizes. Four hundred grams WWF of each particle size group was prepared each time. All experiments were repeated three times.

**Particle Size Analysis.** The particle size distributions of WWF obtained from different milling times were measured by the Laser Particle Size Analyzer (S3500, Microtrac Inc., USA), and the measurements were triplicates. The data were fitted by Origin (version 8.5), and the average particle size was obtained from the fitted curve.

**Breadmaking.** Bread loaves (each made from 150 g of dough) were made in duplicate using AACC Approved Method 10-10B (optimized straight-dough; AACC International, 2000) with some adjustments. Formulation was as follows: WWF, 500 g; sugar, 30 g; salt, 7.5 g; shortening, 15 g; and instant dry yeast, 15 g. Control bread

was prepared from a commercial white bread flour (China Oil and Foodstuffs Corp., Qinhuangdao, Hebei, China). Commercial bread flour quality parameters were as follows: ash content, 0.40% (14% mb) and protein content, 14.0% (14% mb). Yeast was dissolved in water containing 0.1% sugar at 30 °C before use. Optimum absorption of 68% was acquired from the Farinogram data (11.3% mb). Dough was mixed in a bread mixer (hook-mixer with a 1 kg mixing bowl; Guangzhou Chenggong Baking Machinery Co., Ltd. China). Ingredients were mixed at speed 2 for 5–8 min (optimized in preliminary assays). Then the dough was divided into 150 g per piece, placed into a rectangular baking pan (10 × 5 × 3 cm), and fermented at 27 °C for 30 min, which was adjusted from the 90 min adopted in AACC International Approved Method 10-10B (2000) to avoid dough collapse after a long fermentation time. Then, the dough was punched down and proofed for 90 min (increased from 33 min, because this was found to greatly improve the volume of WWB) at 38 °C with 85% relative humidity in a proofing cabinet. Baking was conducted in an oven (HXM-CS11-10, Shanghai Qingyou Industrial Co., Ltd., China) for 25 min at 170 °C upper temperature and 210 °C bottom temperature. After cooling for 1 h, bread samples were placed into plastic bags and stored in a freezer at –18 °C until analyses. Bread slices (1.0 cm) were cut by an electronic bread cutter for MRI analysis.

**Evaluation of Bread Quality. Determination of Bread Specific Volume.** After cooling for 1 h at room temperature on metal grids, the bread weight and volume were measured in triplicates. Bread volume was determined by the rapeseed displacement method (AACC International Approved Method 10-05). The specific volume ( $\text{cm}^3 \text{g}^{-1}$ ) of bread was calculated by dividing the volume by the weight.

**Calculation of the Bread Porosity from MR Images.** The crumb structure of the WWB slices was evaluated for porosity, as observed with an MRI system (Mini MR-60, Shanghai Niumag Electronics Technology Co., Ltd., Shanghai, China). Image analysis was performed by the spin-echo 2D-FT method using an echo time of 0.1 ms and a repetition time of 0.5 s according to the testing parameters provided by the instrument manufacturer (Shanghai Niumag Electronics Technology Co. Ltd.). The images were recreated on a 192 × 192 matrix for 2D images, which were scanned for three layers with a 4.9 mm thickness of each layer. The porosity was calculated by the image twice-threshold segmentation method<sup>33</sup> using Matlab (version R2010a) to offset the variation error caused by the signal-to-noise ratio of the scanned images. The gray value range of image was 0–255. The contrast of the images was adjusted and selected from the gray value for detecting the rim of the bread sample; the pixel amount of bread sample was designated  $N_1$ . The threshold value was adjusted and selected again for testing the internal gas cell of the bread; the pixels lower than the threshold were counted and designated  $N_2$ , representing the gas cells of the bread crumb. Therefore, the pixels that were higher than the threshold represented the backbone structure of the bread. The porosity can be calculated from eq 1 provided by the instrument manufacturer (Shanghai Niumag Electronics Technology Co. Ltd.).  $N$  is the number of pixels,  $S_{\text{pixel}}$  is the physical area of a single pixel, and  $h$  is the thickness of a bread cross section.  $V_{\text{pore}}$  is the total volume of the gas cells, and  $V_{\text{total}}$  is the total volume of the bread, including the gas cell volume and the volume of bread crumb.

$$\varphi_{\text{MRI}} = \frac{V_{\text{pore}}}{V_{\text{total}}} \times 100\% = \frac{N_2 S_{\text{pixel}} h}{N_1 S_{\text{pixel}} h} \times 100\% = \frac{N_2}{N_1} \times 100\% \quad (1)$$

**Evaluation of Effect of WWF Particle Size on Bread-Baking Quality. SEM.** The interaction between the wheat bran and gluten matrix was observed by scanning electron microscope (Quanta-200, FEI Co., Ltd., USA). The WWB (dough samples were taken after they were properly mixed during the bread-baking process) was fixed with aqueous 3.0% (v/v) glutaraldehyde for 72 h and washed six times with 0.1 M sodium phosphate buffer (pH 7.2) followed by aqueous 1.0% (w/v)  $\text{OsO}_4$  for 2 h at 4 °C. Samples were then rinsed for 1 h in distilled water and dehydrated in a graded acetone series in five steps. After drying with a critical point dryer, the samples were mounted on

bronze stubs and sputter-coated with gold (50 Å thick). Then specimens were observed and photographed with an accelerating voltage of 5.0 kV and viewed at magnification levels of 1200×.

**Fourier Transform Infrared Spectroscopy (FT-IR).** Three doughs (100 g/each) were produced by mixing three different particle sizes of WWF with 68% D<sub>2</sub>O (w/w) (for deducting the background of the pure water) for 3 min using the same bread mixer as described previously. The secondary structure of gluten protein in WWD was determined in triplicates by FT-IR (NEXUS, Nicolet Co., Ltd., USA). The data were processed by Omnic and Peak Fit software (version 4.12).<sup>34</sup>

**Determination of FA Content by Reversed Phase High-Performance Liquid Chromatography (RP-HPLC).** *Extraction of FA from WWF.* WWF (2 g) and distilled water (11.3 g) were weighed into a 250 mL shake flask, and the mass fraction of WWF was 15% (w/w). Thermostable  $\alpha$ -amylase (0.002 g; 30 U/mg, Novozyme, Denmark) was added. The starch component in WWF was hydrolyzed in a 84 °C thermostatic water bath for 40 min. The  $\alpha$ -amylase was inactivated in a 100 °C boiling water bath for 10 min. After the samples were hydrolyzed, alkali protease (0.001 g, 100 U/mg, Novozyme) was added to the solution, the pH value was adjusted to 8.0 with sodium hydroxide (1.5% w/v), and the mixture was shaken in a water bath (55 °C) for 120 min. After hydrolysis by alkali protease, the enzyme was inactivated by a 100 °C boiling water bath for 10 min. Glucoamylase (0.5 mg; 100 U/mg, Novozyme) was added, and the pH of the solution was adjusted to 4.5 with 2 mol/L hydrochloric acid. The samples were shaken in a water bath (60 °C) for 120 min, after which the glucoamylase was inactivated in a boiling water bath for 10 min. The suspension was centrifuged at 4 °C for 15 min at 5000 rpm, and the residue was decanted into another 250 mL shake flask. Finally, 150 mL of sodium hydroxide (1.5% w/v) was added for alkali hydrolyzation in a water bath (85 °C) for 2 h. The suspension was centrifuged for 15 min at 8000 rpm. The pH of the supernatant (5 mL) was adjusted to 2.5 with 2 mol/L hydrochloric acid. The FA was extracted by 10 mL of diethyl ether for 5 min, and the diethyl ether was evaporated using a rotary evaporator (RV 10 basic, IKA, Germany) at 45 °C. The FA extract was dissolved by 2 mL of methanol. All of the experiments were conducted in three replicates.

**RP-HPLC Analysis of FA.** The FA extract was identified and quantified in triplicate by RP-HPLC (Agilent Technologies, Palo Alto, CA, USA) with UV-diode array absorption. The samples were eluted using a Lichrosphere C-18 (2.1 × 250 mm) column at 30 °C. The mobile phase was 70:30 (v/v) acetonitrile/water with 0.05% trifluoroacetic acid (TFA). The flow rate was 0.8 mL/min, and the detection wavelength was 320 nm. The concentration of FA standard (HPLC ≥ 98%; supplied by Shanghai Yuanye Biotechnology Co., Ltd., Shanghai, China) was 1 mg/mL, and the injection volume was 1  $\mu$ L. All solvents were of HPLC grade and filtered through a 0.45  $\mu$ m membrane. The FA content of samples was calculated from the peak area.<sup>35</sup>

**Determination of  $T_2$  Relaxation Time by NMR.** The relaxation measurements were performed on a Niumag Desktop Pulsed NMR Analyzer (Shanghai Niumag Electronics Technology Co. Ltd.) with a magnetic field strength of 0.54 T and a corresponding resonance frequency for protons of 23.01 MHz. The NMR instrument was equipped with a 60 mm probe. Transverse relaxation ( $T_2$ ) was measured using the Carr–Purcell–Meiboom–Gill (CPMG) pulse sequence, with a  $\tau$  value (time between the 90° and 180° pulses) of 75  $\mu$ s. Data from 2000 echoes were acquired as eight-scanned repetitions. The repetition time between two successive scans was 2 s. All relaxation measurements were performed at 25 °C. The  $T_2$  relaxation time was analyzed by the distributed exponential fitting analysis using the Multi Exp Inv Analysis Software developed by Niumag Co., Ltd., China. A continuous exponentials distribution of the CPMG experiment was defined by eq 2

$$g_i = \int_0^{\infty} A(T) e^{-\tau_i/T} dT \quad (2)$$

where  $g_i$  is the intensity of the decay at time  $\tau_i$  and  $A(T)$  is the amplitude of the component with transverse relaxation time  $T$ .

Equation 2 was solved using Multi Exp Inv Analysis software by minimizing the function 3

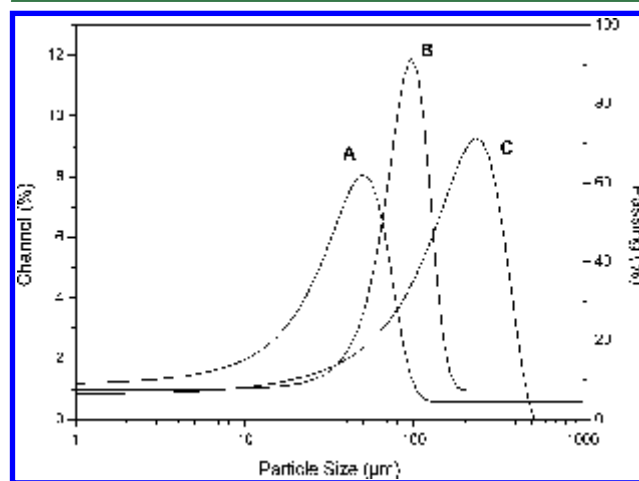
$$\left( g_i - \int_{x=1}^m f_x e^{-\tau_i/T_x} dT \right)^2 + \lambda \sum_{x=1}^m f_x^2 \quad (3)$$

In formula 3,  $\lambda$  is the weighting and  $\lambda \sum_{x=1}^m f_x^2$  is a linear combination of functions added to the equation to perform a zero-order regularization.<sup>36</sup> The data were pruned from 2000 to 200 points using sampling pruning. This analysis resulted in a plot of relaxation amplitude for individual relaxation processes versus relaxation time. The time constant for each peak was calculated from the peak position, and the corresponding water contents were determined by cumulative integration. All calculations were measured using an in-house program written in combination of Matlab (Mathworks Inc., Natick, MA, USA) and Delphi (Borland, USA).

Three grams of bread dough prepared as described under Breadmaking was taken and placed into a test tube immediately after mixing. The water migration between AX gels and gluten in WWD systems with different particle size flours was observed using the NMR system that is represented by spin–spin relaxation times ( $T_2$ ).

## RESULTS AND DISCUSSION

**Effects of WWF Granulation on Bread Volume and Specific Volume.** Generally, flour particle size that was measured by the laser particle size analyzer was a multippeak distribution. To obtain the average particle size of flour, the normal multippeak data were further processed with Origin software to fit a Gaussian distribution curve. The average particle sizes of the flour were the peak values of the fitted curves (Figure 1). The average particle sizes of three types of



**Figure 1.** Fitted particle size distribution curves of whole wheat flour (WWF): (A) WWF with an average particle size of 50.21  $\mu$ m, which was superfine ground by the ultramicro pulverizer for 15 min; (B) superfine ground for 25 min, average particle size of 96.99  $\mu$ m; (C) superfine ground for 35 min, average particle size of 235.40  $\mu$ m. The average particle size of the control flour (commercial flour) was 91.20  $\mu$ m.

WWF from the milling experiment were 50.21  $\mu$ m (A), 96.99  $\mu$ m (B), and 235.40  $\mu$ m (C), respectively. The average particle size of commercial bread flour (control) was 91.20  $\mu$ m.

In the baking experiment, the effect of WWF of different particle sizes on baking quality was investigated. The results showed that the volume and specific volume of bread from WWF were lower than those of the white bread (Table 1). In addition, the WWB made from a medium particle size (96.99

$\mu\text{m}$ ) WWF had larger volume and specific volume than those of the coarse (235.40  $\mu\text{m}$ ) or refined groups (50.21  $\mu\text{m}$ ).

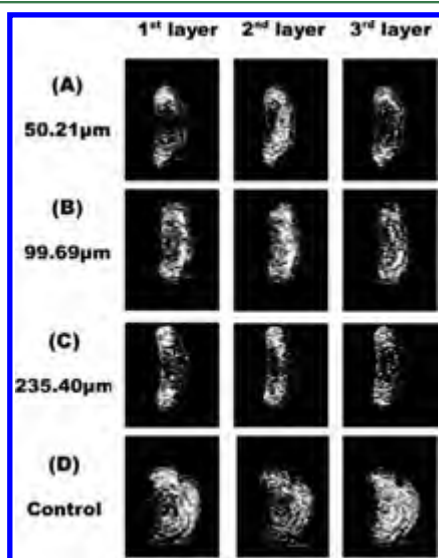
**Table 1. Volume and Specific Volume of Whole Wheat Bread Baked from Whole Wheat Flour of Different Particle Sizes<sup>a</sup>**

particle size ( $\mu\text{m}$ )	volume ( $\text{cm}^3$ )	weight (g)	specific volume ( $\text{cm}^3/\text{g}$ )
control <sup>b</sup>	311.7 $\pm$ 16.1 a	61.2 $\pm$ 1.8 a	5.1 $\pm$ 0.2 a
50.21	193.3 $\pm$ 7.6 c	57.1 $\pm$ 0.8 c	3.4 $\pm$ 0.2 c
96.99	250.0 $\pm$ 13.2 b	59.2 $\pm$ 0.6 b	4.2 $\pm$ 0.2 b
235.40	223.3 $\pm$ 5.8 b	59.7 $\pm$ 2.0 b	3.7 $\pm$ 0.1 b

<sup>a</sup>Data are the mean value  $\pm$  standard deviation. Values in the same column with the same letters are not significantly different ( $P < 0.05$ ).

<sup>b</sup>The control groups were made with commercial white flour. The average particle size of the control flour was 91.20  $\mu\text{m}$ .

**Effect of WWF Granulation on the Porosity of WWB.** Three-layer scanned images (Figure 2) of WWB cross sections



**Figure 2.** Weighted density of proton images scanned for three layers by the MRI system and processed using the threshold segmentation method: (A, B, C, D) scanned images of longitudinal sections of bread baked from whole wheat flour of particle sizes of 50.21, 96.99, 235.40, and 91.20  $\mu\text{m}$  (control), respectively. The bright area of the scanned images is gas cells, and the dark part represents the bread skeleton.

were examined by the MRI system. The breads were baked from WWF of particle sizes of 50.21  $\mu\text{m}$  (Figure 2A), 96.99  $\mu\text{m}$  (Figure 2B), 235.40  $\mu\text{m}$  (Figure 2C), and the control group (made from the commercial white flour) (Figure 2D), respectively. The bright areas of the images were gas cells, whereas the dark parts were bread skeleton. The greatest number and best distribution of gas cells were observed in the control group (Figure 2D) due to noninterference of wheat bran in the structure of the gluten network. Figure 2B shows more gas cells and better gas cell distribution than Figure 2A,C, especially on the second scanned layer, but slightly fewer than the control group. Although the differences of bright area between panels A and C of Figure 2 were not significant, the distribution of gas cells can still be observed. Also, the calculation of porosity can give secondary proof of the differences more precisely. The porosity (Table 2) calculated

by the twice-threshold segmentation method also showed a similar trend. The breads made with WWF of particle size of 96.99  $\mu\text{m}$  had a better crumb structure and baking performance than the other two WWF with larger or smaller bran particle sizes, but was second to the control group. The large particle wheat bran in WWF (235.40  $\mu\text{m}$ ) caused shearing and diluted the gluten matrix, inhibiting the formation of the gluten network and the structure and integrity of gas cells, which led to reduced gas retention by gluten protein membrane.<sup>37</sup> Thus, an uneven distribution of gas cells was formed during the releasing process of  $\text{CO}_2$  gas in the early stage of baking. Small particles of wheat bran had a less destructive effect on the formation of the gluten network. However, Figure 2C also shows that the WWB with the smallest bran particle size had less porosity than the medium bran size group. To explain this phenomenon, we tentatively proposed that the dispersion of certain active compounds increased with the refinement of WWF particle size, especially the FA (a component of the AX gels), which has the ability to strengthen the AX gels.<sup>38</sup> Due to the better water sequestering capability of the AX gels than of the gluten matrix, the AX gels competed for water with the gluten network in WWD.<sup>20</sup> Thus, the formation of gluten was inhibited, because sufficient water for adequate protein hydration is a prerequisite for the development of gluten network. The quality of the gluten network determines the baking performance, so the fine particle size WWF (50.21  $\mu\text{m}$ ) led to less porosity than the medium particle size groups.

The competitive water sequestering between the AX gels and gluten network in the dough system was confirmed by the measurement of  $T_2$  relaxation time using the MRI technique as detailed under Determination of  $T_2$  Relaxation Time by NMR.

#### Effect of WWF Granulation on the Gluten Network.

Wheat bran can dilute and disrupt the gluten network, impair gas retention and bread texture and appearance,<sup>7</sup> and decrease the degree of softening and loaf volume.<sup>39</sup> Figure 3 shows various effects on the gluten network by wheat bran of various particle sizes: 50.21  $\mu\text{m}$  (A), 96.99  $\mu\text{m}$  (B), 235.40  $\mu\text{m}$  (C), and 91.20  $\mu\text{m}$  (control, D), respectively. In Figure 3A, a continuous and compact gluten network was observed resulting from the small particle size of the wheat bran. The continuous gluten matrix provided the precondition for superior baking quality, but an excessively compact gluten matrix was detrimental in obtaining good loaf volume.<sup>40</sup> In Figure 3B, the particle size of the bran was increased (indicated by the arrow), the shearing effect on the gluten matrix was increased, and the gas retention ability was weakened. In Figure 3C, the large particle size of wheat bran (indicated by the arrow) was present in the dough system; it sheared the gluten matrix significantly. The internal structure of the gluten network was fractured, discontinuous, and full of "clutter holes". During the fermentation and proofing stages of the baking process, the gas cells expand into an open network of pores.<sup>41</sup> The fragmented gluten network was unable to retain the  $\text{CO}_2$  gas, and the gas was released in the early stages of breadmaking,<sup>42</sup> leading to small bread volume and inferior baking results.

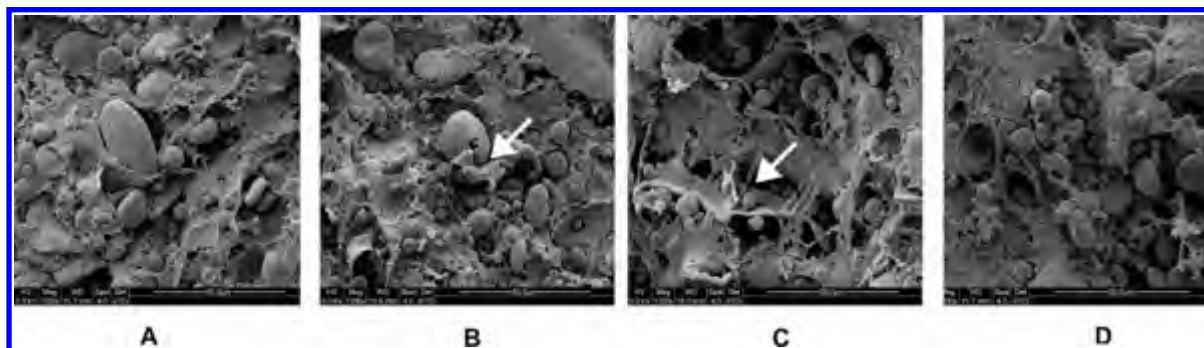
**Effect of WWF Granulation on the Secondary Structures of Gluten Protein.** Seyer and Gelinas proposed that the deleterious effect on the gluten matrix of large wheat bran particles could be attributed to the breakage of secondary structure of gluten macropolymer during dough kneading.<sup>43</sup> To confirm this hypothesis, the dough system was investigated by FT-IR. The secondary structures of gluten protein (Table 3) are the  $\alpha$ -helix,  $\beta$ -sheet,  $\beta$ -turn, random coil, and  $\beta$ -antiparallel.



**Table 2. Calculation of the Porosity of Whole Wheat Bread Cross Section, Scanned by Magnetic Resonance Imaging, Processed Using the Threshold Segmentation Method<sup>a</sup>**

particle size ( $\mu\text{m}$ )	scanned layers	threshold value 1	$N_1$	threshold value 2	$N_2$	porosity <sup>b</sup> (%)
control (91.20)	1	30	134290	5	58218	37.74 $\pm$ 5.25
	2	40	128756	5	64332	
	3	40	128096	5	48364	
50.21	1	50	208517	10	37163	33.35 $\pm$ 9.32
	2	40	217024	10	56776	
	3	40	211807	10	36215	
96.99	1	50	123669	5	88162	38.21 $\pm$ 9.22
	2	50	136608	5	60010	
	3	50	125912	5	94685	
235.40	1	80	154704	80	43971	29.96 $\pm$ 5.08
	2	70	149476	50	39200	
	3	80	148623	80	32288	

<sup>a</sup>The pixels of twice threshold segmentation are represented by  $N_1$  and  $N_2$ . Each bread sample was scanned for three layers. <sup>b</sup>Data are the mean value  $\pm$  standard deviation.


**Figure 3.** SEM images of whole wheat dough prepared with flour particle sizes of 50.21  $\mu\text{m}$  (A), 96.99  $\mu\text{m}$  (B), 235.40  $\mu\text{m}$  (C), and 91.20  $\mu\text{m}$  (control) (D), respectively. The arrows point to the wheat bran particles.

**Table 3. Content of Secondary Structure ( $\alpha$ -Helix,  $\beta$ -Sheet,  $\beta$ -Turn, Random Coil, and  $\beta$ -Antiparallel)<sup>a</sup> of Gluten Protein in Whole Wheat Dough Prepared with Flour of Different Particle Sizes**

flour particle size:	peak frequency ( $\text{cm}^{-1}$ )			percentage <sup>b</sup> (%)		
	50.21 $\mu\text{m}$	96.99 $\mu\text{m}$	235.40 $\mu\text{m}$	50.21 $\mu\text{m}$	96.99 $\mu\text{m}$	235.40 $\mu\text{m}$
$\alpha$ -helix	1655.8	1656.7	1657	26.74 $\pm$ 2.75	26.60 $\pm$ 2.03	24.08 $\pm$ 1.21
$\beta$ -sheet	1617.2/1632	1617/1631.7	1617.1/1630.2	23.60 $\pm$ 2.66	23.18 $\pm$ 1.92	21.32 $\pm$ 1.07
$\beta$ -turn	1668.9	1669.5	1668.2	19.21 $\pm$ 1.37	18.70 $\pm$ 1.46	17.19 $\pm$ 0.86
random coil	1644.5	1644.7	1648.6	20.10 $\pm$ 1.40	21.41 $\pm$ 2.05	28.14 $\pm$ 1.15
$\beta$ -antiparallel	1681.5	1682	1681	10.35 $\pm$ 0.79	10.11 $\pm$ 0.89	9.27 $\pm$ 0.54

<sup>a</sup>The content of secondary structure of gluten protein was determined by FT-IR, represented by the percentage of peak area calculated from the fitted infrared spectrum. <sup>b</sup>Mean  $\pm$  standard deviation (three replications).

**Table 4. Content of Ferulic Acid Determined by RP-HPLC in Whole Wheat Flour of Different Particle Sizes**

	particle size <sup>a</sup>			standard sample
	50.21 $\mu\text{m}$	96.99 $\mu\text{m}$	235.40 $\mu\text{m}$	
peak area	6691.6 $\pm$ 6.4	2870.0 $\pm$ 5.7	1816.7 $\pm$ 4.4	7293.8 $\pm$ 0.5
FA content (mg/mL)	0.9200 $\pm$ 0.0010	0.3900 $\pm$ 0.0008	0.2500 $\pm$ 0.0006	1.00

<sup>a</sup>Mean  $\pm$  standard deviation (three replications).

The content of  $\alpha$ -helix,  $\beta$ -sheet,  $\beta$ -turn, and  $\beta$ -antiparallel increased with the refinement of bran (reduction in particle size) contained in the WWF, while the content of random coil showed the opposite trend. Textural properties of gluten protein are mainly determined by the amount and balance of

weak and strong physical linkages, hydrogen bond, hydrophobic interactions, electrostatic forces, covalent bonds, and disulfide bonds in dough system.<sup>44</sup> The secondary structures of gluten protein play an important role in forming the gluten network structure. Hydrogen bonds can be broken easily by

Table 5.  $T_2$  Relaxation Time Distribution of Whole Wheat Dough of Different Flour Particle Sizes

	particle size								
	50.21 $\mu\text{m}$			96.99 $\mu\text{m}$			235.40 $\mu\text{m}$		
	$T_{21}$	$T_{22}$	$T_{23}$	$T_{21}$	$T_{22}$	$T_{23}$	$T_{21}$	$T_{22}$	$T_{23}$
percentage	0.0891	0.9042	0.0071	0.0563	0.9180	0.0123	/ <sup>a</sup>	0.9880	0.0122
SD <sup>b</sup>	0.0011	0.0020	0.0005	0.0008	0.0020	0.0008	/	0.0030	0.0007

<sup>a</sup>/ indicates that no signal was detected. <sup>b</sup>SD, standard deviation.

Table 6.  $T_2$  Relaxation Time Distribution of Whole Wheat Dough with Added Wheat Bran

	bran addition											
	control <sup>a</sup>			20%			40%			60%		
	$T_{21}$	$T_{22}$	$T_{23}$	$T_{21}$	$T_{22}$	$T_{23}$	$T_{21}$	$T_{22}$	$T_{23}$	$T_{21}$	$T_{22}$	$T_{23}$
% <sup>b</sup>	/ <sup>c</sup>	0.9981	0.0020	/	0.9892	0.0111	0.0274	0.9590	0.0143	0.0293	0.9571	0.0142
SD <sup>d</sup>		0.0028	0.0001		0.0030	0.0002	0.0001	0.0022	0.0001	0.0006	0.0025	0.0001

<sup>a</sup>The control groups were made with commercial white flour. <sup>b</sup>Percentage of each peak area in total areas ( $T_{21}$ ,  $T_{22}$ , and  $T_{23}$ ). <sup>c</sup>/ indicates that no signal was detected. <sup>d</sup>SD, standard deviation.

wheat bran during kneading,<sup>19</sup> so the orderly secondary structures of proteins can be split into disordered structures like random coils. The higher content of  $\alpha$ -helix,  $\beta$ -sheet,  $\beta$ -turn and  $\beta$ -antiparallel structures in the refined particle size of WWD, compared to the coarse group, suggested the conformation of gluten structure of refined particle size was more stable.<sup>45</sup> These results indicate that the large particle size of WWF, especially the wheat bran with hard texture, had more severe shearing effect on gluten proteins.

**Effect of WWF Granulation on the Content of Ferulic Acid.** To investigate the mechanism through which WWF of refined particle sizes had a destructive effect on the volume of bread, the content of FA (Table 4) was determined by RP-HPLC. Results showed that with the decreasing particle size of WWF, more FA was released from the wheat bran to participate in oxidative gelation. This can be attributed to the disruption of cells and the increased specific surface area of wheat bran.<sup>37</sup> Considering this theory, we confirmed that the strength of AX gels would increase with reducing particle size of WWF. This observation confirmed the hypothesis of competitive water sequestration between the AX gels and the gluten network, which verified that the bread made with refined particle size WWF had less porosity.

**Demonstration of Water Migration between AX Gels and Gluten by  $T_2$  Relaxation Time.** To confirm that water migration and competitive water sequestration between the AX gels and gluten matrix were the primary causes for the inferior baking quality of WWF, the  $T_2$  relaxation times of WWD with different particle size flours (Table 5) and wheat bran additions (Table 6) were examined by MRI.

The  $T_2$  relaxation time graph includes three peaks:  $T_{21}$  (0–1 ms),  $T_{22}$  (1–100 ms), and  $T_{23}$  (100–1000 ms), which represent bound water, immobilized water, and free water, respectively. The X-axis of the  $T_2$  relaxation time represents the water activity in the food system. A longer  $T_2$  relaxation time indicates a higher degree of water freedom. The Y-axis in the  $T_2$  graph represents the signal amplitude of protons. The peak area of  $T_2$  represents the relative content of hydrogen protons and the water absorption by hydrophilic components. The data (Table 5) show that the proportion of  $T_{21}$  peak area percentage had a negative correlation ( $r = -0.991$ ) with the decrease in particle size of the WWF. A positive correlation ( $r = 0.996$ ) was found between the proportion of  $T_{22}$  peak area percentage and

the average particle size of WWF. There was no change in the peak area proportion of  $T_{23}$ . On the basis of the measurement of  $T_2$  relaxation time from MRI, we inferred that the  $T_{21}$  peak area may represent the amount of water bound by the esterified AX, essentially the cell wall material. The AX gels sequester water and make it unavailable to migrate freely,<sup>46</sup> but there is no effect on water activity (free water). These results implied that the content of FA that participated in an oxidative gelation reaction increased with the decrease in particle size of the WWF. The AX gel strength was reported to have a positive correlation with the content of FA,<sup>35</sup> therefore, as the particle size of the WWF decreases, the AX gels will be strengthened because of increased unesterified FA. In addition, AX gels contain many hydrophilic groups such as hydroxyl groups, which bond with water molecules through hydrogen bonds.<sup>47</sup> Although the porous structure of the gluten network also had strong water absorption ability,<sup>48</sup> the water retention ability of the gluten network is weaker than that of the AX gels, and the AX has much greater water-holding capacity than gluten proteins;<sup>49</sup> therefore, water tends to move from the gluten matrix to AX gels. It was hypothesized that the AX gels sequestered water, limiting the amount of water available to participate in gluten formation in the bread dough,<sup>50</sup> and the amount of AX gel influenced dough stickiness and water retention capacity.<sup>51</sup>

$T_{22}$  may represent the water trapped in the gluten network (immobilized water), which was the major existing form of water.  $T_{23}$  may represent the free water distributed in the matrix between the AX gels and the gluten network in the WWD system. The amount of free water remained constant during the entire water migration process between the AX gels and the gluten network, which indicated that the amount of water lost from the gluten network was similar to the amount of the water obtained by the AX gels. This observation was in agreement with the fact that the AX gels only sequester water and do not affect water activity. This form of free water may be thought of as “water migration channels” between the AX gels and the gluten matrix.

The water sequestration competition mechanism between the AX gels and the gluten matrix, as well as the identification of each peak in the  $T_2$  relaxation time experiment, was confirmed by the study of wheat bran addition (Table 6). The proportion of  $T_{21}$  peak area percentage had a positive

correlation ( $r = 0.888$ ) with the increase in wheat bran addition in white flour dough (Table 6); a negative correlation ( $r = -0.893$ ) was shown in the proportion of  $T_{22}$  peak area percentage. However,  $T_{22}$  and  $T_{23}$  had strong signals in dough systems that contained additional wheat bran. In the control group and the dough with 20% wheat bran added, no  $T_{21}$  peak was detected due to its weak signal. When the addition of wheat bran was increased to 40%,  $T_{21}$  signals were detected.

In conclusion, the water migration from the gluten network to AX gels as determined by the MRI technique confirmed that it was the main cause leading to the inferior baking quality of whole grain bread made with the refined particle size WWF.

## AUTHOR INFORMATION

### Corresponding Author

\*(G.G.H.) E-mail: ghou@wmcinc.org. Phone: +1 (503) 295-0823. Fax: +1 (503) 295-2735. (Z.X.C.) E-mail: zxchen2007@126.com. Phone: +86 510-8587911. Fax: +86 510-85867273.

### Notes

The authors declare no competing financial interest.

## ACKNOWLEDGMENTS

We acknowledge Jin Lenong Agriculture Development Co., Ltd. (Henan Province, China), for providing the wheat sample and technical assistance by the Shanghai Niumag Electronics Technology Co., Ltd. (Shanghai, China).

## ABBREVIATIONS USED

AX, arabinoxylan; WWB, whole wheat bread; WWD, whole wheat dough; WWF, whole wheat flour; MRI, magnetic resonance imaging; FA, ferulic acid; AU, absorbance units; RP-HPLC, reversed-phase high-performance liquid chromatography; SEM, scanning electron microscope; FT-IR, Fourier transform infrared spectroscopy.

## REFERENCES

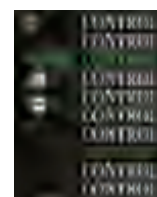
- Rosell, C. M.; Victor, R. P.; Ronald Ross, W.; Vinood, B. P. The science of doughs and bread quality. In *Flour and Breads and their Fortification in Health and Disease Prevention*; Academic Press: San Diego, CA, 2011; pp 3–14.
- Liu, R. H.; Okarter, N. Health benefits of whole grain phytochemicals. *Crit. Rev. Food Sci. Nutr.* **2010**, *50*, 193–208.
- Vitaglione, P.; Napolitano, A.; Fogliano, V. Cereal dietary fibre: a natural functional ingredient to deliver phenolic compounds into the gut. *Trends Food Sci Technol.* **2008**, *19*, 451–463.
- Schatzkin, A.; Park, Y.; Leitzmann, M. F.; Hollenbeck, A. R.; Cross, A. J. Prospective study of dietary fiber, whole grain foods, and small intestinal cancer. *Gastroenterology* **2008**, *135*, 1163–1167.
- Liu, R. H. Whole grain phytochemicals and health. *J. Cereal Sci.* **2007**, *46*, 207–219.
- Gelinas, P.; McKinnon, C. A finer screening of wheat cultivars based on comparison of the baking potential of whole-grain flour and white flour. *Int. J. Food Sci. Technol.* **2011**, *46*, 1137–1148.
- Jacobs, M. S.; Izydorczyk, M. S.; Preston, K. R.; Dexter, J. E. Evaluation of baking procedures for incorporation of barley roller milling fractions containing high levels of dietary fibre into bread. *J. Sci. Food Agric.* **2008**, *88*, 558–568.
- Yu, L.; Slavin, M. All natural whole-wheat functional foods for health promotion and disease prevention. In *Functional Food and Health. ACS Symp. Series* **2008**, No. 993, 125–142.
- Moore, Z. Wheat bran particle size effects on bread baking performance and quality. *J. Sci. Food Agric.* **1999**, *79*, 805–809.
- Salmenkallio-Marttila, M.; Katina, K.; Autio, K. Effects of bran fermentation on quality and microstructure of high-fiber wheat bread. *Cereal Chem.* **2001**, *78*, 429–435.
- Gan, Z.; Ellis, P. R.; Vaughan, J. G.; Galliard, T. Some effects of non-endosperm components of wheat and of added gluten on wholemeal bread microstructure. *J. Cereal Sci.* **1989**, *10*, 81–91.
- Moore, J. S. Shape-persistent molecular architectures of nanoscale dimension. *Acc. Chem. Res.* **1997**, *30*, 402–413.
- Gan, Z.; Galliard, T.; Ellis, P. R.; Angold, R. E.; Vaughan, J. G. Effect of the outer bran layers on the loaf volume of wheat bread. *J. Cereal Sci.* **1992**, *15*, 151–163.
- Moder, K. F.; Bruinsma, B. L.; Ponte, J. G. Bread-making potential of straight-grade and whole-wheat flours of Triumph and Eagle-Plainsman V hard red winter wheats. *Cereal Chem.* **1984**, *61*, 269–273.
- Piber, M.; Koehler, P. Identification of dehydroferulic acid-tyrosine in rye and wheat: evidence for a covalent cross-link between arabinoxylans and proteins. *J. Agric. Food Chem.* **2005**, *53*, 5276–5284.
- Fausch, H.; Kundig, W.; Neukom, H. Ferulic acid as a component of a glycoprotein from wheat flour. *Nature* **1963**, *199*, 287–287.
- Markwalder, H. U.; Neukom, H. Diferulic acid as a possible crosslink in hemicelluloses from wheat germ. *Phytochemistry* **1976**, *15*, 836–837.
- Wang, M. W.; Hamer, R. J.; Van Vliet, T.; Oudgenoeg, G. Interaction of water extractable pentosans with gluten protein: effect on dough properties and gluten quality. *J. Cereal Sci.* **2002**, *36*, 25–37.
- Autio, K. Effects of cell wall components on the functionality of wheat gluten. *Biotechnol. Adv.* **2006**, *24*, 633–635.
- Labat, E.; Rouau, X.; Morel, M. H. Effect of flour water-extractable pentosans on molecular associations in gluten during mixing. *Lebensm.-Wiss. -Technol. (Food Sci. Technol.)* **2002**, *35*, 185–189.
- Gill, S.; Vasanthan, T.; Ooraikul, B.; Rossnagel, B. Wheat bread quality as influenced by the substitution of waxy and regular barley flours in their native and extruded forms. *J. Cereal Sci.* **2002**, *36*, 219–237.
- Roman-Gutierrez, A. D.; Guilbert, S.; Cuq, B. Distribution of water between wheat flour components: a dynamic water vapour adsorption study. *J. Cereal Sci.* **2002**, *36*, 347–355.
- Stapley, A. G. F.; Hyde, T. M.; Gladden, L. F.; Fryer, P. J. NMR imaging of the wheat grain cooking process. *Int. J. Food Sci. Technol.* **1997**, *32*, 355–375.
- Hwang, S. S.; Cheng, Y. C.; Chang, C.; Lur, H. S.; Lin, T. T. Magnetic resonance imaging and analyses of tempering processes in rice kernels. *J. Cereal Sci.* **2009**, *50*, 36–42.
- Horigane, A. K.; Takahashi, H.; Maruyama, S.; Ohtsubo, K. i.; Yoshida, M. Water penetration into rice grains during soaking observed by gradient echo magnetic resonance imaging. *J. Cereal Sci.* **2006**, *44*, 307–316.
- Ghosh, P. K.; Jayas, D. S.; Gruwel, M. L. H.; White, N. D. G. A magnetic resonance imaging study of wheat drying kinetics. *Biosyst. Eng.* **2007**, *97*, 189–199.
- Shigehiro, N. I.; Hiroyuki, T.; Mika, K.; Hiromi, K. Routine evaluation of the grain structures of baked breads by MRI. *Food Sci. Technol. Res.* **2003**, *9*, 155–161.
- Sapirstein, H. D.; Roller, R.; Bushuk, W. Instrumental measurement of bread crumb grain by digital image analysis. *Cereal Chem.* **1994**, *71*, 383–391.
- Takano, H.; Ishida, N.; Koizumi, M.; Kano, H. Imaging of the fermentation process of bread dough and the grain structure of baked breads by magnetic resonance imaging. *J. Food Sci.* **2002**, *67*, 244–250.
- Naito, S.; Ishida, N.; Takano, H.; Koizumi, M.; Kano, H. Routine evaluation of the grain structures of baked breads by MRI. *Food Sci. Technol. Res.* **2003**, *9*, 155–161.
- Lodi, A.; Abduljalil, A. M.; Vodovotz, Y. Characterization of water distribution in bread during storage using magnetic resonance imaging. *Magn. Reson. Imaging* **2007**, *25*, 1449–1458.
- Ishida, N.; Takano, H.; Naito, S.; Isobe, S.; Uemura, K.; Haishi, T.; Kosse, K.; Koizumi, M.; Kano, H. Architecture of baked breads depicted by a magnetic resonance imaging. *Magn. Reson. Imaging* **2001**, *19*, 867–874.

- (33) Brescia, M. A.; Sacco, D.; Sgaramella, A.; Pasqualone, A.; Simeone, R.; Peri, G.; Sacco, A. Characterisation of different typical Italian breads by means of traditional, spectroscopic and image analyses. *Food Chem.* **2007**, *104*, 429–438.
- (34) Wellner, N.; Mills, C.; Brownsey, G.; Wilson, R. H.; Brown, N.; Freeman, J.; Halford, N. G.; Shewry, P. R.; Belton, P. S. Changes in protein secondary structure during gluten deformation studied by dynamic Fourier transform infrared spectroscopy. *Biomacromolecules* **2005**, *6*, 255–261.
- (35) Wang, M. W.; Oudgenoeg, G.; van Vliet, T.; Hamer, R. J. Interaction of water unextractable solids with gluten protein: effect on dough properties and gluten quality. *J. Cereal Sci.* **2003**, *38*, 95–104.
- (36) Teukolsky, S. A.; Vetterling, W. T.; Flannery, B. P. Modeling of data. In *Numerical Recipes in C: The Art of Scientific Computing*, 2nd ed.; Cambridge University Press: New York, 1992; Vol. 2, pp 656–706.
- (37) Noort, M. W. J.; van Haaster, D.; Hemery, Y.; Schols, H. A.; Hamer, R. J. The effect of particle size of wheat bran fractions on bread quality – evidence for fibre-protein interactions. *J. Cereal Sci.* **2010**, *52*, 59–64.
- (38) Cura, D. E.; Lantto, R.; Lille, M.; Andberg, M.; Kruus, K.; Buchert, J. Laccase-aided protein modification: effects on the structural properties of acidified sodium caseinate gels. *Int. Dairy J.* **2009**, *19*, 737–745.
- (39) Stojceska, V.; Ainsworth, P. The effect of different enzymes on the quality of high-fibre enriched brewer's spent grain breads. *Food Chem.* **2008**, *110*, 865–872.
- (40) Gan, Z.; Angold, R. E.; Williams, M. R.; Ellis, P. R.; Vaughan, J. G.; Galliard, T. The microstructure and gas retention of bread dough. *J. Cereal Sci.* **1990**, *12*, 15–24.
- (41) Salmenkallio-Marttila, M.; Autio, K. Light microscopic investigations of cereal grains, doughs and breads. *Lebensm.-Wiss.-Technol. (Food Sci. Technol.)* **2001**, *34*, 18–22.
- (42) Campbell, G. M.; Herrero-Sanchez, R.; Payo-Rodriguez, R.; Merchan, M. L. Measurement of dynamic dough density and effect of surfactants and flour type on aeration during mixing and gas retention during proofing. *Cereal Chem.* **2001**, *78*, 272–277.
- (43) Seyer, M.-E.; Gélinas, P. Bran characteristics and wheat performance in whole wheat bread. *Int. J. Food Sci. Technol.* **2009**, *44*, 688–693.
- (44) Selinheimo, E.; Autio, K.; Krijus, K.; Buchert, J. Elucidating the mechanism of laccase and tyrosinase in wheat bread making. *J. Agric. Food Chem.* **2007**, *55*, 6357–6365.
- (45) Shewry, P. R.; Popineau, Y.; Lafiandra, D.; Belton, P. Wheat glutenin subunits and dough elasticity: findings of the EUROWHEAT project. *Trends Food Sci. Technol.* **2001**, *11*, 433–441.
- (46) Elizabeth, C. M. Arabinoxylan gels: impact of the feruloylation degree on their structure and properties. *Biomacromolecules* **2005**, *6*, 309–317.
- (47) Izydorczyk, M. S.; Biliaderis, C. G. Cereal arabinoxylans: advances in structure and physicochemical properties. *Carbohydr. Polym.* **1995**, *28*, 33–48.
- (48) Izydorczyk, M. S.; Chornick, T. L.; Paulley, F. G.; Edwards, N. M.; Dexter, J. E. Physicochemical properties of hull-less barley fibre-rich fractions varying in particle size and their potential as functional ingredients in two-layer flat bread. *Food Chem.* **2008**, *108*, 561–570.
- (49) Kweon, M.; Slade, L.; Levine, H. Solvent retention capacity (SRC) testing of wheat flour: principles and value in predicting flour functionality in different wheat-based food processes and in wheat breeding—a review. *Cereal Chem.* **2011**, *88*, 537–552.
- (50) Day, L.; Augustin, M. A.; Batey, I. L.; Wrigley, C. W. Wheat-gluten uses and industry needs. *Trends Food Sci. Technol.* **2006**, *17*, 82–90.
- (51) Bettge, A. D.; Morris, C. F. Oxidative gelation measurement and influence on soft wheat batter viscosity and end-use quality. *Cereal Chem.* **2007**, *84*, 237–242.



Contents lists available at SciVerse ScienceDirect

## Food Control

journal homepage: [www.elsevier.com/locate/foodcont](http://www.elsevier.com/locate/foodcont)

## Rapid detection of *Cronobacter sakazakii* in dairy food by biofunctionalized magnetic nanoparticle based on nuclear magnetic resonance



Yu Zhao<sup>a,b,\*</sup>, Yuting Yao<sup>a</sup>, Ming Xiao<sup>a,b</sup>, Yan Chen<sup>a</sup>, Charles C.C. Lee<sup>c</sup>, Li Zhang<sup>d</sup>, Kelvin Xi Zhang<sup>e</sup>, Shiping Yang<sup>a</sup>, Ming Gu<sup>f</sup>

<sup>a</sup> Department of Life and Environment Science College, Shanghai Normal University, 100 Guilin Road, Shanghai 200234, People's Republic of China

<sup>b</sup> Development Center of Plant Germplasm Resources, 100 Guilin Road, Shanghai 200234, People's Republic of China

<sup>c</sup> School of Environmental and Life Sciences, University of Newcastle, Singapore 169567, Singapore

<sup>d</sup> Howard Hughes Medical Institute, Department of Pathology and Laboratory Medicine, David Geffen School of Medicine, University of California, Los Angeles, 675 Charles E. Young Drive South, Los Angeles, CA 90095, USA

<sup>e</sup> Howard Hughes Medical Institute, Department of Biological Chemistry, David Geffen School of Medicine, University of California, Los Angeles, 675 Charles E. Young Drive South, Los Angeles, CA 90095, USA

<sup>f</sup> Shanghai Entry-Exit Inspection and Quarantine Bureau of the People's Republic of China, 1208, Mingsheng Road, Shanghai 200135, People's Republic of China

## ARTICLE INFO

## Article history:

Received 15 September 2012

Received in revised form

3 May 2013

Accepted 6 May 2013

## Keywords:

Immunoassay

Magnetic nanoparticles

*Cronobacter sakazakii*

Magnetic relaxation

## ABSTRACT

In order to ensure the safety of infant formula powder in China, a rapid and sensitive detection method for food-borne bacteria is urgently needed. We have developed a reliable immunoassay based on nuclear magnetic resonance for the specific detection of *Enterobacter sakazakii* in dairy samples with bio-functionalized magnetic nanoparticles. This method is able to detect *Cronobacter sakazakii* in milk powder and cheese samples at 1.1 to 11 MPN using the most-probable-number (MPN) assay, within an incubation period of less than 2 h. Longer incubation time (>4 h) or higher pH (>7) will decrease the sensitivity of this method. This method does not fit for the detection of bacteria at higher concentrations (>1100 MPN). This method has great potential to become a useful tool for the rapid detection of bacterial contaminations in food, environmental and agricultural samples.

© 2013 Elsevier Ltd. All rights reserved.

## 1. Introduction

*Cronobacter sakazakii*, which was formerly known as “yellow-pigmented *Enterobacter cloacae*”, is a motile, peritrichous, Gram-negative food-borne pathogen. Since its first report in 1958, this bacteria has been shown to be responsible for severe necrotizing enterocolitis (Klostranec & Chan) (NEC), bacteraemia and meningitis, with case fatality rates ranging between 40 and 80% as reported (Bowen & Braden, 2006; Friedemann, 2009; Yan et al., 2012). This bacteria has also been reported to associate with life-threatening infections in low-birth-weight babies (Farmer Iii, Asbury, Hickman, & Brenner, 1980). Traditional methods for the identification and quantification of *C. sakazakii* generally require

multiple steps of enrichment and biological tests, which can take as many as 6–7 days to finish. In recent years, a number of rapid methods have been developed to detect *C. sakazakii* (Almeida et al., 2009; Iversen, Lancashire, Waddington, Forsythe, & Ball, 2006; Liu et al., 2012), such as multiplex polymerase chain reaction (PCR) assay (Chen, Song, Brown, & Lampel, 2010; Hassan et al., 2007), infrared spectroscopy (Lin et al., 2009), fluorescence in situ hybridization (Almeida et al., 2009), DNA microarray (Wang et al., 2009), and sandwich enzyme-linked immunosorbent assay (Park et al., 2012). Although these methods can achieve high specificity and low minimum detection limit for the detection of *C. sakazakii*, they are excessively expensive and complicated to be utilized in industrial settings. Therefore, it is necessary to develop a rapid, sensitive, accurate, and cost-efficient detection assay in the dairy industry.

With the development of nanotechnology, superparamagnetic nanoparticles, conjugated with oligonucleotides, small molecules, peptides and antibodies, have been attracting attention because of their inherent magnetic features and potential applications in the

\* Corresponding author. Department of Life and Environment Science College, Shanghai Normal University, 100 Guilin Road, Shanghai 200234, People's Republic of China. Tel.: +86 21 64321033; fax: +86 21 64322933.

E-mail addresses: zhaoyu@shnu.edu.cn, yyt\_334@hotmail.com (Y. Zhao).

medical, environmental and food sciences (Kaittanis, Nath, & Perez, 2008; Merkoci, 2010; Yang et al., 2011). Noticeably, the utilization of these nanoparticles also offers a unique alternative for the detection of bacterial targets to improve detection sensitivity, and reduced preparation time with smaller samples (Esteban-Fernández de Ávila, Pedrero, Campuzano, Escamilla-Gómez, & Pingarrón, 2012; Kim, Josephson, Langer, & Cima, 2007; Perez, Josephson, O'Loughlin, Högemann, & Weissleder, 2002; Perez, Simeone, Saeki, Josephson, & Weissleder, 2003). Mechanistically, this technology is based on nuclear magnetic resonance-based magnetic relaxation switches (MRSw). In the presence of molecular targets with changes in the spin–spin relaxation time of water ( $T_2$ ), magnetic nanoparticles (NPs) are switched from a dispersed state to a clustered state. This switch (MRSw) has been shown to be able to detect nucleic acid and protein targets with high sensitivity (Josephson, Perez, & Weissleder, 2001; Josephson, Tung, Moore, & Weissleder, 1999; Kaittanis, Naser, & Perez, 2007; Kaittanis, Santra, Asati, & Perez, 2012).

The utilization of MRSw biosensor has been explored in a series of practical applications, including the detection of viruses and bacteria. A report on the detection of microcystin-LR in the water of Tai Lake (Jiangsu Province, China) based on the relaxation of magnetic nanoparticles has achieved a detection range of 1–18 ng/g (Ma et al., 2009). Koh and his colleagues demonstrated that the limit value of “projected sensitivity concentration” could be significantly reduced to  $1.4 \times 10^{-4}$  nm when using a high-sensitivity MRSw biosensor to detect the influenza antibodies (Koh, Hong, Weissleder, & Josephson, 2008). Kaittanis and colleagues established immuned magnetic beads probes to identify *Mycobacterium avium* spp. *Paratuberculosis* in milk and blood samples and demonstrated that the detect limit reached as low as 15.5 MPN (Kaittanis et al., 2007). Using cationic-magnetic beads as sensors, *C. sakazakii* can be detected at 1–5 MPN/500 g of infant milk formula in less than 24 h (Mullane et al., 2006).

In this paper, we report a novel method for the rapid detection of *C. sakazakii* in dairy products with high sensitivity. We constructed a *C. sakazakii* specific NMR biosensor by coupling a polyclonal rabbit anti-*C. sakazakii* antibody to superparamagnetic iron oxide nanoparticles. We found that as the number of bacteria increased in the solution, the increased *C. sakazakii* epitopes interacted with more magnetic nanoparticles in the solution, therefore causing substantial changes in the  $T_2$  value. This simple method has yielded high detection sensitivity for *C. sakazakii* and thus can potentially be developed into a rapid detection tool for infectious food-borne bacteria.

## 2. Materials and methods

### 2.1. Reagents

Polyclonal rabbit anti-*C. sakazakii* antibody (6.82 mg/mL) was prepared by Shanghai Youke Biotechnology Co. Limited. 1-[3-(dimethylamino)-propyl]-3-ethylcarbodiimide HCL (EDC·HCL) and N-hydroxy-succinimide (NHS) were purchased from SinopHarm. Nutrient broth medium (Restaino, Frampton, Lionberg, & Becker, 2006) and blood agar were provided from Beijing Land Bridge Technology Co. Ltd. Chemical reagents and salts were supplied by Shanghai Ling Feng Chemical reagent Co. Ltd.

### 2.2. Synthesis of magnetic beads

The synthesis of superparamagnetic nanoparticles ( $\text{Fe}_3\text{O}_4$ ) was implemented by a previously reported method (Ma et al., 2009). Synthesis of  $\text{Fe}(\text{acac})_3$  Precursor: according to literature, Ferrum (a) acetylaceton ate was synthesized. A 20 mL aqueous solution of

$\text{FeCl}_3$  (3.25 g, 20 mmol) was added with 2, 4-pentanedione (12.3 mL, 120 mmol) under magnetic stirring. After 15 min, triethylamine (6.0 mL) was added to the above mixture. Red precipitates were filtered off to give a crude product. The product was recrystallized in a mixture of ethanol and water to yield pure  $\text{Fe}(\text{acac})_3$  crystals. The crystals were dried at 80 °C under vacuum and then stored at a desiccator before use.

Preparation of  $\text{Fe}_3\text{O}_4$  nanoparticles: A slurry of  $\text{Fe}(\text{acac})_3$  (1.06 g) was dissolved in 15 mL oleylamine and 15 mL phenylate in a 100 mL three-neck flask. The mixture solution was heated at 110 °C for 1 h, then was refluxed at 210 °C for 30 min, thereafter was continued to be heated to 300 °C and maintain 1 h. The above steps were all under a nitrogen atmosphere. The resulting mixture was cooled down to room temperature to form a black suspension. After centrifugation at 12,000 rpm for 10 min, the supernatant was removed and a black precipitate was obtained. The resulting black precipitate was washed with ethanol three times to acquire pure  $\text{Fe}_3\text{O}_4$  NPs. Finally, the  $\text{Fe}_3\text{O}_4$  NPs were dried in vacuum at 120 °C before use.

To empower the magnetic beads with broad compatibility to biomacromolecules, formation and functionalization of  $\text{Fe}_3\text{O}_4@SiO_2$  nanocomposite particles steps were carried out. Igepal CO-520 (2.0 g, 4.75 mmol) was dispersed in cyclohexane (35 mL) by sonication until the mixture turned to limpidity. Dry  $\text{Fe}_3\text{O}_4$  NPs (10 mg) were added to the above solution. The resulting mixture was stirred vigorously to disperse the NPs, and ammonium hydroxide (29.4%, 0.35 mL) was added to form a transparent and black solution of reverse microemulsion. TEOS (0.2 mL) and APS (35  $\mu$ L) were added, and the mixture was gently stirred. The reaction was continued for 48 h at room temperature. The resulting  $\text{Fe}_3\text{O}_4@SiO_2-NH_2$  NPs were precipitated by addition of acetone and were collected by centrifugation at 12,000 rpm for 10 min. The collected  $\text{Fe}_3\text{O}_4@SiO_2-NH_2$  NPs were dispersed in ethanol or water and purified by repeating the centrifugation and redispersion process. The size, distribution and morphology of the amino-modified silica-coated  $\text{Fe}_3\text{O}_4$  were characterized by atomic force microscope (AFM).

### 2.3. Coupling the antibodies to the magnetic beads

The amino-modified silica-coated  $\text{Fe}_3\text{O}_4$  was used to conjugate the antibody. According to a previous report (Ma et al., 2009), 1-p-3-ethylcarbodiimide HCL (EDC·HCL) and N-hydroxy-succinimide (NHS) were used to activate the carboxyl of the antibody. In particular, 200 mg EDC·HCL and 250 mg NHS were added into 0.1 mL anti-*C. sakazakii*-antibody (6.82 mg/mL). Then the mixture was diluted into 5 mL PBS (pH 7.4). After incubation at 4 °C overnight, 10 mg amino-modified silica-coated  $\text{Fe}_3\text{O}_4$  was dispersed in 5 mL PBS (pH 7.4). Subsequently, 5 mL activated anti-*C. sakazakii*-antibody was poured into the upper mixture and left to react for 4 h at room temperature. Finally, the products were separated by magnetic separators and washed by PBS (pH 7.4) for three times, then suspended in PBS (pH 7.4) and kept at 0–4 °C.

In order to further estimate the protein immobilization capacity of the functional  $\text{Fe}_3\text{O}_4@SiO_2-NH_2$  NPs, the bovine serum albumin (BSA) was taken as a control sample. A series of known concentrations of BSA were measured with ultraviolet spectrophotometer to get the  $OD_{280}$  values. A standard curve between known concentrations and  $OD_{280}$  values of BSA was obtained. 10 mg functional  $\text{Fe}_3\text{O}_4@SiO_2-NH_2$  NPs were poured into a 5 mL system with BSA of unknown concentration activated by EDC·HCL and NHS. Then, the mixed solutions were left at room temperature for 4 h. The BSA immobilized by the magnetic beads was separated by magnetic separators. The amount of the BSA proteins immobilized by the magnetic beads was determined by measuring the absorption at 280 nm of the initial and the final supernatant.

#### 2.4. Bacterial culture

*C. sakazakii* (ATCC 29544) was used throughout this study for all optimization and sensitivity experiments. In addition, *Escherichia coli* O157 (ATCC 25922), *Shigella flexneri* (ATCC 51081), *Salmonella typhimurium* (ATCC 14028), *Vibrio parahaemolyticus* (ATCC 17802) and *Staphylococcus aureus* (ATCC 12600) were used in competition experiments to determine the specificity of the biofunctionalized nanoparticles. All bacterial strains were cultured in nutrient broth (Restaino, et al. 2006). *V. parahaemolyticus* was cultured in NB containing 3% NaCl. All the bacterium were incubated at  $36 \pm 1$  °C for 18–24 h in an orbital shaker. The number of *C. sakazakii*, *E. coli* O157, *S. flexneri*, *S. typhimurium* and *S. aureus* were determined by aerobic plate count method (GB 4789.2-2010) (National food safety standard Food microbiological examination: *Enterobacter sakazakii*, 2010) with plate count agar (PCA) *V. parahaemolyticus* was cultured on PCA containing 3% NaCl. One sample containing mixed culture broth (1 mL of *C. sakazakii*, *E. coli* O157, *S. flexneri*, *S. typhimurium* and *S. aureus*. at dilution of  $10^6$ ) is named cocktail culture. For safety and controlling the number of bacteria, all the bacterial samples were placed in an autoclave at 100 °C for 20 min after tested. 0.5% formaldehyde was applied to inactivate bacteria in some special tests.

#### 2.5. Counting of bacteria

The number of bacteria was determined by the most-probable-number (MPN) assay, using serial dilutions in Buffer peptone water (BPW). Based on the growth observed at higher dilutions, the MPN of survivors was calculated using a “nine-tube” technique according to China national food safety standard (GB 4789.40-2010) (GB 4789.2-2010). The lowest bacteria concentration detected by MPN is 1.1. And the higher concentrations were confirmed by the same way.

#### 2.6. MR relaxometry measurements

MR relaxometry were performed using an NMI20-Analyst (Shanghai Niumag Corporation, Shanghai, PRC). The instrumental parameters were set as follows: a 0.5 T magnet, point resolution =  $156 \times 156$   $\mu\text{m}$ , section thickness = 0.6 mm, TE = 60 ms, TR = 4000 ms, number of acquisitions = 1. The whole detection procedure is shown in Fig. 1. Self-assemble of the antibody-modified magnetic beads which can serve as magnetic relaxation switches on the surface of a bacterial target inducing large changes in T2. As the number of bacteria increases, the ratio of available nanoparticles that self-assemble on the surface of one bacterium decreases, causing a

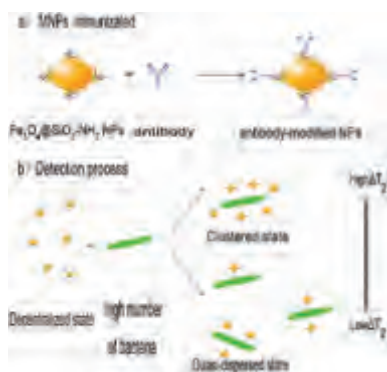


Fig. 1. Schematic illustration of the detection based on the forming of the magnetic aggregates.

quasi-dispersed state and low values of  $\Delta T_2$ . In this procedure, 0.15 mL inactivated target bacterial sample (*C. sakazakii*) (having been properly diluted) and 0.15 mL antibody-modified magnetic bead solution (having been properly diluted) were added into the centrifuge tube and mixed for 30 min. Then 2.7 mL 2% milk (stabilizer) was poured into the mixture and mixed for 30 min. Finally, the matrix was incubated at 37 °C for 1 h and determined by NMR. To investigate the specificity of this method, *E. coli* O157, *S. flexneri*, *S. typhimurium*, *V. parahaemolyticus*, *S. aureus* and mixed bacterial samples were used as contrast strains. The sample that did not contain bacterial sample was set as a blank control.

#### 2.7. Optimization of components ratio

In order to investigate the optimized concentration of magnetic beads, magnetic bead titration experiment was carried out. The density of *C. sakazakii* was fixed at 1.1 MPN and 11 MPN, whereas the bead concentration was varied (0.06 mg/mL, 0.08 mg/mL, 0.10 mg/mL, 0.12 mg/mL, 0.14 mg/mL and 0.16 mg/mL). After the incubation at 37 °C for 1 h, each sample was detected by NMR. The value of  $\Delta T_2$  was determined by 3 averages.

#### 2.8. Optimization of the stabilizers and reaction conditions

To investigate the effect of stabilizer for  $\Delta T_2$  value, four different materials and concentrations, such as 0.05% agar, 2% milk, 0.5% sodium carboxy Methyl Cellulose (CMC) and 0.1% Xanthan, were used as stabilizers in NMR detection. According to the ordinary food pH value, seven different pH gradients (pH 6–9) were set in the experimental systems. Seven different incubation time gradients (15 min–105 min) were also carried out. All the test samples contained 0.15 mL antibody-modified magnetic, 0.15 mL inactivated target bacterial sample and 2.7 mL stabilizer agent. The experiments were carried out in triplicate.

In order to investigate the detection limit of this method, according to the results of optimization experiments, the optimal experiment parameters were adopted, while the concentration of *C. sakazakii* was varied (1.1 MPN, 10 MPN, and 24 MPN, 48 MPN, 110 MPN, 1100 MPN and 11,000 MPN). Each sample was detected by NMR. The value of  $\Delta T_2$  was determined by 3 averages.

#### 2.9. Dairy sample preparation

This procedure was used to determine the presence of *C. sakazakii* in milk powder (Light, Bright Dairy & Food Co., Ltd) and cheese (Light, Bright Dairy & Food Co., Ltd) which were purchased in Shanghai. *C. sakazakii* and two control strains (*S. typhimurium* and *S. aureus*) were cultured overnight in a flask with 100 mL NB broth medium at 37 °C and shaken at 100 rpm. According to the protocol of China national standard of microbiology examination of food hygienic determination (GB 4789.40-2010), the diluted *C. sakazakii* and control strains were separately added into these food samples to obtain microorganism-in-food samples at the concentration level of 110 MPN. Then 100 g mixed samples were separately diluted into 900 mL buffered peptone water (BPW) to prepare the first concentration levels ( $10^{-1}$  g/mL). After that, the liquid sample was also diluted with BPW and two other concentrations were  $10^{-2}$  g/mL and  $10^{-3}$  g/mL. And then antibody-modified magnetic beads and stabilizer were mixed, added to these dairy samples and incubated for 45 min, 2 h, 4 h, 8 h, 22 h and 24 h, respectively. 1.5 mL sample was used for NMR method, and confirmed by streak inoculation on DFI agar (Druggan-Forsythe-Iversen formulation). The complex matrix also test for *C. sakazakii* according to the procedure of GB 4789.40-2010. The  $\Delta T_2$  value was determined by three groups of parallel samples.

### 2.10. Statistical analysis

All the data was statistical by SPSS (Version 11.0.1 for windows. SPSS Inc, 2002).

## 3. Results and discussion

### 3.1. Synthesis and characterization of functionalized magnetic beads

The  $\text{Fe}_3\text{O}_4$  magnetic nanoparticles used in this experiment tend to aggregate into large clusters. According to a previous report (Weissleder et al., 2000), silica-coated magnetic particles were shown to have good dispersibility in organic and aqueous solutions. Therefore, in this study, silica was used to coat the  $\text{Fe}_3\text{O}_4$  magnetic beads to empower the particles with a high dispersibility and broad compatibility to biomacromolecules. The amino-silane-modified  $\text{Fe}_3\text{O}_4$  particles are ideally mono-dispersed and the average diameter of the nanoparticles is about 60 nm (Fig. 2). In addition, the shape and size of the coated nanoparticles are uniform.

To investigate the immobilization ability of magnetic particles to protein molecules, BSA was used as the control sample. We first established a standard curve for a series of known concentrations of BSA and their correlated OD<sub>280</sub> values (Fig. 3). The correlation coefficient of the standard curve is 0.9945. We next measured the OD<sub>280</sub> values in the supernatant before and after immobilization (Fig. 4), and the BSA concentrations in these samples are extrapolated to the standard curve. The difference in the BSA concentrations in the supernatant before and after immobilization would represent BSA immobilized to the beads, and we determined that the immobilization ability of the functional  $\text{Fe}_3\text{O}_4@\text{SiO}_2\text{-NH}_2$  NPs is estimated to be 0.1571 mg/mL.

### 3.2. The properties of NMR method

In this study, we used five other bacteria strains (*E. coli* O157, *S. flexneri*, *S. typhimurium*, *V. parahemolyticus* and *S. aureus*) to test the specificity of our technique. We found that the sample with *C. sakazakii* alone showed the highest change in T<sub>2</sub>, which allows us to differentiate *C. sakazakii* from the samples containing other bacteria strains (Fig. 5). More importantly, the sample contained *C. sakazakii* mixed with other bacteria also showed a substantial change in the T<sub>2</sub> value. These results indicate that the magnetic beads used in this study can detect the bacterial target (*C. sakazakii*) with high specificity, despite of the presence of interference from other microbes.

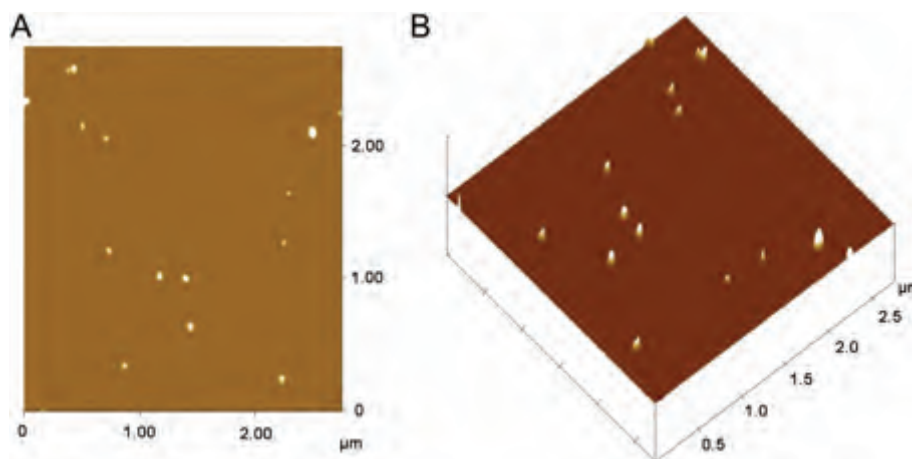


Fig. 2. AFM micrograph of amino-silane-modified  $\text{Fe}_3\text{O}_4$  beads. (A) Planar graph of AFM micrograph. (B) Three-dimension stereo of AFM micrograph.

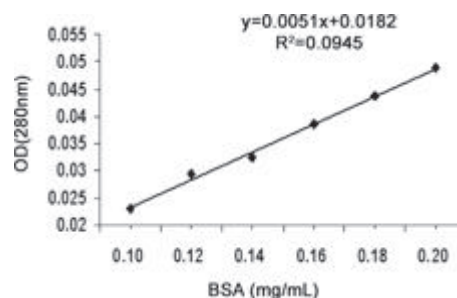


Fig. 3. Standard curve of bovine serum albumin (BSA) density and OD<sub>280</sub>.

To investigate the effects of different concentrations of magnetic beads in the NMR method, we tested eight different concentrations (0.06–0.19 mg/mL). The results revealed that the highest  $\Delta T_2$  value was detected at a magnetic bead concentration of 0.14 mg/mL for both 1.1 and 11 MPN (Fig. 6). However, there is no significant change of  $\Delta T_2$  values when the concentration of magnetic beads increased from 0.08 to 0.18 mg/mL. At the lowest magnetic bead concentration of 0.06 mg/mL, the value of  $\Delta T_2$  is about 60% lower than the average  $\Delta T_2$  value of the other six magnetic concentrations (0.08–0.18 mg/mL). To ensure the optimal performance, the concentration (0.14 mg/mL) of magnetic beads was adopted in the subsequent experiments.

Interestingly, we were able to detect background  $\Delta T_2$  values of 5–12 counts in the background sample consisting of magnetic beads with no bacterial cells or unspecified strains (Fig. 5). This result suggests that we can not rule out the possibility that there are non-specific bindings between magnetic beads. Furthermore, there may also be the cross reactivity between bacterial cells and antibodies on the magnetic beads (Perez et al., 2003). To eliminate the influence of these nonspecific signals, a threshold that  $\Delta T_2$  counts are less than 12 ms was set assuming that the value below the threshold is undetectable. It is worth noting that the  $\Delta T_2$  value of magnetic beads with *Cronobacter mytjensii* was about 14.3 ms, which indicated there was a slight cross reactivity between *C. sakazakii* and other *Cronobacter* strains in this method.

### 3.3. Selection of optimal stabilizer

To optimize the test conditions for this NMR detection method, it is important to improve the dispersion of magnetic beads and magnetic beads–bacterial complex before and after the treatment with the magnetic field. Four different kinds of materials: 0.05%



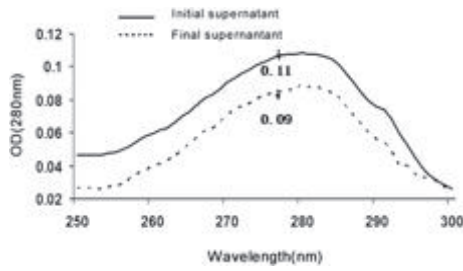


Fig. 4. OD<sub>280</sub> of the initial and the final supernatant of BSA solution.

agar, 2% milk, 0.1% xanthan and 0.5% Sodium carboxy methyl cellulose (CMC), were adopted in this study as stabilizers. We found that regardless of the stabilizer agents used, the  $\Delta T_2$  values decreased while the concentration increased from  $10^0$  to  $10^4$ . (Fig. 7) All the stabilizers showed low  $\Delta T_2$  values at a bacterial concentration of 1.1 MPN: 65 ms for 2% milk, 45 ms for 0.05% agar, 58 ms for 0.1% xanthan and 46 ms in 0.5% CMC. However, increasing the bacteria concentrations from 1.1 to 1100 MPN resulted in a dramatic  $\Delta T_2$  change from 20 to 55 ms, therefore demonstrating a significant influence of the stabilizers on NMR detection. The incubation time required to reach minimum detection limit for each stabilizer tested varies. Low fat (2%) milk required the least amount of incubation time (45 min), while the 0.1% xanthan and 0.5% CMC required overnight incubation; 0.05% Agar required 2 h incubation. Thus, low fat (2%) milk was adopted as the preferred stabilizer agent by considering the detection limit, range and preparation time.

#### 3.4. Reaction conditions (pH and incubation period)

In this study, two important reaction conditions (pH and incubation time) affecting  $\Delta T_2$  values were studied. In terms of the effects of pH (6–9) on  $\Delta T_2$  values, we found that the highest  $\Delta T_2$  value was detected at pH 6.5. However,  $\Delta T_2$  values sharply decreased from 90 ms to 2 ms as pH increased from 6.5 to 9.0 (Fig. 8a).

We also investigated the effects of the incubation period on  $\Delta T_2$  (Fig. 8b). During the first 30 min (15–45 min), the  $\Delta T_2$  value

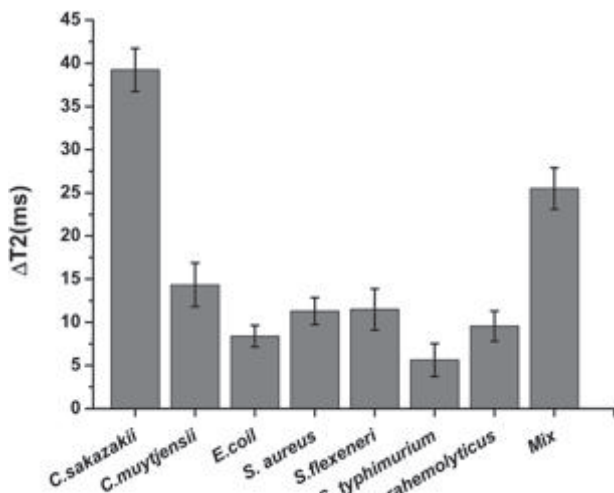


Fig. 5. Specificity of the detection method using *C. sakazakii* and five control strains. Error bars =  $\pm$ SD ( $n = 3$ ).

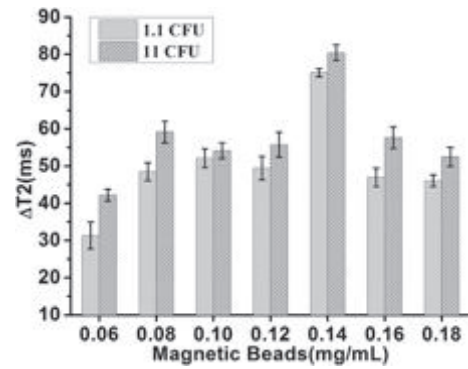


Fig. 6. The concentration of *C. sakazakii* was fixed at 1.1 and 11 MPN. Error bars =  $\pm$ SD ( $n = 3$ ).

increased from 40 to 50 ms. We believe that this phenomenon reflects the stronger binding capacity and hybridization of the magnetic bead–bacterium complex. However, after the  $\Delta T_2$  value reached a peak of 50 ms, the value rapidly decreased from 50 to 20 with an extended incubation period of 45–90 min. It appears that with the binary fission of the tagged bacteria, the size of the nanoparticle–bacterium complex becomes smaller which could therefore decrease the  $\Delta T_2$  value. Interestingly, during the last 15 min of this test,  $\Delta T_2$  value increased. We speculate that the long incubation time causes the deliquescence of bacteria cells resulting in a discharge of magnetic nano-particles thereby causing a  $\Delta T_2$  increase.

#### 3.5. The sensitivity and detection limit of NMR method

To examine the sensitivity of this detection assay, seven different concentrations of *C. sakazakii* (from  $10^0$  to  $10^4$ ) were applied as targets for detection. When the concentrations of *C. sakazakii* increased from 11 MPN to 11,000 MPN, the  $\Delta T_2$  value reduced from 82 ms to 10 ms. We observed a strong correlation between the bacteria concentration and the  $\Delta T_2$  value ( $R^2 = 0.9958$ ) (Fig. 9). Interestingly, when the concentration of *C. sakazakii* was as low as 1.1 MPN, the value of  $\Delta T_2$  could still be detected with high changes ( $\Delta T_2 = 75$  ms). This result demonstrates that *C. sakazakii* could be detected at very low concentrations in our method.

The linear range of detection is estimated to range from 1 to 1100 MPN. At the lower limit of detection, the concentration of *C. sakazakii* is estimated at 1.1 MPN (Point A;  $\Delta T_2 = 75$  ms). At the upper limit of detection, the bacterial concentration is at 1100 MPN (Point B;  $\Delta T_2 < 12$  ms). The real-time PCR assay is the most popular method to detect *C. sakazakii*. In previous reports, *C. sakazakii* could be detected at 100 CFU/mL in pure culture in (Seo & Brackett, 2005), and the quantitative detection range for pure cultures was  $10^3$ – $10^8$  CFU/ml, which were evidently higher than our values (Hyeon, Park, Choi, Holt, & Seo, 2010). Therefore, it was supposed that using biofunctionalized MNPs based on NMR was a sensitive method for the detection of *C. sakazakii*.

#### 3.6. Results of tests on dairy samples

To examine the effectiveness of our method in practical applications, we measured the concentrations of *C. sakazakii* in two dairy samples, milk powder and cheese. The results are shown in Table 1. It is important to notice that the samples contaminated with *S. typhimurium* and *S. aureus* were not detected ( $\Delta T_2 < 12$  ms) in any of the tested dilution levels, which proved the specificity of this method only to *C. sakazakii* and not to any other bacterium.

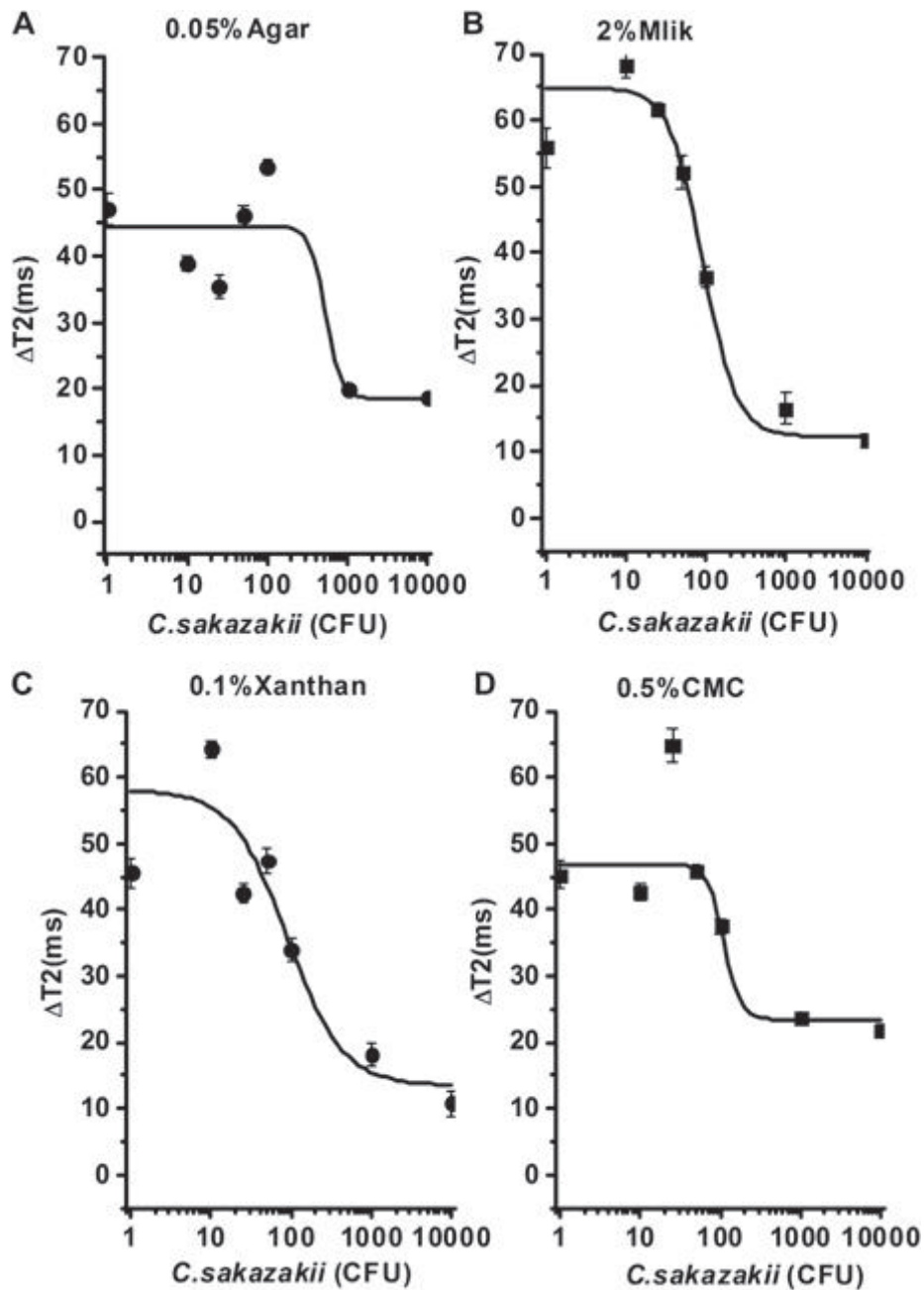


Fig. 7. Relationship between *C. sakazakii* concentrations on  $\Delta T_2$  values for four stabilizers (A) 0.05% agar, (B) 2% low fat milk, (C) 0.1% xanthan, and (D) 0.5% CMC on  $\Delta T_2$ . Error bars =  $\pm$ SD ( $n = 3$ ).

While it was at lower diluted of  $10^{-1}$  and  $10^{-2}$  in milk powder samples, *C. sakazakii* was optimally detected with an incubation period of 45 min. And it was not detected at a higher dilution of  $10^{-3}$  or with an increasing incubation period more than 4–8 h.

For cheese samples, the optimal detection of *C. sakazakii* was similar to the milk powder samples. However, incubation periods over 2 h led to a non-detect response to *C. sakazakii*, which suggested that longer incubation periods might lower the sensitivity of the NMR method.

Comparing detection results between NMR method and national standard procedure, the data indicated that the dilution rate of sample would have no effect on the result obtained according to GB 4789.40-2010, but greatly influence the stability and detectable

rate of NMR method. It is implied that pretreatment of sample is important in the testing procedure. The standard procedure lasts at least 24 h to obtain the result while NMR method only needs 1 h.

In addition, the result showed that high concentration ( $>1100$  MPN) of target bacteria induced low  $\Delta T_2$  value. We reason that the more bacteria exists in the solution means the higher number of multiple bacterial epitopes compete with the available number of nanoparticles. Consequently, the lower ratio of nanoparticles bind to the bacteria causing that the quasi-dispersed state and the lower changes of T2 are not detectable ( $\Delta T_2 < 20$  ms).

In conclusion, we have demonstrated a highly specific, sensitive and fast method for the detection of *C. sakazakii*. In this method, biofunctionalized nano-magnetic beads were used for efficient

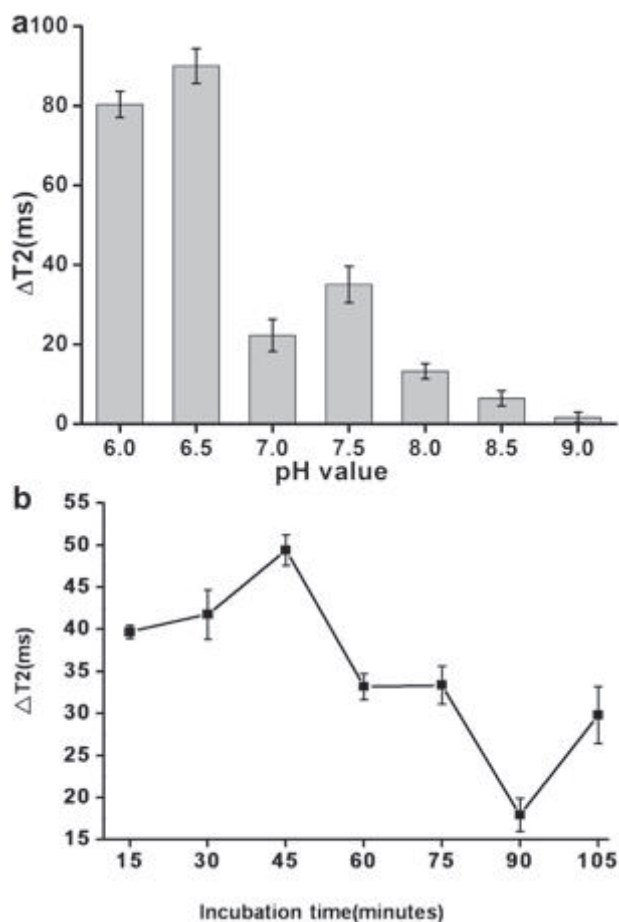


Fig. 8. Effects of (a) pH and (b) incubation period on the reaction between antibody immobilized magnetic beads and *C. sakazakii* by NMR assays. Error bars =  $\pm$ SD ( $n = 3$ ).

target capture. *C. sakazakii* can be quickly detected in dairy samples through nuclear magnetic resonance analysis. Although the detection limit for this method could reach as low as 1.1 MPN, we have set a limit of  $\Delta T_2$  value at 12 ms and a concentration of 11 MPN in consideration of the reliability and efficiency of this method. Evidently, this method provides a rapid and simple approach for the detection of food-borne bacteria in different food matrices. Moreover, the established detection system could be widely used in a broad range of fields including the medical, environment and agricultural sectors.

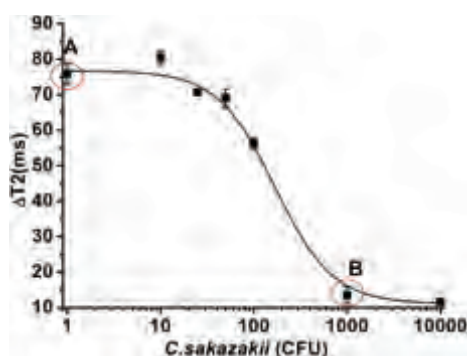


Fig. 9. The detection limit of NMR method. Error =  $\pm$ SD ( $n = 3$ ).

Table 1

Results of *C. sakazakii* detection in dairy samples.

Dairy samples	Dilution of sample	$\Delta T_2$ (ms)						GB 4789.40-2010 <sup>e</sup>
		45 min	2 h	4 h	8 h	22 h	24 h	
Milk powder	10 <sup>-1</sup>	49.55 <sup>a</sup>	51.5	47.6	ND <sup>b</sup>	ND	21.02	+ <sup>d</sup>
	10 <sup>-2</sup>	21.79	30.7	32.8	43.6	ND	ND	+
	10 <sup>-3</sup>	ND	ND	ND	ND	ND	ND	+
Cheese	10 <sup>-1</sup>	37.07	21.73	ND	ND	ND	ND	+
	10 <sup>-2</sup>	21.90	22.12	ND	ND	ND	ND	+
	10 <sup>-3</sup>	ND	ND	ND	ND	ND	ND	+

<sup>a</sup>  $\Delta T_2$  value is the average of triplicate measurements.

<sup>b</sup> ND: not detected at  $\Delta T_2 < 12$  ms;  $\Delta T_2$  value was shown in bracket.

<sup>c</sup> Diluted samples contained 10<sup>-2</sup> target bacteria.

<sup>d</sup> + Means there is target bacterial showed on *Cronobacter sakazakii* Chromogenic media.

## Acknowledgements

We acknowledge the financial support provided by the Food Safety and Nutrition Program of Shanghai Normal University (DXL123) and the Industry-University-Research Project of Shanghai Normal University (DCL201205).

## References

- Almeida, C., Azevedo, N. F., Iversen, C., Fanning, S., Keevil, C. W., & Vieira, M. J. (2009). Development and application of a novel peptide nucleic acid probe for the specific detection of *Cronobacter* genospecies (*Enterobacter sakazakii*) in powdered infant formula. *Applied and Environmental Microbiology*, 75(9), 2925–2930.
- Bowen, A. B., & Braden, C. R. (2006). Invasive *Enterobacter sakazakii* disease in infants. *Emerging Infectious Diseases*, 12(8), 1185–1189.
- Chen, Y., Song, K. Y., Brown, E. W., & Lampel, K. A. (2010). Development of an improved protocol for the isolation and detection of *Enterobacter sakazakii* (*Cronobacter*) from powdered infant formula. *Journal of Food Protection*, 73(6), 1016–1022.
- Esteban-Fernández de Ávila, B., Pedrero, M., Campuzano, S., Escamilla-Gómez, V., & Pingarrón, J. M. (2012). Sensitive and rapid amperometric magnetoimmunosensor for the determination of *Staphylococcus aureus*. *Analytical and Bioanalytical Chemistry*, 403(4), 917–925.
- Farmer III, J. J., Asbury, M. A., Hickman, F. W., & Brenner, D. J. (1980). *Enterobacter sakazakii*: a new species of 'Enterobacteriaceae' isolated from clinical specimens. *International Journal of Systematic Bacteriology*, 30(3), 569–584.
- Friedemann, M. (2009). Epidemiology of invasive neonatal *Cronobacter* (*Enterobacter sakazakii*) infections. *European Journal of Clinical Microbiology and Infectious Diseases*, 28(11), 1297–1304.
- Hassan, A. A., Akineden, O., Kress, C., Estuningsih, S., Schneider, E., & Usleber, E. (2007). Characterization of the gene encoding the 16S rRNA of *Enterobacter sakazakii* and development of a species-specific PCR method. *International Journal of Food Microbiology*, 116(2), 214–220.
- Hyeon, J. Y., Park, C., Choi, I. S., Holt, P. S., & Seo, K. H. (2010). Development of multiplex real-time PCR with internal amplification control for simultaneous detection of *Salmonella* and *Cronobacter* in powdered infant formula. *International Journal of Food Microbiology*, 144(1), 177–181.
- Iversen, C., Lancashire, L., Waddington, M., Forsythe, S., & Ball, G. (2006). Identification of *Enterobacter sakazakii* from closely related species: the use of artificial neural networks in the analysis of biochemical and 16S rDNA data. *BMC Microbiology*, 6, 28.
- Josephson, L., Perez, J. M., & Weissleder, R. (2001). Magnetic nanosensors for the detection of oligonucleotide sequences. *Angewandte Chemie*, 113(17), 3304–3306.
- Josephson, L., Tung, C. H., Moore, A., & Weissleder, R. (1999). High-efficiency intracellular magnetic labeling with novel superparamagnetic-Tat peptide conjugates. *Bioconjugate Chemistry*, 10(2), 186–191.
- Kaittanis, C., Naser, S. A., & Perez, J. M. (2007). One-step, nanoparticle-mediated bacterial detection with magnetic relaxation. *Nano Letters*, 7(2), 380–383.
- Kaittanis, C., Nath, S., & Perez, J. M. (2008). Rapid nanoparticle-mediated monitoring of bacterial metabolic activity and assessment of antimicrobial susceptibility in blood with magnetic relaxation. *PLoS One*, 3(9), 1803–1804.
- Kaittanis, C., Santra, S., Asati, A., & Perez, J. M. (2012). A cerium oxide nanoparticle-based device for the detection of chronic inflammation via optical and magnetic resonance imaging. *Nanoscale*, 4(6), 2117–2123.
- Kim, G. Y., Josephson, L., Langer, R., & Cima, M. J. (2007). Magnetic relaxation switch detection of human chorionic gonadotropin. *Bioconjugate Chemistry*, 18(6), 2024–2028.
- Koh, I., Hong, R., Weissleder, R., & Josephson, L. (2008). Sensitive NMR sensors detect antibodies to influenza. *Angewandte Chemie*, 47(22), 4119.

- Lin, M., Al Holy, M., Al Qadiri, H., Kong, F., Rasco, B. A., & Setiady, D. (2009). Detection and discrimination of *Enterobacter Sakazakii* (*Cronobacter* spp.) by mid infrared spectroscopy and multivariate statistical analyses. *Journal of Food Safety*, 29(4), 531–545.
- Liu, X., Fang, J., Zhang, M., Wang, X., Wang, W., Gong, Y., et al. (2012). Development of a loop-mediated isothermal amplification assay for detection of *Cronobacter* spp. (*Enterobacter sakazakii*). *World Journal of Microbiology and Biotechnology*, 28(3), 1013–1020.
- Ma, W., Chen, W., Qiao, R., Liu, C., Yang, C., Li, Z., et al. (2009). Rapid and sensitive detection of microcystin by immunosensor based on nuclear magnetic resonance. *Biosensors and Bioelectronics*, 25(1), 240–243.
- Merkoci, A. (2010). Nanoparticles-based strategies for DNA, protein and cell sensors. *Biosensors and Bioelectronics*, 26(4), 1164–1177.
- Mullane, N. R., Murray, J., Drudy, D., Prentice, N., Whyte, P., Wall, P. G., et al. (2006). Detection of *Enterobacter sakazakii* in dried infant milk formula by cationic-magnetic-bead capture. *Applied and Environmental Microbiology*, 72(9), 6325.
- National food safety standard food microbiological examination: *Enterobacter sakazakii*. (2010). In *GB 4789.40-2010. The People's Republic of China State standard of the People's Republic of China*.
- Park, S., Shukla, S., Kim, Y., Oh, S., Hun Kim, S., & Kim, M. (2012). Development of sandwich enzyme-linked immunosorbent assay for the detection of *Cronobacter mytjensii* (formerly called *Enterobacter sakazakii*). *Microbiology and Immunology*, 56(7), 472–479.
- Perez, J. M., Josephson, L., O'Loughlin, T., Högemann, D., & Weissleder, R. (2002). Magnetic relaxation switches capable of sensing molecular interactions. *Nature Biotechnology*, 20(8), 816–820.
- Perez, J. M., Simeone, F. J., Saeki, Y., Josephson, L., & Weissleder, R. (2003). Viral-induced self-assembly of magnetic nanoparticles allows the detection of viral particles in biological media. *Journal of the American Chemical Society*, 125(34), 10192–10193.
- Restaino, L., Frampton, E. W., Lionberg, W. C., & Becker, R. J. (2006). A chromogenic plating medium for the isolation and identification of *Enterobacter sakazakii* from foods, food ingredients, and environmental sources. *Journal of Food Protection*, 69(2), 315–322.
- Seo, K., & Brackett, R. (2005). Rapid, specific detection of *Enterobacter sakazakii* in infant formula using a real-time PCR assay. *Journal of Food Protection*, 68(1), 59–63.
- Wang, M., Cao, B., Gao, Q., Sun, Y., Liu, P., Feng, L., et al. (2009). Detection of *Enterobacter sakazakii* and other pathogens associated with powdered infant formula using a DNA microarray. *Journal of Clinical Microbiology*, 47(10), 3178–3184.
- Weissleder, R., Moore, A., Mahmood, U., Borhade, R., Benveniste, H., Chiocca, E. A., et al. (2000). In vivo magnetic resonance imaging of transgene expression. *Nature Medicine*, 6(3), 351–354.
- Yan, Q. Q., Condell, O., Power, K., Butler, F., Tall, B. D., & Fanning, S. (2012). *Cronobacter* species (formerly known as *Enterobacter sakazakii*) in powdered infant formula: a review of our current understanding of the biology of this bacterium. *Journal of Applied Microbiology*, 113(1), 1–15.
- Yang, H., Zhuang, Y., Sun, Y., Dai, A., Shi Xiangyang, X., Wu, D., et al. (2011). Targeted dual-contrast T1- and T2-weighted magnetic resonance imaging of tumors using multifunctional gadolinium-labeled superparamagnetic iron oxide nanoparticles. *Biomaterials*, 32(20), 4584–4593.

## 生命科学领域

上海师范大学

### 多功能配位聚合物纳米粒子的合成及应用



杨仕平

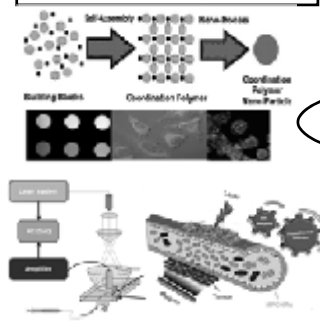
上海师范大学

2013年10月



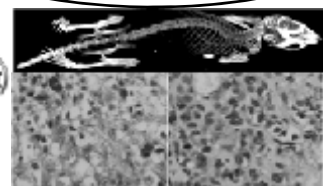
上海师范大学

### 1. 配位聚合物纳米粒子的制备与在生物成像中的应用



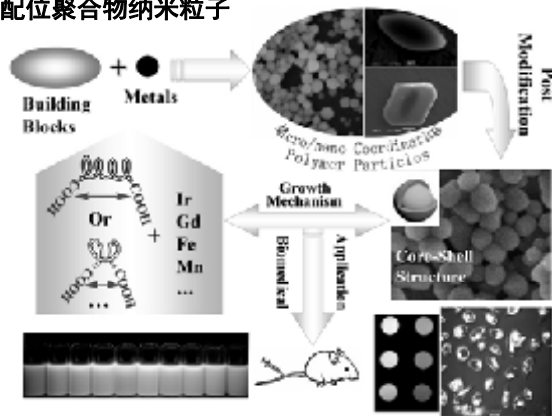
*Adv. Funct. Mater.*, 2010, 20, 1733  
*Biomaterials*, 2010, 31, 3667  
*Biomaterials*, 2011, 32, 4584  
*Biomaterials*, 2011, 32, 4867  
*Acta Biomaterials*, 2011, 7, 3496  
*Biomaterials*, 2012, 33, 8591

### 2. 以磁性纳米粒子为平台构建纳米诊疗材料



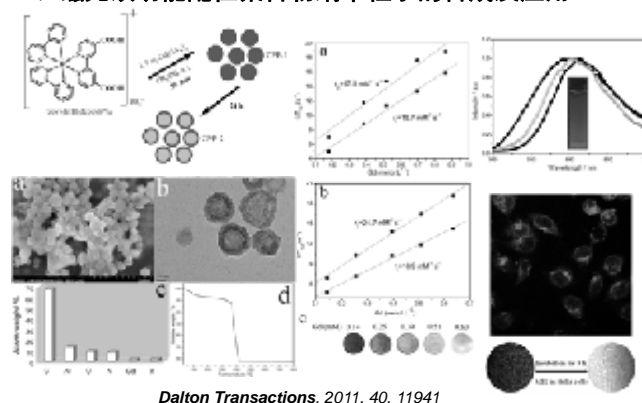
上海师范大学

### 配位聚合物纳米粒子



上海师范大学

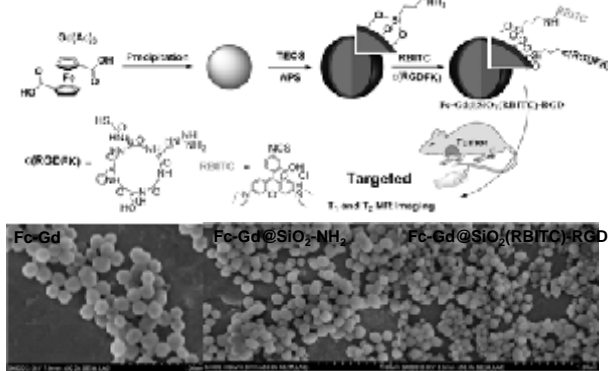
### 一、磁光双功能配位聚合物纳米粒子的合成及应用



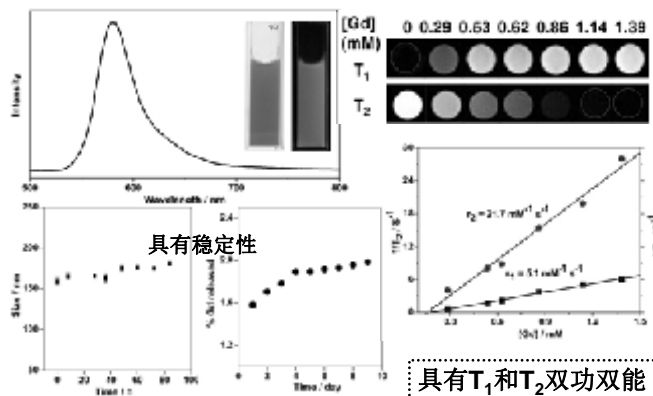
*Dalton Transactions*, 2011, 40, 11941

上海师范大学

### 二、 $T_1/T_2$ 双模式配位聚合物纳米粒子肿瘤靶向中的应用

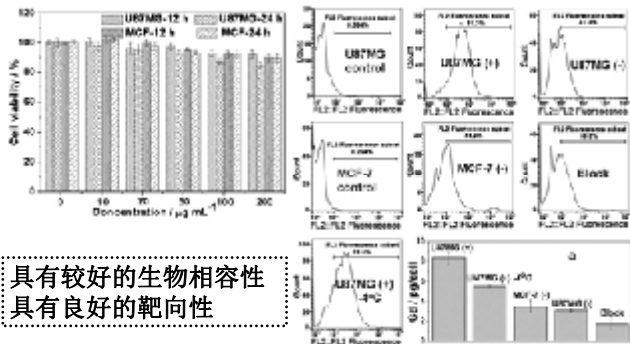


上海师范大学



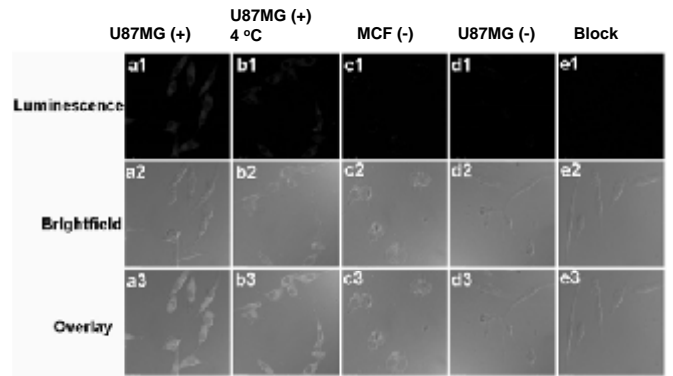
具有 $T_1$ 和 $T_2$ 双功双能

上海师范大学

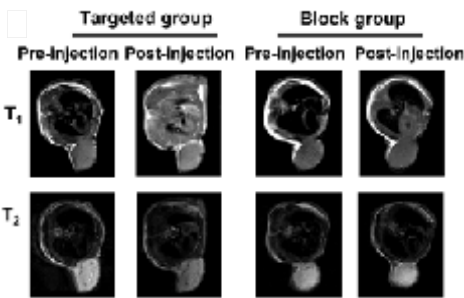


具有较好的生物相容性  
具有良好的靶向性

上海师范大学



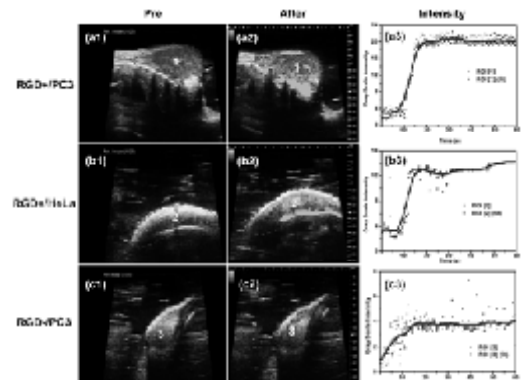
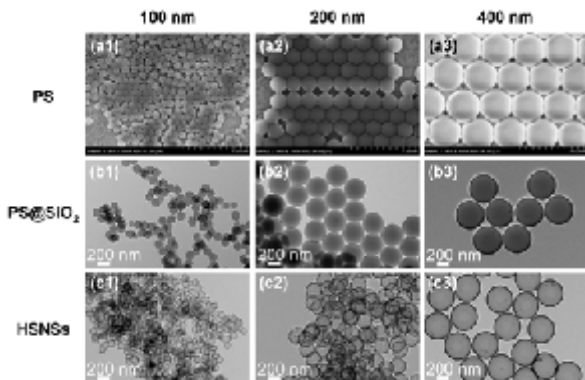
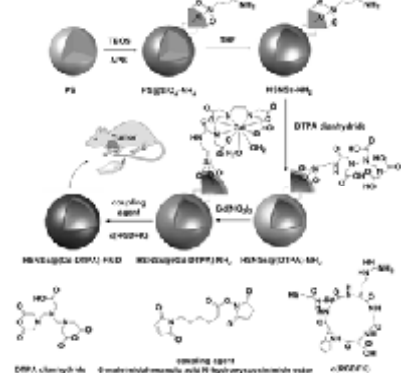
上海师范大学

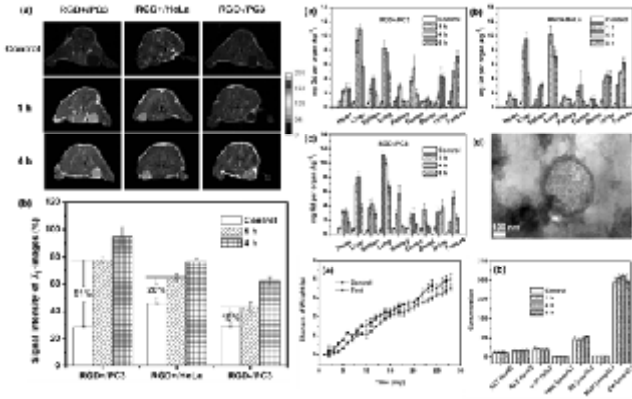


活体层次实现 $T_1/T_2$ 靶向的多功能成像



三、磁/超声双功能纳米粒子在肿瘤靶向成像中的应用





### 致 谢

- 国家自然科学基金委
- 上海市科委
- 杨红 周治国 吴慧霞
- 李大锐 秦长圆 安璐

谢谢大家!



上海交通大学  
SHANGHAI JIAO TONG UNIVERSITY

1896 1920 1987 2006

### A tri-functional probe to track and quantify MSC implanted with different routes in mouse cerebral ischemia model

Chunfu Zhang

School of Biomedical Engineering & Med-X Research Institute, Shanghai Jiao Tong University

上海交通大学  
SHANGHAI JIAO TONG UNIVERSITY

1920 1987 2006

### Stroke in China

Stroke report by W.H.O

China has a high incidence of stroke: **mortality: 1.5 mil/year morbidity: 2 mil/year; disabilities: 8 mil/China**

Med-x Research Institute 2

上海交通大学  
SHANGHAI JIAO TONG UNIVERSITY

2006

### Stem cells reduce infarct volume

Group	Infarct Volume (mm <sup>3</sup> )
Saline	~28
EPC	~14*

Fan, et al. *Ann Neurol.* 2010;67:488

Med-x Research Institute

上海交通大学  
SHANGHAI JIAO TONG UNIVERSITY

Xu et al. *Nanotechnology* 20 (2009) 405102

Xu et al. *ChemPhysChem*, 2012, 13, 336

Shapiro et al. *Magn. Reson. Med* 2005, 53:329. Zhang et al. *ChemPhysChem* 2012, 13, 2016.

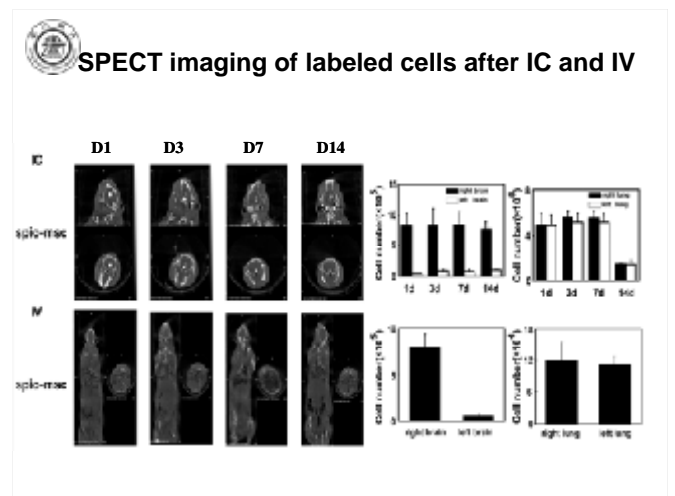
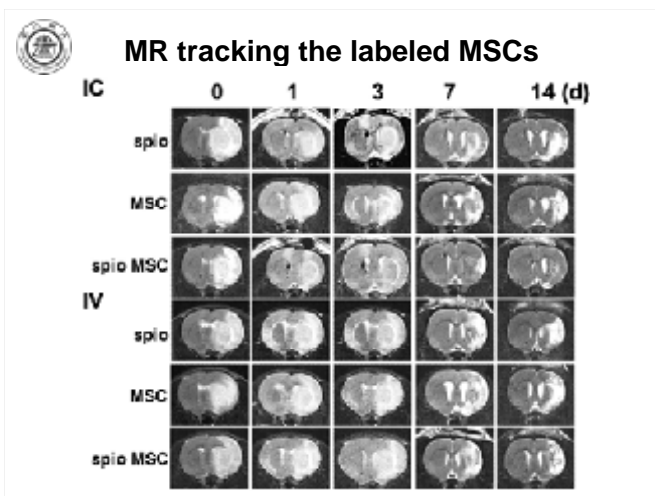
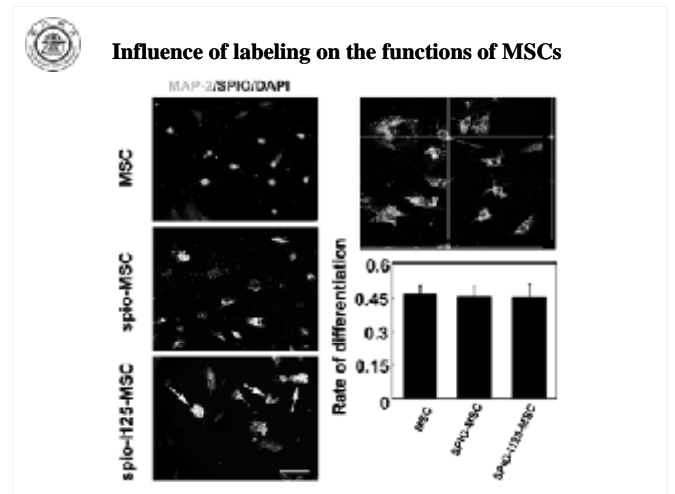
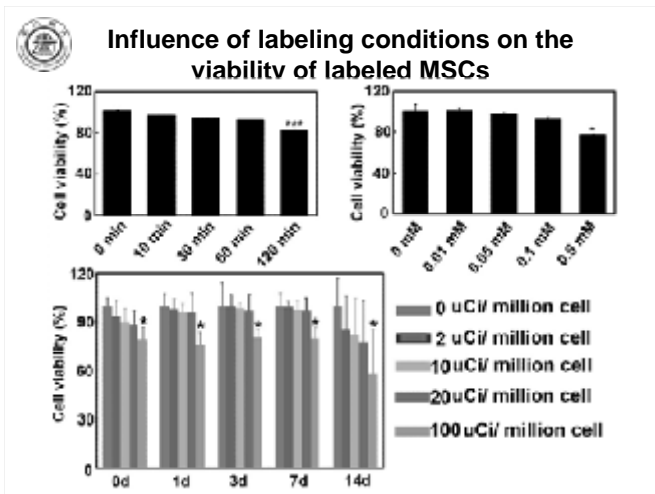
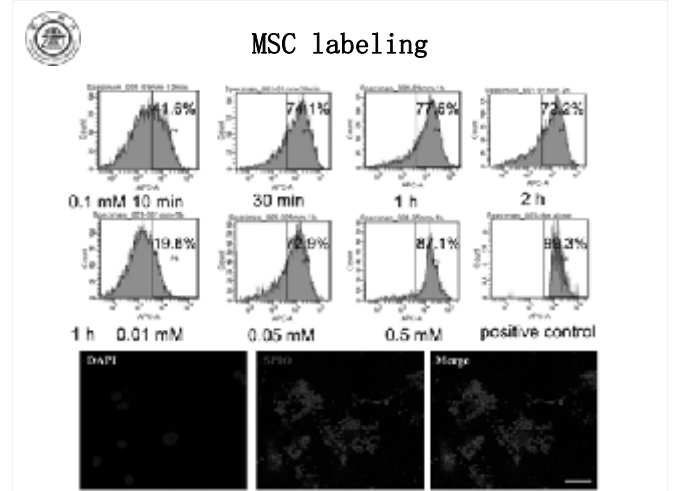
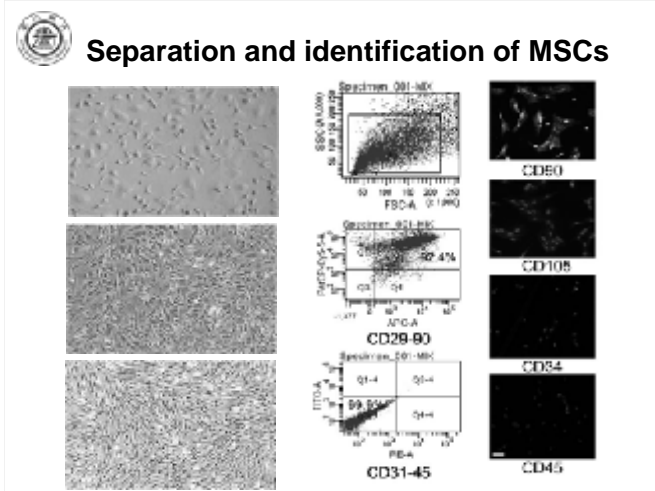
上海交通大学  
SHANGHAI JIAO TONG UNIVERSITY

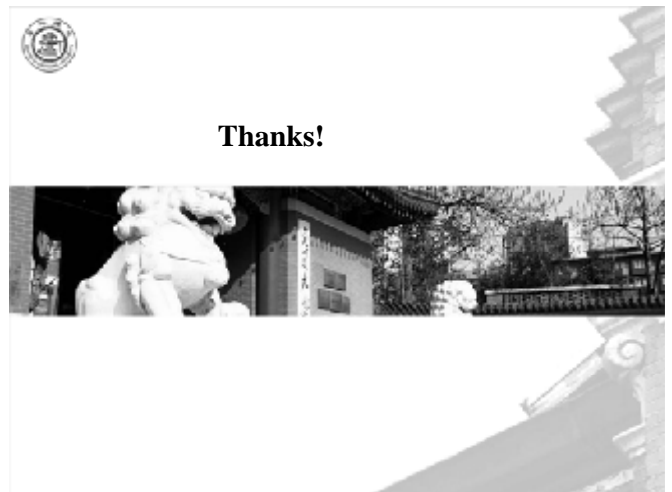
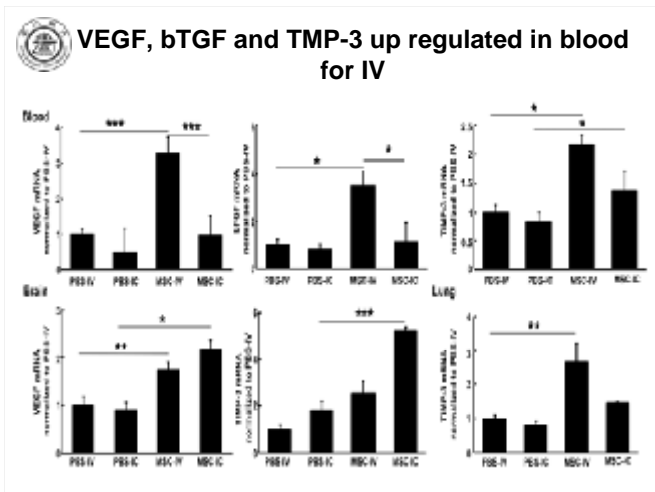
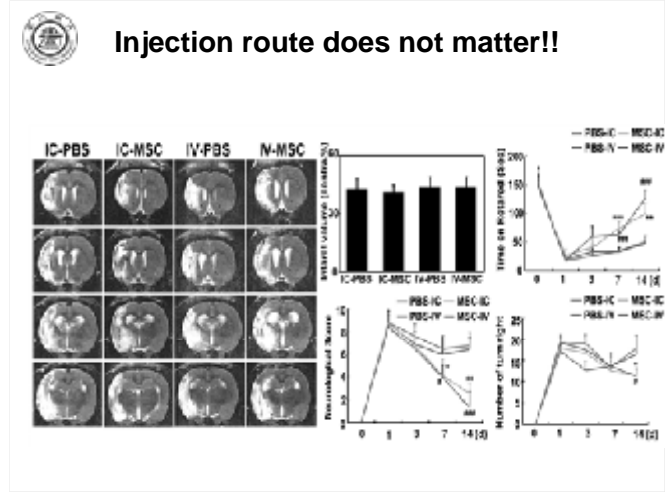
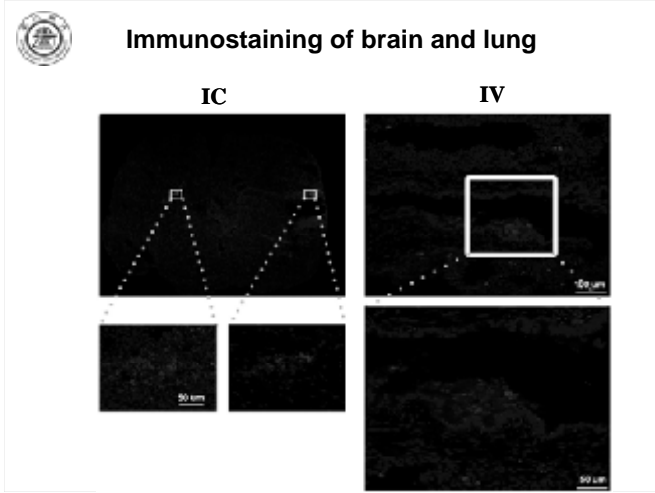
Lu Zhang, Yao Wang, Yaohui Tang, et al. *Nanoscale*, 2013, 5, 4506-4516.

上海交通大学  
SHANGHAI JIAO TONG UNIVERSITY

### MRI/SPECT/FI tri-functional probe

Sn(n-Bu)<sub>3</sub>  
ATP





## 球状大分子结构 MRI 分子探针及其肿瘤靶向成像应用

谭明乾<sup>1</sup>, 吴昊<sup>1</sup>, 宋小杰<sup>1</sup>, Zheng-Rong Lu<sup>2</sup>

<sup>1</sup> 中国科学院大连化学物理研究所生物技术部大连市中山路 457 号, 邮编 116023

<sup>2</sup> Department of Biomedical Engineering, Case Western Reserve University, Cleveland, Ohio 44106

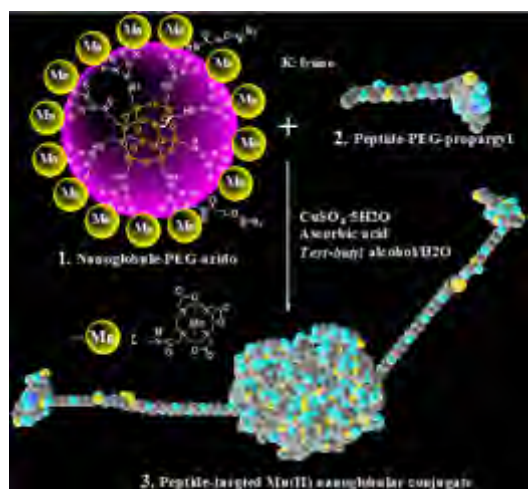
[mqtan@dicp.ac.cn](mailto:mqtan@dicp.ac.cn)

核磁共振分子影像学 (MRI molecular imaging) 在分子影像学中占有重要的地位, 它运用核磁共振成像为手段来研究活体条件下生物细胞内的正常或病理状态下的分子过程的科学。能够无创、可重复提供在体、定量、实时、可视化分子信息, 甚至多分子相互作用信息。其中高特异性的核磁共振分子探针是该技术的关键因素之一。

临床中应用的核磁共振造影剂的主要是小分子钆配合物, 其主要缺点是分子成像的敏感性和特异性比较差。水溶性大分子聚合物为开发核磁共振造影剂提供了有效的载体材料, 因为其能够降低所承载钆配合物的转动速率, 从而提高了造影剂的弛豫度。传统的聚合物造影剂载体材料存在分子量分布范围宽、分子形状不规整和容易发生组织蓄积等缺点, 限制了其作为载体材料的应用。树状高分子 (dendrimer) 是一类具有三维结构的高分子, 与其它线性或枝化高分子相比具有精确的分子结构、大量的官能团、分子内存在空腔及分子链增长具有可控性等特点, 这些特点使其作为药物载体、医疗诊断、表面活性剂、催化剂载体等许多领域有重要的潜在应用价值。成为相关领域的研究热点。现有的树状高分子载体材料一般是以乙二醇等平面小分子为核制备而成, 作为核磁共振分子探针载体材料仍然具有分子形状易变和结构不规整等缺点, 从而导致与生物组织的非特异性相互作用增强, 延长组织残留时间等问题。我们在研究中设计和制备了一种以六面体倍半硅氧烷低聚物 (Polyhedral oligomeric silsesquioxane, POSS) 为核的纳米球状大分子载体材料。它以立方体形状的核为中心, 均匀的生长出 8 个分支, 在结构上更加对称, 形成纳米尺寸的球型大分子, 其表面的功能化氨基为设计和制备靶向核磁共振分子探针提供了很好的基础。

靶向核磁共振分子探针的设计和制备一直是核磁共振分子影像学研究中的难点之一, 如分子结构复杂, 合成难度大, 表征困难等。一般的存在于癌细胞表面的肿瘤标志物由于其含量较少, 达不到核磁共振检测的要求。最近的研究表明, 肿瘤细胞外的间质物质, 例如癌胚性纤维连接蛋白 (fibronectin) 在肿瘤的细胞外基质中大量存在, 而在正常的组织中却没有发现。由于其在肿瘤组织中的大量存在, 癌胚性纤维连接蛋白越来越受到研究者的重视, 将其作为肿瘤标志物用于核磁共振分子探针的研制。最近的文章报道一种由十个氨基酸构成的环状多肽可以特异性的识别肿瘤组织中的纤维连接蛋白, 将环状多肽导入到表面键合有钆配合物的纳米球型大分子载体上, 我们制备出来具有肿瘤靶向识别作用的特异性

核磁共振分子探针，在体小鼠核磁共振成像表明，该靶向分子探针只要注射临床剂量的 1/3 就可以有效地识别肿瘤组织，尤其是能够有效地识别出前列腺原位癌。



**Keywords:** 核磁共振成像，造影剂，球状大分子，肿瘤靶向

### References

1. Tan, M. Q., Wu, X. M., Jeong, E. K., Chen, Q. J., and Lu, Z. R. *Biomacromolecules*, **2010**, *11*, 754.
2. Tan, M. Q., Wu, X. M., Jeong, E. K., Chen, Q. J., Parker, D. L., and Lu, Z. R. *Mol Pharmaceut*, **2010**, *7*, 936.
3. Tan, M. Q., Ye, Z., Jeong, E. K., Wu, X. M., Parker, D. L., and Lu, Z. R. *Bioconjugate Chem*, **2011**, *22*, 931.
4. Tan, M. Q., Burden-Gulley, S. M., Li, W., Wu, X. M., Lindner, D., Brady-Kalnay, S. M., Gulani, V., and Lu, Z. R. *Pharm Res*, **2012**, *29*, 953.
5. Chow, A. M., Tan, M. Q., Gao, D. S., Fan, S. J., Cheung, J. S., Qiao, Z. W., Man, K., Lu, Z. R., and Wu, E. X. *Invest Radiol*, **2013**, *48*, 46.

## High-Performance Iron-oxide-based MRI Contrast Agents

Zijian Zhou, Zhenghuan Zhao, Guoming Huang, and Jinhao Gao\*

State Key Laboratory of Physical Chemistry of Solid Surfaces, The Key Laboratory for Chemical Biology of Fujian Province, and Department of Chemical Biology, College of Chemistry and Chemical Engineering, Xiamen University, Xiamen 361005, P.R. China.

\*Email: jhgao@xmu.edu.cn

Magnetic nanoparticles are attracting extensive interest for their ability to enhance the magnetic resonance contrast effect.<sup>1-3</sup> Spherical superparamagnetic iron oxide (SPIO) nanoparticles (e.g., Feridex and Resovist) have been developed as  $T_2$  negative contrast agents for magnetic resonance imaging (MRI) in clinical use due to their biocompatibility and ease of synthesis. However, the relatively low transverse relaxivity ( $r_2$ ) and poor performance of spherical SPIO nanoparticles as  $T_2$  contrast agents has hampered their clinical applications. In this presentation, we report the rational design strategies to achieve high MR contrast sensitivity by controlling the composition and morphology, including gadolinium-embedded iron oxide (GdIO) nanoparticles as synergistically enhanced  $T_1$ - $T_2$  dual-modal contrast agent and octapod SPIO nanoparticles.<sup>4,5</sup> The octapod SPIO nanoparticles (edge length of 30 nm) exhibit an ultrahigh  $r_2$  value ( $\sim 679.3 \text{ mM}^{-1}\text{S}^{-1}$ ), which is approximately 5.4 times larger than that of spherical SPIO nanoparticles.<sup>6</sup> Compared to conventional SPIO nanoparticles, these high-performance iron oxide based nanoparticles are much more effective contrast agents for *in vivo* MRI and small tumor detection, which holds great promise for highly sensitive, early stage and accurate detection of cancer in the clinic.

**Keywords:** MRI, Contrast agents, High performance, Molecular imaging, Cancer

### References

1. C. Tassa, S. Y. Shaw and R. Weissleder, *Acc. Chem. Res.*, 2011, **44**, 842-852.
2. C. Corot, P. Robert, J. M. Idee and M. Port, *Adv. Drug Deliv. Rev.*, 2006, **58**, 1471-1504.
3. J. H. Gao, H. W. Gu and B. Xu, *Acc. Chem. Res.*, 2009, **42**, 1097-1107.
4. Z. J. Zhou, D. T. Huang, J. F. Bao, Q. L. Chen, G. Liu, Z. Chen, X. Y. Chen and J. H. Gao, *Adv. Mater.*, 2012, **24**, 6223-6228.
5. Z. J. Zhou, L. R. Wang, X. Q. Chi, J. F. Bao, L. J. Yang, W. X. Zhao, Z. Chen, X. M. Wang, X. Y. Chen and J. H. Gao, *ACS Nano*, 2013, **7**, 3287-3296.
6. Z. H. Zhao, Z. J. Zhou, J. F. Bao, Z. Y. Wang, J. Hu, X. Q. Chi, K. Y. Ni, R. F. Wang, X. Y. Chen, Z. Chen and J. H. Gao, *Nature Communications*, 2013, **4**, 2266.

**Acknowledgement:** This work was supported by the National Key Basic Research Program of China (2013CB933901), National Natural Science Foundation of China (21222106, 81370042), and Program for New Century Excellent Talents in University (NCET-10-0709).

## 磷酸钙/聚合物复合组装纳米给药系统

段友容（上海市肿瘤研究所，上海市）

CaP/PL-mPEG hybrid porous nanospheres for drug/gene delivery

Calcium phosphate/Phospholipid (PL)-mPEG hybrid porous nanospheres (CaP/PL-mPEG NSs) were prepared by a facile room-temperature method and employed as carriers to deliver drug/gene. As the polymer segments adsorb on the CaP surface, the rapid growth of CaP can be controlled and the size of the precipitates will be reduced to nanometre scale. Furthermore, the CaP/PL-mPEG nanocomposite can be stable in aqueous solution for a relatively long period, because the polymer can act as a stabilizer and hamper the transformation from ACP to hydroxyapatite (HAp). The BET specific surface area of the CaP/PL-mPEG hybrid porous nanospheres was 136.4 m<sup>2</sup>/g. The relatively large specific surface area is highly advantageous for the loading or adsorbing of drugs or genes. Additionally, both CaP and PL-mPEG are biocompatible and biodegradable thus the as-prepared CaP/PL-mPEG hybrid porous nanospheres are promising for drug/gene delivery.

## 橡胶、材料、高分子领域



**WATER IN WOOD STUDIED BY TIME - DOMAIN NMR**

Minghui Zhang

**College of Material Science and Art Design  
Inner Mongolia Agricultural University**

**INTRODUCTION**

➤ **Problem**

Traditional methods cannot solve the relation between wood and water in micro-scale.

➤ **Question**

1. Is there a special way to probe wood and water relationships without destruction and how?

2. Is that possible to study water molecular dynamics in wood and thereafter to explain water transportation during sorption process in molecular level?

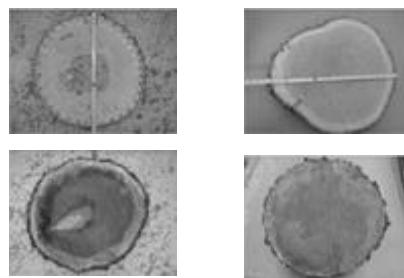
**INTRODUCTION**

➤ **Objectives**

1. The water content in wood investigated quantitatively through the difference of proton sensor's concentration.
2. The water states in wood according to relaxation time.
3. Water transportation process in wood during drying and its mathematical model .

**METHODOLOGY**

**1. Samples are from fresh cut trees: Ash, Red oak, Walnut and Poplar.**



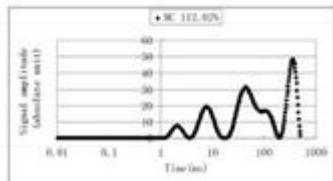
**2. Insert sample into bench top NMR for time relaxation and FID measure.**



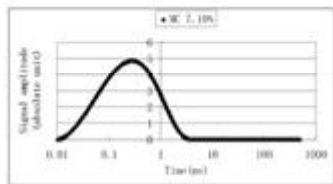
**Samples Positions from Wood Disk**



**RESULTS & DISCUSSION**

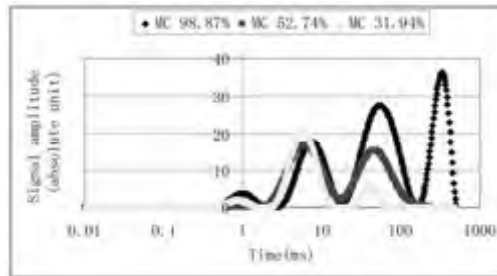


T2 relaxation profile during Yellow poplar drying at MC112.02%



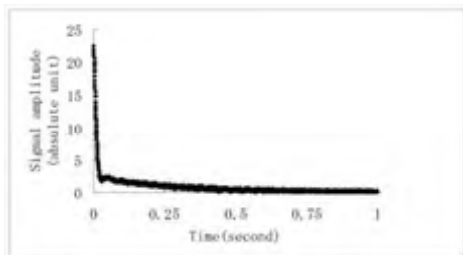
T2 relaxation profile during Yellow poplar drying at MC 7.10%

**Spin-spin relaxation time for different moisture content of yellow poplar.**



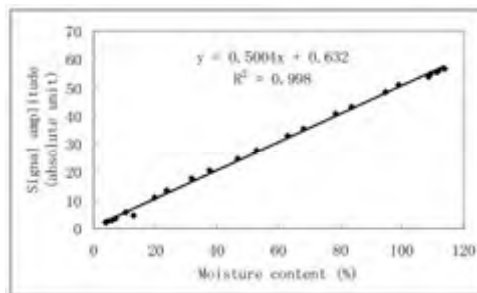
T2 relaxation profile during drying at different MC

**A typical FID curve for the yellow poplar with MC = 4.03%**

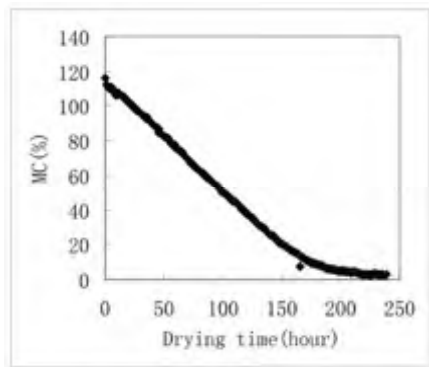


- A. The first part of signal (intensity) is directly related to the number of nuclei in the sample (more NMR signal means more nuclei in the sample);
- B. The rate of decay ( $T_2$ ) is related to mobility of molecules (liquids have longer decay time than solids).

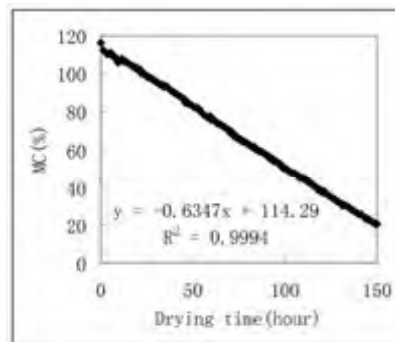
**Relation between MC determined gravimetrically and NMR signal amplitude**



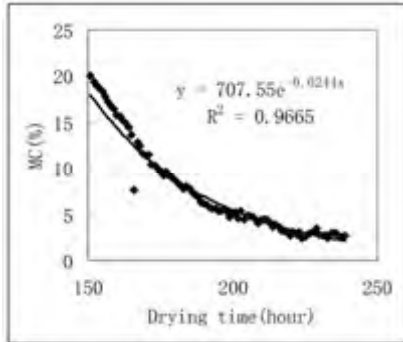
**Yellow poplar MC changes with drying time**



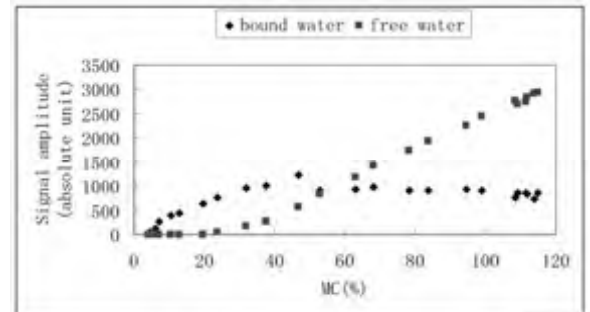
**Yellow poplar MC changes with drying time**



**Yellow poplar MC changes with drying time**



**Free and bound water changes with MC during drying**



**CONCLUSIONS**

1. Yellow poplar has at least 4 water states according to T2 values at moisture content above 100%.
2. Water states in wood will change with drying time. The T2 value will get shorter with MC decreasing.
3. Water migration in yellow poplar drying can be divided into two phase – one is following linear function and the other is exponential function.
4. It is apparent that bound water does not change too much above 50% MC.
5. Both free and bound water in yellow poplar drying happen to lose above fiber saturation point.

**ACKNOWLEDGMENTS**

This research is supported by the National Natural Science Foundation of China (30800866/ C1603 & 31160141/ C1603)

Wood Research Lab of Purdue University

Dr. Daniel L. Cassens

Dr. Eva Haviarova

**THANK YOU !**

**QUESTIONS  
COMMENTS**

全国低场核磁共振技术与应用研讨会

## 轮胎胶粉干法再生过程中自由基浓度与脱硫活化效果的相关性研究



曾冬,张兴凯,童薇,刘俊亮,张明\*  
扬州大学化学化工学院,江苏 扬州

## 主要内容

- 背景
- 实验设计
- 结果与讨论
- 结论

### 1、背景

#### 轮胎的污染

废旧轮胎给人们的生活带来诸多不便!



空气污染

占用土地

水污染

### 1、背景

#### 轮胎的回收

<b>原型直接利用</b>	用作码头的护航, 路标, 园林装饰, 游乐玩具等。 缺点: 消耗轮胎量不大。
<b>轮胎翻新利用</b>	附加值高, 翻新轮胎成本不到原来的1/4。 缺点: 对高速安全性日益苛刻。
<b>生产再生胶和胶粉</b>	生产再生胶价格便宜, 但有一定程度的污染。 生产胶粉污染小, 方法简单, 对环境污染小。
<b>热裂解</b>	生产可燃气、燃料油和炭黑, 钢丝等。 缺点: 技术复杂, 成本高, 有污染。
<b>热能利用</b>	废旧橡胶是一种热值较高的废弃物, 可作为燃料使用。 缺点: 直接燃烧会带来大气污染。

### 1、背景

#### 胶粉存在问题



胶粉

普通胶粉因为交联结构难翻新, 表面缺乏粘合性和活性, 一般作填料使用。为扩大其使用范围, 必须对其进行活化改性。

### 1、背景

胶粉改性分为物理和化学两类方法, 本课题组采用物理和化学相结合的方法: 机械力化学法。  
优点: 清洁、高效、易行。

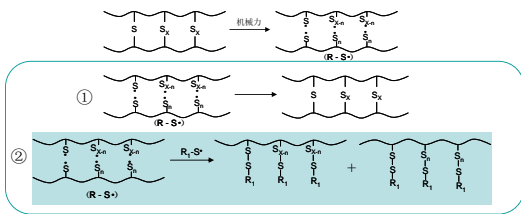
使用开炼机替代双螺杆挤出设备, 对胶粉进行机械力化学改性。



开炼机

### 1、背景

机械力化学改性是将活化体系添加于胶粉中，在一定条件下通过机械加工的方法，起化学反应而再生改性胶粉的一种方法。目的是使交联键裂解而获得塑性，增强与橡胶基体相容性，从而达到再生改性。



机械力化学改性胶粉作用机理

### 1、背景

在机械力改性胶粉过程中，橡胶高分子链上会产生大量自由基，而自由基的浓度会影响胶粉体系交联结构，进而影响胶粉的改性。

**待解决问题：**

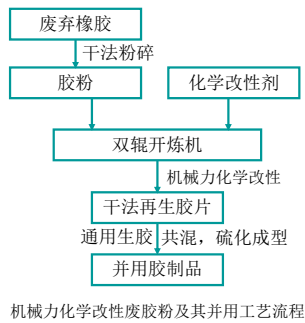
降低改性过程中胶粉体系自由基浓度，从而降低胶粉交联密度，从而达到对胶粉的活化改性。

**实验研究目标：**

在机械力作用过程中，通过对胶粉体系内自由基浓度的准确测定，建立在改性过程中**自由基数量与胶粉脱硫活化效果关系**，寻求最佳的自由基浓度控制方法与工艺条件。

### 2、实验设计

**实验流程**



机械力化学改性废胶粉及其并用工艺流程

### 2、实验设计

**实验流程**

改性胶片配方：无助剂，利用胶粉体系内自身残留的助剂对其进行活化改性。

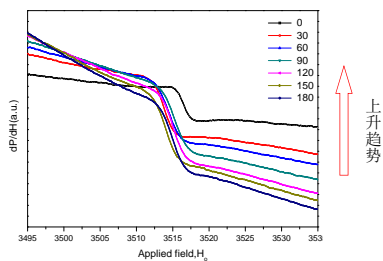
硫化胶片配方：硬脂酸 2；氧化锌 4；促进剂DM 0.4；促进剂CZ 1.0；硫磺 1.5。

**改性胶片的制备：**将开炼机双辊距离调到最小，将定量胶粉在分别薄通0、30、60、90、120、150、180次。

**纯胶粉混炼胶的制备：**调整好开炼机双辊距离，将胶粉在开炼机上薄通数遍，逐步加入硬脂酸、氧化锌等助剂，混匀，下片，硫化成型。

### 3、结果与讨论

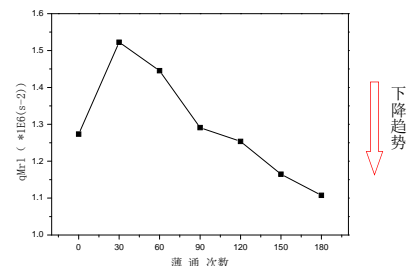
**改性胶粉自由基浓度**



不同薄通次数胶粉的ESR图

### 3、结果与讨论

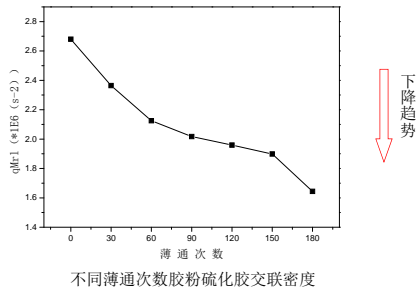
**改性胶粉交联密度**



不同薄通次数胶粉交联密度

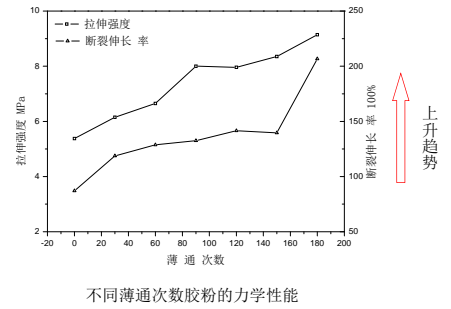
### 3、结果与讨论

#### 胶粉硫化胶片交联密度



### 3、结果与讨论

#### 硫化胶力学性能



### 4、结论

- a. 在机械力作用胶粉的过程中，胶粉体系内自由基的浓度随着薄通次数的增加而上升，交联密度呈先增大后降低的趋势，薄通次数在180次时，胶粉交联密度下降13.05%；
- b. 经过机械力作用的纯胶粉硫化胶其力学性能有明显提高，在薄通次数为180次时，其拉伸强度和断裂伸长率分别提高了69.89%和137.3%。

### 致谢

#### 感谢以下单位的大力支持：

- 国家自然科学基金 (NO. 51273172)
- 昆明普尔顿管业有限公司



谢谢大家！

曾冬

Email: Dongz1988@126.com

Central South University  
中南大学

## 基于核磁共振技术的矿山充填料浆硬化研究

汇报人：艾凯明  
专业：采矿工程  
单位：中南大学资源与安全工程学院

2013年10月12日

Central South University  
中南大学

## 内容提纲

- 1 充填料浆
- 2 实验方案
- 3 实验结果
- 4 探讨

Central South University  
中南大学

## 一、充填料浆

```

    graph TD
      Tailings[尾矿] --> Slurry((充填料浆))
      Cement[水泥] --> Slurry
      Aggregates[其他骨料] --> Slurry
      Additives[外加剂] --> Slurry
      Water[水] --> Slurry
  
```

Central South University  
中南大学

## 实验目的

- 1 观察充填料浆硬化过程中的水分消耗和孔隙形成
- 2 减水剂对充填料浆水分消耗的影响
- 3 充填立方体孔隙度与单轴抗压强度关系

Central South University  
中南大学

## 二、实验方案

**配比方案：**

尾矿来源	尾矿/水泥	质量浓度	减水剂含量
湖南东江湖	6/1	75%	0
湖南东江湖	6/1	75%	0.4%

**水分消耗和孔隙形成观测：**  
选用CPMG连续采样，间隔时间为30min，总观察时间为5d

**减水剂的影响：**  
一组不添加减水剂和另外一组添加0.4%减水剂对比，采样同方法同上，观测7d

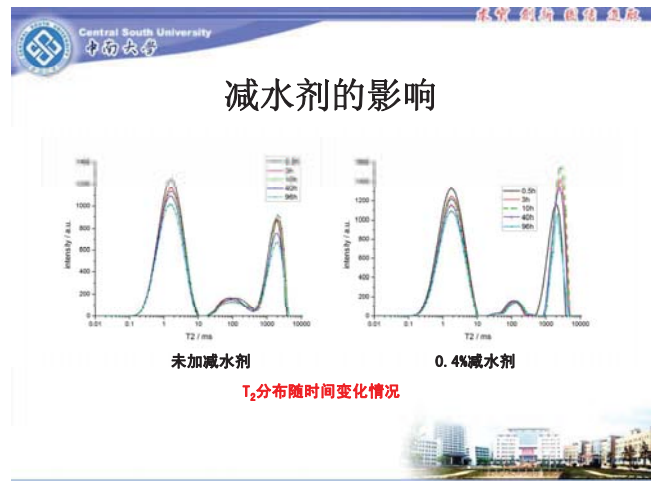
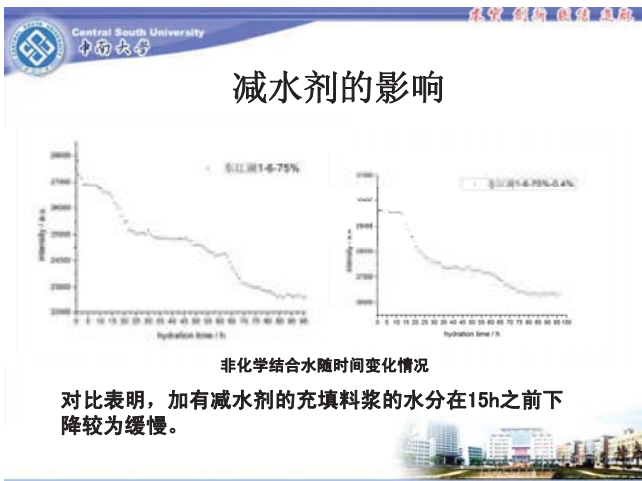
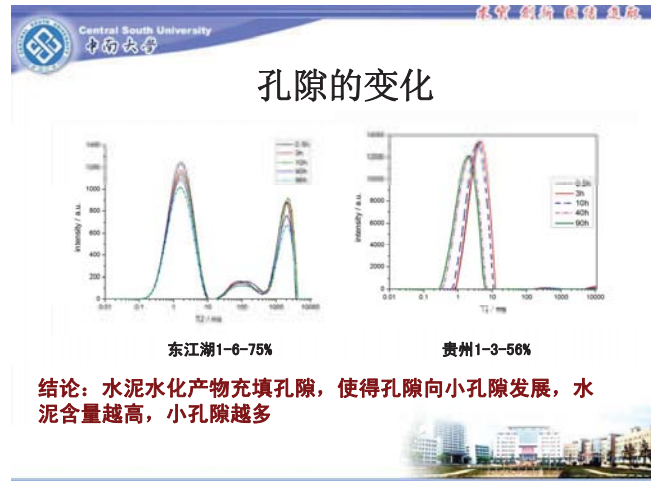
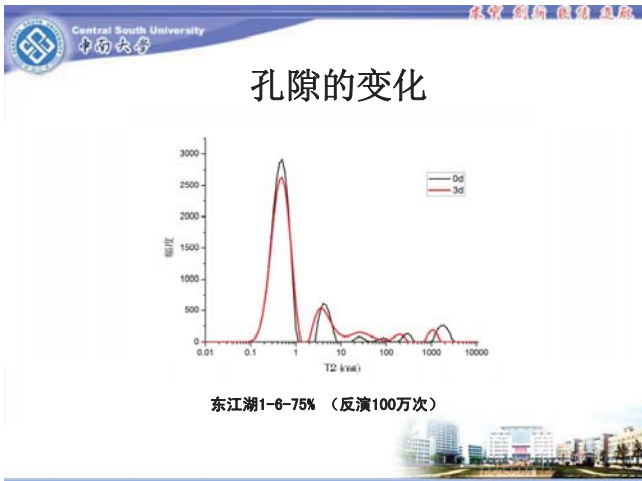
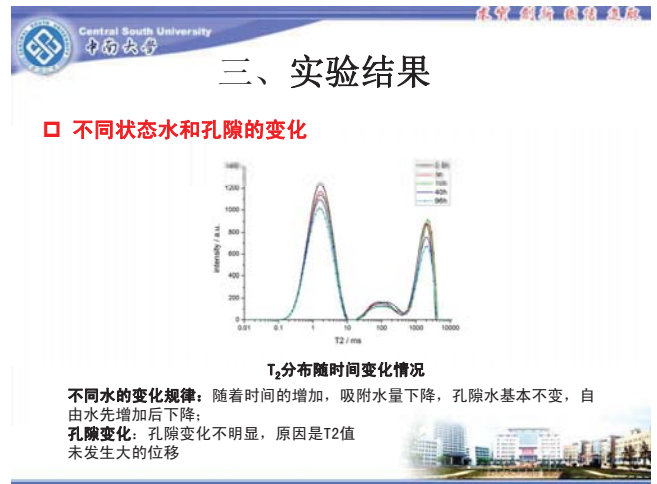
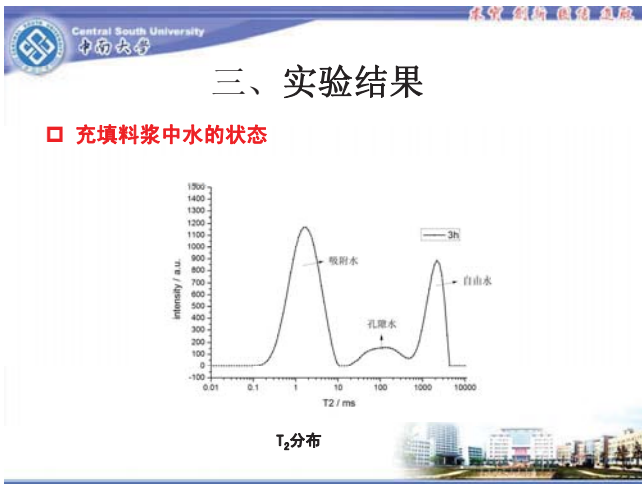
**充填立方体孔隙度与单轴抗压强度测定**  
选用7.07\*7.07模具，标准养护一定天数后饱水一天，再测定孔隙度和单轴抗压强度

Central South University  
中南大学

## 三、实验结果

□ 水分消耗观测

非化学结合水随时间变化情况





Central South University  
中南大学

### 充填体孔隙度与单轴抗压强度

灌模



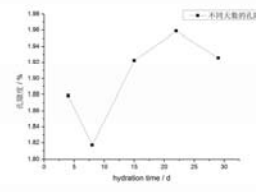
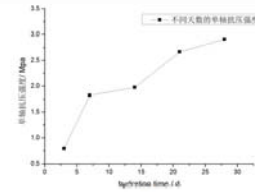
充填立方体






Central South University  
中南大学

### 充填体孔隙度与单轴抗压强度

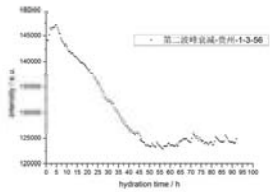
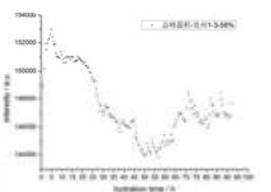






Central South University  
中南大学

### 四、探讨

通过试验数据对比发现，在50h后，水份含量会出现增加的情况，而且最大波峰与总峰面积下降的趋势不一致，因此，如何更好的选取检测指标？是选用峰面积还是最大波峰？

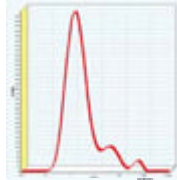
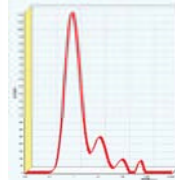
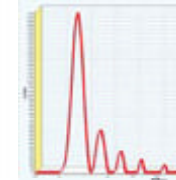






Central South University  
中南大学

### 四、探讨

不同反演次数的T2图谱，选用哪个比较好？

1w次                  10w次                  100w次






# 低场核磁技术在高分子领域的应用

纽迈科技有限公司应用部 杨翼



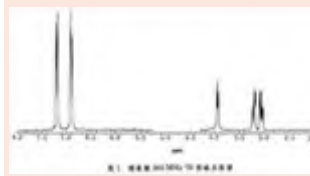
上海纽迈电子科技有限公司

当我们提起核磁共振或磁共振 (NMR or MRI)

第一时间想到的是.....

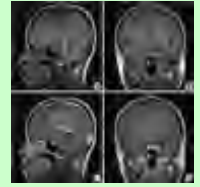


### NMRS 核磁共振波谱仪



核磁共振波谱分析——公认的化学品的最终结构分析方法，可以提供其他分析手段无法获得的决定性信息。广泛用于分子结构分析、结构鉴定、反应监测、定量分析。

### MRI 磁共振成像仪



医学磁共振成像——一项常规的医学检测手段，广泛应用于帕金森氏症、多发性硬化症等脑部与脊椎病变以及癌症的早期诊断与治疗。

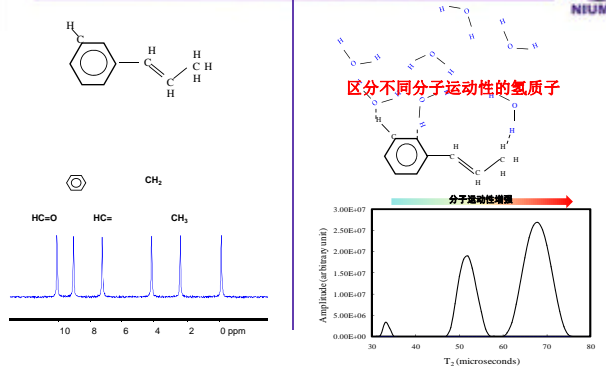
关于核磁共振，还有更多值得您了解的.....



- 台式核磁
- 小核磁
- 低场核磁
- 低分辨率核磁
- 时域核磁
- 核磁共振定量检测仪
- 核磁共振弛豫分析仪
- 微型磁共振成像系统



### 高场、低场比较



### 高场

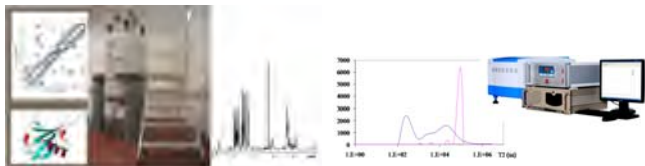
分子化学结构  
(化学位移)

- 1H、13C 常规测量
- 31P、15N、29Sz 等多核谱
- DEPT、HSQC、弛豫测量
- 活性肽、多肽类蛋白的溶液结构研究
- 化合物的结构、组分的鉴定
- 多维梯度实验
- .....

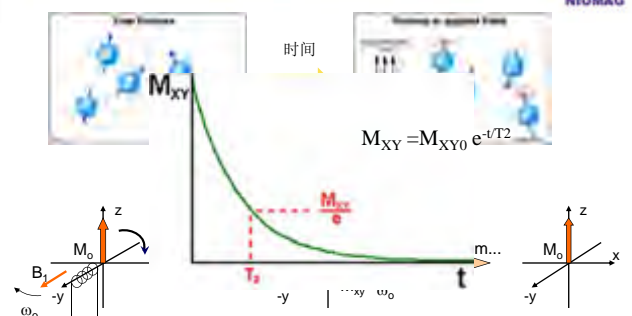
### 低场

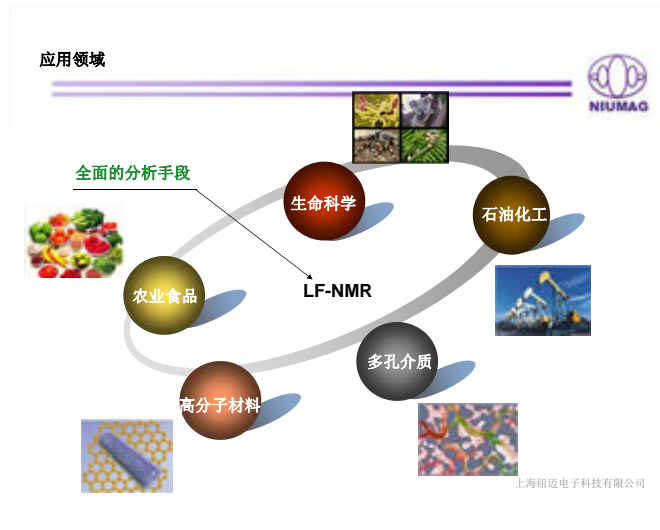
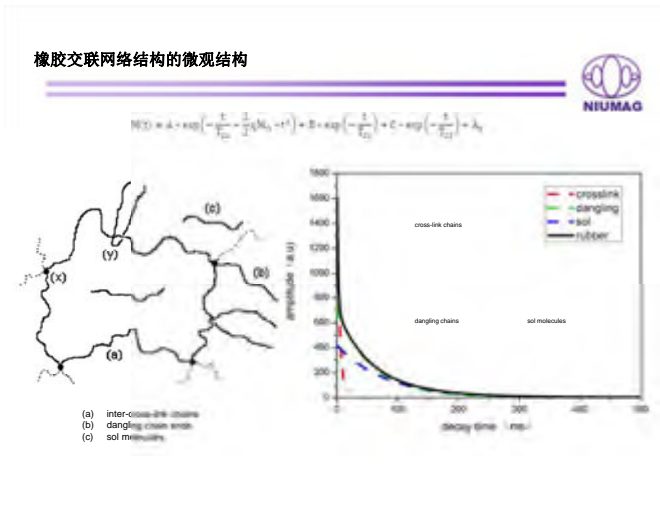
分子运动性  
(氢质子弛豫特性)

- 玻璃态转化温度
- 橡胶交联密度
- 造影剂弛豫率
- 孔径分布及孔隙度
- .....



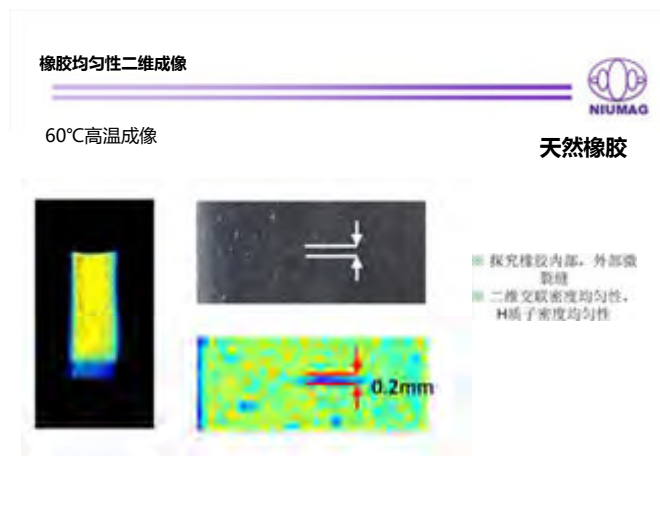
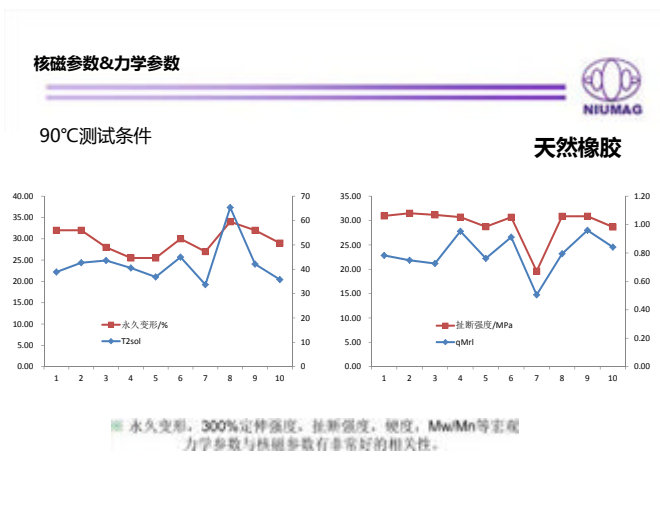
### 弛豫时间





### 应用领域

农业食品	生命科学	石油化工	材料科学
含油含水率 固体脂肪含量 水分相态及分布 明胶检测	动物组织成像 核磁造影剂开发 弛豫率分析 .....	岩心孔隙度 岩心饱和度 岩心渗透率 岩心孔隙分布 .....	水泥孔隙结构 热固性高分子固化 老化 橡胶交联密度 材料亲疏水表征 复合材料多相体系 相容性 结晶动力学 聚合反应程度 动态表征 .....

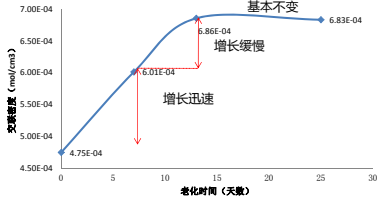


推进剂老化过程交联密度变化



60°C高温老化测试

推进剂老化实验交联密度推进图



参数：  
P1=3, P2=6;  
DL1=0.05;

应用领域



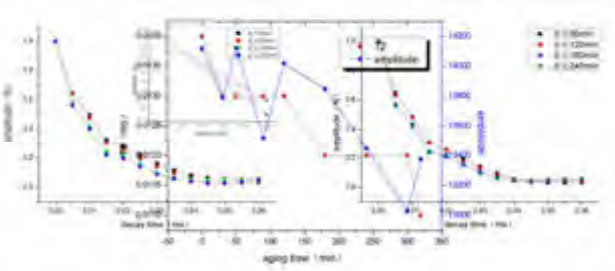
农业食品	生命科学	石油化工	材料科学
含油含水率 固体脂肪含量 水分相态及分布 明胶检测	动物组织成像 核磁造影剂开发 弛豫率分析 .....	岩心孔隙度 岩心饱和度 岩心渗透率 岩心孔隙分布	水泥孔隙结构变化 热固性高分子 橡胶交联密度 材料亲疏水表征 复合材料多相体系 相容性 结晶动力学 聚合反应反应程度 动态表征 .....

环氧树脂老化过程研究



利用FID序列衰减曲线, T2\*研究老化过程

155°C老化

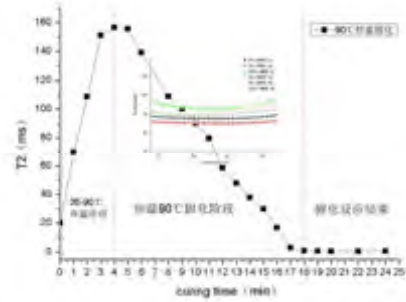


环氧树脂固化过程研究



利用CPMG序列, T2研究固化过程

90°C固化

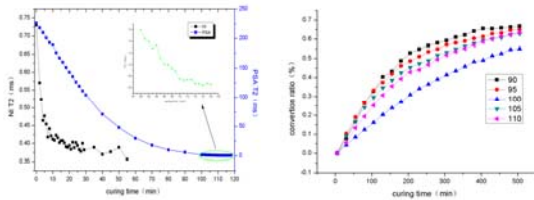


固化反应过程研究



利用T2的变化过程反应固化反应的过程

环氧树脂



T2

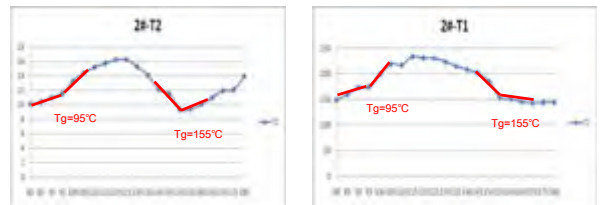
信号量

高分子材料玻璃化转变温度测试



T1, T2拐点即为玻璃化转变温度测试结果与DSC结果吻合

混合物



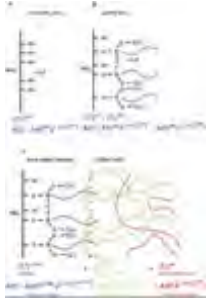
T2弛豫时间反映了样品内部氢质子所处的化学环境, 与氢质子所受的束缚力及其自由度有关, 而氢质子的束缚程度又与样品的内部结构有密不可分的关系。氢质子受束缚越大或自由度越小, T2弛豫时间越短。聚合物由玻璃态转变到橡胶态时, 含有质子的基团的运动频率增加, 链段运动发生急剧变化, 这些变化可由弛豫时间T1和T2来测量。

无机纳米材料与橡胶相容性研究



利用各组分的T2表征两者的结合情况

NR



$T_2^{OH}$ : 接枝在表面的链  
 $T_2^{OH}$ : 接枝在表面的链尾, 吸附水, 吸附材料

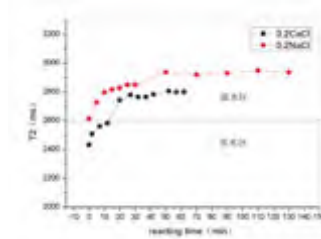
$T_2^N$ : 结合在二氧化硅上的橡胶链, 构成网络结构 (绿色线表示)  
 $T_2^f$ : 自由的橡胶分子链 (红色线表示)

亲疏水材料转变过程研究



动态定量监测材料的亲疏水性变化

纳米材料



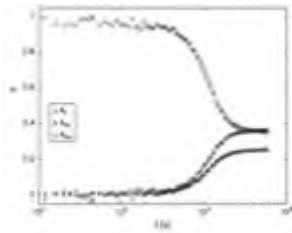
- ※ 纯水T2=2600ms
- ※ 当加入Ca<sup>2+</sup>, Na<sup>+</sup>纳米溶液中的纳米粒子表面的亲水基团变成疏水基团
- ※ 通过T2变化表征纳米颗粒表面亲疏水变化过程

结晶动力学



动态定量监测PP结晶过程中各组分变化

聚丙烯



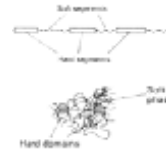
- ※ 样品中melt-like区内氢质子比例越来越少
- ※ 样品中晶体和非定型区内氢质子比例越来越大
- ※ 核磁法相比于X射线散射法和膨胀测定法能有效区分rigid-amorphous, melt-like amorphous phase的信号。

嵌段共聚物软硬段比例测试



采用嵌段共聚物模型模拟T2弛豫过程

软硬段



SS: Soft Segment  
 HS: Hard Segment

样品	1	2
$A_s$	30835	26727
$T_{2s}$	0.154	0.172
$A_h$	32429	32936
$T_{2h}$	0.355	0.427
$A_0$	234.994	400.350
硬段含量 = $A_h / (A_h + A_s)$	48.74%	44.80%
软段含量 = $A_s / (A_h + A_s)$	51.26%	55.20%

数据准确, 稳定

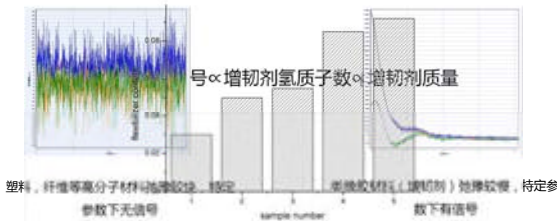
$$M(t) = A_s \exp\left(-\frac{t}{T_{2s}}\right) + A_h \exp\left(-\frac{t}{T_{2h}}\right) + A_0$$

高分子材料增韧剂含量测试



原理展现

含量测试



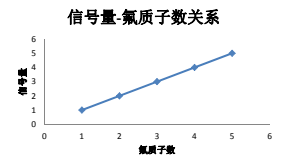
塑料, 纤维等高分子材料增韧剂含量测试, 标定 (增韧剂材料(增韧剂) 纯橡胶, 待定参数下无信号, sample number, 数下有信号)

氟橡胶含氟量



准确 快速 无损

氟橡胶



**谢谢聆听！**

2013-10-12



# 核磁共振技术在木材内水分迁移研究中的应用现状与前景

高鑫<sup>1</sup> 庄寿增\*

(南京林业大学 材料科学与工程学院, 南京)

**摘要** 核磁共振技术在木材科学研究领域已发挥了重要作用, 作为一种重要研究手段展现其他方法不可比拟的优势, 本文主要介绍其在木材内水分迁移研究中的应用现状, 并进一步展望了其发展应用前景。

**关键词** :核磁共振技术;木材;水分迁移;应用现状与前景

**Abstract** NMR the incomparable superiorities to other methods, has become a powerful analytical tool for wood science research. In this paper its application in wood moisture migration are summarized, and its future development is prospected.

**Key words** : NMR technology; wood; moisture migration; application and prospect

在木材科学领域, 木材内水分迁移规律及其动力学特性研究一直是科研人员关注的重点<sup>[1,2]</sup>, 长期以来, 人们一直基于传统的多孔介质流体迁移理论, Darcy与Fick定律, 结合木材构造特性来描述木材中水分的流动与扩散, 形成了较为系统的流体迁移理论体系, 在木材干燥、木材改性、人造板成型等生产环节的质量与能耗控制中发挥了重要作用, 促进了木材工业的发展<sup>[3]</sup>。

然而随着研究的深入, 人们发现用上述理论分析木材内流体实际迁移过程时仍存在一定的偏差。究其原因, 一是与木材结构复杂、变异性大有关, 二是与传统的测量方法测量精度差, 测试过程不连续有关<sup>[4-10]</sup>。

对木材内水分迁移路径的研究往往采用显微结构分析的方法进行, 此法仅能选择有代表性的木材细胞, 且在有限的视野范围内给出相应的评价, 对木材各类细胞叠加组合后形成的立体迁移路径无法进行准确的描述<sup>[4]</sup>。

基于核磁共振现象的波谱分析与成像技术, 可以非侵入式从待检试样中直接提取流体的信息, 不仅可以准确测量流体的分布和含量多少, 提供骨架物质的构造和解剖学信息, 而且可进行动态连续测试, 在多孔介质体系研究中表现出明显的优势<sup>[11]</sup>。木材是一种特殊的毛细管多孔材料, 近年来, NMR技术除在木材化学、木材改性、木材无损检测等领域取得较好研究成果外<sup>[12-14]</sup>, 在木材内部水分分布与迁移特性等研究方面也取得相当的进展。

## 1 木材中水分分布状态研究

应用NMR技术研究木材中水分分布状态可追溯到上世纪 50 年代, 日本学者在利用NMR技术研究纤维类材料性质时发现NMR信号可以区分木材内自由水与结合水<sup>[15]</sup>。此后 70-90 年代, 相关科研人员工作主要开展了NMR信号与木材水分关系的相关研究, 建立了自由衰减信号(FID)和木材含水率的函数关系, 根据测量到的FID信号就可以快速准确的确定木材含水率。大量的研究还表明木材内水分的弛豫特性与水分存在状态有关, 可以根据水分弛豫特性分析, 确定木材中自由水, 结合水分布与比例情况。根据弛豫时间的大小, 还可以对水分存在的位置作进一步的划分, 如细胞壁内水分弛豫时间一般为 0.1ms到几ms, 阔叶材木

<sup>1</sup>作者简介: 高鑫 (1986-), 在读博士研究生, 研究方向-木材干燥

\*通讯作者: 庄寿增 (1953-), 南京林业大学, 材料科学与工程学院教授, Email: szzhuang@njfu.edu.cn

纤维与针叶材管胞腔内自由水的弛豫时间为几十ms至一百ms，导管中自由水为一百至几百ms，通过水分弛豫特性分析，甚至也可以对早、晚材，幼龄材与成熟材，已腐朽、霉变木材与正常材加以区分<sup>[16-22]</sup>。

2000年以来，随着NMR技术的发展与仪器性能进一步提高。有关纤维饱和点的研究取得一定进展。纤维饱和点（Fiber Saturation Point, FSP）是指木材细胞壁基质到达饱和但细胞腔内不含自由水时的木材含水率，FSP是木材科学中非常重要的概念，它几乎是木材所有物理力学性能的转折点，对于各类模型的构建具有重要意义。传统的测量纤维饱和点的方法主要有外推法、干缩法、热分析法、溶液置换法等，由于这些测试过程复杂、耗时长，加之木材树种繁多，所以在实际应用中一般忽略树种之间的差异，统一取30%。随着研究的深入，对不同树种FSP的准确测量也有了新的需求。Ville Veikko探讨了一种利用NMR技术快速、精确测量纤维饱和点的方法，木材生材样品经冷冻处理后，在NMR分析仪内经短时间扫描就可获得与传统溶液置换法高度吻合的FSP数值<sup>[23]</sup>。

## 2 木材内水分迁移过程研究

当前，用核磁共振技术研究木材中自由水迁移过程，主要通过磁共振成像技术进行水分迁移过程的可视化分析，进一步确定水分迁移的主要路径；对结合水扩散主要通过木材内水分迁移方向含水率变化的连续测量及其弛豫特性分层分析，确定水分扩散模型。

James利用医用核磁对不同干燥阶段的木材进行成像分析时，发现在FSP以上木材弦切板木射线一直呈高亮的状态，说明木射线是自由水径向迁移的重要路径<sup>[24]</sup>。Meder在进行成像分析时发现，木材断面晚材带往往保持较高的亮度，说明同样的干燥条件下晚材部分干燥速度较慢<sup>[25]</sup>。

G. Almeida将磁共振成像与膜压室技术相结合，对花旗松内自由水定向迁移过程进行成像分析时发现，其晚材部分首先失水，待晚材自由水几乎迁移完毕后，早材部分水分才开始失水，这与传统认为的木材中自由水迁移路径有明显不同。进一步的研究发现细胞腔直径较大的早材管胞内水分后迁移是由于其早材部分易形成闭塞纹孔，使得早材细胞腔内自由水的表面张力变大的缘故<sup>[26]</sup>。这说明木材内自由水迁移过程是动态变化的，并不完全受细胞腔半径大小的支配，干燥过程中出现的纹孔闭塞等现象可能对水分迁移路径产生显著的影响。

木材中结合水扩散通常认为遵循Fick扩散定律，尽管有人曾提出木材内水分可能存在非Fick扩散现象，但由于目前研究中多采取传统破坏性的切片法，通过试验验证难度较大。Sergey V. Dvinskikh通过利用NMR技术对云杉木材进行弛豫特性分层分析，获得水分扩散方向上的含水率连续变化情况，进一步验证了木材内结合水迁移的非Fick型扩散特征，同时也为NMR技术在木材水分扩散理论研究中的进一步应用提供了参考与经验<sup>[27]</sup>。

国内学者也曾利用NMR技术对木材中结合水吸附机理进行了初步探讨<sup>[28]</sup>。

## 3 NMR技术在木材内水分迁移研究中的应用前景

在木材科学研究中，木材内水分迁移过程通常是在较高的温度和压力条件下完成的，这就需要相关的NMR测试技术能够满足样品测试过程中的变温变压条件需求。近年来国内核磁共振技术，特别是低场核磁共振应用技术发展迅速，仪器测试精度及功能化、个性化程度的不断提高，扩大了其在多孔介质研究领域的应用范围，发挥了一些其他测试技术无法替代的作用。为进一步深入进行木材在



真空、微波等复杂环境下的干燥与改性技术研究提供了必要的保证。

随着核磁共振理论与技术的不断完善,NMR 技术有望在木材水分迁移路径、驱动力及其迁移模型研究中发挥重要作用。

### 参考文献

- [1]王金满,戴澄月,刘一星.木材渗透性的研究.东北林业大学学报.1990, 4:51-56
- [2]侯祝强,庄作峰.木材流体渗透性研究的发展与趋势.世界林业研究.1999, 1:34-37
- [3]鲍甫成,吕建雄.中国重要树种木材流体渗透性的研究.林业科学.1992, 3:238-246
- [4]Lisbeth GT, Thomas E. Moisture in untreated, acetylated, and furfurylated NORWAY spruce studied during drying using time domain NMR. Wood and Fiber Science. 2008, 40(3):309 – 320
- [5]Siau JF. Flow in wood. Syracuse Univ Press. Syracuse, 1971
- [6]Siau JF. Transport processes in wood: Springer series in wood science Springer-Verlag. 1984
- [7]D.Wu, XF.Peng. Saturation evolution induced by inner pore structural effects in a porous material during wetting. International Journal of heat and mass transfer. 2009, 52:4664-4668
- [8]Martine G. A film-flow model to describe free water transport during drying of a hygroscopic capillary porous medium. Transport in Porous Media. 2002, 48: 125–158
- [9]Wadso L. Unsteady-state water vapor adsorption in wood: An experimental study. Wood Fiber Sci. 1994, 26:36–50.
- [10]Wadso L. Describing non-Fickian water vapor sorption in wood. J.Mater.Sci.1994, 29:2367–2372.
- [11]肖立志.核磁共振成像测井与岩石核磁共振及其应用[M].北京:科学出版社. 1998
- [12]梅超群, 樊永明, 江进学等. 核磁共振波普在木材改性中的应用. 应用化工. 2009, 38(6):880-883
- [13]陆方, 程海涛, 王戈, 郭雪峰. 核磁共振技术在竹木研究中的应用. 竹子研究汇刊. 2007, 26(1): 37-41
- [14]王立海, 杨学春, 徐凯宏. 木材缺陷无损检测技术研究现状. 林业科技. 2002, 27(3): 35-38
- [15] Akira Odajima. Nuclear Magnetic Resonance Studies of Water Sorbed on Fibrous Materials. J. Phys. Soc. Jpn. 1959, 14:308-312
- [16]Sharp AR, Riddin MT. Determination of moisture content of wood by pulsed nuclear magnetic resonance. Wood Fiber. 1978, 10 (2):74-81
- [17]Riggin MT, Sharp AR, Kaiser R, Schneider MH. Transverse NMR relaxation of water in wood. Journal of Applied Polymer Science. 1979, 23:3147-3154
- [18]Menon RS, Mackay AL. An NMR determination of the physiological water distribution in wood during drying. J. Appl. Polym.Sci. 1987, 33:1141-1155
- [19]Flibotte S, Menon AL, MacKay AL, Hailey JRT. Proton magnetic resonance of western red cedar. Forest. Prod. J. 1990, 22:362–376.
- [20] Araujo CD, MacKay AL, Hailey JRT, Whittall KP, Le H. Proton magnetic resonance techniques for characterization of water in wood: application to white spruce. Wood Sci. Technol. 1992, 26:101–113
- [21] Nicole L, Bernard De J. Time-domain 1H NMR characterization of the liquid phase in greenwood. Holzforschung. 2006 60:265-270
- [22]李超,张明辉,于建芳.利用核磁共振自由感应衰减曲线测定木材含水率.北京林业大学学报. 2012, 34 (4):142-145
- [23]Ville V.Telkki, Miikka Yliniemi and Jukka Jokisaari .Moisture in softwoods: fiber saturation point, hydroxyl site content, and the amount of micropores as determined from NMR relaxation time distributions. Holzforschung 2013, 67(3):291-300
- [24]James RO. Nuclear magnetic resonance imaging: a noninvasive analysis of moisture distribution in white oak lumber. Can.J.For.Res. 1990, 20: 586-591

- [25]R Meder. Observation of anisotropic water movement in Pinus radiata, D. Don sapwood above fiber saturation using magnetic resonance micro-imaging. Holz als Roh- und Werkstoff. 2003, 61:251–256
- [26]G. Almeida, S. Leclerc, P. Perre. NMR imaging of fluid pathways during drainage of softwood in a pressure membrane chamber. International Journal of Multiphase Flow 2008, 34 :12–321
- [27] Sergey V.Dvinskikh, Marielle Henriksson et al, NMR imaging study and multi-Fickian numerical simulation of moisture transfer in Norway spruce samples. Engineering Structures. 2011, 33 :3079-3086
- [28]马大燕,王喜明,张明辉.核磁共振研究木材吸着过程中水分吸附机理.波普学杂志.2011, 28(1):135-141

# A Method To Measure Internal Contact Angle in Opaque Systems by Magnetic Resonance Imaging

Wei Qin Zhu,<sup>†</sup> Ye Tian,<sup>‡</sup> Xue Feng Gao,<sup>†</sup> and Lei Jiang<sup>\*,‡,§</sup>

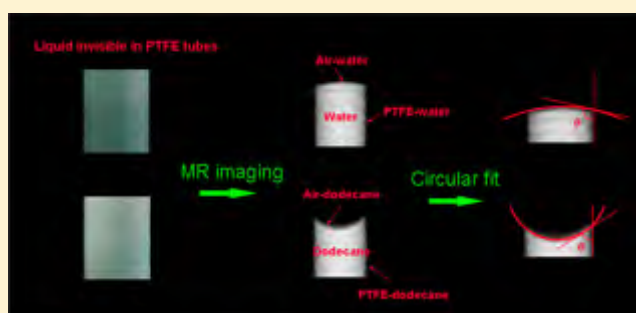
<sup>†</sup>Nanobionic Research Division, Suzhou Institute of Nano-technology and Nano-bionics, Chinese Academy of Science, No. 398 Ruoshui Road, Suzhou, Jiangsu Province 215123, People's Republic of China

<sup>‡</sup>Beijing National Laboratory for Molecular Sciences (BNLMS), Key Laboratory of Organic Solids, Institute of Chemistry, Chinese Academy of Science, Beijing 100190, People's Republic of China

<sup>§</sup>School of Chemistry and Environment, Beihang University, Beijing 100191, People's Republic of China

## S Supporting Information

**ABSTRACT:** Internal contact angle is an important parameter for internal wettability characterization. However, due to the limitation of optical imaging, methods available for contact angle measurement are only suitable for transparent or open systems. For most of the practical situations that require contact angle measurement in opaque or enclosed systems, the traditional methods are not effective. Based upon the requirement, a method suitable for contact angle measurement in nontransparent systems is developed by employing MRI technology. In the Article, the method is demonstrated by measuring internal contact angles in opaque cylindrical tubes. It proves that the method also shows great feasibility in transparent situations and opaque capillary systems. By using the method, contact angle in opaque systems could be measured successfully, which is significant in understanding the wetting behaviors in nontransparent systems and calculating interfacial parameters in enclosed systems.



## INTRODUCTION

Contact angle is an important parameter in wettability characterization.<sup>1–6</sup> During the past decades, a number of approaches have been developed to measure the liquid contact angle on solid surfaces, such as Wilhelmy plate method,<sup>7</sup> drop shape analysis method,<sup>8,9</sup> and tip-based method for micro-/nanoscale wettability characterization.<sup>10–12</sup> However, limited by the imaging and analyzing processes, the methods are only suitable for transparent or open systems. For many practical situations in which contact angle measurements in opaque or enclosed systems are required, these methods are not effective. For instance, in the pipeline drag-reducing research, the contact angle of the liquid flow that is closely related to the drag reduction efficiency is hard to calculate due to the difficulty of fluid imaging in nontransparent pipelines,<sup>13</sup> or in the blood transportation researches, the blood contact angle in the vessels that gives knowledge about the blood–vessel interaction is difficult to measure due to the noninvasive property of blood vessels,<sup>14</sup> likewise for the internal contact angle measurement in Lab-on-a-chip systems<sup>15,16</sup> and fuel cell systems.<sup>17</sup> Therefore, the presentation of a method that is available for the liquid contact angle measurement in opaque systems is necessary.

Magnetic resonance imaging (MRI) is a technology that outputs images by collecting the MR signals emitted from the irradiated <sup>1</sup>H nucleus in gradient magnetic fields.<sup>18–20</sup> Because of the special sensitivity to hydrogen nucleus, MRI technology

has been widely used in internal body structure imaging,<sup>21</sup> fluidic research,<sup>22,23</sup> oil–water content analysis in rock cores,<sup>24</sup> and also proved effective in interfacial researches.<sup>25,26</sup> Because no optical transparency is required during the imaging process, MRI technology provides a great opportunity for liquid imaging in opaque systems. In this Article, the technology is employed to image the liquid profiles in opaque cylindrical tubes, and a method suitable for internal contact angle measurement in opaque systems is presented. It is indicated that the MRI method is highly feasible for contact angle measurement, especially suitable for opaque or enclosed systems. The method also shows great feasibility in transparent situations and opaque capillary systems. The research is expected significant in developing new ways to understand wetting behaviors in nontransparent systems, such as fluid control in lab-on-a-chip systems and interfacial parameter measurement in inaccessible systems.

## EXPERIMENTAL SECTION

**Materials.** Distilled water, dodecane (99%, Ourchem, Sinopharm Chemical Reagent Co. Ltd.), poly tetrafluoroethylene (PTFE), and polyamide (PA) tubes with inner diameters of 4, 6, 8, and 10 mm and

Received: December 13, 2012

Revised: February 9, 2013

Published: February 11, 2013

wall thickness of 1 mm were used, as well as a glass tube with an inner diameter of 5 mm.

**Equipment.** MRI measurements were performed on a 0.5 T MRI system (NMI20-Analyst, Niumag, China). Snapshots of the samples were taken by a digital camera (Canon Lunix 1860). The transmitting optical images of the liquid-glass systems were taken by a high resolution optical camera equipped on a contact angle measurement device (OCA20, Dataphysics, Germany). The interfacial curve fitting and contact angle computation was accomplished by using the software of SCA20 (Dataphysics, Germany).

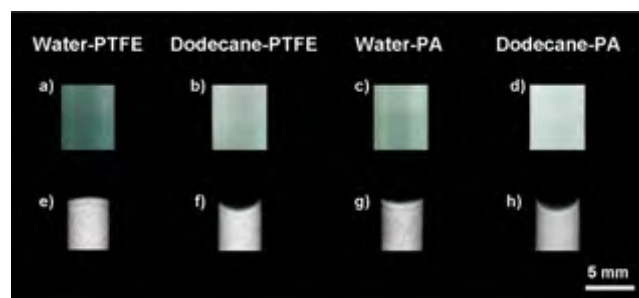
**Sample Preparation.** Two types of opaque cylindrical tubes were employed for the opaque system construction. For hydrophobic systems, PTFE tubes were used; for hydrophilic systems, PA tubes were used. In the experiment, the tubes were cut into small pieces with the length of 25–30 mm, and the small pieces were plugged with PTFE plugs at one end, leaving the other end open. The liquid then was injected into the small tubules by a syringe from the open end. The volume of the liquid was carefully controlled according to the internal diameter of the tubes, making sure that the height of liquid column inside the tubes is less than 20 mm (equipment limitation). The open end of the tubule then was enclosed by PTFE tapes. The liquid-tube systems were placed vertically into a 15 mm glass tube and positioned using PTFE O-rings so that the cross-section to be imaged was through the central axis of the probe coil. Finally, the glass tube was inserted into the MRI coil probe for MRI measurement.

**MRI Measurement.** MR images were achieved at a nominal proton resonance frequency of 23 MHz using the multispin echo (MSE) sequence, the timing diagram of which was shown in Figure S1a (Supporting Information). The echo time (TE) for the MR imaging is 10.6 ms. The repetition times (TR) of 1028.6 and 528.6 ms were used for water and dodecane imaging, respectively. 128 phase encodes were used during the imaging process. The image slice and its correlation with the gradient fields were schematically shown in Figure S1b (Supporting Information). For the MRI measurement, the image slice could be located vertically either to the X axis or to the Z axis due to the symmetry of the tubing systems. In this study, the Z axis was used as the imaging direction. The results obtained by the X axis are similar. The temperature of the MRI probe is 32 °C.

**Contact Angle Measurement.** The MR images were enlarged 5–10 times to their original sizes for contact angle measurement. The contact angles of the liquid inside the tubes then were measured by three steps: baseline determination, circle fitting, and contact angle measurement. In the experiments, the contact angles on the left and right side were measured three times, respectively, and the average value was used as the internal contact angle value.

## RESULTS AND DISCUSSION

**MR Images of Liquid in Opaque Systems.** Shown in Figure 1 are the optical and MR images of the liquid/opaque-tube systems, in which the water/PTFE-tube, dodecane/PTFE-tube, water/PA-tube, and dodecane/PA-tube systems are included. The internal diameters of the opaque tubes are 4 mm. Figure 1a–d shows the optical images of the liquid-tube systems, in which all of the opaque systems appear similar and the liquid profile inside the tubes cannot be viewed. Figure 1e–h exhibits the MR images of the liquid-tube systems. According to the imaging mechanism of MRI, the white areas in the images represent the distribution of protons in the systems. Because no hydrogen nuclei were contained in the PTFE tubes, the white areas in Figure 1e and f are only attributed to water and dodecane. In the liquid-PA tube systems, although the PA tubes are H-contained, the MR signals of protons in PA tubes cannot be collected by the MSE imaging method because the relaxation time of the hydrogen nucleus of the PA materials is much shorter than that of protons in the water and dodecane. Therefore, the protons in PA tubes do not show up in the MR images, and the white areas in Figure 1g and h only present the

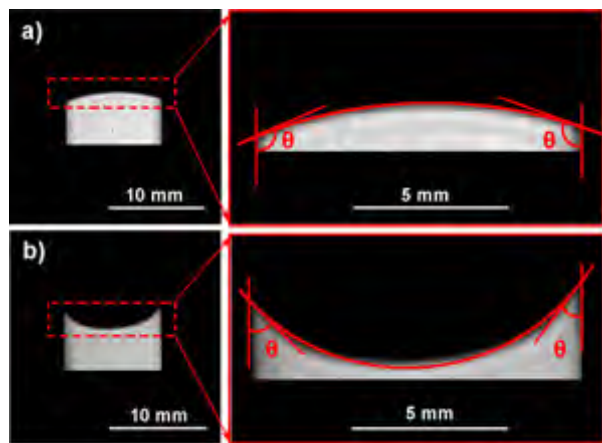


**Figure 1.** Liquid profiles in 4 mm opaque cylindrical tubes, where the water/PTFE-tube, dodecane/PTFE-tube, water/PA-tube, and dodecane/PA-tube systems are included. (a–d) Optical images of the opaque liquid-tube systems, in which the appearances of the systems are similar and the liquid profiles inside the tubes are invisible due to the nontransparency. (e–h) MR images of the liquid-tube systems. The white areas in the MR images represent the liquid profiles inside the opaque tubes. The air–liquid and liquid–solid interfaces are clearly exhibited in the MR images, which makes it feasible to measure contact angles.

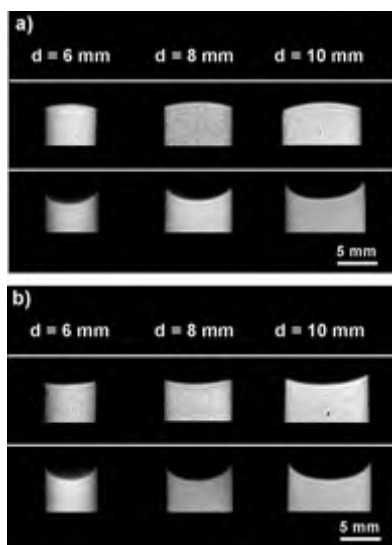
proton distribution in water and dodecane. The images prove that, by MR imaging, the liquid profiles that are invisible optically can be imaged clearly and the curvature of the air–liquid interfaces and the straight line of the liquid–solid interfaces could be observed distinctively.

**MRI-Based Contact Angle Measurement.** MR images of the liquid profiles were amplified, and the contrast and brightness of the images were adjusted carefully so that the liquid boundaries were exhibited clearly. In the experiments, the baseline was determined by drawing a straight line at the solid–liquid boundary, and a circle was fitted to the air–liquid interface by picking plenty of air–liquid boundary points. The contact angles were then measured between the baseline and the line tangent to the air–liquid circle at the three-phase contact angle. On the basis of the MR images in Figure 1e–h, the values measured are  $110.7^\circ \pm 2.0^\circ$ ,  $35.3^\circ \pm 2.5^\circ$ ,  $61.8^\circ \pm 3.1^\circ$ , and  $33.3^\circ \pm 2.8^\circ$ , respectively, which correspond to the systems of water/PTFE-tube, dodecane/PTFE-tube, water/PA-tube, and dodecane/PA-tube, respectively. The results indicate that the inner surfaces of the PTFE tubes are hydrophobic and oleophilic, while the inner surfaces of PA tubes are hydrophilic and oleophilic. As compared to the value of  $108^\circ$  on the flat PTFE surfaces, the internal contact angle of water inside the 4 mm PTFE tube is a little higher, which might be caused by the capillary effect of the hydrophobic tube.<sup>27,28</sup> The process for the contact angle measurement is schematically shown in Figure 2, in which the circular fit, baseline determination, and contact angle measurement were illustrated.

**Tube Diameter Dependence.** An important observation is that, unlike a constant value on flat surfaces, the liquid contact angles inside cylindrical tubes vary slightly with the tube diameter increasing. Figure 3 exhibits the MR images of water and dodecane in the PTFE (Figure 3a) and PA (Figure 3b) tubes with tube diameters of 6, 8, and 10 mm, respectively. With the tube diameter increasing from 6 to 10 mm, the air–liquid interfaces are flattened slightly and the contact angle measurement is subsequently influenced. Figure 4a plots the diameter dependence of water and dodecane contact angle in PTFE tubes. It is indicated that, with the tube diameter increasing, the water contact angles inside the PTFE tubes decrease slightly, while the dodecane contact angles increase slightly. Figure 4b exhibits that both the water and the

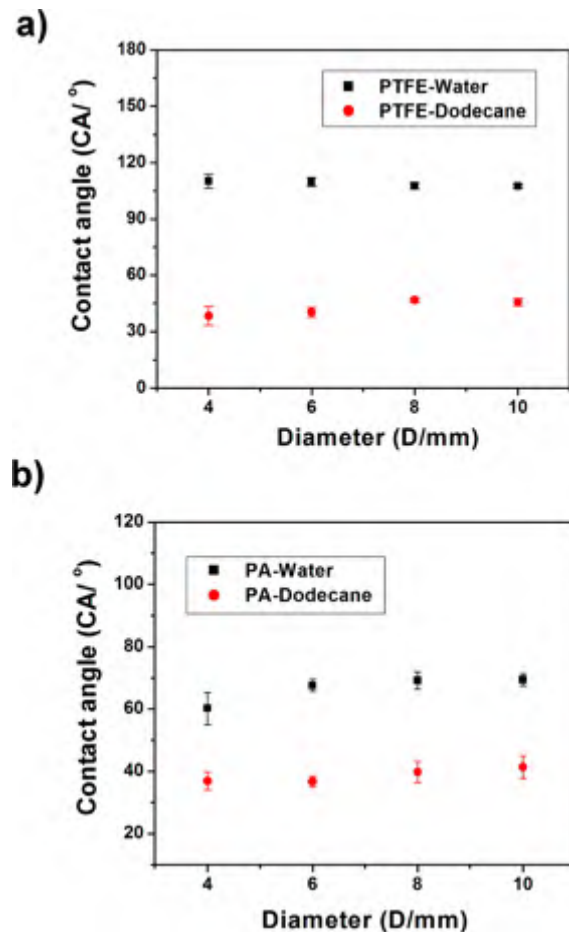


**Figure 2.** Process of the contact angle measurement based upon MR images. (a) Contact angle measurement on a convex air–liquid interface. (b) Contact angle measurement on a concave air–liquid interface. For the contact angle measurement, the areas of the air–liquid interfaces, together with the solid–liquid interfaces, are amplified 5 times to their original sizes. A circle is then fitted to the air–liquid interface, and the baseline is determined by drawing a straight line along the liquid–solid interface. By measuring the angle between the baseline and the line tangent to the circle at the three-phase contact point, the value of the internal contact angle is obtained.



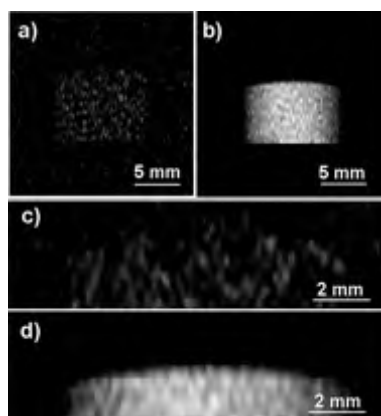
**Figure 3.** Variation of the MR images of liquid profiles in opaque tubes with the tube diameter increasing. (a) Water (upper part) and dodecane (lower part) in PTFE tubes; (b) water (upper part) and dodecane (lower part) in PA tubes. With the tube diameter increasing, the air–liquid interfaces tend to be flattened by the gravity of the liquid.

dodecane contact angle inside PA tubes increase slightly with the tube diameter increasing. The phenomenon is believed induced by the competition between the nonignorable gravity of the liquid and capillary pressure.<sup>29</sup> With the tube diameter increasing, the effect of capillary pressure that keeps the air–liquid interfaces spherical decreases, and the effect of liquid gravity that tends to flatten the air–liquid interfaces increases. Therefore, the curvatures of the air–liquid interfaces tend to be flattened, and a deviation from spherical cap is formed, which induces the slight variation of the contact angle values.<sup>30,31</sup>



**Figure 4.** Tube diameter dependence of the internal contact angles. (a) Variations of water and dodecane contact angles against the PTFE tube diameters. With the tube diameter increasing, the water contact angle inside PTFE tubes decreases slightly and the dodecane contact angle increases. (b) Variations of water and dodecane contact angle against PA tube diameters. Both the water and the dodecane contact angle increase slightly with tube diameter increasing.

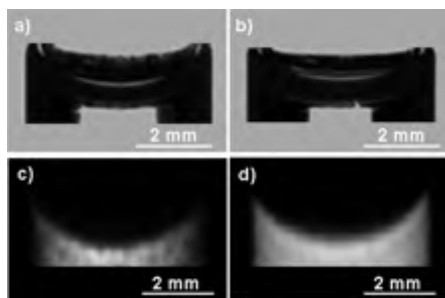
**Influence of MRI Parameters.** MRI method for contact angle measurement is based upon the MR image of liquid profile. Therefore, the acquisition of MR images with clear boundaries is of special importance. During the MR imaging procedures, a number of MRI parameters have an influence on the image quality.<sup>32</sup> For specific equipment and samples, however, TR and the slice thickness play the main role. Figure 5 shows the effect of TR on the appearance of the MR images of water. Shown in Figure 5a is the MR image of water profile inside a 10 mm PTFE tube, which is collected by using the TR of 128.6 ms. The image has a mottled appearance due to the low signal/noise (S/N) ratio. By increasing the TR to 828.6 ms, the image appearance is smoothed dramatically, as shown in Figure 5b. The standard deviation of the contact angle value measured based upon the magnified liquid boundary in Figure 5c is 4.8%, while that measured by Figure 5d is 1.7%, which indicated that, for contact angle measurement, longer TR is preferred. However, it should be noted that the increase of TR is at the expense of imaging time. In this study, the TR of 1028.6 ms for water samples and 528.6 ms for dodecane samples proves suitable. The slice thickness also has an influence on image quality. Because of the insufficient MR signals, MR image collected by a thin slice has a speckled



**Figure 5.** (a,b) MR images of water inside 10 mm PTFE tubes that were collected by using the TR of 128.6 and 828.6 ms, respectively. (c,d) Amplifications of the air–water interfaces in (a) and (b), respectively. The image acquired by short TR has a mottled appearance, and the appearance of the image collected by long TR is much smoother. The amplified liquid boundaries in (c) and (d) indicated that long TR was preferred for contact angle measurement.

appearance and low S/N ratio. Comparatively, that obtained by a thick slice appears much smoother. The MR images of water in PTFE tubes, which are collected by 2 and 10 mm slice thickness, are shown in Figure S2a and b (Supporting Information), respectively. The standard deviations of the contact angle measured based on the images are 2.8% and 0.7%, corresponding to the slice thicknesses of 2 and 10 mm, respectively.

**Application in Transparent Systems.** Even in transparent systems, the MRI method exhibits a distinct advantage in internal contact angle measurement. Shown in Figure 6a and

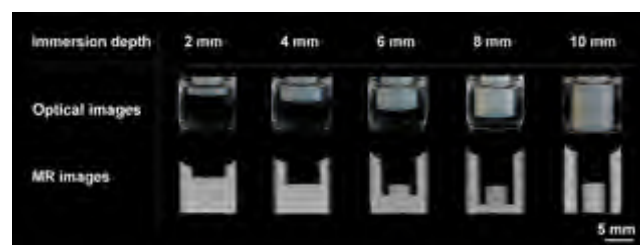


**Figure 6.** Optical and MR images of liquid profiles in 5 mm glass tubes. (a) Optical image of water/glass-tube system; (b) optical image of dodecane/glass-tube system; (c) MR image of water profile in the glass tube; and (d) MR image of dodecane profile in the glass tube. Although the liquid profiles can be viewed by optical imaging, the accurate cross-section of the liquid boundaries is difficult to be imaged. By MR imaging, the cross-section of the liquid boundaries is imaged clearly, and contact angle measurement can be performed easily. The contact angles measured on the basis of MR images are  $24.5^\circ \pm 2.8^\circ$  for the water/glass-tube system and  $24.3^\circ \pm 2.7^\circ$  for the dodecane/glass-tube system.

b are the optical images of water and dodecane in 5 mm glass tubes. In the glass tubes, although the liquid profile can be imaged optically, the air–liquid interfaces, the liquid–solid boundaries, and the three phase contact points, which are the key factors for contact angle measurement, are difficult to locate. Thus, it is hard to measure the contact angle accurately. Contrastively, by the MRI technology, the images of liquid

profiles were obtained with clear boundaries and contact points. As shown in Figure 6c and d, the concave air–liquid interfaces, straight liquid–solid interfaces, and the three-phase contact points were clearly exhibited, which made it easy to fit the interface curves and measure contact angle values. The values of internal contact angles measured based on the MR images are  $24.5^\circ \pm 2.8^\circ$  for water and  $24.3^\circ \pm 2.7^\circ$  for dodecane with the standard deviations of 11.4% and 11.1%, respectively. The standard deviations of contact angle values measured based on the optical images are 17% for water/glass-tube system and 20% for dodecane/glass-tube system, which is caused by the uncertainty in locating the interface curves and three-phase contact points during the contact angle measurement procedure.

**Capillary Effect in Opaque Systems.** By optical methods, the capillary effect in a nontransparent system is difficult to observe. As shown in the optical images in Figure 7, the water



**Figure 7.** Visualization of the capillary effect in an opaque 4 mm PTFE tube, which is placed vertically into a water reservoir. By MR imaging, the capillary effect inside the opaque hydrophobic tube was exhibited clearly, which is significant in driving force calculation and fluid manipulation.

profile inside a PTFE cylindrical tube ( $d = 4$  mm) placed vertically in a water reservoir is hard to view by optical imaging. With the immersion depth increasing from 2 to 10 mm, no difference inside the PTFE tube could be observed. In contrast, in the MR images, the variation of water column inside the PTFE tube is exhibited clearly. It is shown that, when the immersion depth of the PTFE tube is lower than 4 mm, no water enters the PTFE tube, which indicates that the hydraulic pressure is not large enough to overcome the water surface tension at the entrance of the hydrophobic tube and thus drive water into the PTFE tube.<sup>33</sup> With the immersion depth approaching 6 mm, a water column with a convex meniscus emerges inside the PTFE tube, indicating that the capillary pressure is overcome by the hydraulic pressure and water is driven into the PTFE tube.<sup>34,35</sup> When the immersion depth increases from 6 to 10 mm, the height of water column inside the PTFE tube increases, while the relative height of the water column (difference between the top of the water column and the outer water level) remains constant, implying that the force equilibrium between the hydraulic pressure and capillary pressure is reached.<sup>35</sup> Thus, the capillary pressure in the opaque hydrophobic tube could be calculated by measuring the height of the water column. Combined with the internal contact angle measurement, the method is promising in developing new ways to calculate fluid driving forces, which is of great significance in fluid manipulation.

## CONCLUSIONS

In summary, a method that allows contact angle measurement in opaque systems was presented by employing MR imaging.

The basic principle of the method was demonstrated by measuring the internal contact angle of liquid in opaque cylindrical tubes. It is indicated that the value of the internal contact angle was slightly influenced by the tube diameters and MRI parameters. The method also exhibits feasibility in transparent systems and shows great potential in opaque capillary effect investigation. It should be noted that, although the MRI method was herein demonstrated by using the circle fitting process, other approaches based upon the liquid-profile analysis are also applicable to the method. For example, when the tube diameter is sufficiently small and the liquid gravity is ignorable in the systems, the contact angle can be calculated by measuring the meniscus height and the tube diameter; when the tube diameter increases to such a large size that the liquid gravity flattens the liquid meniscus dramatically, the contact angle can be computed by the measurement of the height of the meniscus on the tube wall. Another point that needs to be mentioned is that, for liquid with extremely high or low internal contact angle values, measurement error might be increased because of the increase of the operator bias,<sup>29</sup> the difficulties in locating the contact point and liquid boundaries,<sup>36</sup> as well as the insufficient MR signals of liquid adhered to the tube walls. The research reported in this Article proved that the MRI method is highly feasible in contact angle measurement in opaque systems, which is significant in understanding the wetting behaviors in nontransparent systems and calculating interfacial parameters in enclosed systems.

## ■ ASSOCIATED CONTENT

### ● Supporting Information

MRI experiment and influence of the slice thickness. This material is available free of charge via the Internet at <http://pubs.acs.org>.

## ■ AUTHOR INFORMATION

### Corresponding Author

\*Tel.: (+86) 10-82621396. Fax: (+86) 10-82627566. E-mail: [jianglei@iccas.ac.cn](mailto:jianglei@iccas.ac.cn).

### Notes

The authors declare no competing financial interest.

## ■ REFERENCES

- (1) Yao, X.; Song, Y.; Jiang, L. Applications of Bio-Inspired Special Wettable Surfaces. *Adv. Mater.* **2011**, *23*, 719–734.
- (2) Quéré, D. Wetting and Roughness. *Annu. Rev. Mater. Res.* **2008**, *38*, 71–99.
- (3) Krumpfer, J.; McCarthy, T. Dip-Coating Crystallization on a Superhydrophobic Surface: A Million Mounted Crystals in a 1 cm<sup>2</sup> Array. *J. Am. Chem. Soc.* **2011**, *133*, 5764–5766.
- (4) Zhang, X.; Shi, F.; Niu, J.; Jiang, Y.; Wang, Z. Superhydrophobic Surfaces: from Structural Control to Functional Application. *J. Mater. Chem.* **2008**, *18*, 621–633.
- (5) Feng, L.; Zhang, Y.; Cao, Y.; Ye, X.; Jiang, L. The Effect of Surface Microstructures and Surface Compositions on the Wettabilities of Flower Petals. *Soft Matter* **2011**, *7*, 2977–2980.
- (6) Zhang, X.; Zhang, J.; Ren, Z.; Li, X.; Zhang, X.; Zhu, D.; Wang, T.; Tian, T.; Yang, B. Morphology and Wettability Control of Silicon Cone Arrays Using Colloidal Lithography. *Langmuir* **2009**, *25*, 7375–7382.
- (7) Wu, N.; Dai, J.; Micale, F. Dynamic Surface Tension Measurement with a Dynamic Wilhelmy Plate Technique. *J. Colloid Interface Sci.* **1999**, *215*, 258–269.
- (8) Hoorfar, M.; Neumann, A. Recent Progress in Axisymmetric Drop Shape Analysis (ADSA). *Adv. Colloid Interface Sci.* **2006**, *121*, 25–49.
- (9) Meiron, T.; Marmur, A.; Saguy, I. Contact Angle Measurement on Rough Surfaces. *J. Colloid Interface Sci.* **2004**, *274*, 637–644.
- (10) Fabié, L.; Ondarçuhu, T. Writing with Liquid using a Nanodispenser: Spreading Dynamics at the Sub-micron Scale. *Soft Matter* **2012**, *8*, 4995–5001.
- (11) Ishida, N.; Inoue, T.; Miyahara, M.; Higashitani, K. Nano Bubbles on a Hydrophobic Surface in Water Observed by Tapping-Mode Atomic Force Microscopy. *Langmuir* **2000**, *16*, 6377–6380.
- (12) Malotky, D.; Chaudhury, M. Investigation of Capillary Forces Using Atomic Force Microscopy. *Langmuir* **2001**, *17*, 7823–7829.
- (13) Ou, J.; Perot, B.; Rothstein, J. Laminar Drag Reduction in Microchannels Using Ultrahydrophobic Surfaces. *Phys. Fluids* **2004**, *16*, 4635–4643.
- (14) Erbil, H. Bioadhesion to Solids: Contact Angle Hysteresis Effect. *Colloid Polym. Sci.* **2012**, DOI: 10.1007/s00396-012-2819-3.
- (15) Telkki, V.; Zhivonitko, V.; Ahola, S.; Kovtunov, K.; Jokisaari, J.; Koptyug, I. Microfluidic Gas-Flow Imaging Utilizing Parahydrogen-Induced Polarization and Remote-Detection NMR. *Angew. Chem., Int. Ed.* **2010**, *49*, 8363–8366.
- (16) Stone, H.; Stroock, A.; Ajdari, A. Engineering Flows in Small Devices: Microfluidics Toward a Lab-on-a-Chip. *Annu. Rev. Fluid Mech.* **2004**, *36*, 381–411.
- (17) Friess, B.; Hoorfar, M. Measurement of Internal Wettability of Gas Diffusion Porous Media of Proton Exchange Membrane Fuel Cells. *J. Power Sources* **2010**, *195*, 4736–4742.
- (18) Lauterbur, P. Image Formation by Induced Local Interactions: Examples Employing Nuclear Magnetic Resonance. *Nature* **1973**, *242*, 190–191.
- (19) Mansfield, P.; Grannell, P. NMR “diffraction” in solids? *J. Phys. C: Solid State Phys.* **1973**, *6*, L422–426.
- (20) Plewes, D.; Kucharczyk, W. Physics of MRI: A Primer. *J. Magn. Reson. Imaging* **2012**, *35*, 1038–1054.
- (21) Serres, S.; Soto, M.; Hamilton, A.; McAteer, M.; Carbonell, W.; Robson, M.; Ansoorge, O.; Khrapitchev, A.; Bristow, C.; Balathasan, L.; Weissensteiner, T.; Anthony, D.; Choudhury, R.; Muschel, R.; Sibson, N. Molecular MRI Enables Early and Sensitive Detection of Brain Metastases. *Proc. Natl. Acad. Sci. U.S.A.* **2012**, *109*, 6674–6679.
- (22) Mansfield, P.; Bowtell, R.; Blackband, S.; Guilfoyle, D. Magnetic Resonance Imaging: Applications of Novel Methods in Studies of Porous Media. *Magn. Reson. Imaging* **1992**, *10*, 741–746.
- (23) Bajaj, V.; Paulsen, J.; Harel, E.; Pines, A. Zooming In on Microscopic Flow by Remotely Detected MRI. *Science* **2010**, *330*, 1078–1081.
- (24) Davies, S.; Hardwick, A.; Roberts, D.; Spowage, K.; Packer, K. Quantification of Oil and Water in Preserved Reservoir Rock by NMR Spectroscopy and Imaging. *Magn. Reson. Imaging* **1994**, *12*, 349–353.
- (25) Ueno, T.; Fujisawa, M.; Fukuda, K.; Sasaki, Y.; Mizusaki, T. Visualization of Phase-separated Boundary in Liquid <sup>3</sup>He-<sup>4</sup>He Mixtures by MRI. *Physica B* **2000**, 2057–2058.
- (26) Shen, Y.; Yu, X. Application of MRI to Measurements of Liquid–solid–liquid Contact Angles. *College Physics* **2010**, *29*, 53–57.
- (27) Extrand, C.; Moon, S. Indirect Methods to Measure Wetting and Contact Angles on Spherical Convex and Concave Surfaces. *Langmuir* **2012**, *28*, 7775–7779.
- (28) Adamson, A.; Gast, A. *Physical Chemistry of Surfaces*, 6th ed.; Wiley-Interscience: New York, 1997.
- (29) Extrand, C.; Moon, S. When Sessile Drops Are No Longer Small: Transitions from Spherical to Fully Flattened. *Langmuir* **2010**, *26*, 11815–11822.
- (30) Extrand, C. Contact Angles and Their Hysteresis As a Measure of Liquid–Solid Adhesion. *Langmuir* **2004**, *20*, 4017–4021.
- (31) Pitt, W.; Young, B.; Cooper, S. Measurement of Advancing and Receding Contact Angles inside Polymer Tubing. *Colloids Surf.* **1987**, *27*, 345–355.
- (32) Sarkar, S.; Wooten, E.; Komoroski, R. NMR Imaging of Water in Model Porous Materials. *Appl. Spectrosc.* **1991**, *45*, 619–625.

(33) Liang, L.; Feng, X.; Liu, J.; Rieke, P.; Fryxell, G. Reversible Surface Properties of Glass Plate and Capillary Tube Grafted by Photopolymerization of N-Isopropylacrylamide. *Macromolecules* **1998**, *31*, 7845–7850.

(34) Willmott, G.; Neto, C.; Hendy, S. Uptake of Water Droplets by Non-wetting Capillaries. *Soft Matter* **2011**, *7*, 2357–2363.

(35) Willmott, G.; Neto, C.; Hendy, S. An Experimental Study of Interactions between Droplets and a Nonwetting Microfluidic Capillary. *Faraday Discuss.* **2010**, *146*, 233–245.

(36) Johnson, R.; Dettre, R. Wettability and Contact Angles. In *Surface and Colloid Science*; Matijevic, E., Ed.; Wiley-Interscience: New York, 1969; Vol. 2, pp 85–153.



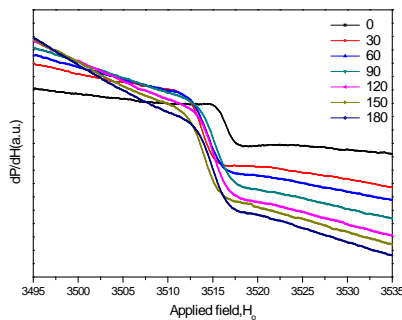
# 轮胎胶粉干法再生过程中自由基浓度与脱硫活化效果的相关性研究

曾冬<sup>1</sup>, 张兴凯<sup>1</sup>, 张棚<sup>1</sup>, 童薇<sup>2</sup>, 刘俊亮<sup>1</sup>, 张明<sup>1\*</sup>

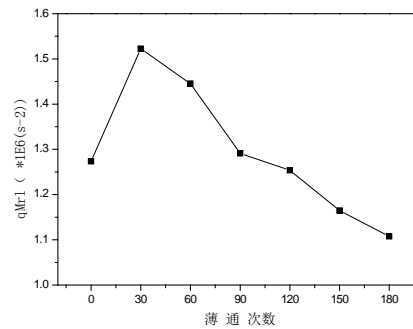
(1、扬州大学化学化工学院,江苏 扬州 225002, 2、昆明普尔顿管业有限公司,云南 昆明 625106)

**摘要:** 轮胎胶粉作为再生胶料中的一种, 由于其具有交联密度大难以翻新、表面缺乏活性等缺点, 使其应用范围受到限制。未经过活化处理的胶粉直接混炼到胶料中会使得制品的物理机械性能下降, 因此必须进行脱硫改性进行活化处理。本文主要通过通过对粗胶粒进行机械力化学改性以切断胶粉的部分硫硫交联键, 并采用电子顺磁共振技术和低场核磁共振仪研究胶粉在改性过程中自由基数目以及交联密度的变化情况, 探讨了干法再生胶基体中自由基浓度变化与交联密度以及硫化胶力学性能的相关性, 从而研究改性过程与硫化胶力学性能的变化规律。研究结果表明: 纯胶粉随着薄通次数的增加, 体系内自由基浓度随之增加, 胶粉交联密度呈先上升后下降趋势, 薄通次数达到 180 次时, 胶粉交联密度降低 13.05%, 其拉伸强度和断裂伸长率分别提高了 69.89%和 137.3%。

**关键词:** 机械力化学; 自由基; 交联密度



自由基浓度随薄通次数增加的变化



交联密度随时间的变化

## 参考文献:

- [1]. Debapriya De, Amit Das, Debasish De, et al. Reclaiming of ground rubber tire(GRT) by a novel reclaiming agent ,European Polymer Journal, 2006,42: 917-927.
- [2]. Mouna Zachary, Susana Camara, Adrian C. Whitwood ,et al. EPR study of persistent free radicals in cross-linked EPDM rubbers [J]. European Polymer Journal, 2008, 44:2099-2107.
- [3]. 国家自然科学基金 (NO.51273172) .

## 地球物理/多孔介质领域



低场核磁共振技术应用于水泥水化和水泥基材料孔结构表征的研究

姚 武

内 容

- 一、实验材料与测试方法
- 二、浆体中水的状态演变与水化反应过程
- 三、水的弛豫特性与浆体微结构的发展
- 四、水泥浆体中水的分布与含量演变
- 五、结论

一、实验材料与测试方法

• 材料体系

➢以硅酸盐水泥、粉煤灰和硅灰制备不同水胶比或不同矿物外加剂掺量的水泥净浆或复合水泥浆体。试样的养护采用饱和和密闭两种养护方式；试样的龄期从数分钟到数月不等。

• 测试方法

- ✓ 低场核磁共振技术(LF-NMR)——评价水的弛豫特性
- ✓ 压汞法 (MIP) ——评价孔结构
- ✓ 热蒸发法——测定可蒸发水量

低场核磁共振技术(LF-NMR)



无损

非侵入

快速

连续

二、浆体中水的状态演变与水化反应过程

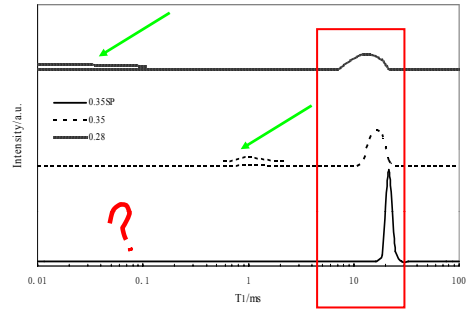
• 2.1 实验

标签	0.28	0.35	0.35SP	0.35F10	0.35S10
	w/c=	w/c=	w/c=	w/b=	w/b=
	0.28	0.35	0.35	0.35	0.35
配比	水泥质量 0.6%的高效 减水剂			水泥质量 10%的粉煤 灰	水泥质量 10%的硅 灰
	水泥净浆			复合浆体	

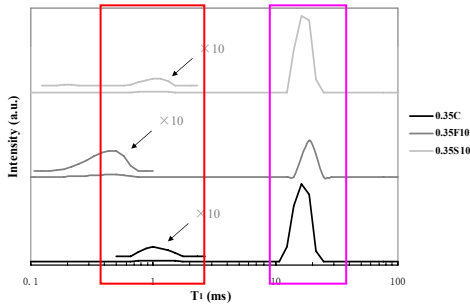


• 2.2 新拌浆体中水的状态与分布

初始时期的T1分布——纯水泥浆体

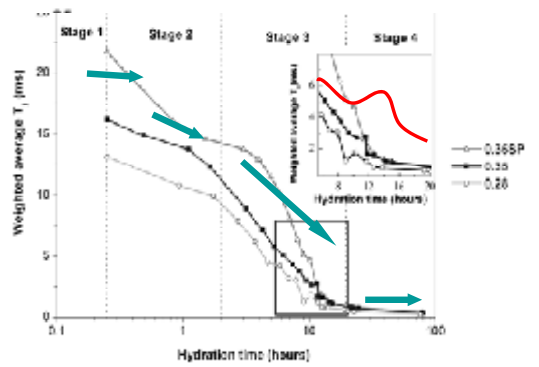


初始时期的T1分布——复合水泥浆体

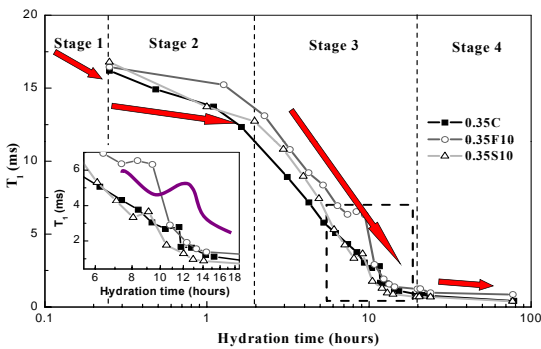


• 2.3 水的弛豫变化与水化过程的关系

T1随水化时间的变化——水泥净浆

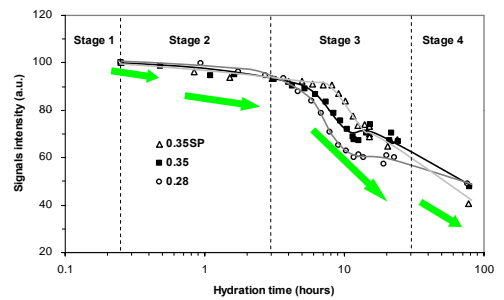


T1随水化时间的变化——复合水泥浆体

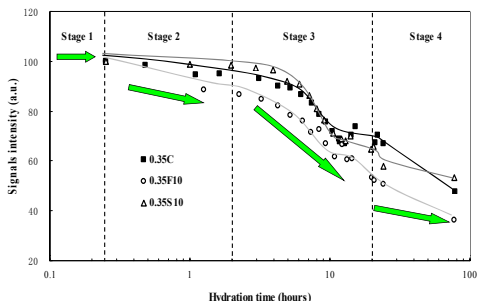


• 2.4 物理结合水量与水化过程的关系

水化期间T1总信号量的变化——水泥净浆



水化期间T1总信号量的变化——复合水泥浆体



### 三、水的弛豫特性与浆体微结构的发展

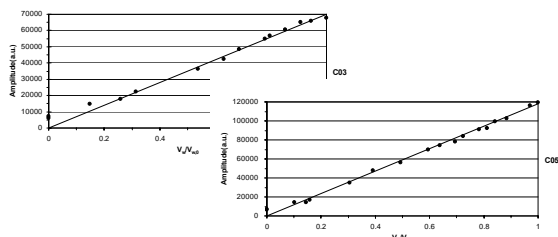
• 孔隙水的信号与表面弛豫

✓ 干燥实验

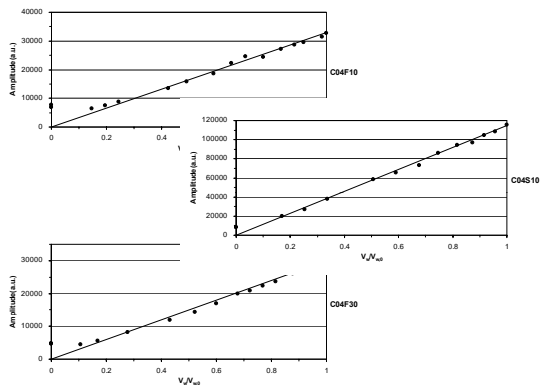
编号	C03	C04	C05	04F10	04F30	04S10
配比	w/c= 0.3	w/c= 0.4	w/c= 0.5	w/b=0.4 水泥质量 10%的粉 煤灰	w/b=0.4 水泥质量 30%的粉 煤灰	w/b=0.4 水泥质量 10% 的硅灰
	水泥净浆			复合浆体		

水的填充指数: 
$$\frac{V_w}{V_{w,0}} = \frac{m_0 - m}{m_0 - m'}$$

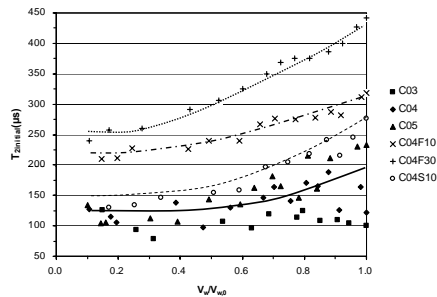
• 干燥过程中水的弛豫信号强度



可蒸发水量与信号量成正比



• 表面弛豫率



• ρ2为12nm/ms

水的弛豫时间与孔隙尺寸的定量关系

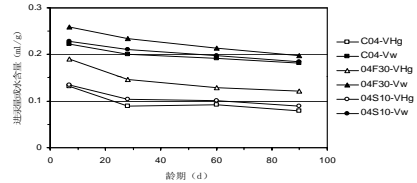
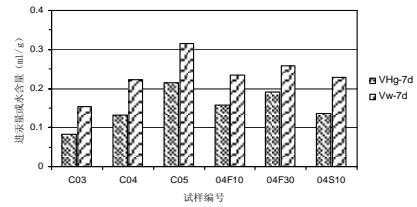
$$\frac{1}{T_2} = \rho_2 \frac{S}{V} = \rho_2 \frac{2}{r}$$

$$\rho_2 = \frac{\lambda}{T_{2S}}$$

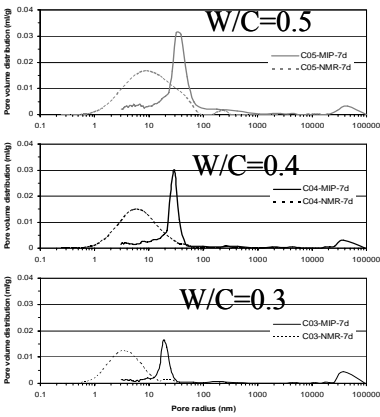
$T_2$ : 横向弛豫时间  
 $\rho_2$ : 表面弛豫率  
 $S$ : 孔表面积  
 $V$ : 孔体积  
 $r$ : 孔半径  
 $\lambda$ : 单层水分子的厚度, 0.3nm  
 $T_{2s}$ : 表面单层吸附水分子的弛豫时间, 25 $\mu$ s

水的弛豫时间与所在孔隙的比表面积成反比, 即孔越小, 弛豫时间越短。  
 基于圆柱孔假设, 可以建立弛豫时间与孔半径的定量关系。

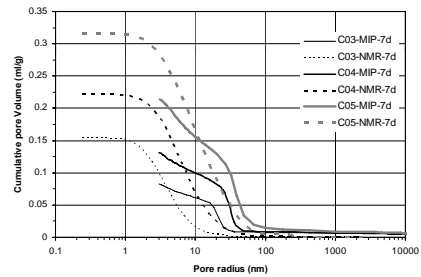
• 孔体积



• 孔分布 (1) 7d不同水灰比的水泥浆体

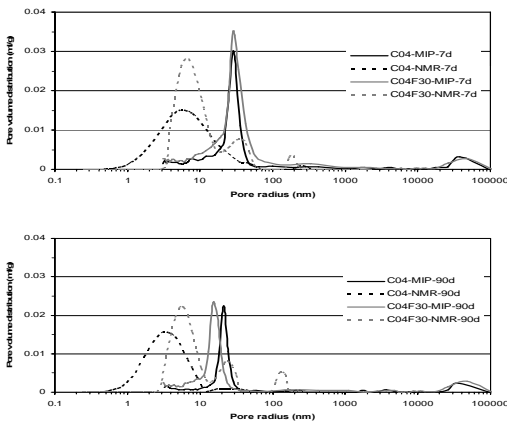


压汞法对孔的连通性较为敏感, 对连通性较差的小孔难以有效表征。最强峰位于10-80纳米范围内, 对应中等毛细孔, 且分布峰窄;  
 核磁共振法得益于水分子较小的直径, 能够表征更小的孔, 最强峰在几个纳米位置, 对应小毛细孔和凝胶孔, 且分布峰宽, 在1-100纳米范围内。



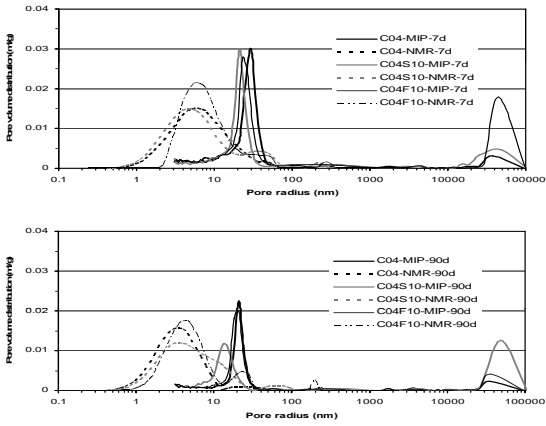
压汞法和核磁共振法两种方法体积累加曲线的上升拐点相近, 但随后累加的程度不同。分别以4nm, 7nm, 10nm为交叉点, 在交叉点以上, 压汞法的累加体积一般高于核磁共振法; 低于交叉点随着孔径的减小, 孔的连通性变差, 进浆体积逐渐减小。核磁共振法的体积累加曲线高于压汞法。

• 孔分布 (2) 7d和90d不同粉煤灰掺量浆体



对于压汞法孔分布峰: 7d时, 粉煤灰尚呈惰性, 掺和不掺粉煤灰浆体孔分布峰几乎重合; 90d时, 粉煤灰发挥火山灰作用, 掺粉煤灰浆体的峰比不掺浆体的峰显著向左偏移;  
 对于核磁共振法孔分布峰: 即便到90d, 掺粉煤灰浆体的峰仍然比不掺浆体的峰更像右偏;  
 表明: 粉煤灰的火山灰效应改善的是毛细孔, 特别是几十个纳米的中等毛细孔, 二次水化产物细化了它们的孔尺寸。但是, 粉煤灰对凝胶孔的改善效果则有限。

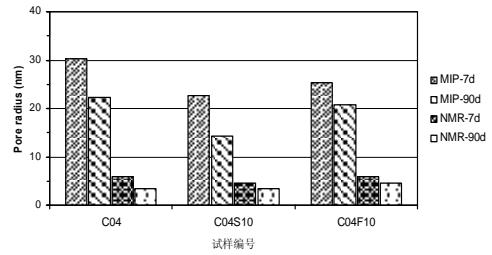
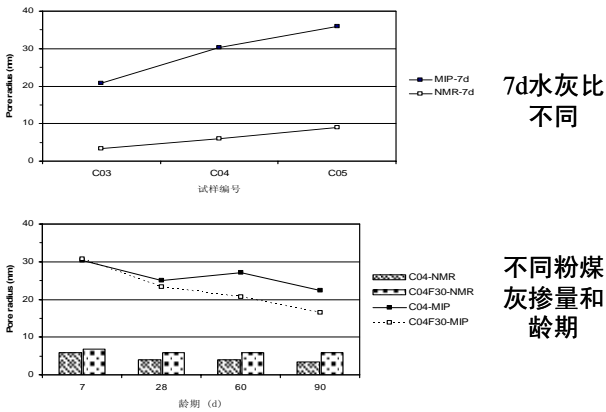
• 孔分布 (3) 7d和90d粉煤灰和硅灰浆体



从压汞法孔分布曲线看，硅灰对孔结构的细化作用最显著，粉煤灰次之；

从两种方法测得的分布曲线对比来看：硅灰和粉煤灰对水泥浆体孔结构的改善主要集中在直径20-80nm的中等毛细孔段；而对于10nm以下的凝胶孔的改善作用则有限。基于不同尺度的孔对宏观性能的不同影响来说，这一结论对于工程实践有一定指导作用。即根据工程需要，选取合适的矿物掺合料有针对性的改善材料的孔结构。

• 最可几孔径



7d和90d粉煤灰和硅灰浆体

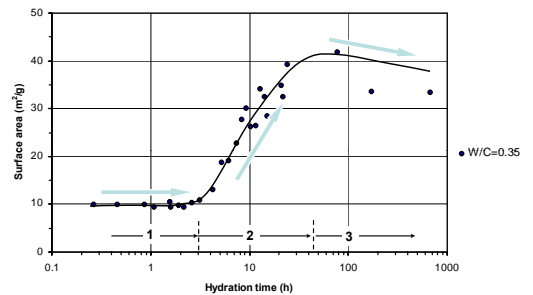
• 水的弛豫与浆体比表面积

$$S = \frac{10^3}{\rho_2} \cdot \frac{V}{T_{2initial}}$$

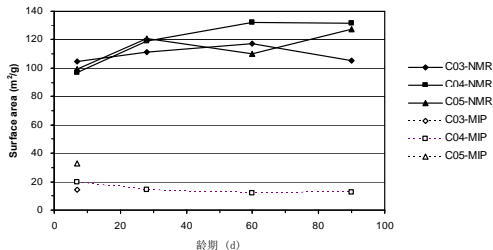
• 实验

- 1、新拌浆体早期比表面积动态增长
- 2、硬化浆体比表面积随龄期的增长

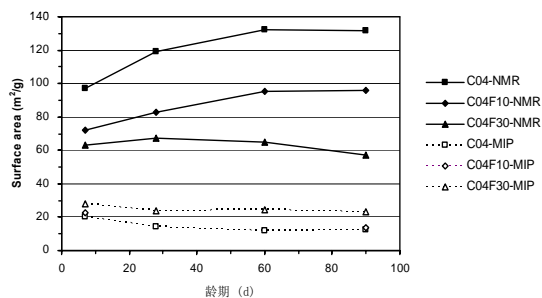
• 早期浆体比表面积的发展



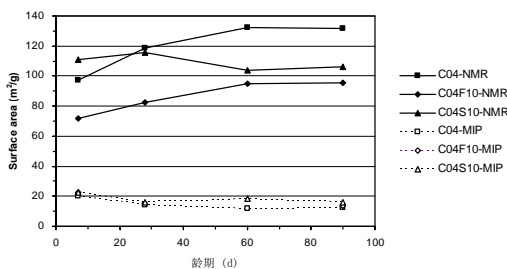
• 硬化浆体的比表面积



不同水灰比的水泥浆体的比表面积随龄期的变化



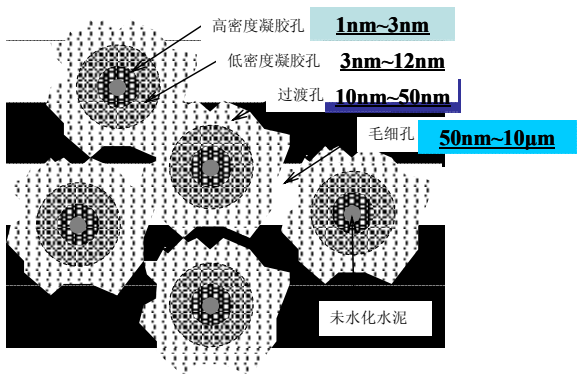
不同粉煤灰掺量的浆体比表面积随龄期的变化



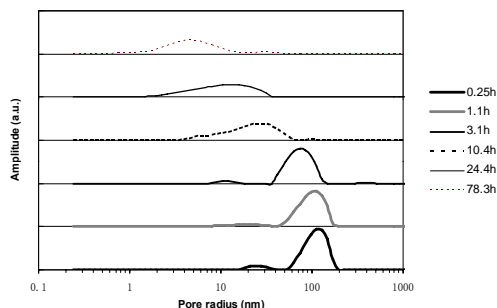
水泥净浆、硅灰浆体、粉煤灰浆体比表面积随龄期的变化

四、水泥浆体中水的分布与含量演变

• 水的分布一般描述

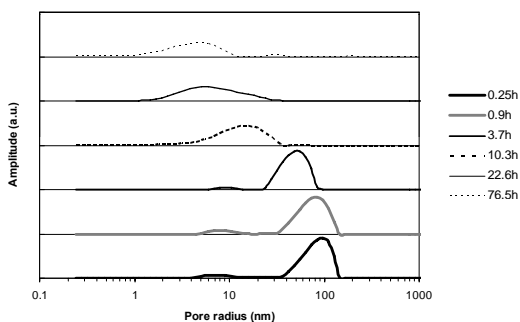


• 早期浆体中水的分布

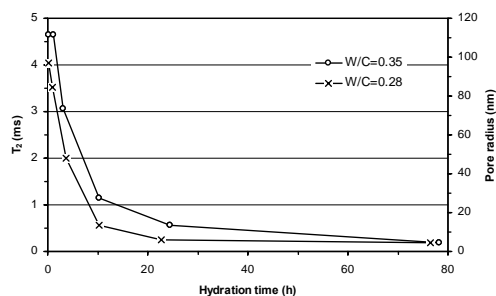


水灰比为0.35的浆体中水的分布变化





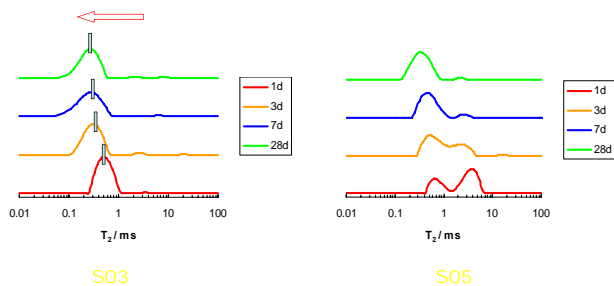
水灰比为0.28的浆体中水的分布变化



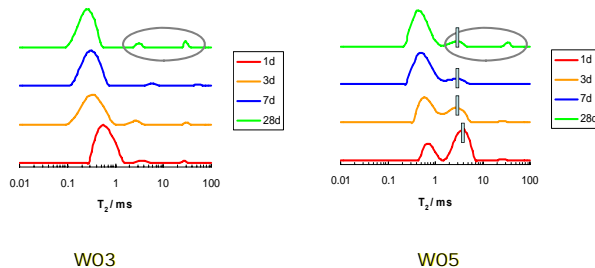
峰最高点对应的弛豫时间和孔径随水化时间的变化

### 硬化浆体中水的分布 水的分布特征

不同龄期的T2分布——水灰比不一样

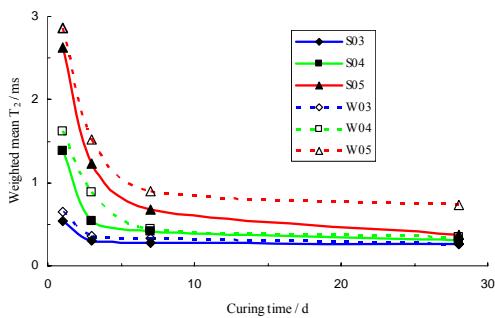


不同龄期的T2分布——养护方式不一样

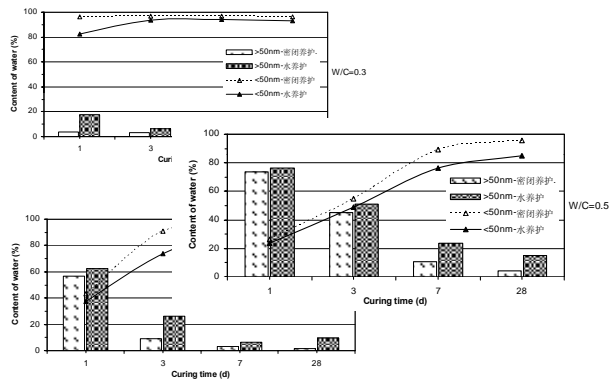


### 平均弛豫时间的变化

T2随水化时间的变化



### 可蒸发水在孔隙中的含量变化

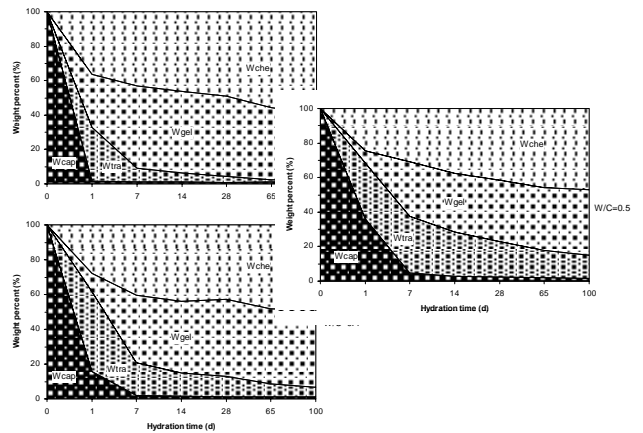


### 浆体中不同状态的水的含量变化

孔的分类及其对应的弛豫时间

孔隙类型	凝胶孔	过渡孔	大毛细孔
孔半径/nm	<6	6~25	>25
T <sub>2</sub> /ms	<0.25	0.25~1.04	>1.04

### 含量变化的定量描述



## 六、结论

### (1) 采用LFNMR表征水泥浆体的水化过程

通过监测早期浆体中水的纵向弛豫时间T1的变化，表征了浆体的水化过程。首次研究了不同组成的硅酸盐水泥浆体和掺粉煤灰和硅灰的复合浆体的水化过程与弛豫时间之间的对应关系和机理。描述了新拌浆体中水的分布状态，直观说明了高效减水剂对絮凝结构的抑制效应。

### (2) 建立水的弛豫特性与水泥浆体微结构的关系

建立了水的横向弛豫时间T2与孔隙结构的定量关系。在此基础上，研究了不同组成和龄期的水泥浆体的孔结构。由于水分子较小的直径，弛豫法能够探测到凝胶孔。通过与压汞法的测孔结果相比较，发现粉煤灰和硅灰对孔系统的影响存在一个“势力范围”，即主要是孔直径在20nm~80nm的中等毛细孔。此外，在原位监测条件下研究了浆体水化过程中比表面积的动态增长过程。

### (3) 揭示了不同孔隙中可蒸发水的定量演变规律

利用低场核磁共振非破损、非侵入、连续测量的优势，研究了不同组成和龄期的浆体中，被限制在不同大小孔径中的可蒸发水的含量变化，弥补了传统方法的不足。研究的结果对于定量地分析水对材料相关性能，如干燥收缩、徐变、自干燥收缩、冻融等问题提供了基础数据。

谢谢!

第五届全国低场核磁共振技术与应用研讨会

## 低场核磁共振技术在岩石冻融损伤研究中的应用

李杰林

中南大学  
资源与安全工程学院

2013年10月12日

### 一、前言

- ◆ 岩石是一种天然的多孔介质材料，其内部存在大量不规则、跨尺度的孔隙，直接影响着岩石的宏观物理、力学和化学性质；
- ◆ “冻融”是指岩土层由于温度降到零度以下和升至零度以上而产生冻结和融化的一种物理地质作用和现象；
- ◆ 在实验室中，冻融条件是用来模拟自然界中高寒地区的夏季和冬季气温交替变化的气候情况；

中南大学

### 一、前言

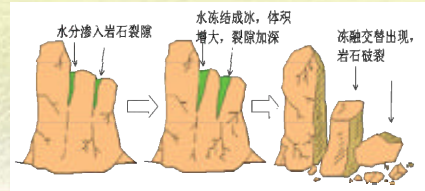
核磁共振技术具有无损检测、样品可重复使用、检测速度快等优点，已广泛应用于裂缝识别、孔隙分布、介质内部结构特性等方面的实验和探测研究。

在岩土工程领域，国内外已有许多学者利用核磁共振技术开展了相关的研究，已取得了许多重要成果。

中南大学

### 二、实验原理

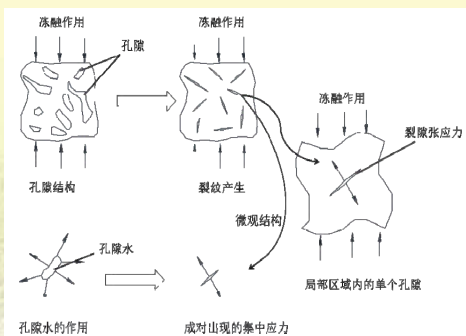
- ◆ 当温度降低时，水冻结成冰时，因水冰相变，导致约9%的体积膨胀，将对岩石内部裂隙的两壁施加张应力，使裂隙增大，岩体破裂。
- ◆ 当温度升高，冰融化成水后，水又进入到新产生的裂隙中，水又冻结成冰，如此反复的冻结和融化，导致了岩石的冻胀、损伤开裂等力学变形，进而导致岩石物理力学发生改变，甚至损伤破坏。



岩石冻融损伤过程示意图

中南大学

### 二、实验原理



岩石冻融损伤的微观结构模型

中南大学

### 三、实验仪器及步骤

#### 主要实验仪器



TDS-300冻融试验机



岩心真空饱和装置



AniMR-150 型核磁共振分析仪

中南大学

### 三、实验仪器及步骤

#### 实验步骤



冻结时间: 4h  
融解时间: 4h  
冻融周期: 8h

真空饱和

真空饱和

中南大学

### 四、花岗岩冻融损伤实验

#### 实验条件

冻结温度:  $-40^{\circ}$

融解温度:  $20^{\circ}$

冻融循环次数: 20次



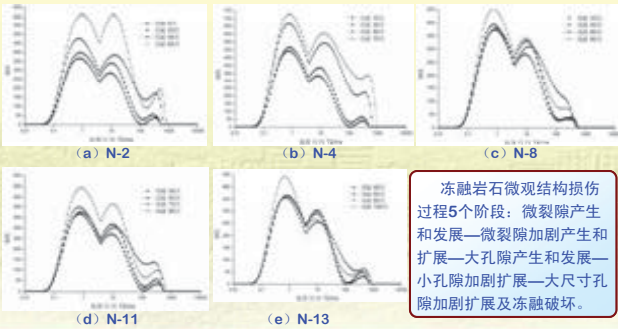
MiniMR-60 型核磁共振分析仪



中南大学

### 四、花岗岩冻融损伤实验

#### 核磁共振T2谱分布

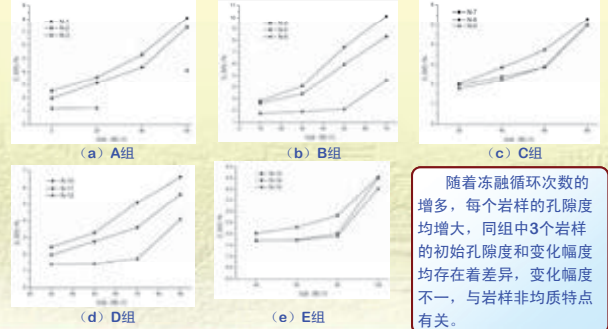


冻融岩石微观结构损伤过程5个阶段: 微裂隙产生和发展—微裂隙加剧产生和扩展—大孔隙产生和发展—小孔隙加剧扩展—大尺寸孔隙加剧扩展及冻融破坏。

中南大学

### 四、花岗岩冻融损伤实验

#### 花岗岩孔隙率变化规律

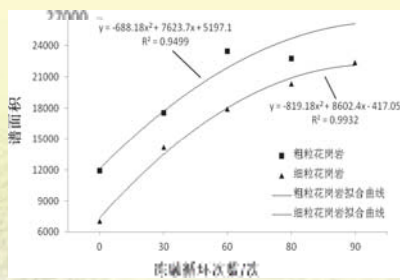


随着冻融循环次数的增多, 每个岩样的孔隙度均增大, 同组中3个岩样的初始孔隙度和变化幅度均存在着差异, 变化幅度不一, 与岩样非均质特点有关。

中南大学

### 四、花岗岩冻融损伤实验

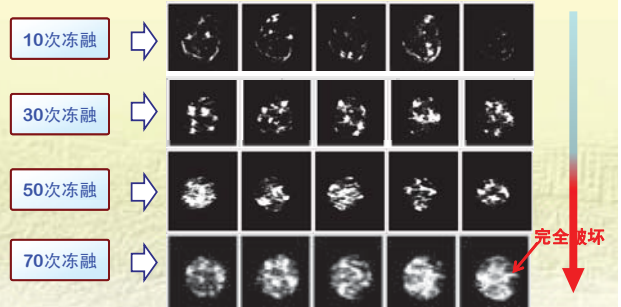
#### 花岗岩T2谱面积



冻融循环次数与不同粒径岩石NMR谱面积关系

中南大学

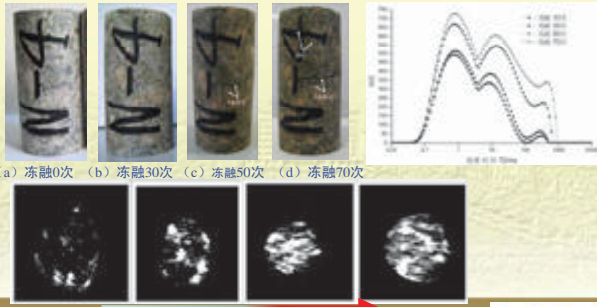
### 四、花岗岩冻融损伤实验



中南大学

### 四、花岗岩冻融损伤实验

将同一个岩样同一位置的T2谱分布及成像图对应关系进行分析，获得了岩石的冻融损伤演化过程。



中南大学

### 五、砂岩冻融损伤实验

#### □ 实验条件

- ◆ 冻结温度:  $-20^{\circ}$
- ◆ 融解温度:  $20^{\circ}$
- ◆ 冻融循环次数: 分10、20、30次循环
- ◆ 冻融结束后进行抗拉力学试验



AniMR-150 型核磁共振分析仪



试验前岩样

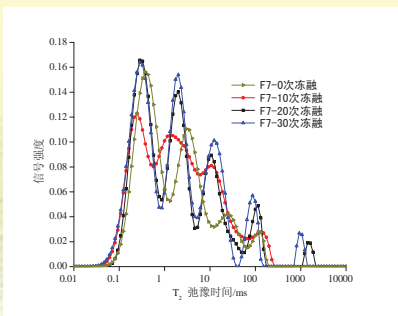


巴西劈裂试验后破坏岩样

中南大学

### 五、砂岩冻融损伤实验

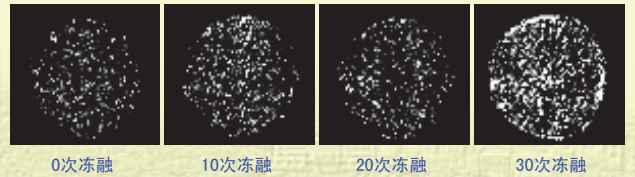
#### □ 试验结果——T2谱分布



中南大学

### 五、砂岩冻融损伤实验

#### □ 试验结果——NMR成像

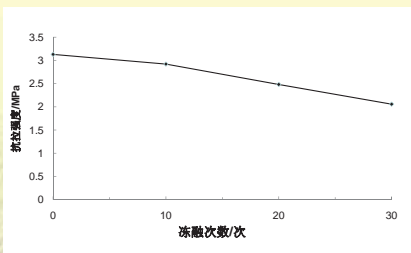


随着冻融次数的增加，砂岩内部孔隙逐渐增大，核磁共振信号增强，展现了冻融作用对砂岩的损伤劣化过程。

中南大学

### 五、砂岩冻融损伤实验

#### □ 试验结果——抗拉强度



随着冻融次数的增加，砂岩的抗拉强度逐渐降低，表明了冻融作用弱化了砂岩的物理力学强度。

中南大学

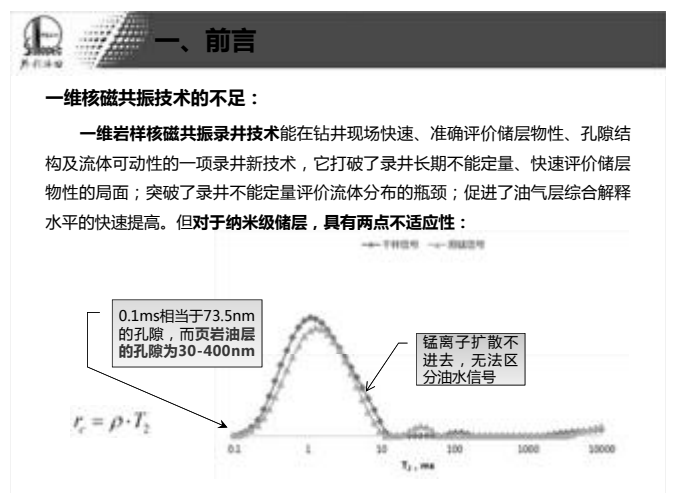
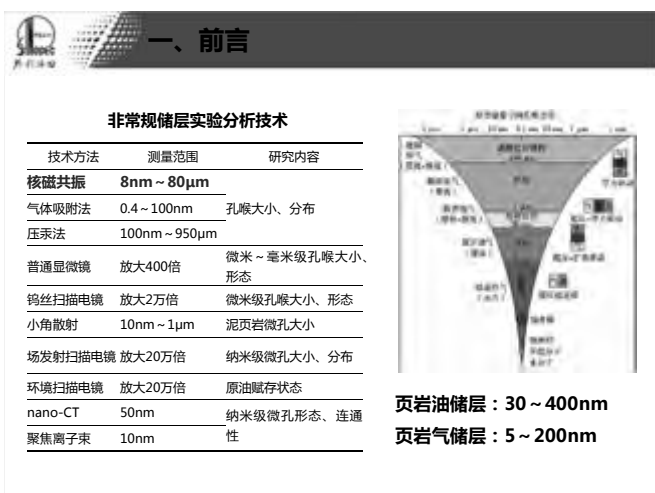
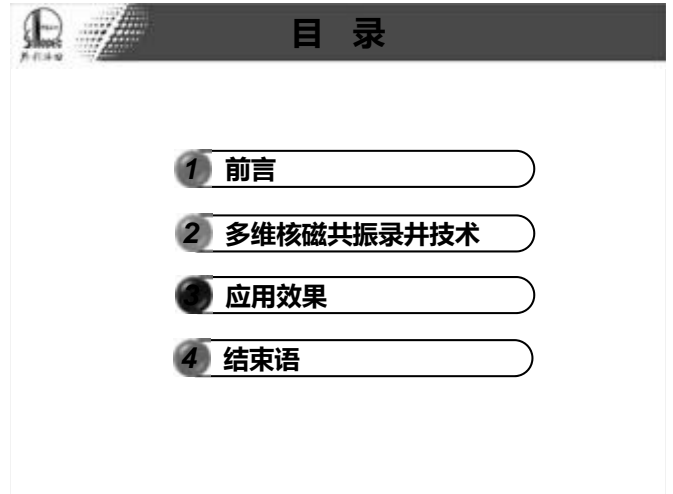
### 六、应用展望

1. 如何提高高致密性岩石的核磁共振成像结果的精度和分辨率?
2. 岩石中易存在微量的金属成分，对核磁共振信号有干扰，如何消除?
3. 岩石孔隙结构核磁共振成像结果的三维模型构建;
4. 荷载条件下(温度、力学、化学等)岩石的核磁共振测试技术与装置的研发。

中南大学

感谢苏州纽迈电子科技有限公司为本文中部分核磁共振实验提供了各种方便和协助!








### 一、前言

**多维核磁共振技术的优势：**

- 多维核磁共振技术增加了扩散系数后在区分流体性质方面具有独到优势，其 $T_2$ 谱的反演是从0.01ms开始，相当于7.35nm的孔隙，能满足非常规泥页岩、致密砂岩油气的勘探需求。
- 地面录井仪器不受井眼空间的限制，不用浸泡样品，一次测量即可进行油气水的识别，可在非常规储层物性及孔隙流体评价方面发挥独到的作用。



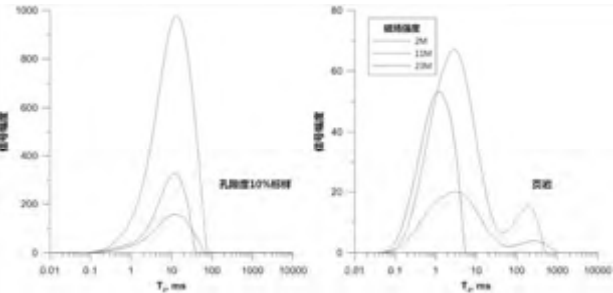
### 目录

- 1 前言
- 2 多维核磁共振录井技术
- 3 应用效果
- 4 结束语

### 二、多维核磁共振录井技术

**(一) 孔隙度评价**

□ 提高磁场强度有助于提高信噪比，但过高的场强会受岩石骨架的影响。

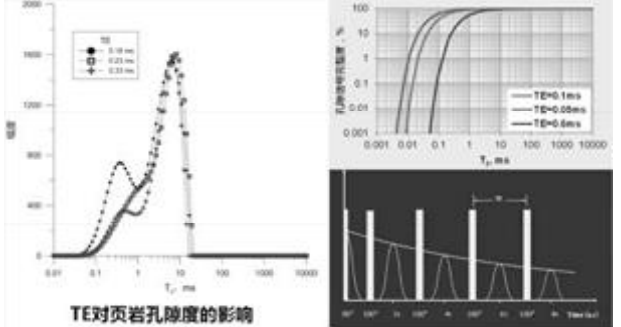


确定11M左右为最佳的磁场强度。

### 二、多维核磁共振录井技术

**(一) 孔隙度评价**

□ TE越大，小孔隙的信息丢失越多；缩短TE，确定最佳的回波间隔（TE），是满足纳米级储层评价的关键。

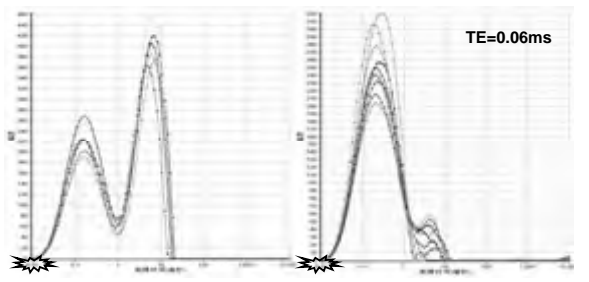


TE对页岩孔隙度的影响

### 二、多维核磁共振录井技术

**(一) 孔隙度评价**




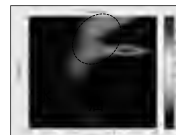


□ 采用0.06ms的回波间隔，可测量到0.01ms（约8nm）的孔隙。



页岩油页岩      页岩油页岩心

### 二、多维核磁共振录井技术

**(二) 油气水识别与评价**

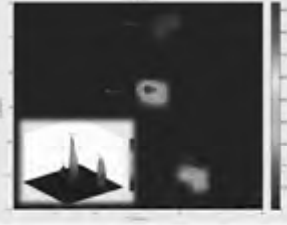
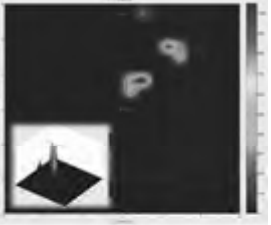
人造饱水岩心	人造烘干岩心	人造饱油岩心
		
		
TE=0.4009 T1=10000 NS=4	TE=0.4009 T1=15000 NS=4	TE=0.4009 T1=15000 NS=4

饱和盐水T11-500, T21-500, 值基本相当, D1.8-7  
饱和油T13000-4000ms, T2300-1000ms, D0.0015-7.6

## 二、多维核磁共振录井技术

### (二) 油气水识别与评价

张应力 等, ICMRM11, 2011.08

10% gas + 40% oil + 50% water

气的扩散系数为 $D=1.5E-7m^2/s$ ，油的扩散为 $D=1.0E-11m^2/s$ ，水(束缚水)的扩散系数 $D=2.5E-9m^2/s$ 。气、油、水的 $T_2$ 弛豫时间分别为40ms, 200ms, 20ms, 采样信噪比为30。在上图中，根据油、气、水不同的扩散系数可以轻易的区分出岩心中油、气、水的部分；一次二维 $D-T_2$ 检测就可以得出油、气的扩散系数和弛豫时间，以及各组分比例。

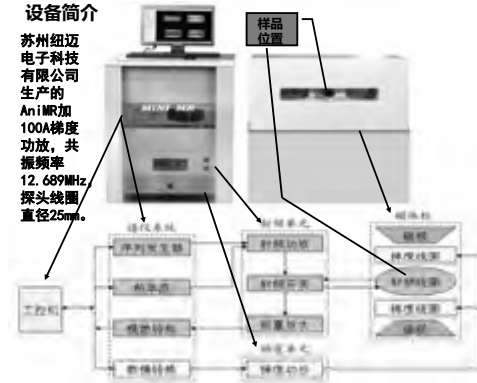
油、水的 $T_2$ 弛豫时间分别为40ms, 200ms, 20ms;  $T_1$ 弛豫时间分别为3000ms, 400ms, 40ms; 采样信噪比为30。在 $T_2$ 分布上，束缚水与天然气信号有很大的重叠，区分比较困难，而一次 $T_1-T_2$ 序列即可区分。 $T_1$ 时间最长的是天然气，而油和束缚水在 $T_2$ 上有区别。

## 二、多维核磁共振录井技术

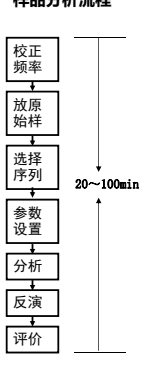
### (三) 对比试验

**设备简介**

苏州纽迈电子科技有限公司生产的Ani增加100A梯度功放，共振频率12.689MHz, 探头线圈直径25mm。



**样品分析流程**





## 二、多维核磁共振录井技术

### (三) 对比试验

□  $T_2$  实验，采用CPMG 序列，序列参数为：P1=4.20us, P2=8.20us, SW=666.667kHz, TW=2000ms, DL1=0.022ms, NECH=8000, NS=64；

□ (2) D-T<sub>2</sub>实验，采用PGSE-CPMG 序列，序列参数为：P1(us)=19, P2(us)=34, TD=102296, SW(KHz)=100, TW(ms)=500, RFD(ms)=0.08, RG1(db)=20, DRG1=3, NS=128 (部分样品NS=32), NECH=3000。

**序列：**

翻转恢复IR序列

D-T<sub>2</sub>序列

## 二、多维核磁共振录井技术

### (三) 对比试验

#### 实验样品

在\*\*\*陷下第三系沙河街组页岩油气主要勘探层段采集\*\*、\*\*、\*\*三口井页岩岩屑(心)样品11块，进行两种样品处理方式下的孔隙度测试，样品处理方式两种：

- 原样测试，不对样品做任何处理；然后对11块页岩岩屑样品进行D-T<sub>2</sub>二维检测其流体含量；
- 使用真空饱和和装置对样品进行矿化水饱和2小时。

## 二、多维核磁共振录井技术

### 1、孔隙度分析对比试验

原样多维核磁共振录井孔隙度测试数据表

样品编号	井深 (m)	井号	体积 (ml)	单位体积核磁信号	孔隙度	样品类型
1	3212	**	8.38	261.82	4.02%	岩屑
2	3272	**	8.38	289.70	4.43%	岩屑
3	3208	**	8.35	414.72	6.29%	岩屑
4	3256	**	8.78	274.50	4.21%	岩屑
5	3644-3646	**	10.01	383.92	5.84%	岩屑
6	3664-3666	**	9.83	239.26	3.68%	岩屑
7	3668-3670	**	11.81	371.69	5.65%	岩屑
8	3672-3678	**	10.03	365.01	5.55%	岩屑
9	3607-3609	**	7.48	140.10	2.21%	岩屑
10	3670-3672	**	8.57	393.29	5.97%	岩屑
11	3683.6	**	6.96	475.25	7.19%	岩芯

原样进行测试，不对样品做任何处理测试样品孔隙度，测试结果样品孔隙度最大7.19%，最小2.21%，平均为5.17%。

## 二、多维核磁共振录井技术

### 1、孔隙度分析对比试验

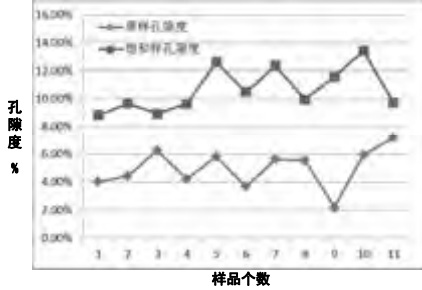
真空矿化水饱和2小时多维核磁共振录井孔隙度测试数据表

样品编号	井深 (m)	井号	体积 (ml)	单位体积核磁信号	孔隙度 (%)	样品类型
1	3212	**	7.28	586.88	8.85%	岩屑
2	3272	**	7.65	643.5	9.70%	岩屑
3	3208	**	7.26	592.85	8.94%	岩屑
4	3256	**	7.26	641.62	9.67%	岩屑
5	3644-3646	**	9.09	840.11	12.62%	岩屑
6	3664-3666	**	8.38	698.25	10.51%	岩屑
7	3668-3670	**	10.03	823.93	12.38%	岩屑
8	3672-3678	**	9.11	662	9.97%	岩屑
9	3607-3609	**	6.08	771.34	11.60%	岩屑
10	3670-3672	**	7.29	893.28	13.41%	岩屑
11	3683.6	**	6.78	648.12	9.76%	岩芯

测试结果样品孔隙度最大13.41%，最小8.85%，平均为10.67%。

## 二、多维核磁共振录井技术

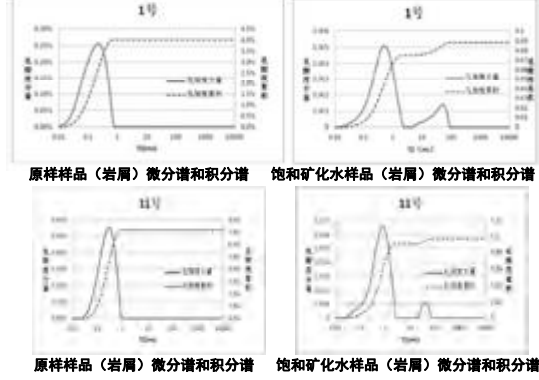
### 1、孔隙度分析对比试验



对比饱和和矿化水和原样孔隙度测试结果，前者孔隙度均大于后者接近两部，同时看出岩屑样品的偏差值更大，岩心样品的偏差值相对较小。分析原因为饱和水的泥页岩样品由于粘土颗粒的吸附作用在表面形成一定量的水，造成孔隙度检测偏大，岩屑呈颗粒其表面积远大于岩心样品的表面积，造成岩屑吸附水量大于岩心样品，从而岩屑样品的偏差值更大。

## 二、多维核磁共振录井技术

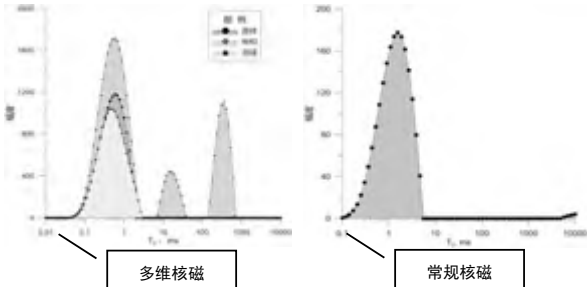
### 1、孔隙度分析对比试验



泥页岩储层一般为纳米级的小孔隙，矿化水难以饱和和进样品中去，无助于孔隙度的检测，反而会人为的增加孔隙的测量值，因此认为利用多维核磁共振技术检测泥页岩样品的孔隙度不能进行饱和和矿化水，应直接检测原始样品。

## 二、多维核磁共振录井技术

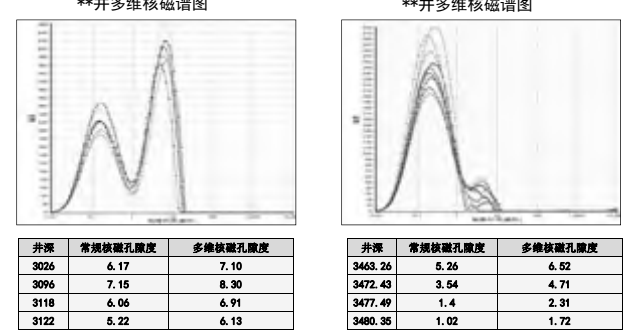
### 1、孔隙度分析对比试验



常规核磁共振技术能检测0.1ms（相当于73.5nm）的孔隙，对小孔隙信号的信息丢失较多，不能满足泥页岩油气储层物性评价的需要。多维核磁共振技术可以检测到弛豫时间为0.01ms（相当于7.35nm）的孔隙，具有较高的孔隙分辨率。

## 二、多维核磁共振录井技术

### 1、孔隙度分析对比试验

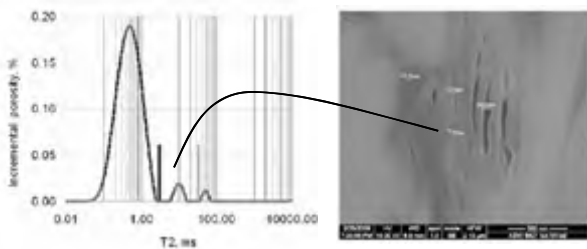


■多维核磁对小孔隙识别精度较高，物性值大于常规核磁物性值；

## 二、多维核磁共振录井技术

### 2、孔隙结构评价

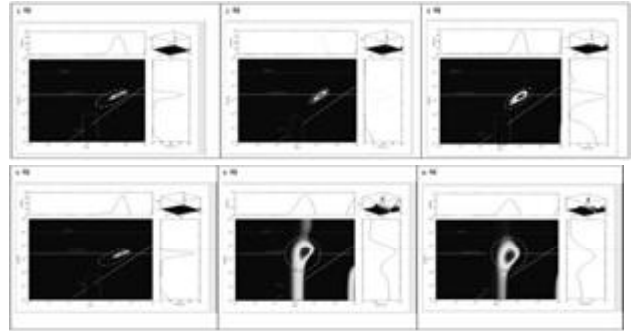
核磁共振 $T_2$ 谱包含了基质孔隙、生烃孔隙和微裂缝三部分，基质孔隙峰反应了吸附气含量的高低，生烃孔隙峰反应了生烃能力的大小，而微裂缝峰则反应了储层改造的难以程度。

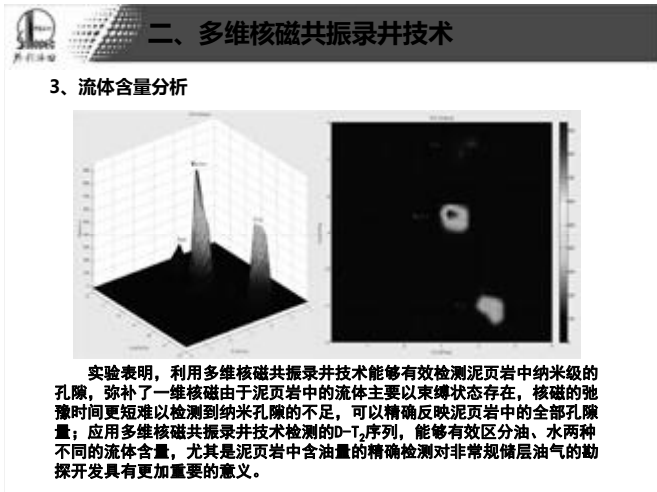
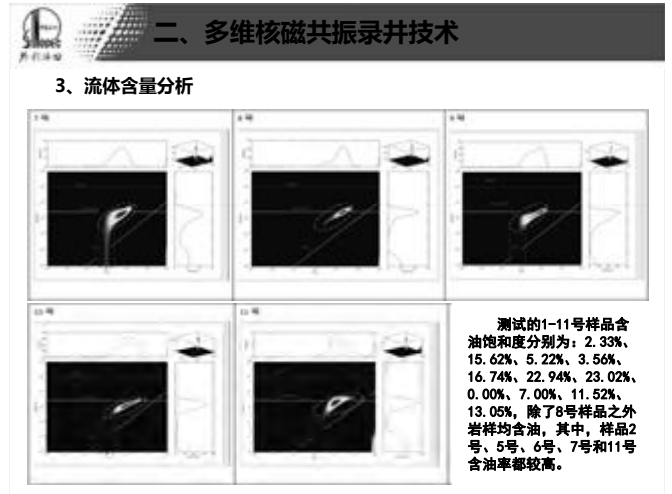
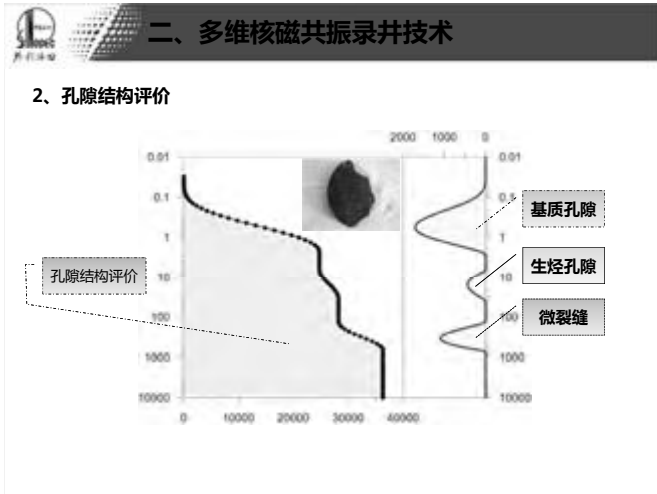


## 二、多维核磁共振录井技术

### 3、流体含量分析

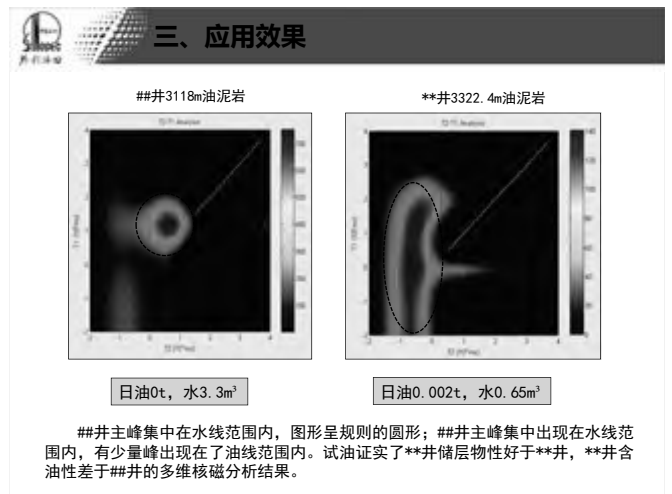
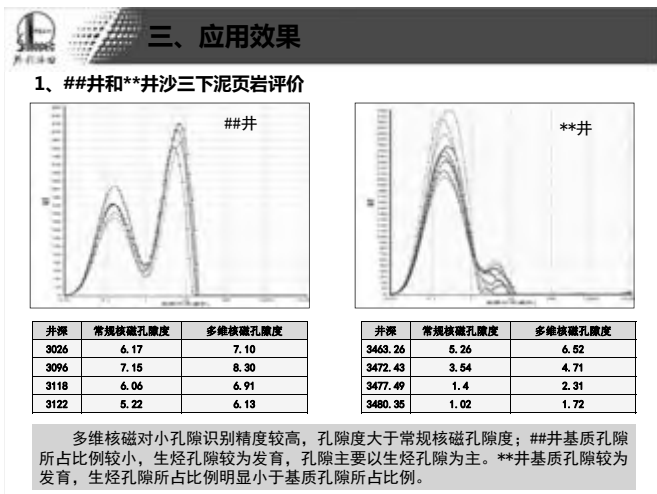
对11块泥页岩样品进行D-T<sub>2</sub>二维流体含量分析，使用CPMG-PGSE序列采集样品信号，根据D-T<sub>2</sub>衰减信号函数，得到扩散系数D、横向弛豫时间T<sub>2</sub>和弛豫分量的信号量。





### 目 录

- 1 前言
- 2 多维核磁共振录井技术
- 3 应用效果
- 4 结束语



### 三、应用效果

#### 2、##地区泥页岩储层评价

\*\*, \*\*, \*\*, \*\*, \*\*井试油资料统计表

井号	顶深	底深	岩性	钻时基值	钻时异常	全烃基值	全烃异常	甲烷基值	甲烷异常	静压	日油	日气	日水	试油结论
**	2828.13	2861	灰褐色油斑油页岩	9	3.3	0.082	0.72			45.2	73.1	4220	0	油层
**	3442.32	3560	灰褐色灰质油泥岩	12.7		37.18	100	15.64	78.3	58.75	140	15625	59.8	油水两层
**	3467	3470	灰色油斑泥灰岩	8.5		4	64.46	2.03	42.29	61.56	154	13400	3.22	油层
	3471	3473	灰色油斑泥灰岩	9		4.83	100	2.77	94					
	3607	3609	灰色荧光泥灰岩	15.3	9.6	2.42	85.37	1.18	65.62					
	3612	3616	灰色荧光泥灰岩	34.9	5.1	5.07	100	2.86	79.76					
**	3238.5	3284	灰褐色油泥岩	13	9	5	27.2	1.5	6					层不稳定性
**	3296	3320	灰褐色油泥岩	13	8	5	62	1	12					
**	3343	3381	灰褐色油泥岩	40	16	5	100	1	30	60.02	36.5	871	1.4	油层
**	3667	3668	深灰色油斑砂质灰岩	9.2	5.1	9.33	86.07	4.24	81.07	47.05	41.5	8754	6.4	油层

### 三、应用效果

#### (1) \*\*井

□ \*\*井井段3635.77-3680m, 岩性深灰色油斑砂质灰岩, 试油日油41.5t, 日气8754m<sup>3</sup>, 水6.4m<sup>3</sup>, 试油结论为油层。

### 三、应用效果

#### (1) \*\*井

3635.77-3680 | 日油41.5 | 日气8754 | 日水6.4

### 三、应用效果

#### (1) \*\*井

\*\*井基质孔隙百分含量直方图

非常规储层多维核磁共振孔隙分级评价。

### 三、应用效果

#### (1) \*\*井

3635.77-3680 | 日油41.5 | 日气8754 | 日水6.4

序号	面积	峰点信息 (s,m2/s)	比例	峰属性
1	218.9722	0.0173, 1.39e-9	83.26%	水峰
2	44.01689	0.017302, 4.64E-12	16.74%	油峰

序号	面积	峰点信息 (s,m2/s)	比例	峰属性
1	661.51	0.0173, 1.9307e-10	76.98%	水峰
2	197.8101	0.0089, 4.642E-12	23.02%	油峰

### 三、应用效果

#### (1) \*\*井

\*\*井试油段有机质丰度评价表

井深 m	厚度 m	岩性	S <sub>0</sub> mg/g	S <sub>1</sub> mg/g	S <sub>2</sub> mg/g	P <sub>g</sub> mg/g	St mg/g	Tmax °C	T00 %	PO %	HI	D %	有机质类型	成熟度	生气量 10 <sup>4</sup> m <sup>3</sup> /t	持烃量 10 <sup>4</sup> t/t	
3468.00-3705.00	230	深灰色泥岩 深灰色灰质油泥岩	0.03	2.03	11.17	13.22	14.85	444	2.36	1.23	631	52	II 1	好	成熟	265.81	86.09

\*\*井有机质为 II 1 型成熟好烃源岩, 储层中微裂缝较为发育, 井段3635.77-3680m试油, 日油41.5t, 日气8754m<sup>3</sup>, 日水6.4m<sup>3</sup>。

三、应用效果

(2) \*\*井

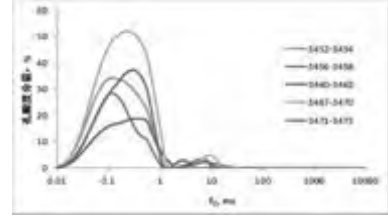


□ \*\*井井段3440.42-3504.47m, 岩性灰色油斑泥灰岩, 试油日油154t, 气13400m<sup>3</sup>, 水3.22m<sup>3</sup>, 试油结论为油层。

三、应用效果

(2) \*\*井

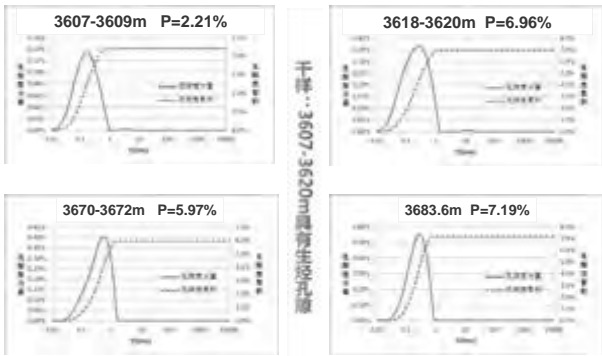
\*\*井试油段核磁谱图



序号	样品名称	质量 (g)	体积 (ml)	峰面积	单位体积峰面积	孔隙度
1	3452-3454	14.032	5.6128	2684.413	478.2663	7.20%
2	3456-3458	13.7802	5.51208	1772.12	321.4975	4.82%
3	3460-3462	11.7361	4.69444	1302.341	277.422	4.15%
4	3467-3470	13.8697	5.54788	4033.907	727.1078	10.98%
5	3470-3473	13.2109	5.28436	2437.646	461.2945	6.94%

三、应用效果

(2) \*\*井



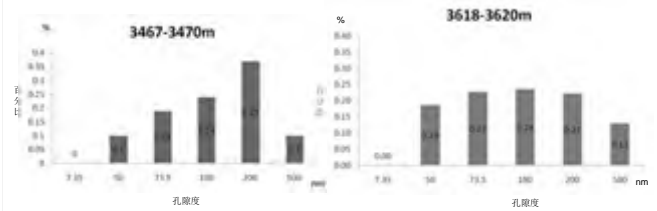
井段: 3607-3620m 岩性: 油斑泥灰岩

三、应用效果

非常规储层多维核磁共振孔隙分级评价。

(2) \*\*井

\*\*井基质孔隙百分含量直方图

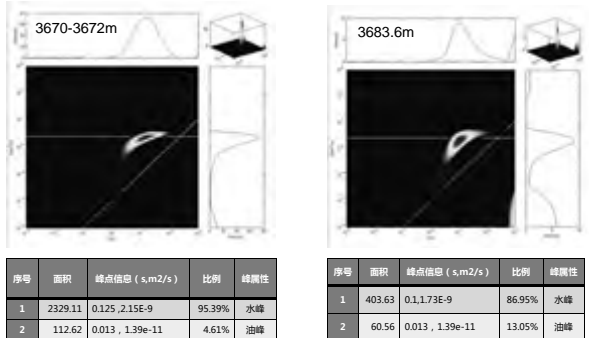


\*\*、##井测井渗透率统计表

井号	**			##	
顶深	3632	3639	3671	3472	3608
底深	3639	3656	3681	3480	3621
渗透率	0.4	0.4	0.4	0.4	0.2

三、应用效果

(2) \*\*井

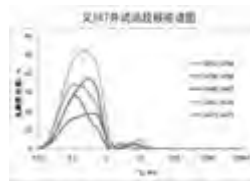


三、应用效果

(2) \*\*井

\*\*井试油段有机质丰度评价表

井深	岩性	S0	S1	S2	Pg	St	Tmax	TOC	PO	HI	D	有机质类型	成熟度	生成量	排烃量	
3440.42-3504.47	暗灰色灰质油斑泥灰岩	0.06	3.32	20.57	23.95	36.08	432	4.49	2.99	804	67	I	很好	成熟	591.42	398.98
3577.10-3691.90	深灰色泥岩	0.08	2.82	13.50	16.10	23.68	440	3.13	1.97	756	63	II	好	成熟	502.16	322.39



\*\*井井段3440.42-3504.47m试油日油154t, 气13400m<sup>3</sup>, 水3.22m<sup>3</sup>, 气测全烃4.83%↑100%, 岩性主要为灰色油斑泥灰岩, 有机质为I型成熟较好烃源岩, 孔隙度最高为10.98%。  
井段3577.11-3691.90m中途测试, 暂未定性, 受储层物性、含油级别、生烃能力影响, 该段未形成工业油流。



## 目 录

- 1 前言
- 2 多维核磁共振录井技术
- 3 应用效果
- 4 结束语



## 四、结束语

认识

利用多维核磁共振录井技术能够有效检测泥页岩、致密砂岩等非常规储层中纳米级的孔隙，利用D-T<sub>2</sub>谱图能够准确地识别储层中流体的展布和含量，直观地评价油气水层，促进录井油气水层综合解释水平的提高，解决了泥页岩、致密砂岩油气层录井评价的需求，对非常规储层油气勘探具有非常重大指导意义，因此应该大力发展多维核磁共振录井技术。



谢谢大家！

敬请前辈专家批评指正！

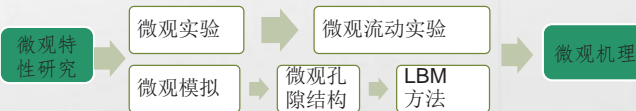
## 微流动可视化的新进展

狄勤丰 顾春元 程毅翀 叶锋

上海大学, 上海市应用数学和力学研究所  
上海市力学在能源工程中的应用重点实验室

## 研究目的

- 储层的宏观性质（渗透率、毛管压力等）取决于岩心固体组成、微观结构以及孔隙空间中的流体性质等微观特性。
- 微观特性的认识对找到研究提高原油采收率技术的正确方向以及技术手段有着重要意义



## 目录

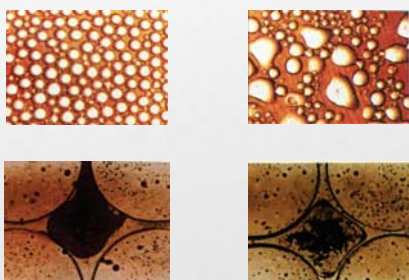
- 现有的可视化方法特性比较
- 核磁共振可视化方法取得的进展
- 结论与展望

## 已有的可视化方法

- 玻璃蚀刻模型（微观驱油）
- SEM扫描电镜
- X-CT

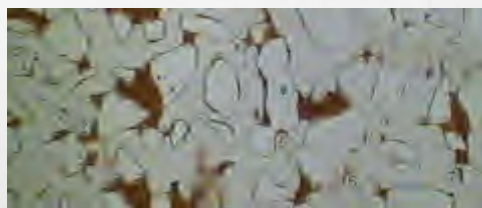
## 微观模型

- 微观模型是指将某些特定的结构刻蚀到二维玻璃平面上，以观察流体在这些结构中的运移规律



## 微观仿真模型

微观仿真模型是把天然岩心切片的孔隙系统通过激光蚀刻到平面玻璃上制成的，这种模型具有储油层的基本特性，它的孔隙网络是以岩心薄片的孔隙系统为基础制作的。所以，作为一个剖面，它具有与岩心完全相同的平面孔隙结构形态。



真实岩心仿真模型

郭尚平, 黄廷章, 胡豫初. 仿真微模型及其在油藏工程中的应用[J]. 石油学报, 1990, 1: 008.  
鞠野. 一元/二元/三元驱油体系微观驱油机理研究[D]. 大庆: 大庆石油学院, 2006.



## 微观仿真模型



a.水驱前      b.水驱后      c.二元驱后  
非均质微观仿真模型二元复配体系驱替效果

杨沛鑫, 宦文超, 曹忠伟. 大庆油田三元复合驱驱油机理研究[J]. 大庆石油地质与开发, 1999, 18(3): 24-26.  
陈涛平, 宋文琦, 高明等. 超低界面张力体系驱油方式与微观驱油效果[J]. 科学技术与工程, 2010, (017): 4259-4262.

## 微观仿真模型



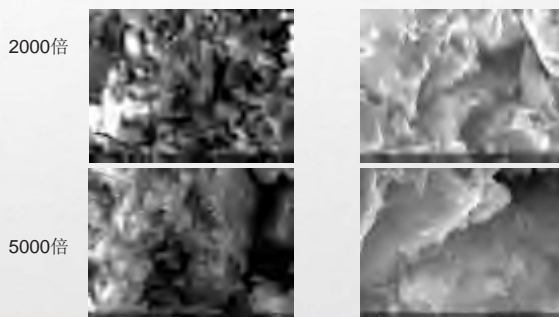
a. 膜状残余油      b. 柱状残余油      c. 簇状残余油  
滞留在油层中不同形式的残余油

杨沛鑫, 宦文超, 曹忠伟. 大庆油田三元复合驱驱油机理研究[J]. 大庆石油地质与开发, 1999, 18(3): 24-26.  
陈涛平, 宋文琦, 高明等. 超低界面张力体系驱油方式与微观驱油效果[J]. 科学技术与工程, 2010, (017): 4259-4262.

## 微观模型

- 二维平面模型
- 孔隙介质单一
- 还原性差

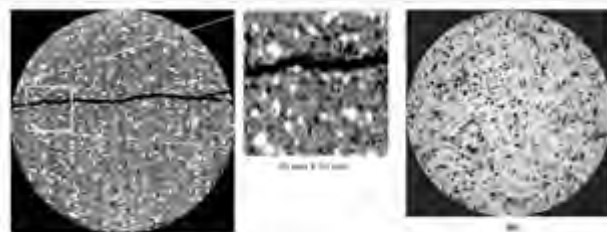
## SEM扫描电镜



## SEM扫描电镜

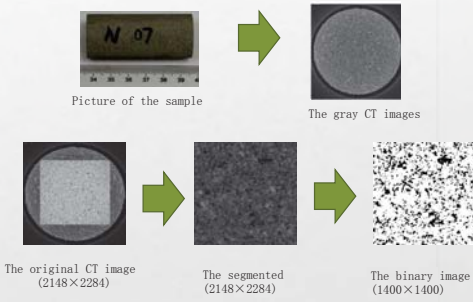
- 分辨率高
- 样品制作复杂
- 对样品有损伤
- 孔隙表层结构

## 天然岩心二维CT成像



Withjack E, Devier C, Michael G. The role of X-ray computed tomography in core analysis: proceedings of the SPE Western Regional/AAPG Pacific Section Joint Meeting, 2003[C].

### CT 成像建立数字岩心



Zhang Y, Zhao J, Zhou K *et al.* Porosity analysis based on the CT images processing for the oil reservoir sandstone: proceedings of the Automatic Control and Artificial Intelligence (ACAI 2012), International Conference on, 2012[C]. IET

### 不同孔隙度CT成像效果



(a) Fontainebleau sandstone ( $\Phi=13\%$ ,  $a = 5.7 \text{ m}$ ), (b) Berea sandstone ( $\Phi= 29\%$ ,  $a = 4.4 \text{ m}$ ), (c) a dual scale reservoir sandstone ( $\Phi = 24\%$ ,  $a=2.6 \text{ m}$ ), and (d) a multiscale carbonate rock ( $\Phi = 14\%$ ,  $a=1.1 \text{ m}$ ). Here notes porosity, and a the voxel size.

Arns CH. A comparison of pore size distributions derived by NMR and X-ray-CT techniques[J]. Physica A: Statistical Mechanics and its Applications, 2004,339(1-2): 159-165.

### CT成像

- 精度高
- 定位准确
- 流体与固体分辨不清
- 成本高
- 辐射

### 可视化方法比较

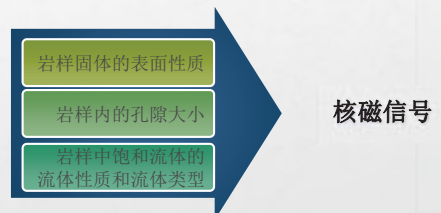
玻璃蚀刻模型	<ul style="list-style-type: none"> <li>• 二维模型、孔隙介质单一</li> <li>• 还原性差</li> </ul>
SEM电镜扫描	<ul style="list-style-type: none"> <li>• 分辨率高</li> <li>• 样品制作复杂</li> <li>• 对样品有损伤</li> <li>• 不能定位孔隙结构的位置</li> </ul>
CT	<ul style="list-style-type: none"> <li>• 精度高</li> <li>• 定位准确</li> <li>• 流体与固体分辨不清</li> <li>• 成本高</li> <li>• 辐射</li> </ul>

### MRI与CT成像效果对比



Herremans E, Melado-Herreros A, Defraeye T *et al.* Comparison of X-ray CT and MRI of watercore disorder of different apple cultivars[J]. Postharvest Biology and Technology, 2014,87: 42-50.

### 核磁共振可视化



上海市力学在能源工程中的应用重点实验室  
上海大学——纽迈科技微纳流动可视化实验室

核磁共振驱替成像系统

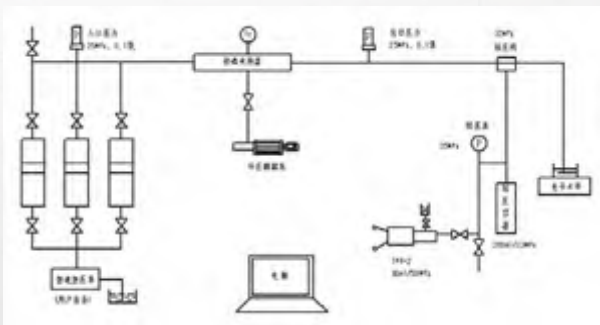


上海市力学在能源工程中的应用重点实验室  
上海大学——纽迈科技微纳流动可视化实验室

实验室挂牌仪式



### 驱替流程示意图



### Lattice Boltzmann 方法

采用Qian等人提出的单松弛时间方法，其演化方程为

$$f_i(\mathbf{x} + \mathbf{e}_i \Delta t, t + \Delta t) - f_i(\mathbf{x}, t) = -\frac{1}{\tau} [f_i(\mathbf{x}, t) - f_i^{eq}(\mathbf{x}, t)]$$

$f_i$  是粒子分布函数， $\tau$  是松弛因子， $f_i^{eq}$  是平衡态分布函数，

$$f_i^{eq} = \omega_i \rho \left[ 1 + \frac{\mathbf{e}_i \cdot \mathbf{u}^{eq}}{c_s^2} + \frac{(\mathbf{e}_i \cdot \mathbf{u}^{eq})^2}{2c_s^4} - \frac{(\mathbf{u}^{eq} \cdot \mathbf{u}^{eq})}{2c_s^2} \right]$$

定义是高散速度，定义为

$$\mathbf{e}_i = \begin{cases} (0,0)c & i=0 \\ \left[ \cos \frac{(i-1)\pi}{2}, \sin \frac{(i-1)\pi}{2} \right] c & i=1, \dots, 4 \\ \sqrt{2} \left[ \cos \frac{(2i-9)\pi}{4}, \sin \frac{(2i-9)\pi}{4} \right] c & i=5, \dots, 8 \end{cases}$$

### 程序框图



### 用到的模型

D2Q9权重系数

$$\omega_i = \begin{cases} 4/9 & i=0 \\ 1/9 & i=1, 2, 3, 4 \\ 1/36 & i=5, 6, 7, 8 \end{cases}$$

流体粘性系数和模型松弛因子之间的关系

$$\nu = \left( \tau - \frac{1}{2} \right) c_s^2 \Delta t$$

宏观密度、宏观动量为

$$\rho = \sum_i f_i$$

$$\rho \mathbf{u} = \sum_i \mathbf{e}_i f_i$$

### Shan-Chen多相流模型

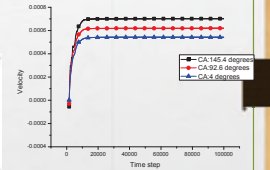
流体间作用力	$\mathbf{F}(\mathbf{x}) = -G\psi(\mathbf{x},t)\sum_i w_i\psi(\mathbf{x}+\mathbf{e}_i\Delta t,t)\mathbf{e}_i$
流体与固体之间的作用力	$\mathbf{F}_{ads}(\mathbf{x}) = -G_{ads}\psi(\mathbf{x},t)\sum_i w_i s(\mathbf{x}+\mathbf{e}_i\Delta t,t)\mathbf{e}_i$
相互作用势能	$\psi(\mathbf{x},t) = \psi_0 e^{-\rho/\rho}$
修正后的平衡态速度	$\mathbf{u}^{eq} = \mathbf{u} + \tau(\mathbf{F} + \mathbf{F}_{ads})/\rho$
流体的真实宏观速度	$\mathbf{U} = \mathbf{u} + (\mathbf{F} + \mathbf{F}_{ads})/(2\rho)$

### 二维多孔介质流动模拟

计算网格633×2400，壁面采用反弹边界条件，左右采用压力边界条件。



多孔介质几何模型



不同润湿性对流动特性的影响

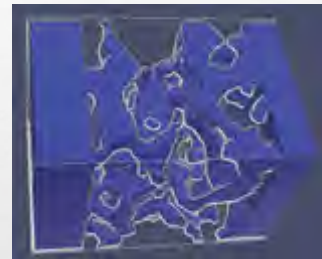
通过改变多孔介质壁面润湿性，可以体现多孔介质内流体流动阻力的大小变化。

### 纳米颗粒吸附法减阻数值模拟



计算可知纳米颗粒吸附后渗透率比纳米颗粒吸附前提高了约为12.8%

### 三维多孔介质流动模拟



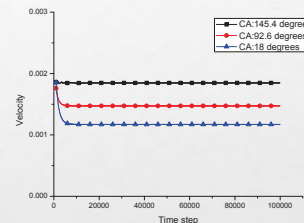
多孔介质几何模型

### 三维多孔介质流动模拟



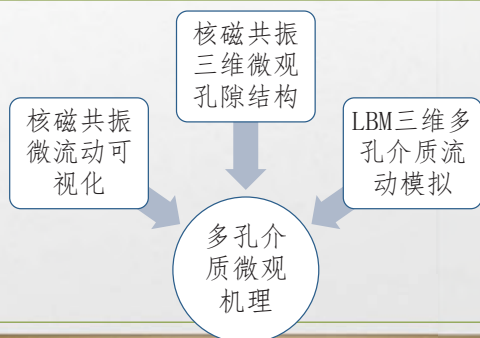
驱替过程截图

### 壁面润湿性对流动特性的影响 (三维)



不同壁面润湿性时，孔隙内流体的平均速度随时间的变化规律

## 结论与展望



Thank You !



# 影响水泥基材料中低场核磁共振信号的诸因素探讨

报告人：孙振平 教授

2013年10月12日



## 主要内容

### 探讨背景

- 水泥组成的复杂性
- 顺磁性物质对弛豫信号的影响

### 实验内容

- 粉煤灰对核磁信号的影响
- 半回波时间对核磁信号的影响
- 氧化物类型对核磁信号的影响

### 问题与解决方向



## 背景

### 低场核磁共振技术在水泥基材料研究中的应用

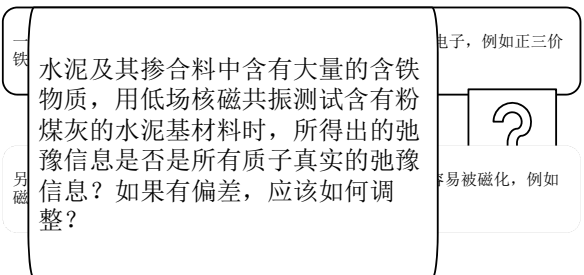
- 水化进程
- 孔隙结构
- 水分迁移
- 结合水分析

### 在水泥基材料中的核磁共振弛豫环境复杂

- 水泥的多组分，且含有含铁矿物
- 掺合料也引入大量的含铁氧化物或矿物

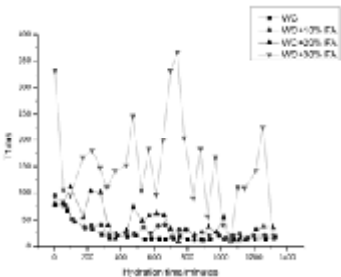


## 对质子弛豫产生影响的两种类型 (Kristina)



## 粉煤灰对自水泥浆体水化过程的影响

- ▶ 纯自水泥纵向弛豫时间随龄期变化曲线较平滑，纵向弛豫时间随龄期变得越来越小；
- ▶ 掺加粉煤灰后，曲线不再平滑，而是呈现锯齿状跳动；
- ▶ 随着粉煤灰掺量的提高，弛豫时间呈增大趋势；
- ▶ 粉煤灰掺量达到一定比例后，纵向弛豫时间的变化已经基本无规律可循了。

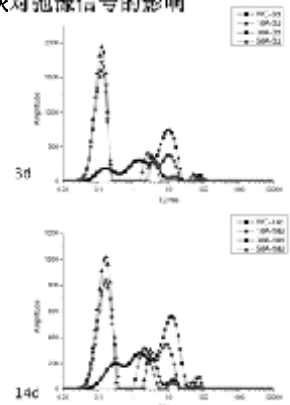


不同掺量粉煤灰浆体的纵向弛豫时间随水化龄期的变化



## 不同龄期粉煤灰对弛豫信号的影响

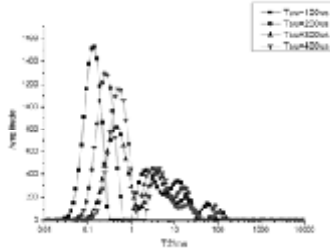
- 在3d龄期时，可以发现：
- ▶ 随着粉煤灰掺量的增加，信号总量减少；
- ▶ 粉煤灰的掺加，可以增加凝胶孔质子的信号量；
- ▶ 粉煤灰的掺加，峰的向低弛豫时间方向移动





回波时间对核磁信号的影响

从图可以看出：  
 > 回波时间对质子弛豫的信号总量有一定影响；  
 > 随着半回波时间的减小，弛豫信号分布峰向小弛豫时间移动

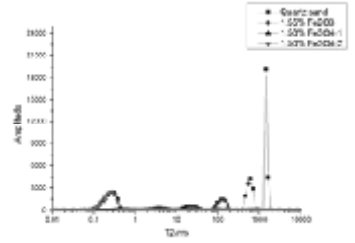


不同半回波时间对测试信号的影响



铁氧化物类型对核磁共振信号的影响

从图可以看出：  
 > 三氧化二铁和四氧化三铁都对核磁共振信号有影响；  
 > 四氧化三铁的作用效果强于三氧化二铁  
 > 它们不仅使信号量减少，而且影响峰向小弛豫时间移动。



铁氧化物与石英砂混合物的T<sub>2</sub>分布曲线



目前研究遇到的问题

不管水泥还是掺合料中的顺磁性物质或者磁性矿物掺加到水泥中都不是以惰性材料存在

对不同类型的铁原子或离子无法进行准确定量的分析

低场核磁共振设备的稳定程度

$$\frac{1}{T_2} = \frac{1}{T_{2,bulk}} + \frac{D}{12} (\gamma G)^2 r^2 + \frac{1}{T_2}$$



FIG. 1. Schematic of the two-dimensional diffusion of water molecules in the vicinity of Fe<sup>3+</sup> paramagnetic ions on the surface of porous media particles. The correlation time for molecular jumps is  $\tau_c$ , the random walk time is  $\tau_w$ .



Thank you!  
 Thank you!  
 Thank you!  
 Thank you!  
 Thank you!  
 Thank you!

Central South University  
中南大学

## 多因素耦合作用下砂岩的核磁共振测孔与成像研究

汇报人：田维刚  
专业：采矿工程  
单位：中南大学  
指导老师：邓红卫 副教授 周科平教授

2013年10月12日

Central South University  
中南大学

## 报告内容

- 一、选题背景和研究价值
- 二、国内外研究现状
- 三、试验方案设计
- 四、研究成果
- 五、致谢

Central South University  
中南大学

### 选题背景 Background

西藏等高寒地区矿产资源开发程度相对较低，开发潜力大。高寒地区，昼夜温差和夏冬温差都很大，因此矿产资源的开发过程中，因气候变化，面临着岩石冻融损伤力学问题。

矿山岩体冻融损伤往往是在多种复杂条件下发生的，比如，经常受到矿山生产酸性废水、区域酸性降雨和除冰盐溶液侵蚀，并且矿山对象岩体大多含有原生或次生裂隙节理，尤其是因爆破等人工开挖产生了新鲜次生裂隙的节理岩体在冻融循环作用下的损伤会更加剧烈。

### 研究价值 Significance

开展多因素耦合作用下岩石冻融循环试验研究，不仅是对冻融岩石力学这一新兴研究方向的深入系统研究，而且能直接指导包括西藏地区在内的广大寒区矿业开发等岩体工程冻融灾害的分析和防治，具有重要的理论价值和现实意义。

Central South University  
中南大学

### 二、国内外研究现状

- 1、冻岩问题是从冻土问题研究中逐渐细化分离出来的，专门的冻岩研究相对起步较晚，研究较少，徐光苗等人指出土和岩的最大区别是岩的胶结强度一般大于土，**岩中一般赋存节理和裂隙，而影响冻岩物理力学性质的主要因素是裂隙水（冰）。**
- 2、Wikner(1965)通过分析岩石内部分相膨胀规律发现指出，**冻结岩石的抗拉强度比抗压强度更值得关注；**
- 3、张继周等通过冻融循环方法，对3种岩石（粉砂质泥岩、辉绿岩和白云质灰岩）在**2种水化环境下（蒸馏水饱和，饱和并经1%硝酸溶液浸泡侵蚀）**分别进行冻融实验研究，研究发现在**酸性条件下，岩石冻融强度损伤较纯水化条件下要剧烈得多。**

Central South University  
中南大学

### 二、国内外研究现状

- 4、寒区工程中，人们发现使用除冰盐将使混凝土冻害显著加剧，后有大量的学者就除冰盐溶液（质量分数约3—5%）对混凝土冻融损伤进行了专门研究，同时用渗透压等冻融破坏理论做了较好的解释，但**岩石冻融研究中还很少有技术报道中考虑除冰盐溶液影响的。**
- 5、冻融岩石微观损伤观察方面，已有的传统方法主要包括超声波探测、压汞法测孔、电子显微镜观察、CT扫描法等，中南大学在国内率先**将核磁共振技术运用到岩石冻融研究中**，产出了一批研究成果，但仍有大量的工作有待完善和补充。

Central South University  
中南大学

### 三、试验方案设计

材料：均质性较好的砂岩

温度范围：±20°C

循环周期：约10小时

强度试验

质量和外观变化

核磁共振测孔与成像

岩石损伤检测

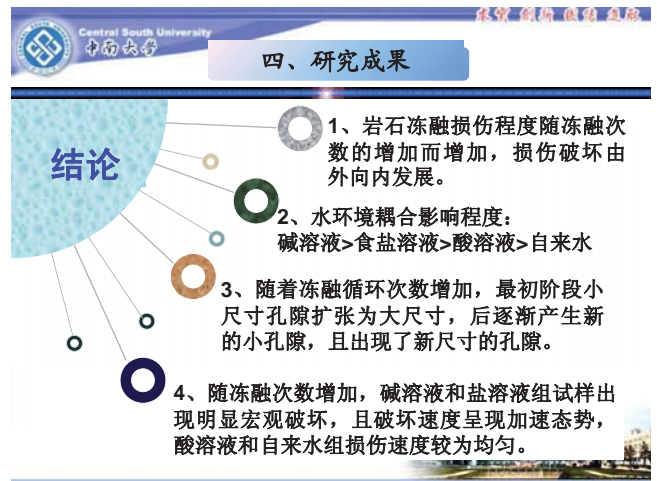
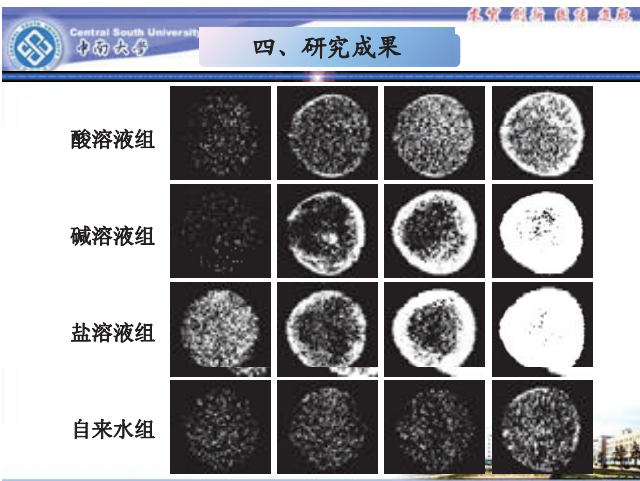
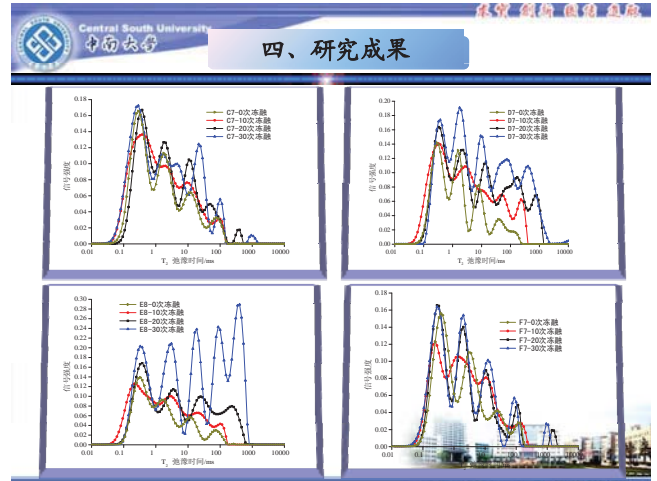
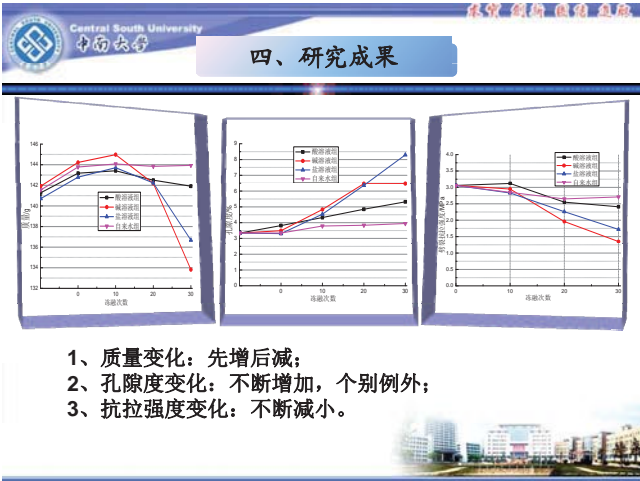
抗拉组

抗压组

点荷载组

试件个数：42  
试件尺寸：Φ50×H30mm  
A-6 对照组，不冻融  
C-9 稀硫酸溶液中冻融10、20、30次  
D-9 NaOH溶液中冻融10、20、30次  
E-9 食盐溶液中冻融10、20、30次  
F-9 自来水中冻融10、20、30次






Central South University  
中南大学

### 五、致谢

本人所做全部研究工作是在邓红卫老师悉心指导下完成的，在课题研究过程中得到了周科平老师和李杰林老师等人的诸多支持和帮助，在这里一并表示真诚的感谢，同时向本次学术会议主办单位工作人员的辛勤劳动致以深深的敬意。

——田维刚



## 一种新型的钻井液荧光背景下的油层识别与评价技术

王志战<sup>1</sup>, 秦黎明<sup>1</sup>, 郑奕挺<sup>1</sup>, 蔡清<sup>2</sup>, 杨培强<sup>2</sup>

(1. 中国石化石油工程技术研究院测录井研究所, 北京 100101; 2. 苏州纽迈电子科技有限公司, 江苏 苏州 215163)

**摘要:** 荧光钻井液包括聚磺钻井液、混油钻井液、油基钻井液三大体系, 该类钻井液的使用有助于保障钻井安全、处理卡钻事故、保护油气层, 却不利于油气显示的发现。为了突破油气勘探与钻井工程之间的这道瓶颈, 创新采用高分辨率低场核磁共振技术分别对聚磺钻井液、混油钻井液、油基钻井液条件下的油层识别技术进行了室内实验和现场应用研究, 结果表明: 固体粉末状荧光添加剂没有核磁共振信号, 对钻井液核磁共振录井发现油层没有影响, 从而可彻底解放对该类添加剂的使用限制; 混油钻井液属于水包油体系, 地层原油与添加油在核磁共振  $T_2$  谱上呈现两个孤立的油峰, 从而实现了油层的及时发现与定量评价; 油基钻井液分为油包水或纯油基两种, 油层被钻开后, 地层油会与钻井液的油峰重合, 是现有录井技术最难解决的类型, 但通过核磁共振技术对  $T_{2g}$  及含油率的精细评价, 仍可实现极端条件下的油层发现。该研究成果完善了录井技术采集系列, 对于提高油气勘探效益、提高钻井时速时效具有十分重要的意义。

**关键词:** 油层识别, 油层评价, 荧光钻井液, 钻井液核磁共振, 含油率。

## 核磁共振确定岩石孔隙结构及应用

刘堂晏<sup>1</sup> 汤天知<sup>2</sup> 杜环虹<sup>2</sup> 章海宁<sup>2</sup> 邬龙<sup>1</sup>

<sup>1</sup>海洋地质国家重点实验室（同济大学），上海，200092

<sup>2</sup>中国石油集团测井技术有限公司技术中心，西安，710075

### 摘要

油气储集层的孔隙结构是油气开采的重要参数，核磁共振的弛豫过程与岩石的孔隙结构相关，因而，核磁共振成为评价岩石孔隙结构的主要方法。本文应用寻优反演的方法，在最优反演的条件下，根据岩石孔隙结构的正演模型，得到关于岩石的球形孔和管形孔的形态参数和分布参数。根据电阻定律的数值模拟结果，本次研究证明，对于不同形态和不同分布的球形孔和管形孔，岩石的电阻率呈现了显著的差异，岩石的实验室电阻率测量也证实了这种差异。核磁共振实验分析、岩石电性的数值模拟，以及实验室测量的综合研究的结果，证明，野外测井和实验室的电性分析的数据分散，不仅仅与测量误差有关，其中，岩石的孔隙结构也是一个重要的影响因素。

**关键词：**核磁共振 电阻定律 测井解释 孔隙结构 阿尔奇 优化反演

## 岩石 T2-G 实验采集参数自动匹配方法及应用

范宜仁<sup>1,2</sup>，吴飞<sup>1,2</sup>，邓少贵<sup>1,2</sup>，邢东辉<sup>1,2</sup>，刘玺<sup>1,2</sup>

(1. 中国石油大学 地球科学与技术学院，山东 青岛 266580

2. 中国石油大学 CNPC 测井重点实验室 山东 青岛 266580)

**摘要：**针对改良式 CPMG 序列测量岩石内部磁场梯度分布时难以确定第一个窗口的持续时间  $t_0$  及回波个数 NE1 的难题，总结 T2-G 实验采集参数人工调节规律后提出  $t_0$ 、NE1 的一种自动匹配方法。利用长、短回波间隔 CPMG 测量估算岩石内部磁场梯度大小，在此基础上构造岩石的等效(T2,G)二维正态分布模型，基于该模型变化  $t_0$ 、NE1 进行 T2-G 回波串正演数值模拟，结合 T2-G 最优化采集参数的约束条件确定  $t_0$ 、NE1。不同地区、不同物性、不同内部磁场梯度大小的 4 块砂岩 T2-G 测量验证了该方法的可行性和普适性，并且该方法使 T2-G 实验检测效率提高了四倍。

**关键词：**改良式 CPMG；内部磁场梯度；采集参数；自动匹配；数值模拟

## NMR 技术在非常规油气层评价中的应用探讨

王志战<sup>1</sup>, 秦黎明<sup>1</sup>, 陆黄生<sup>1</sup>, 蔡清<sup>2</sup>, 杨培强<sup>2</sup>

(1.中国石化石油工程技术研究院测录井研究所, 北京 100101;

2.苏州纽迈电子科技有限公司, 江苏 苏州 215163)

非常规油气储层的突出特征是纳米级孔隙和非达西流渗流特征, 特殊的储层特性决定了油气成藏机理、富集规律、钻采工艺的不同, 也决定了常规核磁共振技术具有诸多的不适应性。结合国内外技术现状<sup>[1-3]</sup>及所开展的实验工作, 阐述了核磁共振技术在: 纳米级孔隙的储层物性评价 (图 1a)、油基钻井液条件下的油层判识 (图 1b)、孔隙流体的多维核磁共振快速识别 (图 1c)、储层结构的核磁共振成像 (图 1d) 等方面的应用; 与此同时, 深入分析了非常规油气对核磁共振软硬件技术所提出的挑战。

图 1(a)显示的是不同的 TE 对纳米级孔隙测量的影响, TE 越大, 小孔隙的信息丢失越多。核磁共振能测到 8nm 左右的孔隙, 比压汞法、纳米 CT 和聚焦离子束等技术的分辨率更高; 图 1(b)显示的在油基钻井液条件下钻遇油层的 T<sub>2</sub> 谱, 其定量程度优于目前的气测录井及三维定量荧光录井技术; 图 1(c)显示的是不同孔隙流体的多维谱分布, 对于非常规油气层, 采用弛豫试剂浸泡的方法区分油水信号是行不通的; 图 1(d)是全直径岩心的核磁共振成像, 从中可以看出孔隙和裂缝的分布, 并可任意切片。

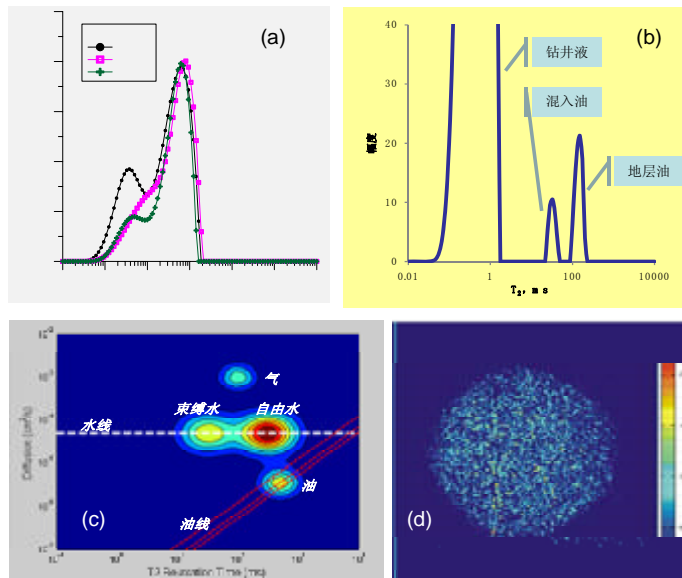


图 1 核磁共振技术在非常规油气评价中的应用。(a)TE 对纳米孔隙测量的影响; (b)油基钻井液条件下的油层识别; (c)利用多维核磁快速、准确识别孔隙流体; (d)岩心的核磁共振成像。  
Fig.1 NMR technology applications in unconventional reservoir evaluation.

(a) Effect of TE on the nanoscale pore measurements; (b) the oil layer identification under oil based drilling fluid; (c) using multiple dimensional NMR to fast detect the pore fluids; (d) NMR imaging of cores.

**通讯联系人:** 王志战 (1969-), 男, 山东栖霞人, 博士, 教授级高级工程师, 主要从事录井技术研究工作; 通讯地址: 北京市朝阳区北辰东路 8 号北辰时代大厦 918 室; 电话: 010-84988382; E-mail: [pjes@163.com](mailto:pjes@163.com)。

## NMR technology applications in unconventional reservoir evaluation

Zhizhan Wang<sup>1</sup>, Liming Qin<sup>1</sup>, Huangsheng Lu<sup>1</sup>, Qing Cai<sup>2</sup>, Peiqiang Yang<sup>2</sup>

(1. SINOPEC Research Institute of Petroleum Engineering, Beijing 100101, China;

2. Niumai Electronic Technology Limited Company, Suzhou 215163, China.)

Unconventional reservoir is prominently characterized by nanoscale pores and non-Darcy flow, which determines its differences compared with the conventional reservoir, such as oil or gas distribution, accumulation mechanism, and drilling or production technology, etc. So, the conventional NMR technology can not satisfy with the reservoir demands. Combining with the current technology in the world and some experiment results, some applications by NMR method have been investigated: (1) the petrophysical evaluation in nanoscale pore reservoir (Fig.1a); (2) the oil layer identification under oil based drilling fluids(Fig.1b); (3) fast identification of pore fluids by multiple dimensional NMR method(Fig.1c); (4) reservoir structure imaging by NMR(Fig.1d). Meanwhile, some challenges to NMR software and hardware technology in unconventional reservoir evaluation have been analyzed.

Fig.1a shows the effect of different TE values on the nanoscale pore measurements. The more TE value increasing, the more information loss in small pores. Compared with the Mercury Intrusion, Nano CT and Focused Ion Beam methods, NMR has higher resolution and can detect approximately 8nm scale pores. Fig. 1b displays the T<sub>2</sub> spectrum of the oil layer under oil based drilling fluid by NMR method, whose quantified accuracy is superior to gas logging and 3D quantitative fluorescence technique; Fig. 1c reveals the multiple dimensional spectrums of different pore fluids. For conventional reservoirs, using relaxation reagent to soak samples by NMR method cannot distinguish the oil and gas signals; Fig.1d indicates the NMR imaging of the full hole cores. The pores and fractures can be obtained and random slices can be cutted.

### References:

- [1] Martínez G A and Davis L A. Petrophysical Measurements on Shales Using NMR[J]. SPE 62851, 2000.
- [2] Arns C H, Washburn K E, and Callaghan P T. Multidimensional NMR Inverse Laplace Spectroscopy in Petrophysics[J]. Petrophysics, 2007,48(5): 380–392.
- [3] Arns C H, Sheppard A P, Sok R M, et al. NMR petrophysical predictions on digitized core images[J]. SPWLA 46th Annual Logging Symposium, 2005.

# 冻融循环条件下岩石核磁共振特性的试验研究

周科平<sup>1</sup>, 李杰林<sup>1</sup>, 许玉娟<sup>1</sup>, 张亚民<sup>1</sup>, 杨培强<sup>2</sup>, 陈路平<sup>2</sup>

(1. 中南大学 资源与安全工程学院, 湖南 长沙 410083; 2. 上海纽迈电子科技有限公司, 上海 200062)

**摘要:** 为研究岩石在冻融循环作用下微观结构的变化特征, 选取寒区花岗岩为试样, 在冻结温度为 $-40\text{ }^{\circ}\text{C}$ , 融解温度为 $20\text{ }^{\circ}\text{C}$ 条件下分别进行0, 10, 20, 30和40次冻融循环试验, 并对冻融循环后的岩样进行核磁共振(NMR)测量, 得到不同冻融循环次数后岩样的横向弛豫时间 $T_2$ 分布及核磁共振成像图像。结果表明: 花岗岩的 $T_2$ 分布主要为3个峰, 第一个峰和第二个峰的面积之和占全部峰总面积的98%以上, 表明微孔隙占绝大多数; 在经历10, 20, 30和40不同冻融循环次数后, 岩石的 $T_2$ 谱面积发生了明显变化, 孔隙率分别增大了14.0%, 0.9%, 16.2%和1.6%。核磁共振图像显示冻融循环后岩样的孔隙空间分布情况。冻融循环条件下岩石核磁共振特征的变化规律, 为岩石冻融损伤机制研究提供可靠的试验数据。

**关键词:** 岩石力学; 冻融循环; 核磁共振; 花岗岩; 孔隙度; 弛豫时间

**中图分类号:** TU 458

**文献标识码:** A

**文章编号:** 1000-6915(2012)04-0731-07

## EXPERIMENTAL STUDY OF NMR CHARACTERISTICS IN ROCK UNDER FREEZING AND THAWING CYCLES

ZHOU Keping<sup>1</sup>, LI Jielin<sup>1</sup>, XU Yujuan<sup>1</sup>, ZHANG Yaming<sup>1</sup>, YANG Peiqiang<sup>2</sup>, CHEN Luping<sup>2</sup>

(1. School of Resources and Safety Engineering, Central South University, Changsha, Hunan 410083, China;

2. Shanghai Niumag Electronic Technology Co., Ltd., Shanghai 200062, China)

**Abstract:** For knowing the variation characteristic of rock microstructure under freezing and thawing cycles, the experimental study on granite sample is conducted under different freezing and thawing cycles of 0 time, 10, 20, 30 and 40 times with the freezing temperature of  $-40\text{ }^{\circ}\text{C}$  and thawing temperature of  $20\text{ }^{\circ}\text{C}$ . The nuclear magnetic resonance(NMR) is used to test the samples after freezing and thawing cycles; and the crosswise relaxation time  $T_2$  distribution and NMR imaging are obtained. The results show that:  $T_2$  distribution of granite exhibits three peaks and the subtotal spectrum area between the first peak and second peak occupies more than 98% of the total area, which means the micro pores are in the majority. After different freezing-thawing cycles of 10, 20, 30 and 40 times, the  $T_2$  spectrum area has changed obviously; and the porosity has increased by 14%, 0.9%, 16.2% and 1.6% respectively. Also, the space distributions of pores have been visually shown by the NMR imaging. The variation law of NMR characteristics in rock under freezing-thawing cycles has provided the reliable experimental results for the research works of rock damage mechanism under freezing and thawing cycles.

**Key words:** rock mechanics; freezing and thawing cycles; nuclear magnetic resonance(NMR); granite; porosity; relaxation time

**收稿日期:** 2011-10-09; **修回日期:** 2011-12-04

**基金项目:** 国家自然科学基金资助项目(51074178); 高等学校博士学科点专项科研基金(20090162110036)

**作者简介:** 周科平(1964-), 男, 博士, 1987年毕业于重庆大学资源与环境工程学院采矿工程专业, 现任教授、博士生导师, 主要从事矿山岩石力学方面的教学与研究工作。E-mail: kpzhou@263.net

## 1 引言

岩石是一种由各种造岩矿物或岩屑在地质作用下按一定规律组合而形成的多种矿物颗粒的集合体,岩石中通常含有节理、裂缝纹和孔隙等,而在孔隙空间中通常包含油、气、水等流体<sup>[1]</sup>。在寒区,由于季节更替、昼夜循环,岩石材料承受着冻融循环而引起的物理风化作用,造成岩石内部的微裂缝扩张和传播,内部材质发生劣化,影响岩石的物理力学性质。因此,分析和了解岩石在冻融循环条件下微观结构的变化特征,对于研究岩石冻融损伤的规律和寒区岩体工程的破坏机制有重要意义。

国内外许多学者就冻融循环作用对岩石材料的影响进行了大量有益的研究: D. T. Nicholson 和 F. H. Nicholson<sup>[2]</sup>对 10 种含有原生裂隙的岩石进行了冻融循环试验,研究了原生裂隙对岩石冻融损伤劣化程度的影响;徐光苗<sup>[3]</sup>研究 2 种岩石在开放饱水条件下的冻融循环试验,分析了相应的力学特性,并建立了岩石冻融的温度-渗流-应力损伤本构模型; M. Bellanger 等<sup>[4]</sup>采用岩石物理学方法,通过研究法国东北部 Lorarine 地区石灰岩的孔隙率、饱和含水量、渗透率、毛细吸水率等,得出了它们之间的相互关系;吴刚等<sup>[5]</sup>研究了大理岩循环冻融后的质量、体积以及超声波纵波波速特性,归纳出循环冻融下大理岩的物理力学特性;张继周等<sup>[6]</sup>对岩石冻融损伤劣化的影响因素进行了归纳总结,并研究了岩石在冻融条件下的损伤劣化机制和相应的力学特性。

目前观测岩石微观结构主要是利用图像分析技术、电镜扫描和 CT 扫描等手段,也有许多学者开展了冻融循环后岩石微观结构方面的研究: R. V. G. De Argandona 等<sup>[7]</sup>对来自西班牙的 Laspra 白云岩进行了循环冻融,利用 CT 技术对岩样进行扫描,分析岩样的孔隙结构在冻融条件下的演化;杨更社等<sup>[8-10]</sup>应用 CT 技术研究了不同冻结速度、冻结温度和冻融循环次数等条件下岩石内部的细观损伤扩展机制及损伤结构的变化和影响;刘成禹等<sup>[11]</sup>利用电镜扫描对冻融循环后的花岗岩进行了冻融损伤机制研究。

核磁共振技术已经成功应用在医学诊断、石油勘探开发、农业、食品和生物医药等领域,在岩石孔隙结构、储层岩石孔隙流体特性研究等方面也已得到广泛的应用<sup>[12-14]</sup>,但目前将其应用于岩石冻融

损伤机制方面的研究还较少。笔者选取了黑龙江省黑河地区的花岗岩,在进行不同冻融循环次数试验后,采用核磁共振分析仪进行弛豫测量和成像测量,对花岗岩的  $T_2$  谱分布、 $T_2$  谱面积的变化特征和岩石的内部孔隙分布特性进行了分析和讨论。

## 2 试验概况

### 2.1 岩样的选取

花岗岩岩样取自黑龙江省黑河市某金矿,按高径比 2:1 要求加工成圆柱体标准试件,物理参数如表 1 所示。岩样共 15 个,编号从 N-1~N-15,每 3 个岩样为一组,共 5 组,每组对应一个冻融循环次数。

表 1 花岗岩岩样的物理参数

Table 1 Physical parameters of granite samples

循环次数	试件编号	物理参数				
		高度/mm	直径/mm	冻融前质量/g	冻融后质量/g	冻融前、后质量变化率/%
0	N-1	96.32	48.62	448.69	-	0.00
	N-2	96.82	48.56	454.54	-	0.00
	N-3	98.64	48.44	475.10	-	0.00
10	N-4	98.84	48.52	457.52	463.09	1.22
	N-5	99.72	48.56	463.72	468.08	0.94
	N-6	97.32	48.44	460.32	462.67	0.51
20	N-7	98.28	48.62	461.82	464.53	0.59
	N-8	95.76	48.59	456.42	460.24	0.84
	N-9	98.12	48.52	470.12	472.76	0.56
30	N-10	98.16	48.50	464.12	469.41	1.14
	N-11	98.30	48.54	465.82	470.16	0.93
	N-12	100.74	48.45	480.02	482.38	0.49
40	N-13	95.60	48.61	457.92	467.30	2.05
	N-14	98.72	48.47	478.82	481.06	0.47
	N-15	100.00	48.53	478.52	480.54	0.42

岩样为中粗粒碱长花岗岩,呈肉红色,块状构造,中粗粒花岗结构。碱长石主要由微斜长石和正长石组成,呈他形粒状,粒度 0.2~7.0 mm,卡式双晶发育,呈弱绢云母化、泥化,碱长石含量 46%~56%。部分花岗岩岩样如图 1 所示。

### 2.2 试验仪器

试验中使用的主要仪器有:冻融循环试验机、真空饱和装置、核磁共振成像分析系统等,各种仪器参数指标如下:





图 1 部分花岗岩岩样

Fig.1 Part of granite samples

(1) 苏州市东华试验仪器有限公司生产的 TDS - 300 型冻融循环试验机见图 2。该设备采用空气中冷冻、水中解融的工作原理, 冻融过程实现自动控制。



图 2 TDS - 300 型冻融循环试验机

Fig.2 TDS - 300-typed freezing-thawing cycles testing machine

(2) 真空饱和装置采用上海纽迈电子科技有限公司研制的设备, 设置抽气时间和压力后, 自动运行, 压力值读数为 0.1 MPa。

(3) 核磁共振测试采用上海纽迈电子科技有限公司生产的 MiniMR - 60 核磁共振成像分析系统, 见图 3。该设备的主磁场为 0.51 T, H 质子共振频率为 21.7 MHz, 射频脉冲频率为 1.0~49.9 MHz, 磁体控温 25 °C~35 °C, 磁体均匀度为 12.0 ppm, 射频功率 300 W。



图 3 MiniMR - 60 核磁共振成像分析系统

Fig.3 MiniMR - 60 type of NMR imaging analysis system

## 2.3 试验方法及方案

### (1) 冻融循环试验

参照冻融循环试验的操作规程<sup>[15]</sup>, 以取样地最低气温(-40 °C)为冻结温度, 夏季平均气温(20 °C)为融解温度, 进行冻融循环试验。岩样在-40 °C 温度下冻结 4 h, 然后在 20 °C 的水中融解 4 h, 即每个冻融循环周期为 8 h, 如此反复。每 3 块岩样为 1 组, 分别进行 5 组冻融循环, 循环次数分别为 0, 10, 20, 30 和 40 次。

### (2) 核磁共振测试试验

核磁共振测试试验在苏州市低场核磁共振仪器工程技术研究中心完成, 首先采用 MiniMR - 60 型核磁共振成像分析系统对冻融后的岩样进行一次常温自然饱和(将样品在水中浸泡 48 h)条件下的核磁共振弛豫测量; 然后采用真空饱和装置对岩样进行饱和, 真空压力值为 0.1 MPa, 抽气时间为 4 h, 抽完后再将样品放入蒸馏水中浸泡 24 h; 最后再次进行核磁共振弛豫测量, 用于对比分析。

### (3) 核磁共振成像测试

为消除测试过程中水分挥发对试验结果的影响, 将样品从水中取出后, 擦干表面水分, 用保鲜膜包好再做测试。

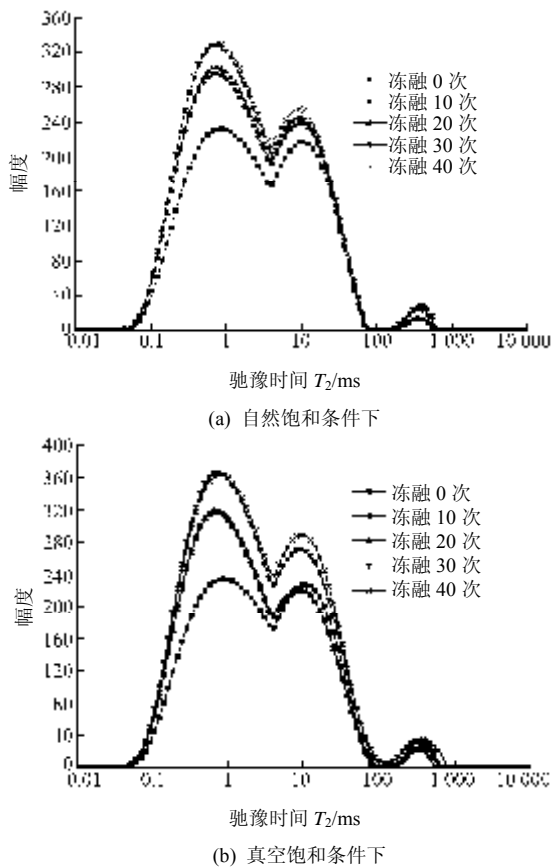
## 3 试验现象及结果分析

### 3.1 质量变化

对经历不同冻融循环次数后的岩样剩余质量进行了测定, 见表 1, 结果表明: 各岩样的质量在冻融后均出现了增大, 其中 N - 13 岩样变化最大, 增大值为 2.05%。这主要是由于岩样在冻结后, 孔隙中的水冻结成冰, 体积膨胀, 对孔隙的壁面产生挤压力, 导致已有微孔隙的扩展和新微孔隙的产生; 而当处于融解阶段时, 冰融解成水, 水会进入到新的微孔隙中, 外部的水分也会沿着孔隙通道向岩石内部迁移, 如此反复, 从而导致质量增大。

### 3.2 核磁共振 $T_2$ 谱分布

核磁共振  $T_2$  谱分布与孔隙尺寸相关,  $T_2$  值越小, 代表的孔隙越小, 孔隙大,  $T_2$  值也大<sup>[16]</sup>, 所以  $T_2$  谱分布反映了孔隙的分布情况。峰的位置与孔径大小有关, 峰面积的大小与对应孔径的孔隙数量有关。图 4 为经历不同冻融循环次数后, 自然饱和和真空饱和 2 种情况下岩样的  $T_2$  谱分布。

图4 不同饱和条件下  $T_2$  谱分布Fig.4  $T_2$  spectrum distribution under different saturation conditions

从图4可以看出,经过40次冻融循环后,花岗岩的  $T_2$  谱分布主要表现为3个峰图,部分为4个峰图,随着冻融次数的增加,  $T_2$  谱形态上发生了左移,即向小孔隙的  $T_2$  谱方向偏移,小孔隙  $T_2$  谱的核磁共振信号强度增加。这也说明了在冰的冻胀和融缩作用下,岩石内部产生了新的微孔隙。随着冻融次数的增多,第一和第二个峰的幅度均明显增大,尤其是岩样经过真空饱和后,第一个峰的幅度增大得更明显,表明在花岗岩中产生了新的微孔隙,并且水分进入了微孔隙中,因此核磁共振信号强度增大。

随着冻融次数的增加,右侧的第三个峰所对应的稍大尺寸微孔隙,变化并不明显,而且由表2可知,第三和第四个峰的峰面积之和所占比例小于2%,表明在岩样内部并未出现明显的裂纹扩展、孔隙尺寸大幅度增大的现象,据此推测出岩样内部还未出现较为严重的冻融损伤。根据 A. C. Iñigo 等<sup>[17]</sup>的试验结果,冻融循环对花岗岩这类致密型岩石的损伤较小,核磁共振试验结果得出了相似的结论。

### 3.3 $T_2$ 谱面积分析

表2 不同冻融循环下真空饱和和岩石核磁共振谱面积

Table 2 NMR spectrum area under vacuum saturation condition with different freezing and thawing cycles

循环次数	峰总面积	第一个峰所占百分比/%	第二个峰所占百分比/%	第三个峰所占百分比/%	第四个峰所占百分比/%
0	8 442	59.150	38.963	1.887	-
10	9 821	66.814	31.814	1.372	-
20	9 914	66.287	31.519	2.194	-
30	11 830	64.358	33.524	2.117	0.001
40	12 019	63.225	34.810	1.951	0.014

核磁共振的全部  $T_2$  谱面积可以视为核磁共振孔隙度,是反映孔隙结构变化的一个重要参数,它等于或略小于岩石的有效孔隙度。弛豫时间谱积分面积的大小,与岩石中所含流体的多少成正比,因此岩样在经历不同的冻融循环次数后,  $T_2$  谱分布积分面积的变化,反映了岩石孔隙体积的变化<sup>[18]</sup>。不同冻融循环次数后,花岗岩岩样  $T_2$  谱面积的变化特性及每个峰所占比例如表2所示。

从表2可以看出,随着冻融循环次数的增加,  $T_2$  谱面积逐渐增大,表明岩石的孔隙体积随着冻融次数的增大而增大。对应小尺寸微孔隙的第一个峰和第二个峰的峰面积之和占峰总面积的98%以上,表明小尺寸的微孔隙占绝大多数。在经历10次冻融循环后,岩石的孔隙有一个明显的增大,孔隙率增大了14.0%,而在经历从10次到20次冻融循环过程中,  $T_2$  谱面积均未发生明显的变化,真空饱和情况下的孔隙变化率也仅为0.9%。总体而言,在经历20次冻融循环后,岩石的内部结构受冻融循环的影响较小,因而孔隙体积变化不大。在经历30次冻融循环后,真空饱和后的  $T_2$  谱面积有一个较为明显的变化,增大了16.2%,但经历40次冻融循环后,谱面积的变化趋势又变得缓慢,变化率仅为1.6%。

图5为岩样在经历不同冻融次数后自然饱和和真空饱和2种条件下  $T_2$  谱面积的变化情况。随着冻融循环次数的增加,2种条件下的  $T_2$  谱面积均会增加,表明岩石内部产生了新的微孔隙,从而使得岩石中的总孔隙体积也逐渐变大。在20次冻融循环后,2种条件下的  $T_2$  谱面积差别很小,但经过30,40次冻融循环后,增加的幅度出现了明显的差距,表明在自然饱和条件下,水分无法迁移到小尺寸的微孔隙中,并未达到完全意义上的饱和。从图5可

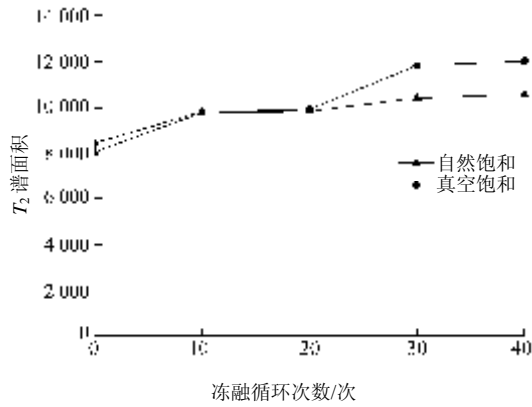


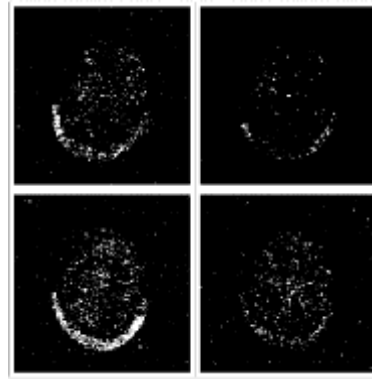
图 5 不同冻融循环次数  $T_2$  谱面积变化情况

Fig.5  $T_2$  spectrum area variation under different freezing and thawing cycles

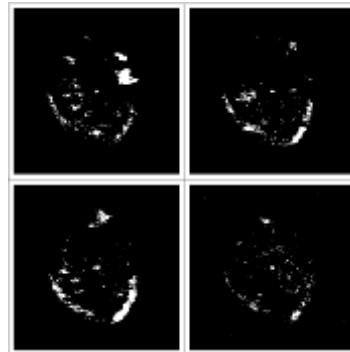
知, 经历 30, 40 次冻融循环后, 真空饱和条件下的谱面积比自然饱和条件下的谱面积分别增大了 11.9% 和 12.0%, 据此推算出岩石中微孔隙体积分别增大了 11.9% 和 12.0%。

#### 4 核磁共振成像分析

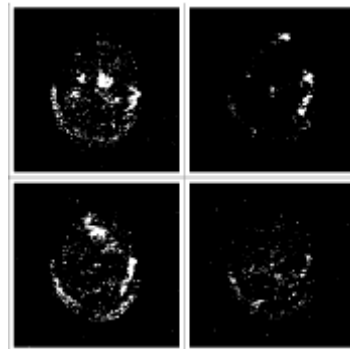
对经历不同冻融循环次数后的岩样进行了核磁共振成像测量, 获得了沿岩样轴向方向依次排列 4 个不同位置的横截面二维成像, 图 6 为每组冻融循环中典型岩样的核磁共振成像结果。在图 6 中, 横



(c) N - 9 岩样



(d) N - 11 岩样



(e) N - 13 岩样

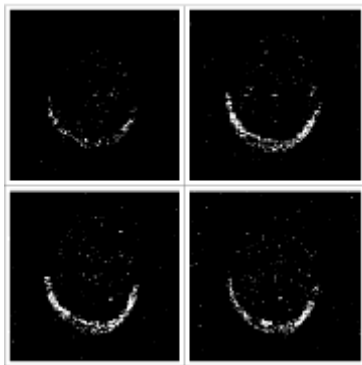
(注: (1) 各截面图中下侧半月型较亮部分为试验中用于托放样品的载床; (2) 沿岩样轴向方向依次成像, 4 个成像图查看方向为: 从左至右, 先上后下, 依次排列)

图 6 冻融循环后典型岩样的核磁共振成像结果

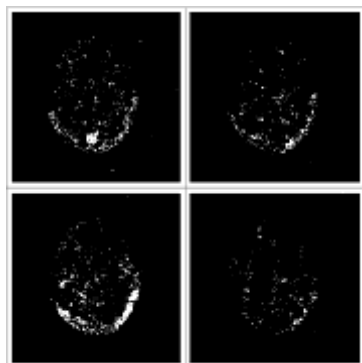
Fig.6 NMR images of some typical samples under freezing and thawing cycles

向切片图像为岩样形状(因岩样中含有微量铁质成分, 对核磁共振信号有所干扰, 图像稍有变形), 图像中亮色区域为水分子所在区域, 周围黑色区域为底色, 图像的亮度反映了岩石中含水量的多少, 即色泽越亮, 代表此区域水分就越高, 说明此区域孔隙越大。

图 6(a)为未经过冻融循环的岩样, 图像较暗, 含水量少, 各个截面的图像亮暗均匀, 说明孔隙分



(a) N - 3 岩样



(b) N - 6 岩样

布均匀,未见较大孔隙。图 6(b)为经过 10 次冻融循环后的图像,图像亮度增大,在左上方截面图中的下部区域出现了一个较大孔隙,其余各个截面图像亮暗均匀。

图 6(c)为经历 20 次冻融后的岩样,图像亮度明显增大,亮暗均匀,但未见较大孔隙。右上截面图中图像较暗,表明岩样轴向中部的岩石结构致密。

图 6(d)表明,经历 30 次冻融循环后,在左侧 2 个截面图中的周边位置上出现了明显的大孔隙结构,亮度较强,可以明显看出孔隙的大小和形状。在右上截面图中的上部区无亮点,表明该处为无孔隙结构。

从图 6(e)可以看出,经历 40 次冻融循环后,在岩心的中心、周边都出现了较大的孔隙,而且孔隙沿岩样的轴向方向延伸,2 个截面图之间的大孔隙是连通的。图像亮暗不均,均匀度也非常差,孔隙分布非常不均匀,孔隙的分布情况进一步解释了表 1 中该岩样为冻融前后质量变化最大的原因。

由图 6(d)和 6(e)可知,在试件的周边和中心都出现了大孔隙结构。笔者分析有 2 个原因导致大孔隙出现在周边位置:一是试件表面存在着微裂隙(尤其是肉眼可辨的微裂纹),冻融作用下,裂隙向内扩展产生孔隙,外部水分也容易进入这些孔隙中;二是在冻融过程中,试件表面位置受冻融温度变化的影响最大,而温度变化是影响岩石冻融损伤劣化的重要因素之一<sup>[19]</sup>,因此也会导致大孔隙先出现在试件周边。

大孔隙出现在试件的中心主要是由于岩石为多孔介质材料,岩石内部有存在着大孔隙结构的可能性;此外,图 6(e)中左上图截面对应于试件的轴向端部位置,可以视为试件的周边位置,因此在冻融作用下产生了损伤,在截面中心处出现了大孔隙。

## 5 结 论

(1) 花岗岩的核磁共振  $T_2$  谱分布主要为 3 个峰,部分为 4 个峰,第一个峰和第二个峰的面积占峰总面积的 98%以上,表明微裂隙占绝大多数。随着冻融循环次数的增大,第一个峰和第二个峰面积均逐渐增大,说明低温冻融循环作用使花岗岩中产生了新的孔隙,但在经历了 40 次冻融循环后,较大尺寸的孔隙所占比例仍然极少,表明未出现孔隙明

显变宽的现象,可以推测,岩样内部还未出现较为严重的冻融损伤。

(2) 在分别经历 10, 20, 30 和 40 次冻融循环次数后,岩石的  $T_2$  谱面积发生了明显变化,孔隙率分别增大了 14.0%, 0.9%, 16.2%和 1.6%。不同的冻融阶段,谱面积变化幅度不同,但总体变化趋势是不断增大的,表明随着冻融次数的增加,岩石内部产生了新的孔隙,小孔隙所占比例逐渐增大。

(3) 核磁共振成像结果展现出了不同冻融循环次数后岩样内部孔隙的分布情况,直观地看出了岩石的内部微观结构,为分析岩石的冻融损伤过程提供了信息,这也是核磁共振技术特有的优势。

(4) 冻融循环条件下岩石核磁共振特征的变化规律,为岩石冻融损伤的研究提供了可靠的试验数据。核磁共振成像技术的发展与应用,为岩石物理试验研究提供了一种新的无损检测方法,必将推动岩石物理试验技术的发展。

## 参考文献(References):

- [1] 赵文. 岩石力学[M]. 长沙:中南大学出版社,2010:4-5.(ZHAO Wen. Rock mechanics[M]. Changsha: Central South University Press, 2010: 4-5.(in Chinese))
- [2] NICHOLSON D T, NICHOLSON F H. Physical deterioration of sedimentary rocks subjected to experimental freeze-thaw weathering[J]. Earth Surface Processes and Landforms, 2000, 25(12): 1 295 - 1 307.
- [3] 徐光苗. 寒区岩体低温、冻融损伤力学特性及多场耦合研究[博士学位论文][D]. 武汉:中国科学院武汉岩土力学研究所,2006.(XU Guangmiao. Study on mechanical characteristics of rock at low temperature due to freezing-thawing and multi-physical coupling problems of rock in cold regions[Ph. D. Thesis][D]. Wuhan: Institute of Rock and Soil Mechanics, Chinese Academy of Sciences, 2006.(in Chinese))
- [4] BELLANGER M, HOMAND F, REMY J M. Water behavior in limestone as a function of pores structure: application to frost resistance of some lorraine limestones[J]. Engineering Geology, 1993, 36(1/2): 99 - 108.
- [5] 吴刚,何国梁,张磊,等. 大理岩循环冻融试验研究[J]. 岩石力学与工程学报,2006,25(增1):2 930-2 938.(WU Gang, HE Guoliang, ZHANG Lei, et al. Experimental study of cycles of freeze-thaw of marble[J]. Chinese Journal of Rock Mechanics and Engineering, 2006, 25(Supp.1): 2 930 - 2 938.(in Chinese))
- [6] 张继周,缪林昌,杨振峰. 冻融条件下岩石损伤劣化机制和力学特

- 性研究[J]. 岩石力学与工程学报, 2008, 27(8): 1 688 - 1 694.  
(ZHANG Jizhou, MIAO Linchang, YANG Zhenfeng. Research on rock degradation and deterioration mechanisms and mechanical characteristics under cyclic freezing-thawing[J]. Chinese Journal of Rock Mechanics and Engineering, 2008, 27(8): 1 688 - 1 694.(in Chinese))
- [7] DE ARGANDONA R V G, REY A R, CELORIO C, et al. Characterization by computed X-Ray tomography of the evolution of the pore structure of a dolomite rock during freeze-thaw cyclic tests[J]. Physics and Chemistry of the Earth, Part A: Solid Earth and Geodesy, 1999, 24(7): 633 - 637.
- [8] 杨更社, 张全胜, 蒲毅彬. 冻结温度影响下岩石细观损伤演化 CT 扫描[J]. 长安大学学报: 自然科学版, 2004, 24(6): 40 - 42.(YANG Gengshe, ZHANG Quansheng, PU Yibin. CT scanning test of meso-damage propagation of rock under different freezing temperatures[J]. Journal of Chang'an University: Natural Science, 2004, 24(6): 40 - 42.(in Chinese))
- [9] 杨更社, 张全胜, 任建喜, 等. 冻结速度对铜川砂岩损伤 CT 数变化规律研究[J]. 岩石力学与工程学报, 2004, 23(24): 4 099 - 4 104.(YANG Gengshe, ZHANG Quansheng, REN Jianxi, et al. Study of the effect of freezing rate on the damage CT values of Tongchuan sandstone[J]. Chinese Journal of Rock Mechanics and Engineering, 2004, 23(24): 4 099 - 4 104.(in Chinese))
- [10] 张全胜. 冻融条件下岩石细观损伤力学特性研究初探[硕士学位论文][D]. 西安: 西安科技大学, 2003.(ZHANG Quansheng. The preliminary research on mesodamage mechanical characteristics of rock under condition of freezing and thawing[M. S. Thesis][D]. Xi'an: Xi'an University of Science and Technology, 2003.(in Chinese))
- [11] 刘成禹, 何满潮, 王树仁, 等. 花岗岩低温冻融损伤特性的实验研究[J]. 湖南科技大学学报: 自然科学版, 2005, 20(1): 37 - 40.(LIU Chengyu, HE Manchao, WANG Shuren, et al. Experimental investigation on freeze-thawing damage characteristics of granite at low temperature[J]. Journal of Hunan University of Science and Technology: Natural Science, 2005, 20(1): 37 - 40.(in Chinese))
- [12] 张超谟, 陈振标, 张占松, 等. 基于核磁共振  $T_2$  谱分布的储层岩石孔隙分形结构研究[J]. 石油天然气学报, 2007, 29(4): 80 - 86.(ZHANG Chaomo, CHEN Zhenbiao, ZHANG Zhansong, et al. Characteristics of reservoir rock pore fractal structure based on nuclear magnetic resonance(NMR)  $T_2$  distribution[J]. Journal of Oil and Gas Technology, 2007, 29(4): 80 - 86.(in Chinese))
- [13] 肖立志. 核磁共振成像测井与岩石核磁共振及其应用[M]. 北京: 科学出版社, 1998: 1 - 26.(XIAO Lizhi. NMR imaging logging principles and applications[M]. Beijing: Science Press, 1998: 1 - 26.(in Chinese))
- [14] 王 胜. 用核磁共振分析岩石孔隙结构特征[J]. 新疆石油地质, 2009, 30(6): 768 - 770.(WANG Sheng. Analysis of rock pore structural characteristic by nuclear magnetic resonance[J]. Xinjiang Petroleum Geology, 2009, 30(6): 768 - 770.(in Chinese))
- [15] 中华人民共和国行业标准编写组. SL264—2001 水利水电工程岩石试验规程[S]. 北京: 中国水利水电出版社, 2001.(The Professional Standards Compilation Group of People's Republic of China. SL264—2001 Specifications for rock tests in water conservancy and hydroelectric engineering[S]. Beijing: China Water Power Press, 2001.(in Chinese))
- [16] COATES G, 肖立志, PRAMMER M. 核磁共振测井原理与应用[M]. 孟繁莹译. 北京: 石油工业出版社, 2007: 6 - 7.(COATES G, XIAO Lizhi, PRAMMER M. Nuclear magnetic resonance(NMR) logging principles and its application[M]. Translated by MENG Fanying. Beijing: Petroleum Industry Press, 2007: 6 - 7.(in Chinese))
- [17] IÑIGO A C, VICENTE M A, RIVES V. Weathering and decay of granitic rocks: its relation to their pore network[J]. Mechanics of Materials, 2000, 32(9): 555 - 560.
- [18] 张元中, 肖立志. 单轴载荷下岩石核磁共振特征的实验研究[J]. 核电子学与探测技术, 2006, 26(6): 731 - 734.(ZHANG Yuanzhong, XIAO Lizhi. Experimental study of the nuclear magnetic resonance(NMR) characteristics in rock under uniaxial load[J]. Nuclear Electronics and Detection Technology, 2006, 26(6): 731 - 734.(in Chinese))
- [19] 徐光苗, 刘泉声. 岩石冻融破坏机制分析及冻融力学试验研究[J]. 岩石力学与工程学报, 2005, 24(17): 3 076 - 3 082.(XU Guangmiao, LIU Quansheng. Analysis of mechanism of rock failure due to freeze thaw cycling and mechanical testing study of frozen-thawed rocks[J]. Chinese Journal of Rock Mechanics and Engineering, 2005, 24(17): 3 076 - 3 082.(in Chinese))

## 煤中水可动性的核磁共振响应及其影响因素

吕玉民<sup>1</sup>, 胡爱梅<sup>2</sup>, 汤达祯<sup>1</sup>, 宋波<sup>2</sup>, 梁为<sup>2</sup>, 许浩<sup>1</sup>, 林文姬<sup>2</sup>, 胡雄<sup>2</sup>

1. 中国地质大学(北京)煤储层实验室, 北京 100083; 2. 中联煤层气国家工程研究中心, 北京 100095

**摘要:** 依托韩城地区主要煤层, 开展了饱和水煤岩在两种不同离心速率下离心1.5 h后的核磁共振实验。同时, 结合称重测煤芯饱和度的方法, 分析了不同离心速率下煤岩内部可动流体和束缚流体的消长关系。实验表明, 离心速率增大, 煤岩核磁整体信号衰减, 横向弛豫时间( $T_2$ )的几何均值和截止值逐渐下降。与饱和水煤岩相比, 2000 r/min速率离心后的煤岩 $T_2$ 谱强度下降5.14%~52.39%, 几何均值下降24.72%~71.22%; 4000 r/min速率离心后的煤岩 $T_2$ 谱强度下降49.51%~63.36%, 几何均值下降44.69%~81.59%;  $T_2$ 截止值下降44.09%~74.30%。研究发现, 离心前后煤岩内部残留水量变化率与 $T_2$ 谱累计强度变化率具有很好的一致性, 但与几何均值之间的相关性明显较差。分析认为, 离心速率和孔渗特征共同决定煤层水可动性的NMR响应。

**关键词:** 煤; 束缚水; 可动性; 离心; 核磁共振响应

中图分类号: P618.11

文献标识码: A

文章编号: 1006-7493(2012)03-0548-04

## Nuclear Magnetic Resonance (NMR) Response of Mobile Water in Coals and Influencing Factors

LV Yumin<sup>1</sup>, HU Aimei<sup>2</sup>, TANG Dazhen<sup>1</sup>, SONG Bo<sup>2</sup>, LIANG Wei<sup>2</sup>, XU Hao<sup>1</sup>, LIN Wenji<sup>2</sup>, HU Xiong<sup>2</sup>

1. Coal Reservoir Laboratory, China University of Geoscience, Beijing 100083, China;

2. China United Coalbed Methane National Engineering Research Center, Beijing 100095, China

**Abstract:** Taking a case of major coal seams in the Hancheng area, the nuclear magnetic resonance (NMR) responses of water-saturated coal samples were measured at two centrifugal rates for 1.5 hours. Weight-saturation method was applied to analyze the relationship between saturations of mobile and bound fluids at various centrifugal rates. It was shown that the NMR signal of coal samples weakens and geometric mean and cutoff value of the transverse relaxation time ( $T_2$ ) descend as the centrifugal rate increases. Compared with water-saturated coal samples, the  $T_2$  spectrum intensity of coal samples centrifuged at 2000r/min reduces by 5.14% to 52.39% and the geometric mean decreases by 24.72% to 71.22%, the  $T_2$  spectrum intensity of coal samples at 4000 r/min reduces by 49.51% to 63.36% and the geometric mean decreases by 44.69% to 81.59%, and the cutoff value of  $T_2$  spectrum drops by 44.09% to 74.30%. It was found that the change rate of residue water amount in centrifuged coal samples has a good saggessed with the change rate of NMR accumulative intensity, but has a poor relationship with the change rate of cutoff value. It was suggested that the NMR response of mobile water in coal is controlled jointly by the centrifugal rate and porosity-permeability of coals.

**Key words:** coal; bound water; mobile; centrifugation; nuclear magnetic resonance response

**First author:** LV Yumin, Ph. D. candiadate; E-mail: yale1210@163.com

收稿日期: 2012-03-11; 修回日期: 2012-04-19

基金项目: 国家重点基础研究发展计划(902009CB219604); 国家科技重大专项(2011ZX05038-001)和中央高校基本科研业务费(2011PY0211)联合资助

作者简介: 吕玉民, 1985年生, 男, 博士研究生, 油气及煤层气地质研究方向; E-mail: yale1210@163.com

核磁共振 (NMR) 作为一种先进的实验手段, 可直接探测煤层中流体及其与煤表面的相互作用 (王为民, 2001; 姚艳斌, 2008)。国内引入该项技术开展石油地质基础性实验 (刘堂宴等, 2003; 何雨丹等, 2005; 刘堂宴等, 2004; 周宇等, 2011), 在煤层气赋存特点和吸附机理、煤层气水两相渗流、煤层物性定量表征等方面也取得较多研究成果 (唐巨鹏等, 2005; 石强等, 2006; 胡爱军等, 2007; 潘一山等, 2008; 姚艳斌等, 2008; 杨正明等, 2009)。本文考虑煤岩易碎以及NMR在研究孔隙流体中的技术优势等, 针对性地设计了两种离心速率的离心实验, 对实验前后煤样进行核磁共振测试, 在煤岩束缚流体变化规律及其NMR响应方面取得新的认识。

## 1 样品与实验方法

3件贫煤样品采自韩城地区盛捷煤矿 (SJ) 3号煤层、象山煤矿 (XS) 5号煤层和禹昌煤矿 (YC) 11号煤层, 在600 psi围压下测定了煤样的水相孔隙度和氦气渗透率 (表1)。

实验采用的核磁共振分析仪磁场强度大于

表1 煤样基本性质  
Table 1 Basic properties of coal samples

序号	样品编号	孔隙度(%)	渗透率(mD)	工业分析(%)		
				M <sub>ad</sub>	A <sub>ad</sub>	V <sub>ad</sub>
1	SJ-3	5.06	0.043	0.61	11.18	11.63
2	XS-5	5.35	0.091	0.92	9.72	10.49
3	YC-11	4.09	0.019	0.43	12.54	10.38

0.5 T, 共振频率21~23 MHz, 磁场稳定工作温度32℃。测试条件为: 工作频率23.354 MHz, 回波时间175 μs, 恢复时间1500 ms, 回波数8195, 信噪比控制在80:1以上, T<sub>2</sub>谱拟合点数64。实验过程中, 始终保持核磁共振仪测试参数前后测试的一致性。

将煤样置于烘干箱内, 在110℃的温度下烘干4 h, 冷却后对干燥煤样称重; 将煤样置于真空泵内抽真空负压饱和水4 h, 再常压饱和水96 h, 对饱和水煤样称重, 得出饱和水的重量。测试得到饱和水煤样核磁共振T<sub>2</sub>弛豫时间及谱图。接着, 分别在离心速率2000 r/min和4000 r/min, 32℃恒温条件下离心1.5 h, 分别对离心后的煤样称重得到残余水的重量, 并测试得到残余水煤样的T<sub>2</sub>弛豫时间及谱图 (表2, 图1)。

表2 不同束缚水含量煤样的NMR特征参数

Table 2 NMR characteristic parameters of coal samples with various bound water content

煤样	对比项	水的重量(g/g)	信号总强度(H)	T <sub>2</sub> 几何均值(ms)	T <sub>2</sub> 截止值(ms)
SJ-3	饱和水	0.0193	16498.37	2.81	—
	2000 r/min离心	0.0158	7854.37	1.80	2.22
	4000 r/min离心	0.0062	6044.98	1.55	1.25
XS-5	饱和水	0.0155	9222.67	6.99	—
	2000 r/min离心	0.0121	5227.56	2.01	12.68
	4000 r/min离心	0.0105	4215.26	1.29	5.90
YC-11	饱和水	0.0140	8393.70	69.31	—
	2000 r/min离心	0.0099	7962.15	52.17	368.98
	4000 r/min离心	0.0059	4238.25	16.42	95.06

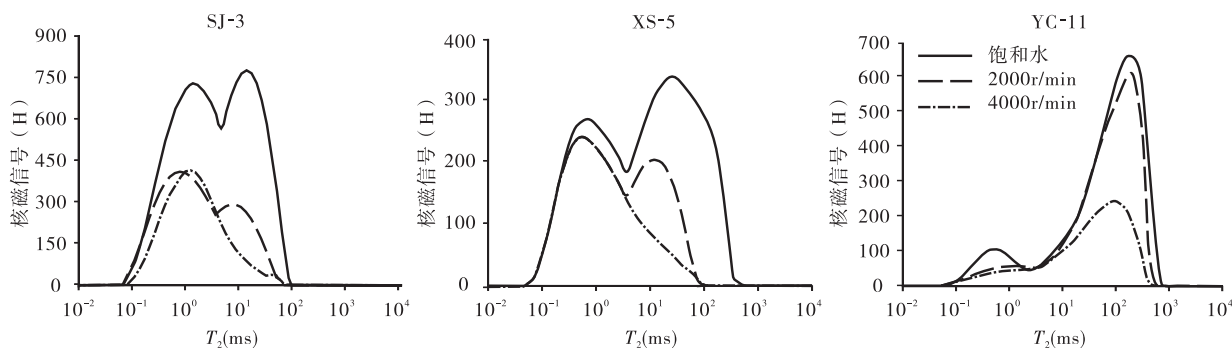


图1 煤样离心前后的核磁谱图

Fig.1 NMR spectra of coal samples before and after centrifugation

## 2 结果与讨论

### 2.1 含水量的NMR响应

实验结果显示,随着离心速率的逐步提高,单位重量煤样的含水量、核磁信号总强度以及 $T_2$ 几何均值均出现不同程度的下降(图2)。2000 r/min速率离心后,煤样残余水量下降18.28%~29.04%,信号总强度下降5.14%~52.39%; $T_2$ 几何均值下降24.72%~71.22%。4000 r/min离心处理后,煤样残余水量下降32.32%~67.71%,信号总强度下降49.51%~63.36%, $T_2$ 几何均值下降44.69%~81.59%, $T_2$ 截止值下降44.69%~81.59%。含水量大小与NMR响应强度一致,且随着离心速率的增加,单位重量煤样含水量与 $T_2$ 几何均值及截止值出现一致性下降。

SJ-3和XS-5饱和水煤样的弛豫谱为双峰形态,且偏中部分布,显示煤中较大和较小孔径的孔隙均较为发育,两者之间的连续性相对较稍差;YC-11饱和水煤样的弛豫谱图为单峰形态且峰偏右,表明较大孔径的孔隙十分发育,中-小孔径的孔隙发育较差(图1)。

2000 r/min速率离心后,SJ-3和XS-5煤样弛豫谱峰值信号明显减弱,但仍为双峰形态,且右峰比左峰信号强度下降明显,表明较大孔隙内的束缚水排出较多;YC-11煤样弛豫谱图单峰下降较弱,表明该煤样孔隙的孔径虽然较大,但所含的束缚水仍难以排出(图1)。

4000 r/min速率离心后,SJ-3和XS-5煤样较大孔隙内的水基本排出,弛豫谱双峰消失,仅保留左峰且该峰强度基本不变,指示较大孔隙内的水已完全排出;YC-11煤样中的水大量排出,弛豫谱峰

值强度明显地降低(图1)。

### 2.2 孔渗特征对煤层水可动性的影响

随着离心速率的增大,煤样孔隙水突破毛管力束缚而逐渐排出。一般来说,较大孔隙内的水所受毛管力作用较弱,在同等离心力作用下较易排出,较小孔隙内的水因毛管力束缚较强而残留在煤岩内部。SJ-3和XS-5煤样均发育明显的大孔和小孔,过渡孔发育较差,且离心前右峰比左峰更为明显,但二次离心后右峰逐渐减弱,直至消失。因此,孔隙度较大的煤样,其孔隙水可动性较强,同等条件下离心后 $T_2$ 几何均值及截止值同样消减得较为显著(图3)。

煤层水可动性也明显受到渗透性的影响。煤样渗透率增高,NMR信号总强度、 $T_2$ 几何均值、 $T_2$ 截止值均随之降低,但后两者的降低趋势更为明显(图4)。渗透性差的煤层,其孔隙间吼道小、连通性差,即使具有较大的孔径也难以排出水,如YC-11煤样。核磁谱图显示,YC-11煤样大孔发育、中小孔发育较差,但由于渗透率差(表1),连通孔径间的吼道小、毛管力强(图1),造成煤层水发生流动需要更大的离心力。

### 2.3 煤层水可动性NMR响应影响因素综合分析

综合上述分析,作者认为煤层水可动性受离心速率(离心力)和孔渗特征的双重影响。离心速率越大,即离心力越大,煤层水可动性越强。同时,煤层孔渗性越好,其孔隙水越容易发生流动。究其根本原因,煤层水可动性受控于离心力与毛管力相互间的大小关系。离心力越大,能克服的毛管力越大,造成大孔和小孔内煤层水易于流出,导致煤层束缚水NMR响应强度越弱, $T_2$ 几何均值和截止值越小,导致煤层水可动性NMR

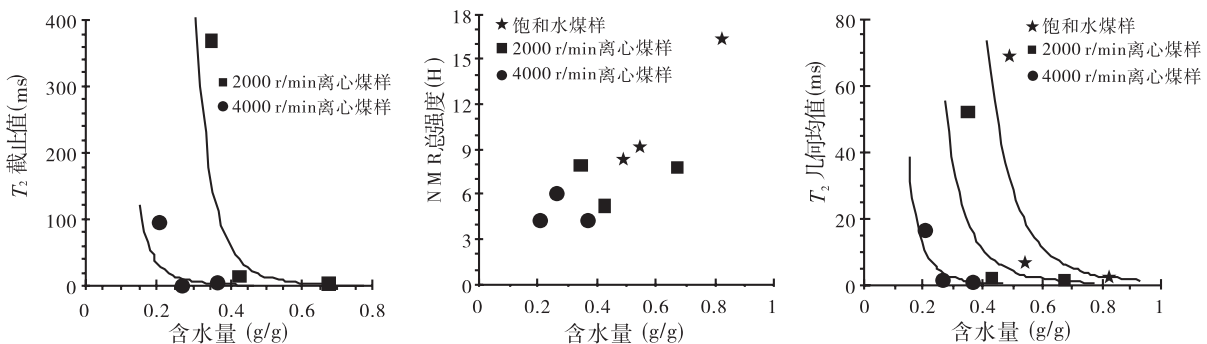


图2 煤中束缚水含量与NMR特征参数之间关系

Fig. 2 Plots of bound water content to NMR parameters of coal samples



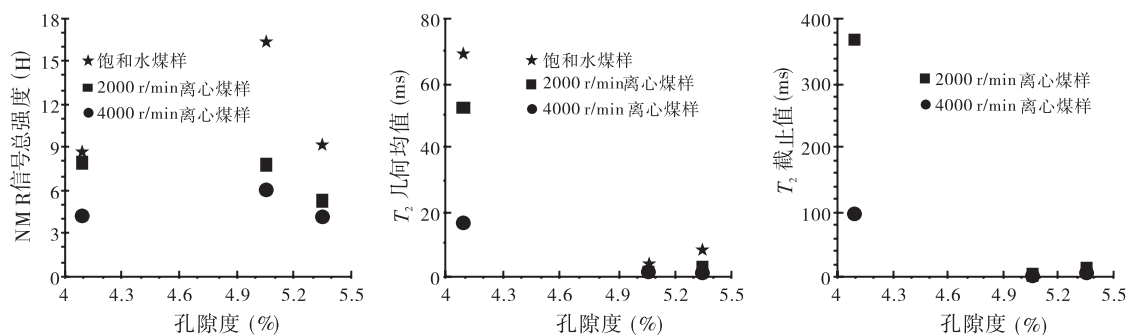


图3 煤样孔隙度与核磁共振响应之间关系

Fig.3 Plots of porosity to NMR responses of coal samples

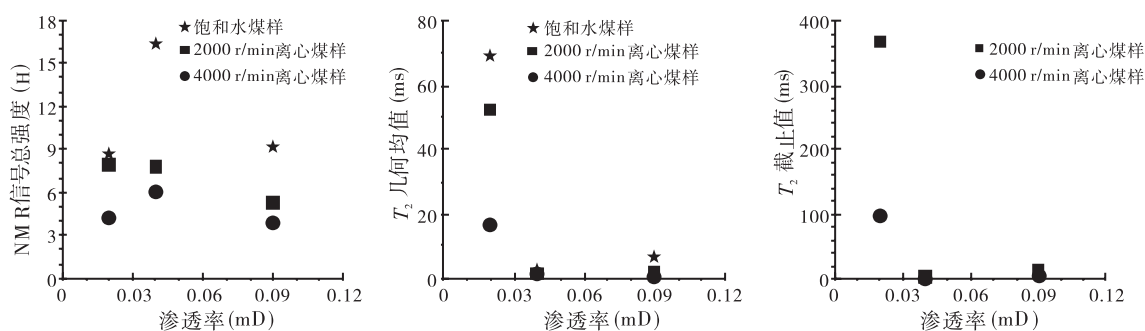


图4 煤样渗透率与核磁共振响应之间关系

Fig. 4 Plots of permeability to NMR responses of coal samples

响应的变化越强。煤层毛管力越小，煤层水流动的阻力越小，同等条件下离心出来的水也越多，NMR响应变化也越显著。

### 3 结论

1) 随着离心速率的增大，煤岩核磁整体信号越来越弱，右峰逐渐消减，左峰逐渐凸显，同时也造成横向弛豫时间 ( $T_2$ ) 的几何均值和截止值逐渐下降，表明较大孔隙内的水在离心力作用下逐步克服毛管力作用而逐渐排出，而较小孔径内的水因受强烈的毛管力作用而难以排出。

2) 离心前后煤岩内部残留水量与核磁  $T_2$  信号强度变化具有很好的一致性，但与  $T_2$  几何均值、截止值间的相关性明显较差。

3) 离心速率（离心力）和孔渗特征决定煤层水可动性的NMR响应。离心速率越大和孔渗特征越好，排出的煤层水越多，其可动性NMR响应的变化幅度也越大。

### 参考文献:

- 何雨丹, 毛志强, 肖立志, 等. 2005. 核磁共振  $T_2$  分布评价岩石孔径分布的改进方法[J]. 地球物理学报, 48(2): 373-378.
- 胡爱军, 潘一山, 唐巨鹏, 等. 2007. 型煤的甲烷吸附以及NMR实验研究[J]. 洁净煤技术, 13(3): 37-40.
- 刘堂宴, 肖立志, 傅容珊. 2004. 球管孔隙模型的核磁共振(NMR)弛豫特征及应用[J]. 地球物理学报, 47(4): 663-671.
- 刘堂宴, 王绍民, 傅容珊, 等. 2003. 核磁共振谱的岩石孔喉结构分析[J]. 石油地球物理勘探, 38(3): 328-333.
- 潘一山, 唐巨鹏, 李成全. 2008. 煤层中气水两相运移的NMR试验研究[J]. 地球物理学报, 51(5): 1620-1626.
- 石强. 2006. 煤体结构及渗流特性的核磁共振成像实验研究[D]. 沈阳: 辽宁工程技术大学.
- 唐巨鹏, 潘一山, 张佐刚. 2005. 煤层气赋存和运移规律的NMR研究[J]. 辽宁工程技术大学学报, 24(5): 674-676.
- 王为民. 2001. 核磁共振岩石物理研究及其在石油工业中的应用[D]. 北京: 中国科学院: 1-2.
- 杨正明, 鲜保安, 姜汉桥, 等. 2009. 煤层气藏核磁共振技术实验研究[J]. 中国煤层气, 6(4): 20-23.
- 姚艳斌. 2008. 煤层气储层精细定量表征与综合评价模型[D]. 北京: 中国地质大学: 107-108.
- 周宇, 魏国齐, 郭和坤. 2011. 核磁共振孔隙度影响因素分析与校准[J]. 测井技术, 35(3): 210-214.

## 其它

附件 2（征文格式要求）：

## 一种微型核磁共振探头的制作工艺

陆荣生，吴卫平，周新龙，倪中华\*

（东南大学机械工程学院，江苏省南京市 211189）

**摘要：**探头是微型核磁共振设备的重要组成部分，它在检测过程中有容纳样本、将样本置于磁场空间、发射射频脉冲、接收磁共振信号等功能。提出了一种基于 PDMS 的螺线管线圈探头的制作工艺。该工艺首先将铜丝缠绕在均匀金属棒上，利用已固化的 PDMS 均匀基底固定金属棒，用 PDMS 预聚物浇注固化金属棒，固化后抽出金属棒，切割、打孔、封装后安装到设计好的电路板上，然后进行阻抗匹配，匹配成功后既完成探头的制作。实验证明，依此法制作的螺线管线圈探头具有较高的信噪比，能够获得较好的信号，进一步说明的该方法的可行性和有效性。

**关键词：**探头，PDMS，螺线管，微通道。





